JSCSEN 87(7-8)785–967(2022)

ISSN 1820-7421(Online)

Journal of the Serbian Chemical Society

eVersion
electronic

Serbian
Chemical Society
125
ANNIVERSARY

VOLUME 87

No 7-8

BELGRADE 2022

Available on line at

СХД
1897

www.shd.org.rs/JSCS/

The full search of JSCS
is available through

DOAJ DIRECTORY OF OPEN ACCESS JOURNALS
www.doaj.org

The **Journal of the Serbian Chemical Society** (formerly Glasnik Hemijskog društva Beograd), one volume (12 issues) per year, publishes articles from the fields of chemistry. The **Journal** is financially supported by the **Ministry of Education, Science and Technological Development of the Republic of Serbia.**

Articles published in the **Journal** are indexed in **Clarivate Analytics products: Science Citation Index-Expanded**^{TM} – accessed *via* **Web of Science**$^{®}$ and **Journal Citation Reports**$^{®}$.

Impact Factor announced 2022: **1.100; 5-year Impact Factor**: **1.175**.

Articles appearing in the **Journal** are also abstracted by: **Scopus, Chemical Abstracts Plus (CAplus**^{SM}**), Directory of Open Access Journals, Referativnii Zhurnal (VINITI), RSC Analytical Abstracts, EuroPub, Pro Quest** and **Asian Digital Library.**

Publisher:	**Serbian Chemical Society**, Karnegijeva 4/III, P. O. Box 36, 1120 Belgrade 35, Serbia tel./fax: +381–11–3370–467, E-mails: **Society** – shd@shd.org.rs; **Journal** – jscs@shd.org.rs Home Pages: **Society** – http://www.shd.org.rs/, **Journal** – http://www.shd.org.rs/JSCS/
Internet Service:	Contents, Abstracts and full papers (from Vol 64, No. 1, 1999) are available in the electronic form at the Web Site of the **Journal** (http://www.shd.org.rs/JSCS/).
Former Editors:	**Nikola A. Pušin** (1930–1947), **Aleksandar M. Leko** (1948–1954), **Panta S. Tutundžić** (1955–1961), **Miloš K. Mladenović** (1962–1964), **Đorđe M. Dimitrijević** (1965–1969), **Aleksandar R. Despić** (1969–1975), **Slobodan V. Ribnikar** (1975–1985), **Dragutin M. Dražić** (1986–2006).
Editor-in-Chief:	BRANISLAV Ž. **NIKOLIĆ**, Serbian Chemical Society (E-mail: jscs-ed@shd.org.rs)
Deputy Editor:	DUŠAN **SLADIĆ**, Faculty of Chemistry, University of Belgrade
Sub editors:	
Organic Chemistry	DEJAN **OPSENICA**, Institute of Chemistry, Technology and Metallurgy, University of Belgrade JÁNOS **CSANÁDI**, Faculty of Science, University of Novi Sad
Biochemistry and Biotechnology	OLGICA **NEDIĆ**, INEP – Institute for the Application of Nuclear Energy, University of Belgrade
Inorganic Chemistry	MILOŠ **ĐURAN**, Serbian Chemical Society
Theoretical Chemistry	IVAN **JURANIĆ**, Serbian Chemical Society
Physical Chemistry	LJILJANA **DAMJANOVIĆ-VASILIĆ**, Faculty of Physical Chemistry, University of Belgrade
Electrochemistry	SNEŽANA **GOJKOVIĆ**, Faculty of Technology and Metallurgy, University of Belgrade
Analytical Chemistry	SLAVICA **RAŽIĆ**, Faculty of Pharmacy, University of Belgrade
Polymers	BRANKO **DUNJIĆ**, Faculty of Technology and Metallurgy, University of Belgrade
Thermodynamics	MIRJANA **KIJEVČANIN**, Faculty of Technology and Metallurgy, University of Belgrade
Chemical Engineering	TATJANA **KALUĐEROVIĆ RADOIČIĆ**, Faculty of Technology and Metallurgy, University of Belgrade
Materials	RADA **PETROVIĆ**, Faculty of Technology and Metallurgy, University of Belgrade
Metallic Materials and Metallurgy	ANA **KOSTOV**, Mining and Metallurgy Institute Bor, University of Belgrade
Environmental and Geochemistry	VESNA **ANTIĆ**, Faculty of Agriculture, University of Belgrade
History of and Education in Chemistry	DRAGICA **TRIVIĆ**, Faculty of Chemistry, University of Belgrade
English Language Editors:	LYNNE **KATSIKAS**, Serbian Chemical Society VLATKA **VAJS**, Serbian Chemical Society JASMINA **NIKOLIĆ**, Faculty of Technology and Metallurgy, University of Belgrade
Technical Editors:	VLADIMIR **PANIĆ**, ALEKSANDAR **DEKANSKI**, VUK **FILIPOVIĆ**, Institute of Chemistry, Technology and Metallurgy, University of Belgrade
Journal Manager & Web Master:	ALEKSANDAR **DEKANSKI,** Institute of Chemistry, Technology and Metallurgy, University of Belgrade
Office:	VERA **ĆUŠIĆ**, Serbian Chemical Society

Subscription: The annual subscription rate is **150.00 €** including postage (surface mail) and handling. For Society members from abroad rate is **50.00 €**. For the proforma invoice with the instruction for bank payment contact the Society Office (E-mail: shd@shd.org.rs) or see JSCS Web Site: http://www.shd.org.rs/JSCS/, option Subscription.

Godišnja pretplata: Za članove SHD: **2.500,00 RSD**, za penzionere i studente: **1000,00 RSD**, a za ostale: **3.500,00 RSD**:za organizacije i ustanove: **16.000,00 RSD**. Uplate se vrše na tekući račun Društva: **205-13815-62**, poziv na broj **320**, sa naznakom "pretplata za JSCS".

Nota: Radovi čiji su svi autori članovi SHD prioritetno se publikuju.

Odlukom Odbora za hemiju Republičkog fonda za nauku Srbije, br. 66788/1 od 22.11.1990. godine, koja je kasnije potvrđena odlukom Saveta Fonda, časopis je uvršten u kategoriju međunarodnih časopisa (**M-23**). Takođe, aktom Ministarstva za nauku i tehnologiju Republike Srbije, 413-00-247/2000-01 od 15.06.2000. godine, ovaj časopis je proglašen za publikaciju od posebnog interesa za nauku. **Impact Factor** časopisa objavljen 2022. godini iznosi **1,100**, a petogodišnji **Impact Factor 1,175**.

INSTRUCTIONS FOR AUTHORS (2021)

GENERAL

The *Journal of the Serbian Chemical Society* (the *Journal* in further text) is an international journal publishing papers from all fields of chemistry and related disciplines. Twelve issues are published annually. The Editorial Board expects the editors, reviewers, and authors to respect the well-known standard of professional ethics.

Types of Contributions

Original scientific papers	(up to 15 typewritten pages, including Figures, Tables and References) report original research which must not have been previously published.
Short communications	(up to 8 pages) report unpublished preliminary results of sufficient importance to merit rapid publication.
Notes	(up to 5 pages) report unpublished results of short, but complete, original research
Authors' reviews	(up to 40 pages) present an overview of the author's current research with comparison to data of other scientists working in the field
Reviews[a]	(up to 40 pages) present a concise and critical survey of a specific research area. Generally, these are prepared at the invitation of the Editor
Surveys	(about 25 pages) communicate a short review of a specific research area.
Book and Web site reviews	(1 - 2 pages)
Extended abstracts	(about 4 pages) of Lectures given at meetings of the Serbian Chemical Society Divisions
Letters to the Editor	report miscellaneous topics directed directly to the Editor

[a] Generally, Authors' reviews, Reviews and Surveys are prepared at the invitation of the Editor.

Submission of manuscripts

Manuscripts should be submitted using the **OnLine Submission Form**, available on the JSCS Web Site (**http://www.shd-pub.org.rs/index.php/JSCS**). The manuscript must be uploaded as a Word.doc or .rtf file, with tables and figures (including the corresponding captions – above Tables and below Figures), placed within the text to follow the paragraph in which they were mentioned for the first time.

Please note that **Full Names (**First Name, Last Name), **Full Affiliation** and **Country** (from drop down menu) of **ALL OF AUTHORS** (written in accordance with English spelling rules - the first letter capitalized) must be entered in the manuscript Submission Form (Step 3). Manuscript Title, authors' names and affiliations, as well as the Abstract, **WILL APPEAR** in the article listing, as well as in **BIBLIOGRAPHIC DATABASES (WoS, SCOPUS...)**, in the form and in the order entered in the author details

Graphical abstract

Graphical abstract is a one-image file containing the main depiction of the authors work and/or conclusion and must be supplied along with the manuscript. It must enable readers to quickly gain the main message of the paper and to encourage browsing, help readers identify which papers are most relevant to their research interests. Authors must provide an image that clearly represents the research described in the paper. The most relevant figure from the work, which summarizes the content, can also be submitted. The image should be submitted as a separate file in **Online Submission Form - Step 2**.

Specifications: The graphical abstract should have a clear start and end, reading from top to bottom or left to right. Please omit unnecessary distractions as much as possible.

- **Image size:** minimum of 500×800 pixels (W×H) and a minimum resolution of 300 dpi. If a larger image is sent, then please use the same ratio: 16 wide × 9 high. Please note that your image will be scaled proportionally to fit in the available window in TOC; a 150x240 pixel rectangle. Please be sure that the quality of an image cannot be increased by changing the resolution from lower to higher, but only by rescanning or exporting the image with a higher resolution, which can be set in usual "settings" option.
- **Font:** Please use Calibri and Symbol font with a large enough font size, so it is readable even from the image of a smaller size (150 × 240 px) in TOC.
- **File type:** JPG and PNG only.

No additional text, outline or synopsis should be included. Please do not use white space or any heading within the image.

Cover Letter

Manuscripts must be accompanied by a cover letter (strictly uploaded in **Online Submission Step 2**) in which the type of the submitted manuscript and a warranty as given below are given. The Author(s) has(have) to warranty that the manuscript submitted to the *Journal* for review is original, has been written by the stated author(s) and has not been published elsewhere; is currently not being considered for publication by any other journal and will not be submitted for such a review while under review by the *Journal*; the manuscript contains no libellous or other unlawful statements and does not contain any materials that violate any personal or proprietary rights of any other person or entity. All manuscripts will be acknowledged on receipt (by e-mail).

Illustrations

Illustrations (Figs, schemes, photos…) in TIF or EPS format (JPG format is acceptable for colour and greyscale photos, only), must be additionally uploaded (Online Submission Step 2) as a separate file or one archived (.zip, .rar or .arj) file. Figures and/or Schemes should be prepared according to the **Artwork Instructions -** http://www.shd.org.rs/JSCS/jscs-pdf/Artwork_Instructions.pdf!

For any difficulties and questions related to **OnLine Submission Form -** https://www.shd-pub.org.rs/index.php/JSCS/submission/wizard, please refer to **User Guide -** https://openjournal-systems.com/ojs-3-user-guide/ , Chapter **Submitting an Article -** https://openjournalsystems.com/ojs-3-user-guide/submitting-an-article/. If difficulties still persist, please contact JSCS Editorial Office at **JSCS@shd.org.rs**

A manuscript not prepared according to these instructions will be returned for resubmission without being assigned a reference number.

Conflict-of-Interest Statement*: Public trust in the peer review process and the credibility of published articles depend in part on how well a conflict of interest is handled during writing, peer review, and editorial decision making. A conflict of interest exists when an author (or the author's institution), reviewer, or editor has financial or personal relationships that inappropriately influence (bias) his or her actions (such relationships are also known as dual commitments, competing interests, or competing loyalties). These relationships vary from those with negligible potential to those with great potential to influence judgment, and not all relationships represent true conflict of interest. The potential for a conflict of interest can exist whether or not an individual believes that the relationship affects his or her scientific judgment. Financial relationships (such as employment, consultancies, stock ownership, honoraria, paid expert testimony) are the most easily identifiable conflicts of interest and the most likely to undermine the credibility of the journal, the authors, and of science itself. However, conflicts can occur for other reasons, such as personal relationships, academic competition, and intellectual passion.

Informed Consent Statement*: Patients have a right to privacy that should not be infringed without informed consent. Identifying information, including patients' names, initials, or hospital numbers, should not be published in written descriptions, photographs, and pedigrees unless the information is essential for scientific purposes and the patient (or parent or guardian) gives written informed consent for publication. Informed consent for this purpose requires that a patient who is identifiable be shown the manuscript to be published. Authors should identify Individuals who provide writing assistance and disclose the funding source for this assistance. Identifying details should be omitted if they are not essential. Complete anonymity is difficult to achieve, however, and informed consent should be obtained if there is any doubt. For example, masking the eye region in photographs of patients is inadequate protection of anonymity. If identifying characteristics are altered to protect anonymity, such as in genetic pedigrees, authors should provide assurance that alterations do not distort scientific meaning and editors should so note. The requirement for informed consent should be included in the journal's instructions for authors. When informed consent has been obtained it should be indicated in the published article.

Human and Animal Rights Statement* When reporting experiments on human subjects, authors should indicate whether the procedures followed were in accordance with the ethical standards of the responsible committee on human experimentation (institutional and national) and with the Helsinki Declaration of 1975, as revised in 2000 (5). If doubt exists whether the research was conducted in accordance with the Helsinki Declaration, the authors must explain the rationale for their approach, and demonstrate that the institutional review body explicitly approved the doubtful aspects of the study. When reporting experiments on animals, authors should be asked to indicate whether the institutional and national guide for the care and use of laboratory animals was followed.

---

*International Committee of Medical Journal Editors (“Uniform Requirements for Manuscripts Submitted to Biomedical Journals”), February 2006

PROCEDURE

All contributions will be peer reviewed and only those deemed worthy and suitable will be accepted for publication. The Editor has the final decision. To facilitate the reviewing process, authors are encouraged to suggest up to three persons competent to review their manuscript. Such suggestions will be taken into consideration but not always accepted. If authors would prefer a specific person not be a reviewer, this should be announced. The Cover Letter must be accompanied by these suggestions. Manuscripts requiring revision should be returned according to the requirement of the Editor, within 60 days upon reception of the reviewing comments by e-mail.

The *Journal* maintains its policy and takes the liberty of correcting the English as well as false content of manuscripts **provisionally accepted** for publication in the first stage of reviewing process. In this second stage of manuscript preparation by JSCS Editorial Office, the author(s) may be required to supply some **additional clarifications and corrections**. This procedure will be executed during copyediting actions, with a demand to author(s) to perform corrections of unclear parts before the manuscript would be published OnLine as **finally accepted manuscript (OLF Section of the JSCS website)**. Please note that the manuscript can receive the status of **final rejection** if the author's corrections would not be satisfactory.

When finally accepted manuscript is ready for printing, the corresponding author will receive a request for proof reading, which should be performed within 2 days. Failure to do so will be taken as the authors agree with any alteration which may have occurred during the preparation of the manuscript for printing.

Accepted manuscripts of active members of the Serbian Chemical Society (all authors) have publishing priority.

MANUSCRIPT PRESENTATION

Manuscripts should be typed in English (either standard British or American English, but consistent throughout) with 1.5 spacing (12 points Times New Roman; Greek letters in the character font Symbol) in A4 format leaving 2.5 cm for margins. For Regional specific, non-standard characters that may appear in the text, save documents with Embed fonts Word option: *Save as -> (Tools) -> Save Options… -> Embed fonts in the text.*

The authors are requested to seek the assistance of competent English language expert, if necessary, to ensure their English is of a reasonable standard. The Serbian Chemical Society can provide this service in advance of submission of the manuscript. If this service is required, please contact the office of the Society by e-mail (jscs-info@shd.org.rs).

Tables, figures and/or schemes must be embedded in the main text of the manuscript and should follow the paragraph in which they are mentioned for the first time. **Tables** must be prepared with the aid of the **WORD table function**, without vertical lines. The minimum size of the font in the tables should be **10 pt**. Table columns must not be formatted using multiple spaces. Table rows must not be formatted using any returns (enter key; ↵ key) and are **limited to 12 cm width**. Tables should not be incorporated as graphical objects. **Footnotes to Tables** should follow them and are to be indicated consequently (in a single line) in superscript letters and separated by semi-column.

Table caption must be placed above corresponding Table, while **Captions of the Illustrations** (Figs. Schemes...) must follow the corresponding item. **The captions, either for Tables or Illustrations**, should make the items comprehensible without reading of the main text (but clearly referenced in), must follow numerical order (Roman for Tables, Arabic for Illustrations), and should not be provided on separate sheets or as separate files.

High resolution Illustrations (named as Fig. 1, Fig. 2… and/or Scheme 1, Scheme 2…) in **TIF or EPS format** (JPG format is acceptable for photos, only) **must be additionally uploaded as a separate files or one archived (.zip, .rar) file.**

Illustrations should be prepared according to the ARTWORK INSTRUCTIONS - http://www.shd.org.rs/JSCS/jscs-pdf/Artwork_Instructions.pdf. **!**

All pages of the manuscript must be numbered continuously.

DESIGNATION OF PHYSICAL QUANTITIES AND UNITS

IUPAC recommendations for the naming of compounds should be followed. SI units, or other permissible units, should be employed. The designation of physical quantities must be in italic throughout the text (including figures, tables and equations), whereas the units and indexes (except for indexes having the meaning of physical quantities) are in upright letters. They should be in Times New Roman font. In graphs and tables, a slash should be used to separate the designation of a physical quantity from the unit (example: p / kPa, j / mA cm^{-2}, t / °C, T_0 / K, τ / h, ln (j / mA cm^{-2})…). Designations such as: p (kPa), t [min]…, are not acceptable. However, if the full name of a physical quantity is unavoidable, it should be given in upright letters and separated from the unit by a comma (example: Pressure, kPa; Temperature, K; Current density, mA cm^{-2}…). Please do not use the axes of graphs for additional explanations; these should be mentioned in the figure captions and/or the manuscript (example: "pressure at the inlet of the system, kPa" should be avoided). The axis name should follow the direction of the axis (the name of y-axis should be rotated by 90°). Top and right axes should be avoided in diagrams, unless they are absolutely necessary.

Latin words, as well as the names of species, should be in *italic*, as for example: *i.e., e.g., in vivo, ibid, Calendula officinalis* L., *etc*. The branching of organic compound should also be indicated in *italic*, for example, *n*-butanol, *tert*-butanol, *etc*.

Decimal numbers must have decimal points and not commas in the text (except in the Serbian abstract), tables and axis labels in graphical presentations of results. Thousands are separated, if at all, by a comma and not a point.

Mathematical and chemical equations should be given in separate lines and must be numbered, Arabic numbers, consecutively in parenthesis at the end of the line. All equations should be embedded in the text Complex equations (fractions, integrals, matrix…) should be prepared with the aid of the **Microsoft Equation 3.0** (or higher) or **MathType** (Do not use them to create simple equations and labels). **Using the Insert -> Equation option, integrated in MS Office 2010 and MS Office 2013, as well as insertion of equation objects within paragraph text IS NOT ALLOWED.**

ARTICLE STRUCTURE

- TITLE PAGE;
- MAIN TEXT – including Tables and Illustrations with corresponding captions;
- SUPPLEMENTARY MATERIAL (optional**)**

Title page

- **Title** in bold letters, should be clear and concise, preferably 12 words or less. The use of non-standard abbreviations, symbols and formulae is discouraged.
- AUTHORS' NAMES in capital letters with the full first name, initials of further names separated by a space and surname. Commas should separate the author's names except for the last two names when 'and' is to be used. In multi-affiliation manuscripts, the author's affiliation should be indicated by an Arabic number placed in superscript after the name and before the affiliation. Use * to denote the corresponding author(s).
- *Affiliations* should be written in italic. The e-mail address of the corresponding author should be given after the affiliation(s).
- *Abstract:* A one-paragraph abstract written of 150 – 200 words in an impersonal form indicating the aims of the work, the main results and conclusions should be given and clearly set off from the text. Domestic authors should also submit, on a separate page, an Abstract - Izvod, the author's name(s) and affiliation(s) in Serbian (Cyrillic letters). (Домаћи аутори морају доставити Извод (укључујући имена аутора и афилијацију) на српском језику, исписане ћирилицом, иза Захвалнице, а пре списка референци.) For authors outside Serbia, the Editorial Board will provide a Serbian translation of their English abstract.
- *Keywords:* Up to 6 keywords should be given. Do not use words appearing in the manuscript title
- RUNNING TITLE: A one line (maximum five words) short title in capital letters should be provided.

Main text – should have the form:

- **INTRODUCTION,**
- **EXPERIMENTAL (RESULTS AND DISCUSSION),**
- **RESULTS AND DISCUSSION (EXPERIMENTAL),**
- **CONCLUSIONS,**
- **NOMENCLATURE (optional) and**
- ***Acknowledgements*: If any.**
- REFERENCES (Citation of recent papers published in chemistry journals that highlight the significance of work to the general readership is encouraged.)

The sections should be arranged in a sequence generally accepted for publication in the respective fields. They subtitles should be in capital letters, centred and NOT numbered.

- The INTRODUCTION should include the aim of the research and a concise description of background information and related studies directly connected to the paper.
- The EXPERIMENTAL section should give the purity and source of all employed materials, as well as details of the instruments used. The employed methods should be described in sufficient detail to enable experienced persons to repeat them. Standard procedures should be referenced and only modifications described in detail. On no account should results be included in the experimental section.

Chemistry

Detailed information about instruments and general experimental techniques should be given in all necessary details. If special treatment for solvents or chemical purification were applied that must be emphasized.

Example: Melting points were determined on a Boetius PMHK or a Mel-Temp apparatus and were not corrected. Optical rotations were measured on a Rudolph Research Analytical automatic polarimeter, Autopol IV in dichloromethane (DCM) or methanol (MeOH) as solvent. IR spectra were recorded on a Perkin-Elmer spectrophotometer FT-IR 1725X. ^{1}H and ^{13}C NMR spectra were recorded on a Varian Gemini-200 spectrometer (at 200 and 50 MHz, respectively), and on a Bruker Ultrashield Advance III spectrometer (at 500 and 125 MHz, respectively) employing indicated solvents (*vide infra*) using TMS as the internal standard. Chemical shifts are expressed in ppm (δ / ppm) values and coupling constants in Hz (J / Hz). ESI-MS spectra were recorded on Agilent Technologies 6210 Time-Of-Flight LC-MS instrument in positive ion mode with CH_3CN/H_2O 1/1 with 0.2 % HCOOH as the carrying solvent solution. Samples were dissolved in CH_3CN or MeOH (HPLC grade purity). The selected values were as follows: capillary voltage = 4 kV, gas temperature = 350 °C, drying gas flow 12 L min^{-1}, nebulizer pressure = 310 kPa, fragmentator voltage = 70 V.The elemental analysis was performed on the Vario EL III- C,H,N,S/O Elemental Analyzer (Elementar Analysensysteme GmbH, Hanau-Germany). Thin-layer chromatography (TLC) was performed on precoated Merck silica gel 60 F254 and RP-18 F254 plates. Column chromatography was performed on Lobar LichroPrep Si 60 (40-63 μm), RP-18 (40-63 μm) columns coupled to a Waters RI 401 detector, and on Biotage SP1 system with UV detector and FLASH 12+, FLASH 25+ or FLASH 40+ columns pre packed with KP-SIL [40-63 μm, pore diameter 6 nm (60 Å)], KP-C18-HS (40-63 μm, pore diameter 9 nm (90 Å) or KP-NH [40-63 μm, pore diameter 10 nm (100 Å)] as adsorbent. Compounds were analyzed for purity (HPLC) using a Waters 1525 HPLC dual pump system equipped with an Alltech, Select degasser system, and dual λ 2487 UV-VIS detector. For data processing, Empower software was used (methods A and B). Methods C and D: Agylent Technologies 1260 Liquid Chromatograph equipped with Quat Pump (G1311B), Injector (G1329B) 1260 ALS, TCC 1260 (G1316A) and Detector 1260 DAD VL+ (G1315C). For data processing, LC OpenLab CDS ChemStation software was used. For details, see Supporting Information.

1. Synthesis experiments

Each paragraph describing a synthesis experiment should begin with the name of the product and any structure number assigned to the compound in the Results and Discussions section. Thereafter, the compound should be identified by its structure number. Use of standard abbreviations or unambiguous molecular formulas for reagents and solvents, and of structure numbers rather than chemical names to identify starting materials and intermediates, is encouraged.

When a new or improved synthetic method is described, the yields reported in key experimental examples, and yields used for comparison with existing methods, should represent amounts of isolated and purified products, rather than chromategraphically or spectroscopically determined yields. Reactant quantities should be reported in weight and molar units and for product yields should be reported in weight units; percentage yields should only be reported for materials of demonstrated purity. When chromatography is used for product purification, both the support and solvent should be identified.

2. Microwave experiments

Reports of syntheses conducted in microwave reactors must clearly indicate whether sealed or open reaction vessels were used and must document the manufacturer and model of the reactor, the method of monitoring the reaction mixture temperature, and the temperature-time profile. Reporting a wattage rating or power setting is not an acceptable alternative to providing temperature data. Manuscripts describing work done with domestic (kitchen) microwave ovens will not be accepted except for studies where the unit is used for heating reaction mixtures at atmospheric pressure.

3. Compound characterization

The Journal upholds a high standard for compound characterization to ensure that substances being added to the chemical literature have been correctly identified and can be synthesized in known yield and purity by the reported preparation and isolation methods. For **all new** compounds, evidence adequate to establish both **identity** and **degree of purity** (homogeneity) must be provided.

Identity *- Melting point.* All homogeneous solid products (*e.g.* not mixtures of isomers) should be characterized by melting or decomposition points. The colors and morphologies of the products should also be noted.

Specific rotations. Specific rotations based on the equation $[\alpha]^{t};D = (100\ \alpha) / (l\ c)$ should be reported as unitless numbers as in the following example: $[\alpha]^{20}; D = -25.4$ (c 1.93, $CHCl_3$), where c / g mL^{-1} is concentration and l / dm is path length. The units of the specific rotation, (deg mL) / (g dm), are implicit and are not included with the reported value.

Spectra/Spectral Data. Important IR adsorptions should be given.

For all new diamagnetic substances, NMR data should be reported (^{1}H, ^{13}C, and relevant heteronuclei). ^{1}H NMR chemical shifts should be given with two digits after the decimal point. Include the number of protons represented by the signal, signal multiplicity, and coupling constants as needed (J italicized, reported with up to one digit after the decimal). The number of bonds through which the coupling is operative, ^xJ, may be specified by the author if known with a high degree of certainty. ^{13}C NMR signal shifts should be rounded to the nearest 0.01 ppm unless greater precision is needed to distinguish closely spaced signals. Field strength should be noted for each spectrum, not as a comment in the general experimental section. Hydrogen multiplicity (C, CH, CH_2, CH_3) information obtained from routine DEPT spectra should be included. If detailed signal assignments are made, the type of NOESY or COSY methods used to establish atom connectivity and spatial relationships should be identified in the Supporting Information. Copies of spectra should also be included where structure assignments of complex molecules depend heavily on NMR interpretation. Numbering system used for assignments of signals should be given in the Supporting Information with corresponding general structural formula of named derivative.

HPLC/LCMS can be substituted for biochemistry papers where the main focus is not on compound synthesis.

HRMS/elemental analysis. To support the molecular formula assignment, HRMS data accurate within 5 ppm, or combustion elemental analysis [carbon and hydrogen (and nitrogen, if present)] data accurate within 0.5 %, should be reported for new compounds. HRMS data should be given in format as is usually given for combustion analysis: calculated mass for given formula following with observed mass: (+)ESI-HRMS *m/z*: [molecular formula + H]$^+$ calculated mass, observed mass. Example: (+)ESI-HRMS *m/z*: calculated for [$C_{13}H_8BrCl_2N$ + H^+] 327.92899, observed 327.92792.

NOTE: in certain cases, a crystal structure may be an acceptable substitute for HRMS/elemental analysis.

Biomacromolecules. The structures of biomacromolecules may be established by providing evidence about sequence and mass. Sequences may be inferred from the experimental order of amino acid, saccharide, or nucleotide coupling, from known sequences of templates in enzyme-mediated syntheses, or through standard sequencing techniques. Typically, a sequence will be accompanied by MS data that establish the molecular weight.

Example: Product was isolated upon column chromatography [dry flash (SiO_2, eluent EA, EA/MeOH gradient 95/5 → 9/1, EA/MeOH/NH_3 gradient 18/0.5/0.5 → 9/1/1, and flash chromatography (Biotage SP1, RP column, eluent MeOH/H_2O gradient 75/25 → 95/5, N-H column, eluent EA/Hex gradient 6/3 → EA). was obtained after flash column chromatography (Biotage SP NH column, eluent hexane/EA 4:6 → 2:6). Yield 968.4 mg (95 %). Colorless foam softens at 96-101 °C. $[\alpha]^{20}; D = +0,163$ (c =2.0×10^{-3} g/mL, CH_2Cl_2). IR (ATR): 3376w, 2949m, 2868w, 2802w, 1731s, 1611w, 1581s, 1528m, 1452m, 1374s, 1331w, 1246s, 1171m, 1063w, 1023m, 965w, 940w, 881w, 850w, 807w, cm^{-1}. ^{1}H NMR (500 MHz, $CDCl_3$, δ): 8.46 (*d,* 1H, J = 5.4, H-2'), 7.89 (*s,* 1H, J = 2.0, H-8'), 7.71 (*d,* 1H, J = 8.9, H-5'), 7.30 (*dd,* 1H, J_1 = 8.8, J_2 = 2.1, H-6'), 6.33 (*d,* 1H, J = 5.4, H-3'), 6.07 (*s,* HN-Boc, exchangeable with D_2O), 5.06 (*s,* 1H, H-12), 4.92-4.88 (*m,* 1H, H-7), 4.42 (*bs,* H-3), 3.45 (*s,*CH_3-N), 3.33 (*bs,* H-9'), 3.05-2.95 (*m,* 2H, H-11'), 2.70-2.43 (*m,* 2H, H-24) and HN, exchangeable with D_2O), 2.07 (*s,* CH_3COO), 2.04 (*s,* CH_3COO), 1.42 (*s,* 9H, $(CH_3)_3$C-N(Boc)), 0.88 (*s,* 3H, CH_3-10), 0.79 (*d,* 3H,J = 6.6, CH_3-20), 0.68 (*s,* 3H, CH_3-13). ^{13}C NMR (125 MHz, $CDCl_3$, δ): 170.34, 170.27, 151.80, 149.92, 148.87, 134.77, 128.36, 125.11, 121.43, 117.29, 99.98, 75.41, 70.82, 50.43, 49.66, 47.60, 47.33, 44.97, 43.30, 41.83, 41.48, 37.65, 36.35, 35.44, 34.89, 34.19, 33.23, 31.24, 28.79, 28.35, 27.25, 26.45, 25.45, 22.74, 22.63, 21.57, 21.31, 17.85, 12.15. (+)ESI-HRMS (*m*/*z*): calculated for $[C_{45}H_{67}ClN_4O_6 + H]^+$ 795.48219, observed 795.48185. Combustion analysis for $C_{45}H_{67}ClN_4O_6$: Calculated. C 67.94, H 8.49, N 7.04; found C 67.72, H 8.63, N 6.75. HPLC purity: method A: RT 1.994, area 99.12 %; method C: RT 9.936, area 98.20 %.

Purity - Evidence for documenting compound purity should include one or more of the following:

a) Well-resolved high field 1D ^{1}H NMR spectrum showing at most only trace peaks not attributable to the assigned structure and a standard 1D proton-decoupled ^{13}C NMR spectrum. Copies of the spectra should be included as figures in the Supporting Information.
b) Quantitative gas chromatographic analytical data for distilled or vacuum-transferred samples, or quantitative HPLC analytical data for materials isolated by column chromatography or separation from a solid support. HPLC analyses should be performed in two diverse systems. The stationary phase, solvents (HPLC), detector type, and percentage of total chromatogram integration should be reported; a copy of the chromatograms may be included as a figure in the Supporting Information.
c) Electrophoretic analytical data obtained under conditions that permit observing impurities present at the 5 % level.

HRMS data may be used to support a molecular formula assignment **but cannot be used as a criterion of purity**.

4. Biological Data

Quantitative biological data are required for all tested compounds. Biological test methods must be referenced or described in sufficient detail to permit the experiments to be repeated by others. Detailed descriptions of biological methods should be placed in the experimental section. Standard compounds or established drugs should be tested in the same system for comparison. Data may be presented as numerical expressions or in graphical form; biological data for extensive series of compounds should be presented in tabular form. Tables consisting primarily of negative data will not usually be accepted; however, for purposes of documentation they may be submitted as supporting information. Active compounds obtained from combinatorial syntheses should be resynthesized and retested to verify that the biology conforms to the initial observation.

Statistical limits (statistical significance) for the biological data are usually required. If statistical limits cannot be provided, the number of determinations and some indication of the variability and reliability of the results should be given. References to statistical methods of calculation should be included. Doses and concentrations should be expressed as molar quantities (*e.g.*, mol/kg, μmol/kg, M, mM). The routes of administration of test compounds and vehicles used should be indicated, and any salt forms used (hydrochlorides, sulfates, *etc.*) should be noted. The physical state of the compound dosed (crystalline, amorphous; solution, suspension) and the formulation for dosing (micronized, jet-milled, nanoparticles) should be indicated. For those compounds found to be inactive, the highest concentration (*in vitro*) or dose level (*in vivo*) tested should be indicated.

- The RESULTS AND DISCUSSION should include concisely presented results and there significance discussed and compared to relevant literature data. The results and discussion may be combined or kept separate.
- The inclusion of a CONCLUSION section, which briefly summarizes the principal conclusions, is recommended.
- NOMENCLATURE is optional but, if the authors wish, a list of employed symbols may be included.
- REFERENCES should be numbered sequentially as they appear in the text. Please note that any reference numbers appearing in the Illustrations and/or Tables and corresponding captions must follow the numbering sequence of the paragraph in which they appear for the first time. When cited, the reference number should be superscripted in Font 12, following any punctuation mark. In the reference list, they should be in normal position followed by a full stop. Reference entry must not be formatted using Carriage returns (enter key; ↵ key) or multiple space key. The formatting of references to published work should follow the *Journal*'s style as follows:

Journals[a]:	A. B. Surname1, C. D. Surname2, *J. Serb. Chem. Soc.* **Vol** (Year) first page Number (https://doi.org/doi)[b]
Books:	A. B. Surname1, C. D. Surname2, *Name of Book*, Publisher, City, Year, pp. 100-101 (https://doi.org/doi)[b]
Compilations:	A. B. Surname1, C. D. Surname2, in *Name of Compilation*, A. Editor1, C. Editor2, Ed(s)., Publisher, City, Year, p. 100 (https://doi.org/doi)[b]
Proceedings:	A. B. Surname1, C. D. Surname2, in *Proceedings of Name of the Conference or Symposium*, (Year), Place of the Conference, Country, *Title of the Proceeding*, Publisher, City, Year, p. or Abstract No. 100
Patents:	A. B. Inventor1, C. D. Inventor2, (Holder), Country Code and patent number (registration year)
Chemical Abstracts:	A. B. Surname1, C. D. Surname2, *Chem. Abstr*. CA 234 567a; For non-readily available literature, the Chemical Abstracts reference should be given in square brackets: [C.A. 139/2003 357348t] after the reference
Standards:	EN ISO 250: *Name of the Standard* (Year)
Websites:	Title of the website, URL in full (date accessed)

[a] When citing Journals, the International Library Journal abbreviation is required. Please consult, *e.g.*, https://images.webofknowledge.com/WOK46/help/WOS/A_abrvjt.html

[b] doi should be replaced by doi number of the Article, for example: http://dx.doi.org/10.2298/JSC161212085B (as active link). If doi do not exist, provide the link to the online version of the publication.

Only the last entry in the reference list should end with a full stop.

The names of all authors should be given in the list of references; the abbreviation *et al.* may only be used in the text. The original journal title is to be retained in the case of publications published in any language other than English (please denote the language in parenthesis after the reference). Titles of publications in non-Latin alphabets should be transliterated. Russian references are to be transliterated using the following transcriptions:

ж→zh, х→kh, ц→ts, ч→ch, ш→sh, щ→shch, ы→y, ю→yu, я→ya, э→e, й→i, ь→’.

Supplementary material

Authors are encouraged to presentthe information and results non-essential to the understanding of their paper as SUPPLEMENTARY MATERIAL (can be uploaded inStep 4 of Online Submission). This material may include as a rule, but is not limited to, the presentation of analytical and spectral data demonstrating the identity and purity of synthesized compounds, tables containing raw data on which calculations were based, series of figures where one example would remain in the main text, etc. The Editorial Board retain the right to assign such information and results to the Supplementary material when deemed fit. Supplementary material does not appear in printed form but can be downloaded from the web site of the JSCS.

Mathematical and chemical equations should be given in separate lines and must be numbered, Arabic numbers, consecutively in parenthesis at the end of the line. All equations should be embedded in the text Complex equations (fractions, integrals, matrix…) should be prepared with the aid of the Microsoft Equation 3.0 (or higher) or MathType (Do not use them to create simple equations and labels). Using the Insert -> Equation option, integrated in MS Office 2010 and MS Office 2013, as well as insertion of equation objects within paragraph text IS NOT ALLOWED.

Deposition of crystallographic data

Prior to submission, the crystallographic data included in a manuscript presenting such data should be deposited at the appropriate database. Crystallographic data associated with organic and metal-organic structures should be deposited at the Cambridge Crystallographic Data Centre (CCDC) by e-mail to **deposit@ccdc.cam.ac.uk**

Crystallographic data associated with inorganic structures should be deposited with the Fachinformationszentrum Karlsruhe (FIZ) by e-mail to **crysdata@fiz-karlsruhe.de**. A deposition number will then be provided, which should be added to the reference section of the manuscript.

For detailed instructions please visit the JSCS website:
https://www.shd-pub.org.rs/index.php/JSCS/Instructions

ARTWORK INSTRUCTIONS

JSCS accepts only **TIFF** or **EPS** formats, as well as **JPEG** format (only for colour and greyscale photographs) for electronic artwork and graphic files. **MS files** (Word, PowerPoint, Excel, Visio) **NOT acceptable**. Generally, scanned instrument data sheets should be avoided. Authors are responsible for the quality of their submitted artwork. Every single Figure or Scheme, as well as any part of the Figure (A, B, C…) should be prepared according to following instructions (every part of the figure, A, B, C…, must be submitted as an independent single graphic file):

TIFF

Virtually all common artwork and graphic creation software is capable of saving files in TIFF format. This 'option' can normally be found under 'the 'Save As...' or 'Export...' commands in the 'File' menu.

TIFF (Tagged Image File Format) is the recommended file format for bitmap, greyscale and colour images.

- Colour images should be in the RGB mode
- When supplying TIFF files, please ensure that the files are supplied at the correct resolution:
    1. Line artwork: minimum of 1000 dpi
    2. RGB image: minimum of 300 dpi
    3. Greyscale image: minimum of 300 dpi
    4. Combination artwork (line/greyscale/RGB): minimum of 500 dpi
- Images should be tightly cropped, without frame and any caption.
- If applicable please re-label artwork with a font supported by JSCS (Arial, Helvetica, Times, Symbol) and ensure it is of an appropriate font size.
- Save an image in TIFF format with LZW compression applied.
- It is recommended to remove Alpha channels before submitting TIFF files.
- It is recommended to flatten layers before submitting TIFF files.

Please be sure that quality of an image cannot be increased by changing the resolution from lower to higher, but only by rescanning or exporting the image with higher resolution, which can be set in usual "settings" facilities.

EPS

Virtually all common artwork creation software, such as Canvas, ChemDraw, CorelDraw, SigmaPlot, Origin Lab…, are capable of saving files in EPS format. This 'option' can normally be found under the 'Save As...' or 'Export...' commands in the 'File' menu.

For vector graphics, EPS (Encapsulated PostScript) files are the preferred format as long as they are provided in accordance with the following conditions:

- when they contain bitmap images, the bitmaps should be of good resolution (see instructions for TIFF files)
- when colour is involved, it should be encoded as RGB
- an 8-bit preview/header at a resolution of 72 dpi should always be included
- embed fonts should always included and only the following fonts should be used in artwork: Arial, Helvetica, Times, Symbol
- the vertical space between the parts of an illustration should be limited to the bare necessity for visual clarity
- no data should be present outside the actual illustration area
- line weights should range from 0.35 pt to 1.5 pt
- when using layers, they should be reduced to one layer before saving the image (Flatten Artwork)

JPEG

Virtually all common artwork and graphic creation software is capable of saving files in JPEG format. This 'option' can normally be found under 'the 'Save As...' or 'Export...' commands in the 'File' menu.

JPEG (Joint Photographic Experts Group) is the acceptable file format **only for colour and greyscale photographs**. JPEG can be created with respect to photo quality (low, medium, high; from 1 to 10), ensuring file sizes are kept to a minimum to aid easy file transfer. Images should have a minimum resolution of 300 dpi. Image width: minimum 3.0 cm; maximum 12.0 cm.

Please be sure that quality of an image cannot be increased by changing the resolution from lower to higher, but only by rescanning or exporting the image with higher resolution, which can be set in usual "settings" facilities.

SIZING OF ARTWORK

- JSCS aspires to have a uniform look for all artwork contained in a single article. Hence, it is important to be aware of the style of the journal.
- Figures should be submitted in black and white or, if required, colour (charged). If coloured figures or photographs are required, this must be stated in the cover letter and arrangements made for payment through the office of the Serbian Chemical Society.
- As a general rule, the lettering on an artwork should have a finished, printed size of 11 pt for normal text and no smaller than 7 pt for subscript and superscript characters. Smaller lettering will yield a text that is barely legible. This is a rule-of-thumb rather than a strict rule. There are instances where other factors in the artwork, (for example, tints and shadings) dictate a finished size of perhaps 10 pt. Lines should be of at least 1 pt thickness.
- When deciding on the size of a line art graphic, in addition to the lettering, there are several other factors to address. These all have a bearing on the reproducibility/readability of the final artwork. Tints and shadings have to be printable at the finished size. All relevant detail in the illustration, the graph symbols (squares, triangles, circles, *etc*.) and a key to the diagram (to explain the explanation of the graph symbols used) must be discernible.
- The sizing of halftones (photographs, micrographs,...) normally causes more problems than line art. It is sometimes difficult to know what an author is trying to emphasize on a photograph, so you can help us by identifying the important parts of the image, perhaps by highlighting the relevant areas on a photocopy. The best advice that can be given to graphics suppliers is not to over-reduce halftones. Attention should also be paid to magnification factors or scale bars on the artwork and they should be compared with the details inside. If a set of artwork contains more than one halftone, again please ensure that there is consistency in size between similar diagrams.

General sizing of illustrations which can be used for the Journal of the Serbian Chemical Society:

- Minimum fig. size: 30 mm width
- Small fig. size - 60 mm width
- Large fig. size - 90 mm width
- Maximum fig. size - 120 mm width

Pixel requirements (width) per print size and resolution for bitmap images:

	Image width	**A**	**B**	**C**
Minimal size	30 mm	**354**	**591**	**1181**
Small size	60 mm	**709**	**1181**	**2362**
Large size	90 mm	**1063**	**1772**	**3543**
Maximal size	120 mm	**1417**	**2362**	**4724**

A: 300 dpi > RGB or Greyscale image
B: 500 dpi > Combination artwork (line/greyscale/RGB)
C: 1000 dpi> Line artwork

The designation of physical quantities and graphs formatting

The designation of physical quantities on figures must be in italic, whereas the units are in upright letters. They should be in Times New Roman font. In graphs a slash should be used to separate the designation of a physical quantity from the unit (example: p / kPa, t °C, T_0 / K, τ / h, ln (j / mA cm^{-2})…). Designations such as: p (kPa), t [min]…, are not acceptable. However, if the full name of a physical quantity is unavoiable, it should be given in upright letters and separated from the unit by a comma (example: Pressure, kPa, Temperature, K…). Please do not use the axes of graphs for additional explanations; these should be mentioned in the figure captions and/or the manuscript (example: “pressure at the inlet of the system, kPa” should be avoided). The axis name should follow the direction of the axis (the name of y-axis should be rotated by 90°). Top and right axes should be avoided in diagrams, unless they are absolutely necessary. Decimal numbers must have decimal points and not commas in the axis labels in graphical presentations of results. Thousands are separated, if at all, by a comma and not a point.

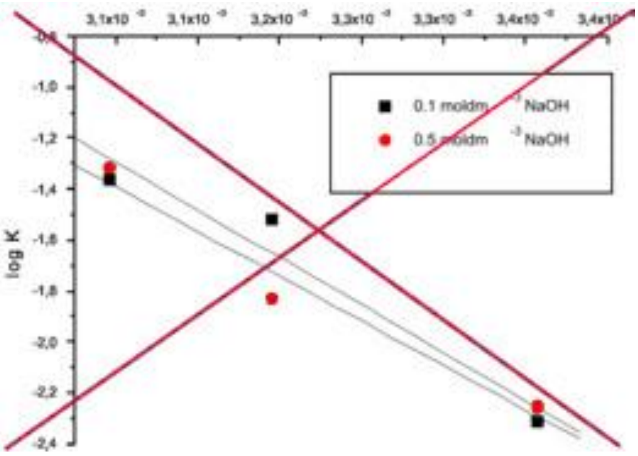

INCORRECT

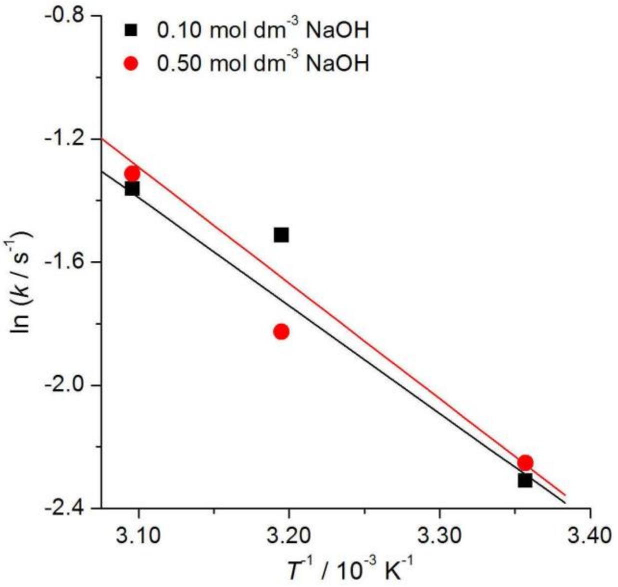

CORRECT

Journal of the Serbian Chemical Society
version electronic
JSCS-info@shd.org.rs • www.shd.org.rs/JSCS

J. Serb. Chem. Soc. Vol. 87, No. 7–8 (2022)

CONTENTS*

Organic Chemistry

Theoretical Chemistry

Electrochemistry

Polymers

Materials

Chemical Engineering

Metallic Materials and Metallurgy

Environmental

Published by the Serbian Chemical Society
Karnegijeva 4/III, P.O. Box 36, 11120 Belgrade, Serbia
Printed by the Faculty of Technology and Metallurgy
Karnegijeva 4, P.O. Box 35-03, 11120 Belgrade, Serbia

* For colored figures in this issue please see electronic version at the Journal Home Page: http://www.shd.org.rs/JSCS/

Journal of the Serbian Chemical Society
JSCS@tmf.bg.ac.rs • www.shd.org.rs/JSCS

J. Serb. Chem. Soc. 87 (7–8) 785–811 (2022)
JSCS–5558

Survey
Published 4 May 2022

SURVEY

Protein degradation induced by PROTAC molecules as an emerging drug discovery strategy

MLADEN KORAVOVIĆ[1*], BOJAN MARKOVIĆ[2], MILENA KOVAČEVIĆ[3],
MILENA RMANDIĆ[4] and GORDANA TASIĆ[1**#]

[1]University of Belgrade – Faculty of Pharmacy, Department of Organic Chemistry, Vojvode Stepe 450, 11221 Belgrade, Serbia, [2]University of Belgrade – Faculty of Pharmacy, Department of Pharmaceutical Chemistry, Vojvode Stepe 450, 11221 Belgrade, Serbia, [3]University of Belgrade – Faculty of Pharmacy, Department of Pharmacokinetics and Clinical Pharmacy, Vojvode Stepe 450, 11221 Belgrade, Serbia and [4]University of Belgrade – Faculty of Pharmacy, Department of Drug Analysis, Vojvode Stepe 450, 11221 Belgrade, Serbia

(Received 9 December 2021, revised 9 March, accepted 14 March 2022)

Abstract: The traditional concept of drug discovery is based on the *occupancy*-driven pharmacology model. It implies the development of inhibitors occupying binding sites that directly affect protein functions. Therefore, proteins that do not have such binding sites are generally considered as pharmacologically intractable. Furthermore, drugs that act in this way must be administered in dosage regimens that often result in high systemic drug exposures in order to maintain sufficient protein inhibition. Thus, there is a risk of the onset of off-target binding and side effects. The landscape of drug discovery has been markedly changed since proteolysis targeting chimera (PROTAC) molecules emerged twenty years ago as a part of the event-driven pharmacology model. These are bifunctional molecules that harness the ubiquitin-proteasome system, and are composed of a ligand that binds the protein of interest (POI), a ligand that recruits E3 ubiquitin ligase (E3UL) and a linker that connects these two parts. Pharmacologically, PROTACs bring POI and E3UL into close proximity, which triggers the formation of a functional ternary complex POI––PROTAC–E3UL. This event drives polyubiquitination and subsequent POI degradation by the 26S proteasome. The development and exceptional properties of PROTAC molecules that brought them to clinical studies will be discussed in this paper.

---

*,** Corresponding authors. E-mail: (*)mladen.koravovic@pharmacy.bg.ac.rs; (**)gordana.tasic@pharmacy.bg.ac.rs

Serbian Chemical Society member.

https://doi.org/10.2298/JSC211209027K

Keywords: bifunctional molecules; ternary complex; cooperativity; polyubiquitination; undruggable proteome; clinical candidates.

CONTENTS

INTRODUCTION

The fundamental concepts embedded in drug discovery science, named medicinal chemistry, have remained mainly unchanged for the last century.[1] Since Ehrlich and Langley, when receptor pharmacology began to appear,[2] drug discovery was based on the following concepts: a) identification and optimization of molecules with decent activities on corresponding biological targets and b) finding safe and tolerable doses and dose regimens that could maintain sufficient drug concentration at the site of action in order to trigger and sustain appropriate pharmacologic effects.[1] Hence, two fundamental principles originating from pharmacology – aplenty receptor occupancy and sustained drug exposure in the target tissue – were the basis for drug discovery and optimization. Hereinafter, only inhibitors will be disclosed since they are much more present in therapy than agonists. Thus, the class of molecules that will be elucidated in the following text actually agonizes certain processes by which the inhibitory function is finally achieved.

The human proteome contains more than 30,000 proteins employed in different biological functions.[3] Taking into account that many of them are included in the onset of many different diseases, scientists attempt to manipulate them in order to achieve certain therapeutic effects. Currently, the United States Food and Drug Administration (FDA) approved drugs against about 400 human proteins.[4] More than 90 % of them are enzymes, transporters, G protein-coupled receptors (GPCRs), cluster of differentiation (CD) markers, voltage-gated ion channels and nuclear receptors.[5] These biological targets are attractive, but easily accessible to agents originating from the traditional pharmacology concept. However, it has been estimated that there are about 3,000 genes involved in disease onset. In summary, the current therapies can target only 13 % (400 out of 3,000 genes) of the therapeutically relevant human proteome. Therefore, about 85 % of disease-associated proteins remain without corresponding agents that could achieve therapeutic effects.[5] To summarize, the genomic revolution found new connections between certain proteins and diseases,[6–9] but traditional drug discovery strategies are not sufficient to exploit all of these emerging chemical biology findings. There are two reasons why so many therapeutically relevant proteins are still considered as pharmacologically intractable, *i.e.*, undruggable biological targets: a) many of them do not have suitable binding sites that directly modulate their function[10] and b) some of them are intracellularly localized and as such unattainable for monoclonal antibodies (mAbs) either.[11]

2. TRADITIONAL INHIBITORS PHARMACOLOGY

Traditional inhibitors cannot always attain desirable pharmacological effects owing to their characteristics as well as attributes of the corresponding biological targets described below:

a) Biological targets for traditional inhibitors are usually enzymes and receptors containing suitable binding sites for the inhibitors, while about 75 % of the human proteome lack such binding sites. Examples of such are transcription factors, scaffolding proteins and other non-enzymatic proteins inside the cell that are unattainable for traditional medicinal chemistry.[12] The challenge of targeting such biological targets can be illustrated through the fact that very few approved agents can exploit such proteins.[13,14]

b) Medicinal chemistry strategies for the development traditional inhibitors focused on targeting specific binding sites may imply high systemic drug exposures in order to attain sufficient and sustained occupancy of biological target *in vivo*.[15] This potentially increases the risk for off-target pharmacological actions and onset of side effects.

c) The potency of traditional inhibitors depends on their affinities towards biological targets.[16]

d) Inhibition of biological targets by traditional inhibitors mainly influences catalytic functions, but not the non-catalytic ones (*e.g.*, scaffolding roles).[16]

e) Competition with overexpressed native ligand for the same biological target can occur after usage of traditional inhibitors.[16]

f) Small-molecule drugs usually disrupt the activity of one domain of multidomain scaffolding proteins, while functions of other domains and their interactions with other proteins remain preserved.[17]

g) Traditional inhibitors may induce compensatory overexpression of corresponding biological targets as well as their accumulation,[18,19] resulting in incomplete inhibition and, consequently, incomplete suppression of downstream signaling pathways.

h) Mutation of genes involved in pathogenesis may generate therapeutically relevant proteins containing conformational changes, which is the reason for the onset of drug resistance.[17] Examples are genes for the epidermal growth factor receptor as well as for the androgen receptor.[20,21]

All the described characteristics of traditional inhibitors and their biological targets originate from the traditional occupancy-driven pharmacology concept, which will be discussed below. Such characteristics severely impede further discovery of drugs belonging to this concept as well as achieving significant and long-term clinical benefits through their usage.[17] On the basis of all the above, it could be concluded that new modalities for targeting therapeutically relevant human proteome are required.

3. INDUCED PROTEIN DEGRADATION: NEW APPROACH IN DRUG DEVELOPMENT

Different pharmacological approaches to manipulate over therapeutically relevant proteins have emerged. Some of them are antisense oligonucleotides (ASOs), small interfering RNAs (siRNAs) and clustered regularly interspaced short palindromic repeats-CRISPR associated protein 9 (CRISPR-Cas9) genetic engineering technology (see Supplementary material to this paper, section S-1). Despite the emergence of new methods for affecting biological targets inside the cells, usage of small-molecule drugs will preserve their place in therapy because they are able to: a) access many organs and sites of action; b) influence multiple biological targets simultaneously; c) be produced without relatively large investments using well known development paths.[1] Hence, new medicinal chemistry strategies relying on the stated advantages of small-molecule drugs could be able to override the shortcomings of traditional pharmacology.

Protein degradation induced by small molecules is an emerging strategy which, as well as nucleic acid-based agents, has the potential to target much more proteins compared to the standard strategies focused on certain binding sites. Furthermore, strategies based on small molecule degraders maintained the pharmaceutical advantages over nucleic acid-based agents.[11] The shift in pharmacological strategy – from protein inhibition to degradation – enables affecting the proteins that have been perceived as pharmacologically intractable.[22,23] Additionally, protein degradation could act synergistically with current therapeutic regimens based on inhibitors. As mentioned above, inhibition of certain cellular pathways could trigger target protein upregulation, which ultimately leads to inhibitor insufficiency.[24,25] Therefore, induced protein degradation (IPD) reduces the number of active proteins to be inhibited, but also resists their compensatory overexpression. Furthermore, many biological targets, which are pharmacologically tractable, have some scaffolding roles that are elusive for traditional pharmacological approaches, but that contribute to resistance mechanisms.[26–32]

In order to understand IPD, it is important to elucidate two main pharmacology concepts: Occupancy-driven pharmacology (ODP) and event-driven pharmacology (EDP, Fig. 1).[11] The onset of many diseases could be related to abnormal protein functioning. This issue has traditionally been addressed using occupancy-driven pharmacology. Namely, the applied inhibitor occupies the disease-related protein, consequently blocking its function and finally achieving therapeutic effect. The longer the protein functions are blocked, the greater is the achieved therapeutic effect. As mentioned above, sustained high local concentrations of an applied inhibitor are required for a therapeutic response and this could lead to off-target binding and adverse effects.[15] An emerging and alternative concept is presented as event-driven pharmacology. In this case the ligand triggers an *event* that ultimately reduces the level of disease-causing protein.

In summary, the ODP model is based on the following postulates:[11]

a) stoichiometric activity of the applied ligand;

b) a ligand must occupy a specific binding site that affects the protein function;

c) if non-covalent inhibitor, a ligand could dissociate from its binding site, which ultimately leads to restoration of the protein functions;

d) ligand selectivity is defined only by its binding profile.

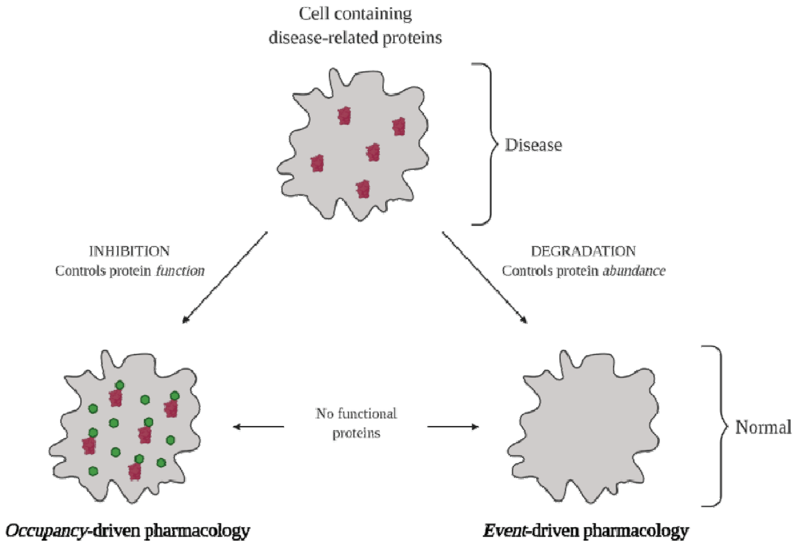

Fig. 1. Occupancy- and event-driven pharmacology models.[33]

On the other hand, the EDP model is based on more advanced postulates:[11]

a) sub-stoichiometric activity of the applied inhibitor;

b) a ligand does not need to occupy a specific binding site that affects protein function;

c) a ligand induce protein degradation, hence restoration of protein functions requires protein resynthesis;

d) ligand selectivity is not only defined by its binding profile.

Many modalities based on the concept of EDP have emerged, and the proteolysis targeting chimera (PROTAC) technology will be further discussed.

4. PROTAC TECHNOLOGY

Proteolysis targeting chimera technology originated from the EDP concept. This approach employs bifunctional molecules where one of their end binds the protein of interest (POI), while the other one recruits cellular quality control mechanisms, which afterwards induce protein degradation. A transient binding only of a PROTAC molecule is sufficient for its activity. In contrast to the stoichiometric occupancy of binding sites within the ODP model, PROTACs can perform multiple cycles of action and thus remove sub-stoichiometric amounts of proteins (*i.e.*, they act catalytically). Furthermore, such molecules do not need to occupy the specific binding site on the protein with high affinity in order to perform as degraders – binding at any suitable region of a biological target could potentially induce its degradation.[11] This advantage could be exploited by using different screens focused on the identification of ligands that simply bind to the biological targets without affecting their function.[34–38] Moreover, turning protein ligands into protein degraders gives an opportunity for utilizing molecules identified by high-throughput screening that were initially rejected because they simply bind to the corresponding biological targets without adequate inhibition.[39–41] As mentioned above, in comparison with the dissociation kinetics of inhibitors originating from the ODP, within the EDP the degradation of the targeted protein occurs, which ultimately requires its resynthesis. This fact gives kinetic advantage to the molecules originating from the EDP. Finally, some studies revealed that PROTACs could undergo less off-target degradation than initially suggested by the POI ligand binding profile.[42] Hence, PROTACs can provide an added layer of selectivity compared to the corresponding inhibitors.

4.1. Mechanistic representation of protein degradation induced by PROTACs

Pharmacologically speaking, PROTACs perform their biological effect (*i.e.*, protein degradation) through the active recruitment of the ubiquitin–proteasome system (UPS, see Supplementary material, Section S-2) that ultimately leads to the POI polyubiquitination and degradation by the 26S proteasome. In summary, PROTACs are bifunctional molecules consisted of a ligand for POI, a ligand for E3 ubiquitin ligase and a linker that connects the two ligands (in the following sections, ligands for POI will be in red, linkers in green and ligands for E3 ubiquitin ligases in blue, Fig. 2).[43]

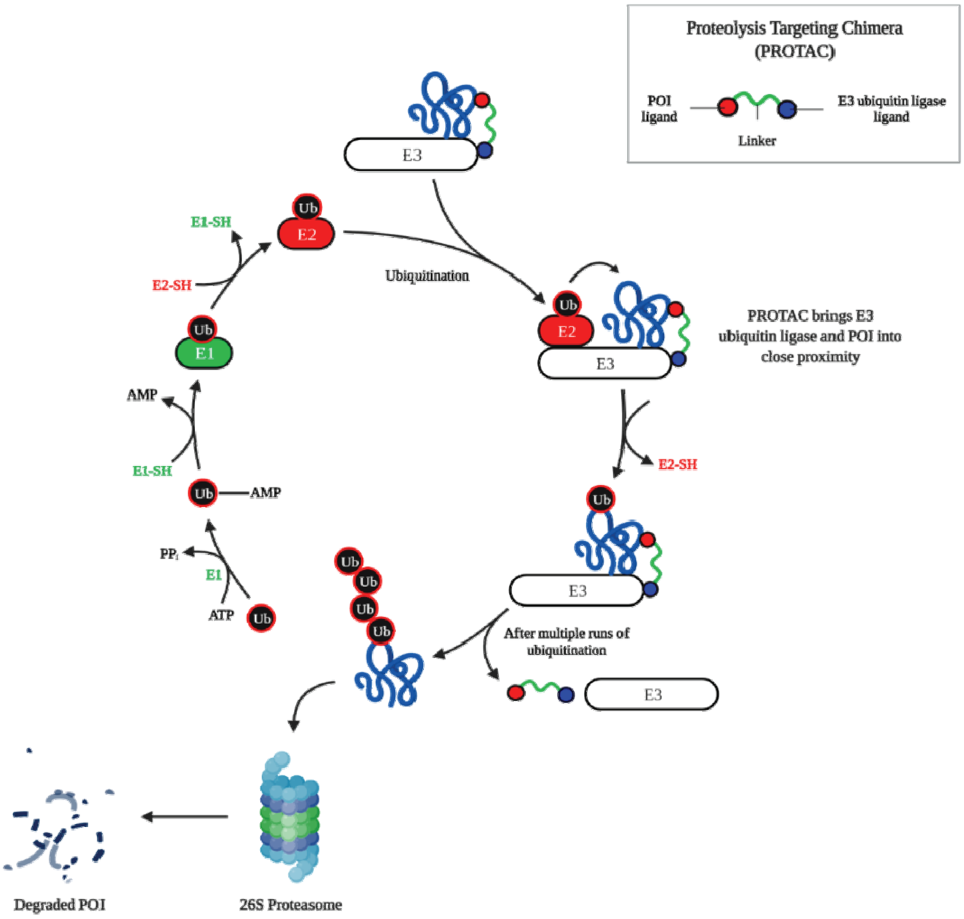

Fig. 2. General structure of PROTAC molecules and their mechanism of action.[46]

Hence, they bind POI and E3 ubiquitin ligase simultaneously which leads to proximity-induced PPIs between these two in the form of ternary complex (TC): POI-PROTAC-E3 ubiquitin ligase[44] (see Supplementary material, section S-3). The recruited E3 ubiquitin ligase mediates multiple runs of ubiquitin transfer from E2 to the POI, the TC dissociates afterwards and finally the polyubiquitinated POI is degraded in the 26S proteasome. Given that PROTAC is not degraded in this process, its destiny can be different depending on its chemical properties:[45] a) non-covalent PROTACs are able to dissociate from the TC and induce multiple cycles of degradation (catalytic mode of action (MOA)); b) if PROTAC is covalently bound to the E3 ubiquitin ligase, but non-covalently to the POI, it is still able to act catalytically (*i.e.*, undergo multiple rounds of degradation); c) PROTAC that is covalently bound to the POI cannot participate in the next round of POI degradation; d) PROTACs bound in a covalent, but reversible manner to either POI or E3 ubiquitin ligase would act catalytically.

Therefore, in contrast to traditional inhibitors where continual drug binding to the biological target is necessary, PROTACs act sub-stoichiometrically and catalytically.[47]

4.2. The development of PROTACs throughout history

The first PROTACs discovered were peptide-based (Fig. 3). Although they could induce POIs degradation, their activities were in the low-micromolar range.[43]

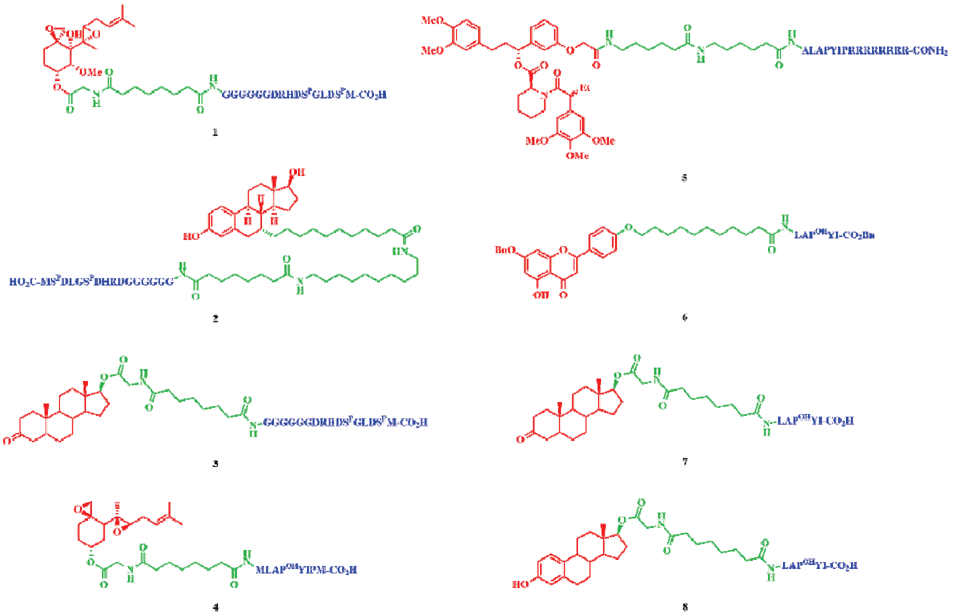

Fig. 3. Chemical structures of the first generation of peptide-based PROTACs (phosphorylated serine is denoted as "S^P" and hydroxyproline is denoted as "P^{OH}").

Additionally, the peptide character made these PROTACs low-permeable, which was their main shortcoming and obstruction toward further development. Ultimately, because of large molecular size, peptide-based PROTACs could potentially be recognized as antigens *in vivo*.[48]

The first PROTAC molecule (**1**, Fig. 3) was reported in 2001 by Crews and Deshaies.[49] It is a peptidic PROTAC containing a peptide ligand for the E3 ubiquitin ligase. This molecule proved the concept of selective protein degradation after their polyubiquitination. On the one hand, it consisted of IκBα phosphopeptide (IPP) as the ligand for $SCF^{\beta\text{-TRCP}}$ E3 ubiquitin ligase, while on the other hand, ovalicin as the ligand for methionine aminopeptidase-2 (MetAP-2) was connected by a hydrocarbon linker. In 2003, new peptidic PROTACs were reported based on the same I*κ*B*α* phosphopeptide linked to estradiol (**2**, Fig. 3) or dihydrotestosterone (**3**, Fig. 3). These PROTACs induced the degradation of estrogen receptor-*α* (ER*α*) and androgen receptor (AR), which expanded the number of degradable biological targets.[50] Degradation of AR in 293AR-GFP cells was achieved after microinjection of **3**, because the phosphate groups on the IκB*α* phosphopeptide impeded its efficient uptake into cells. Hence, this microinjection demonstrated that PROTACs can function in intact cells.[43] The first cell-permeable peptide-based PROTAC (**4**, Fig. 3) was reported in 2003.[51] It consisted of hypoxia-inducible factor-1α (HIF-1*α*) octapeptide as the ligand for VHL (von Hippel–Lindau tumor suppressor) E3 ubiquitin ligase connected *via* the linker with fumagillol as the ligand for MetAP-2. One more cell-permeable PROTAC molecule was reported one year later (**5**, Fig. 3).[52] It consisted of peptide sequence for HIF-1α connected over a linker for the FKBP12 ligand. In 2007, PROTAC molecule was reported for induced degradation of the aryl hydrocarbon receptor (AHR, **6**, Fig. 3).[53] Chemically, it has apigenin as a ligand for AHR connected through the linker for HIF-1*α* peptide. Finally, in 2008 cell-permeable PROTACs were reported that induced the degradation of AR (**7**, Fig. 3) and ER*α* (**8**, Fig. 3).[54] These molecules were composed of estradiol or dihydrotestosterone coupled through the linker with HIF-1*α* pentapeptide.

As research progressed, small-molecule PROTACs emerged in order to over overcome the above mentioned shortcomings of the peptide-based ones.[22,47,55] Significant progress in PROTAC technology was achieved by invention of small-molecule ligands for E3 ubiquitin ligases. The first PROTAC molecule based on them was synthesized in 2008 (**9**, Fig. 4).[56] The mouse double minute 2 homolog (MDM2) E3 ubiquitin ligase was recruited by nutlin, an MDM2-p53 PPI inhibitor,[57] while the other structural element was selective androgen receptor modulator (SARM). The obtained molecule was the first small molecule-based PROTAC that was able to induce the degradation of AR in the HeLa cell line after 7 h. Hence, it was proved that it is possible to make cell-permeable PROTACs, although micromolar concentrations were required to induce AR degradation.[56]

In 2008, it was found that bestatin methyl esters after binding to cellular inhibitor of apoptosis protein 1 (cIAP1) promote its autoubiquitination and degradation.[58] Hence, the Hashimoto laboratory in 2010 utilized bestatin methyl esters for synthesizing the PROTAC molecule denoted as SNIPER-2 (**10**, Fig. 5). It recruited cIAP1 as an E3 ubiquitin ligase to induce the degradation of cellular retionoic acid-binding protein (CRABP-I and CRABP-II) proteins using all-trans retinoic acid (ATRA) as the ligand for the mentioned POIs.[59] However, the synthesized PROTAC had two main shortcomings that could impede the degradation: a) SNIPER-2 induces simultaneous degradation of cIAP1 together with

CRABP-II, which could make POI degradation unsustainable; b) SNIPER-2 has an ester functionality prone to hydrolysis.[60] In order to overcome these drawbacks, in 2011 SNIPER-4 was invented (**11**, Fig. 5) in which the ester was replaced with an amide functionality.[60] It was found that this PROTAC induces sustained CRABP-II degradation without inducing cIAP1 degradation.

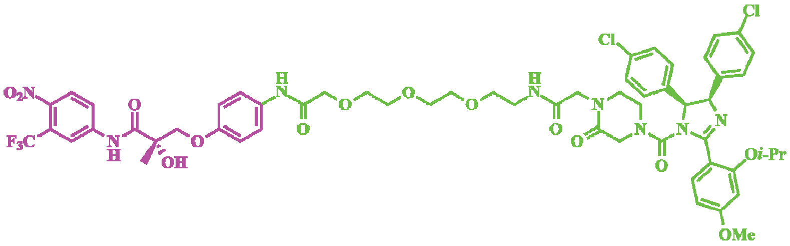

9

Fig. 4. Chemical structure of AR-targeting PROTAC.

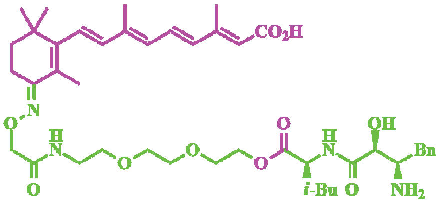

10

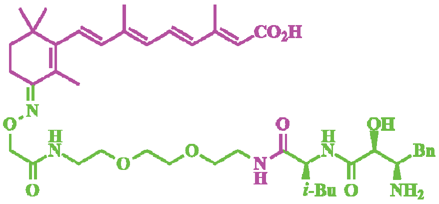

11

Fig. 5. Chemical structures of CRABP-targeting PROTACs.

Despite great progress being made in the development of peptide-based PROTACs that recruit VHL E3 ubiquitin ligase, the road towards small-molecule PROTACs that recruit the same complex was uncertain. However, in 2012, Crews and Ciulli found the first small-molecule ligands for VHL that possessed better physicochemical properties compared to the peptide-based ones as well as adequate affinities for this E3 ubiquitin ligase.[61]

To date, none of the reported PROTACs had been characterized *in vivo*. In 2013, the PhosphoPROTAC molecules emerged. They provided the first evidence that PROTACs could perform biological effects *in vivo* since phosphatidylinositol 3-kinase (PI3K)-targeting PhosphoPROTAC designated as $^{\mathrm{ErbB2}}\mathrm{PP}_{\mathrm{PI3K}}$ (**12**, Fig. 6) inhibited tumor growth in murine models.[62] At the *C*-terminus, the mentioned PhosphoPROTAC was composed of the peptide sequence (marked in blue) derived from the transcription factor HIF-1*α*, which enables binding to the VHL E3 ubiquitin ligase. The sequence downwards (marked in brown) is the octa-*D*-arginine motif that enabled cell permeability of the peptide *via* the same mechanism used by the structurally related HIV transactivator of transcription

(Tat) protein. The *N*-terminus contains a 24-amino acid sequence (marked in red) taken from a PI3K-binding domain on the intracellular region of ErbB3. After phosphorylation of dual tyrosine residues (underlined) in this motif by ErbB2, the 24-amino acid sequence binds to PI3K and ultimately directs it towards polyubiquitination and degradation.

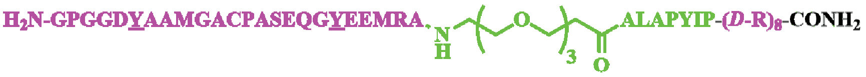

12

Fig. 6. Chemical structure of PI3K-targeting PhosphoPROTAC.

The applicability of the above-mentioned small-molecule-based VHL ligand was first demonstrated in 2015 in the making of HaloPROTAC molecules.[63] Namely, these ones are composed of the small-molecule VHL ligand and a chloroalkane linker, which enables covalent bonding between HaloPROTAC and HaloTag7 (HT7). The latter was a modified bacterial dehalogenase that covalently binds to hexyl chloride moieties.[64] The synthesized HaloPROTACs successfully recruited VHL E3 ubiquitin ligase and induced the degradation of green fluorescent protein (GFP)-HT7 fusion protein. The most potent HaloPROTAC molecule and one of the most potent PROTACs of all the designated as HaloPROTAC 3 (**13**, Fig. 7) performed $D_{\max}$ (maximum percentage of target protein degraded) of 90 % and DC_{50} (concentration at which the target protein is degraded by 50 %) of 19 nM toward GFP-HT7 fusion protein.[63]

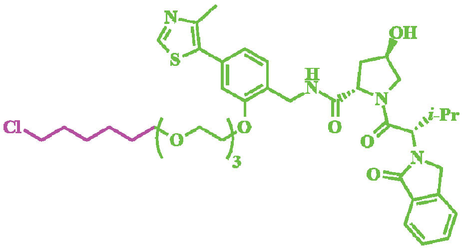

13

Fig. 7. Chemical structure of GFP-HT7-targeting HaloPROTAC.

Another example of a PROTAC based on a similar small-molecule VHL ligand, marked as VH032, is MZ1 (**14**, Fig. 8), which was discovered in 2015. It performed selective removal of BRomoDomain-containing protein (BRD) 4 over BRD2 and BRD3,[40] all of which belong to a family of BET (Bromodomain and Extra-Terminal domain) proteins. During the same year, Bradner and colleagues[65] synthesized dBET1 (**15**, Fig. 8) that contains a thalidomide derivative as a CRL4^{CRBN} (cereblon) E3 ubiquitin ligase recruiter. It induced the degradation of BRD4 with a DC_{50} of 430 nM, which is important for the growth and survival of cancer cells.

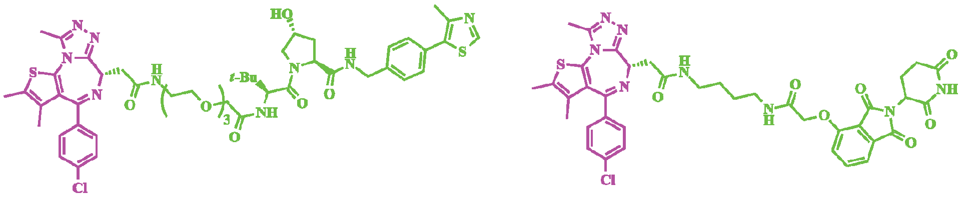

14 **15**

Fig. 8. Chemical structures of (+)-JQ1-based BRD4-targeting PROTACs.

Hence, the discovery of small-molecule PROTACs with drug-like properties enabled the emergence of potent and cell-permeable PROTACs. The third small-molecule-based PROTAC molecule (**16**, Fig. 9) reported in 2015 was developed in the laboratory of Crews with the collaboration of GlaxoSmithKline. It induced the selective degradation of receptor-interacting serine/threonine-protein kinase 2 (RIPK2) protein with low nanomolar DC_{50} of 1.4 nM.[47]

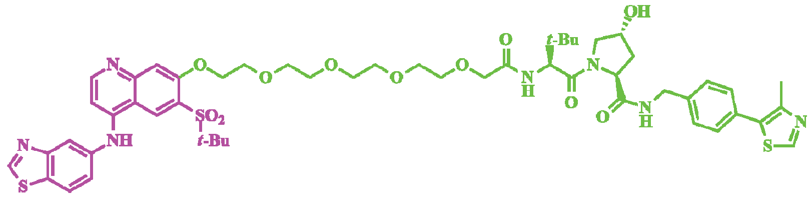

16

Fig. 9. Chemical structure of RIPK2-targeting PROTAC.

Additionally, mechanistic characterization using an *in vitro* ubiquitination assay confirmed that this PROTAC performs a catalytic MOA. Furthermore, the analogous PROTAC, which contains a stereoisomer of the VHL ligand unable to recruit the VHL E3 ubiquitin ligase, was used as a negative control. Since the PROTAC modified in this way was unable to induce RIPK2 degradation, it was confirmed that behind this biological effect stands a mechanism dependent on the E3 ubiquitin ligase.

It is noteworthy that PROTACs are beyond the rule-of-five (bRo5) compounds,[66] meaning that the molar masses of PROTACs are in a significantly higher range than the guidelines of Lipinski. Additionally, such molecules possess high polar surface area (PSA) and all these issues are associated with poor cell permeability, poor solubility and limitation of other drug-like properties. Hence, in 2016 Heightman and colleagues[67] conceived the idea about PROTACs that could be formed intracellularly from two small precursors able to pass through cellular membranes easier than one large compound (*i.e.*, PROTAC).

The molecules arising from this concept were called in-cell CLIck-formed proteolysis targeting chimeras (CLIPTACs). This means that these ones were formed *via* bioorthogonal "click" reaction between the corresponding smaller precursors inside living cells, which overcomes unfavourable physicochemical properties often seen with conventional PROTACs. The reported CLIPTACs successfully degraded two key oncology targets, BRD4 (**17**, Fig. 10) and extracellular signal-regulated kinases (ERK1/2, **18**, Fig. 10). The CLIPTACs were formed after the "click" reaction between the tetrazine-tagged thalidomide derivative and the corresponding *trans*-cyclooctene-tagged POI ligands: (+)-JQ1 for BRD4 and covalent ERK1/2 inhibitor for ERK1/2 (Fig. 10).

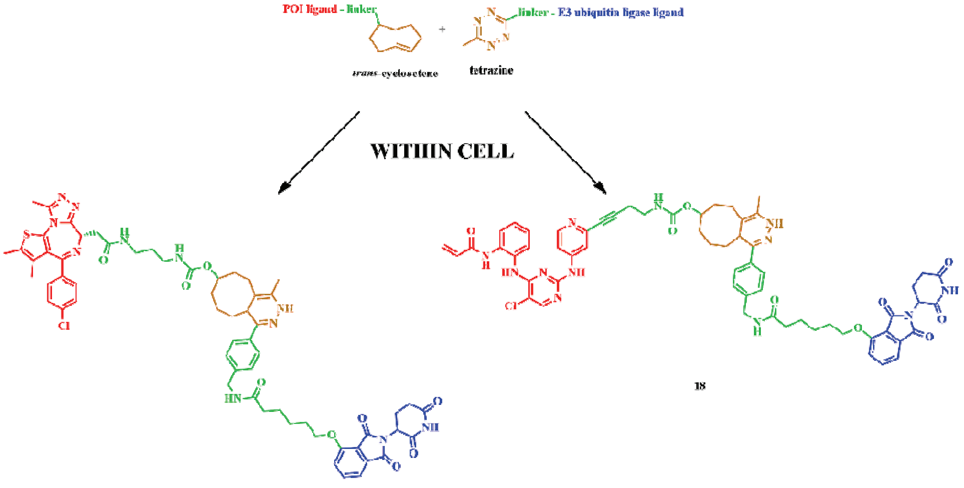

17

Fig. 10. Formation and chemical structures of CLIPTACs targeting BRD4 and ERK1/2.

Beside (+)-JQ1, additional BET inhibitors were used for making potent degraders. One of them, marked as HJB97, was utilized for making BETd-260 degrader (**19**, Fig. 11) reported in 2018, which was capable of inducing the degradation of BRD4 at concentrations as low as 30 pM in the RS4;11 cell line within a 24 h treatment.[68]

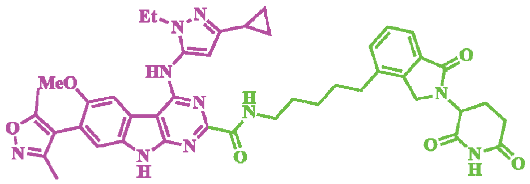

19

Fig. 11. Chemical structure of HJB97-based BRD4-targeting PROTAC.

Ultimately, some PROTACs could potentially hit the clinic as some clinical trials are currently underway. For example, ARV-110 (**20**, Fig. 12), an orally bioavailable, small-molecule PROTAC entered clinical trials in March 2019 for the treatment of patients with metastatic castration resistant prostate cancer (mCRPC) and currently is in phase II.[69] This molecule potently degrades AR with a DC_{50} of 1 nM in VCaP cells.[70] Another PROTAC, ARV-471 (**21**, Fig. 12), an orally bioavailable, small-molecule PROTAC, also entered clinical trials in August 2019 to be examined alone and in combination with palbociclib in patients with ER+/HER2-locally advanced or metastatic breast cancer (mBC). This molecule, as well as ARV-110, is currently in phase II[71] and it induces ER degradation in multiple ER+ breast cancer cell lines, including MCF-7 cells and ESR1-mutant lines with a DC_{50} of 1.8 nM in MCF-7 cells.[70]

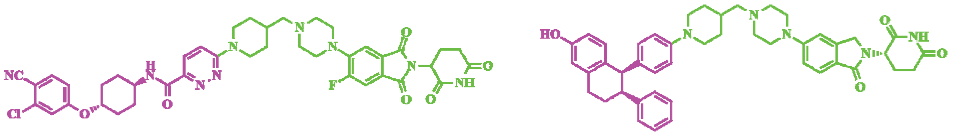

20

21

Fig. 12. Chemical structures of AR- and ER-targeting PROTACs that have entered clinical trials.

4.3. Consideration of the physicochemical properties of PROTACs

The design of PROTAC molecules is challenging since linker-mediated chemical bonding of two molecules with drug-like properties ultimately gives a hybrid molecule with physicochemical properties beyond the Lipinski rule of five.[72,73] It potentially can interfere with cell permeability and oral bioavailability.[74] Despite this, there are numerous examples of PROTACs achieving passive membrane permeability and oral bioavailability.[75] Additionally, the Arvinas company reported that in a preclinical tauopathy model, the PROTAC directed toward the tau protein crosses the blood-brain barrier.[76] Thus, strict adherence to the Lipinski rule of five is not always a good strategy in medicinal chemistry.

A paper published by Maple and colleagues[74] presents a comprehensive database of degrader structures from the peer reviewed literature. More precisely, the aim of this publication was to present physicochemical properties of numerous reported PROTACs and to connected them with biological activities. Physicochemical properties were presented through molecular descriptors and biological activities through degrader scores (*Deg_S*). Five parameters were considered for calculating *Deg_S*: DC_{50}, $D_{\max}$, observed degradation, degrader concentration and incubation time. In order to generate the *Deg_S* values, all scores were summed and normalized against the total number of parameters included for each degrader. The degraders included in the present study could be characterized by a range of high interval molecular descriptors: molecular weight

(*MW*) 614–1,413, calculated log *P* (clog *P*) –2.7–9, number of hydrogen bond donors (*HBD*) 1–10, number of hydrogen bond acceptors (*HBA*) 8–23, number of rotatable bonds (*NRB*) 6–49, number of aromatic rings (*NAR*) 1–7 and topological polar surface area (*TPSA*) 124–389. However, despite relatively high *MW*, the mean *HBD* was ≤ 5, which is within the Lipinski rule of five. The only conclusion that could be drawn by observing the mean vales of the molecular descriptors and *Deg_S* values was that clog *P* increases with increasing *Deg_S*. Correlations between *Deg_S* and other molecular descriptors (*i.e.*, physicochemical properties) were not found. This was expected since the used dataset incorporated a wide range of degraders containing diverse POI ligands, E3 ubiquitin ligase ligands and linkers. Furthermore, PROTACs efficacy depends on their pharmacological properties, such as the kinetics of TC formation as well as POI degradation and resynthesis rate.[77]

Maple and colleagues compared physicochemical properties of the most active PROTACs with other molecules belonging to bRo5 space. Those ones were drugs and clinical candidates with molecular weight greater than 500 Da,[78] orally available preclinical compounds breaking more than one of the Lipinski rules[79] and orally available macrocyclic drugs.[80] It was concluded that PROTACs belong to the physicochemical space which is different from the one to which all of the before mentioned classes of drugs belong. Furthermore, the mean HBD matches with the Lipinski rules and the TPSA values were lower than those for all other bRo5 molecules, which may lead to the conclusion that this molecular descriptor be monitored during PROTACs development. Since highly flexible linkers are usually incorporated into PROTAC molecules, their NRB is greater when compared to the one present within other bRo5 compounds. Noticeable flexibility of PROTACs achieved by great NRB along linkers is potentially significant for cell permeability since recent analysis suggests that dynamically exposed polarity is important for cell permeability and solubility of bRo5 compounds.[81,82]

4.4. The influence of linkers on the physicochemical and pharmacological properties of PROTACs

It is important to note that linkers are not just “ropes” connecting ligands for POI and E3 ubiquitin ligases, their roles are much more complex (see Supplementary material to this paper, Section S-4). Currently there are no general rules regarding the design of the linker the application of which would certainly lead to potent degraders containing any pair of POI/E3 ubiquitin ligase ligands – the whole process is mainly based on the trial and error method. However, when analyzing reported PROTACs some combinations of main structural motifs could be noticed. More precisely, the most common types of linkers are PEG-, alkyl- or modified glycol-based as well as linkers containing more rigid motifs, such as alkyne, piperazine, piperidine and triazole. A summary of different types of linkers is outlined in Table I.[83]

TABLE I. Common structural motifs of linkers and their key features

Linker structure	Structural motif	Key features
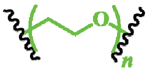	PEG sequence	- Synthetic feasibility and commercial availability - Linker length can be precisely tuned - - Flexibility
	Alkyl sequence	
	Modified glycol sequence	
	Alkyne	- Possible PROTACs potency increase - Possible improvement in PROTACs physicochemical properties - Restricted PROTACs conformation
	Piperazine	
	Piperidine	
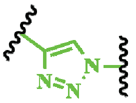	Triazole	- Facilitation in PROTACs syntheses - Possible high-yielding PROTACs syntheses - Possibility to establish additional hydrogen bonds within TC

Linkers containing PEG, alkyl or modified glycol sequences are the most common within PROTACs since they are feasible and flexible. In addition, their length and chemical composition could be modified using common synthetic methods. Combination of PEG and alkyl motifs for making linkers enable tuning of some important physicochemical properties which could be precisely described through clog *P* and TPSA. Values of those ones are in a direct connection with both solubility and cell permeability.

Linkers containing flexible structural motifs were in some PROTACs replaced with those ones containing more rigid elements, such as alkyne or various heterocyclic compounds, in order to increase the rigidity of the final molecule. Improvement in the biological activity of PROTACs by introducing groups that increase the rigidity can be illustrated on BET-targeting PROTACs.[84] Namely, the PROTAC containing an alkyl moiety connected to lenalidomide (CRBN ligand, **22**, Table II) displayed picomolar activity in three leukemia cell lines (MV4;11, MOLM13 and RS4;11). By replacing the amine with an alkyne linkage within thalidomide derivative, a very potent PROTAC denoted as QCA570 (**23**, Table II) was obtained. The resulting molecule showed 6- and 3-fold increased cell activity toward MV4;11 and MOLM13 cells.

TABLE II. Comparative presentation of IC_{50} for two PROTACs containing a flexible and a rigidified linker, respectively

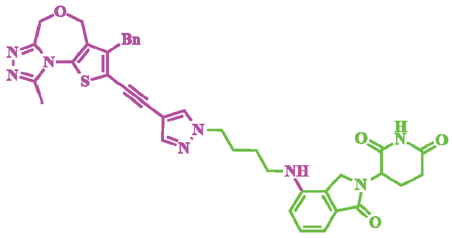 **22**	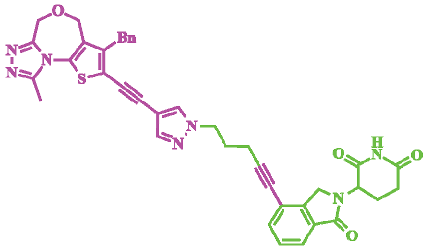 **23**
MV4;11: 51 pM (MV4;11) MOLM13: 180 pM (MOLM13) RS4;11: 1.2 pM (RS4;11)	MV4;11: 8.3 pM MOLM13: 62 pM RS4;11: 32 pM

Using the rigidification strategy, a potent AR degrader denoted as ARD-69 (**24**, Table III) was discovered.[85] Namely, introducing of an ionisable linker containing two adjacent piperidines in the vicinity of an alkyne makes the resultant PROTAC more water soluble compared to the analogous PROTACs containing hydrocarbon-based linkers.

TABLE III. The chemical structure of ARD-69 and its degradation activity represented through DC_{50}

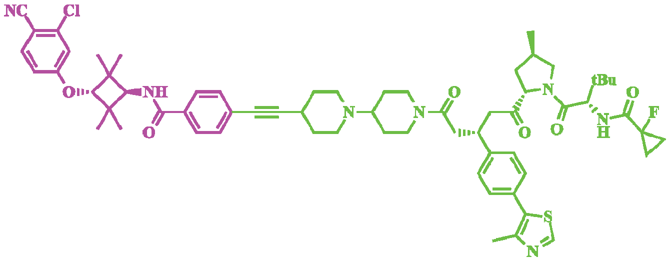 **24**
LNCaP: 0.86 nM VCaP: 0.76 nM

The before-mentioned PROTAC containing a very rigid linker displayed subnanomolar biological activity at degrading AR in LNCaP and VCaP prostate cancer cell lines. Furthermore, downregulation of AR-mediated transcription in the same cell lines was achieved. This highlights the advantages of rigid and polar linkers containing alkynes and heterocyclic motifs with regard to those containing PEG, alkyl or modified glycol sequences. The advantages of the former ones could be explained through their ability to improve the pharmacokinetic properties as well as to rigidify the conformation of PROTACs, which lead to the formation of functional TCs.

Triazole-containing linkers are common in reported PROTACs.[48] The reason for this could be found both in the straightforward triazole synthesis using "click" reaction as well as in chemical robustness of this heterocycle to metabolism.[86] The copper-catalysed Huisgen 1,3-dipolar cycloaddition, often referred as "click" reaction, between an alkyne and an azide has been widely used in the synthesis of triazole derivatives. This is generally a high yielding reaction that shows great regioselectivity toward 1,4-disubstituted 1,2,3-triazoles.[87] Hence, this reaction could be employed for the straightforward synthesis of PROTACs using an alkyne functionality connected to one ligand and an azide functionality connected to the other. Triazole-containing linkers, in addition to be used for feasible PROTACs synthesis, could also be used to modify their physicochemical properties as well as for establishing additional interactions within TC that could stabilize it. More precisely, Schiedel and colleagues[88] developed a triazole-containing SirReal (Sirtuin Rearranging ligand) (**25**, Table IV) that showed improved aqueous solubility compared to the parent compound (**26**, Table IV). Furthermore, the cocrystal structure of Sirtuin 2 (Sirt2) complexed with **25** (PDB code: 5DY5) unveiled that triazole moiety protrudes into the binding channel for acetyllysine where it forms a hydrogen bond with R97 of Sirt2. This resulted in a more efficient blockage of the substrate binding site.

TABLE IV. SirReals' IC_{50} data regarding Sirt2

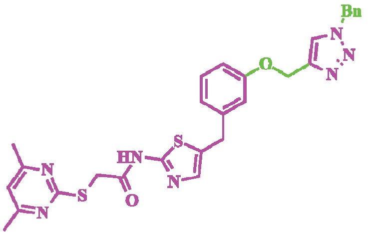 **25**	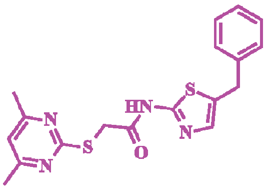 **26**
0.16 µM	3.75 µM

More important, based on the previous study of SirReal-based affinity probe,[89] Schiedel and colleagues[88] had reliable information that placing a linker at N1 of the triazole of SirReal does not diminish the affinity of the resulting PROTAC toward Sirt2. Therefore, the alkyne-functionalized SirReal **27** was "clicked" with the azide-functionalized thalidomide derivative **28** to obtain the corresponding PROTAC **29** (Fig. 13).

It is important to emphasize that docking analysis of **29** in the TC with Sirt2 and CRBN confirmed that the before-mentioned hydrogen bonding originating from the triazole ring remains conserved. More important, the resulting PROTAC **29** inhibited Sirt2 almost 10-fold more potent than the starting alkyne **27**, which confirms the contribution of the hydrogen bond originating from the triazole of PROTAC to the overall inhibitory potential.

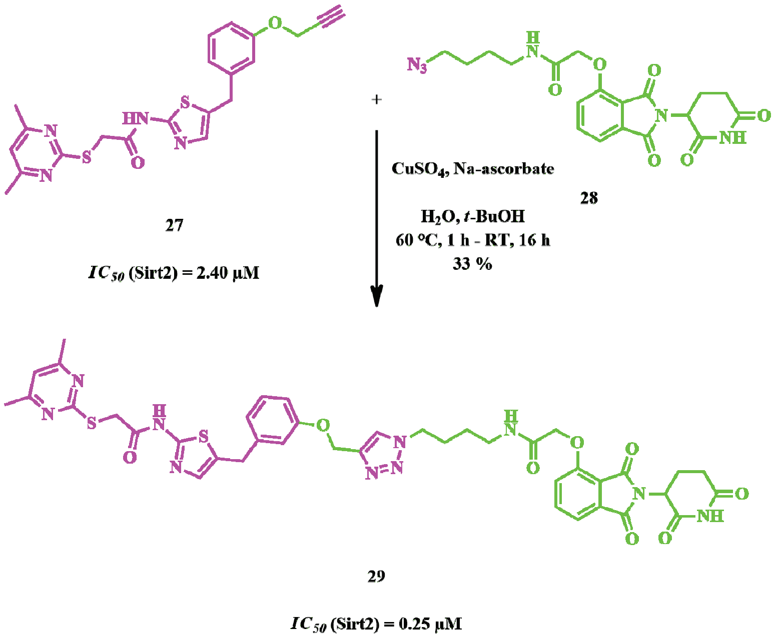

Fig. 13. Synthesis of a Sirt2-targeting PROTAC using a "click" reaction.

4.5. Advantages of the PROTAC -induced POI degradation over the current therapeutic modalities

In the past few decades, several advanced pharmacological approaches have emerged in order to target diseases more efficiently. The traditional inhibitor-based paradigm was modernized by the emergence of methods to block extracellular signaling using mAbs as well as by degrading target mRNA using RNAi approaches.[5]

The crucial advantage of mAbs-based therapies comes from their high binding affinity toward corresponding biological targets as well as a prolonged pharmacokinetic profile due to their endosomal recycling. The main therapeutic application of mAbs isthe blocking of extracellular protein-protein or protein-ligand interactions. However, the main disadvantages of mAbs are their inability to cross cell membanes, the need for parenteral administration and expensive production.[5]

As opposed to mAbs, RNAi molecules (*e.g.*, siRNAs) can pass through cell membranes. Additionally, these molecules can have great pharmacological effects toward mRNAs. Due to their catalytic MOA, siRNAs perform prolonged degradation of mRNAs and display efficacy even at low concentrations, because each siRNA can induce the degradation of multiple mRNA transcripts. However, RNAi molecules have certain shortcomings, such as poor oral bioavailability, poor pharmacokinetics and limited tissue distribution. However, both mAbs and RNAi molecules can affect therapeutically relevant targets more efficiently than ligands belonging to the ODP concept.[5]

Genetic engineering techniques, such as CRISPR-Cas9, usually have a long cycle, irreversible MOA and high cost of goods. All this makes them unsuitable for use in research. Unlike such genetic engineering techniques, PROTACs degrade POIs directly without acting on the genome level. Furthermore, PROTACs provide elegant temporal control over POI degradation. More precisely, such molecules have biological effects over a specific time frame, which enables the recovery of degraded POI (*i.e.*, resynthesis) after discontinuation of the treatment. Thus, as a new method for expeditious POI degradation that *via* influencing the PROTAC concentration can be temporally controlled, PROTAC technology could be perceived as a strategy for reversible and controlled POI degradation, which is an additional and complementary technique to the existing genetic engineering techniques.[90]

On the basis of all the above, it can be concluded that combining the features of traditional inhibitors, mAbs, siRNAs and CRISPR-Cas9 would provide almost ideal molecules. Briefly, such molecules would have the ability to target intracellular proteins and proteins considered pharmacologically intractable, possess high selectivity, oral bioavailability as well as adequate distribution into diverse tissues (including CNS) and perform catalytic MOA which would enable adequate biological effects at low concentrations.[22] The novel pharmacological approach that possess many advantages over the other ones and that could address all previously mentioned features is PROTAC-mediated IPD[91] (see Supplementary material, Section S-5). The summary of the before-mentioned pharmacological modalities is given in Table V.[5,92,93]

TABLE V. The properties of five different pharmacological modalities; PO – oral; IV – intravenous; SC – subcutaneous; IM – intramuscular; IP – intraperitoneal

Property	Traditional inhibitors	mAbs	siRNAs	CRISPR-Cas9	IPD
Effect on intracellular targets	Yes	No	Yes	Yes	Yes
Systemic delivery	Yes	Yes	No	Yes	Yes
Tissue penetration	Yes	Poor	Poor	Yes	Yes
Effect on scaffold proteins	No	Yes	Yes	Yes	Yes
Elimination of pathogenic proteins	No	No	Yes	Yes	Yes
Oral bioavailability	Yes	No	No	No	Yes
The ability to achieve high potency and selectivity	Poor	Yes	Yes	Yes	Yes
Catalytic MOA	No	No	Yes	Yes	Yes
Route of administration	PO/IV/SC	IV/SC	IV/SC	IV/IM/IP	PO/IV/SC

5. CONCLUSIONS AND PERSPECTIVES

Many questions could be asked by observing the PROTAC molecule:[1] a) whether the molecule will enter the cell?; b) whether it will be metabolically stable?; c) whether a rational structure–activity relationship (SAR) study could be performed?; d) whether the molecule will be soluble in water?; e) will it be selective in protein degradation?; f) will it be safe?; g) will it follow the Lipinski rule of five?; h) will chemical synthesis be feasible and cost-effective?; i) can PROTAC technology be applied on a wide range of POIs?

However, the PROTAC technology could have its greatest impact by developing molecules that act on the proteome currently considered as pharmacologically intractable. Examples of PROTAC-mediated degradations so far have been applied to diverse POIs, such as proteases, nuclear hormone receptors, epigenetic factors and kinases. Thus, the PROTAC technology has the potential to target about 80 % of the proteome.[94] However, PROTACs suffer from many shortcomings, such as long synthetic sequences, possible presence of multiple stereocenters, demanding physicochemical characterization and potential for non-crystallinity. Hence, each of those drawbacks has the potential to obstruct the development of PROTAC. Despite this, all the stated results confirm that molecules originating from the EDP concept could have great impact on further drug development and that PROTAC technology could become an important tool in medicinal chemistry thereby making the pharmacologically undruggable proteome pharmacologically vulnerable.[11]

Acknowledgments. This research was funded by the Ministry of Education, Science and Technological Development of the Republic of Serbia through the Grant Agreement with the University of Belgrade – Faculty of Pharmacy No. 451-03-68/2022-14/200161 and by the Science Fund of the Republic of Serbia through the Serbian Science and Diaspora Collaboration Program: Knowledge Exchange Vouchers (Grant No.: 6463913, acronym: DeSyHPRO).

ИЗВОД

ДЕГРАДАЦИЈА ПРОТЕИНА ИНДУКОВАНА PROTAC МОЛЕКУЛИМА КАО НОВА СТРАТЕГИЈА У РАЗВОЈУ ЛЕКОВА

МЛАДЕН КОРАВОВИЋ[1], БОЈАН МАРКОВИЋ[2], МИЛЕНА КОВАЧЕВИЋ[3], МИЛЕНА РМАНДИЋ[4]
и ГОРДАНА ТАСИЋ[1]

[1]Универзитет у Београду – Фармацеутски факултет, Катедра за органску хемију, Војводе Степе 450, 11221 Београд, [2]Универзитет у Београду – Фармацеутски факултет, Катедра за фармацеутску хемију, Војводе Степе 450, 11221 Београд, [3]Универзитет у Београду – Фармацеутски факултет, Катедра за фармакокинетику и клиничку фармацију, Војводе Степе 450, 11221 Београд и [4]Универзитет у Београду – Фармацеутски факултет, Катедра за аналитику лекова, Војводе Степе 450, 11221 Београд

Традиционални концепт открића лекова базиран је на фармаколошком моделу заснованом на окупираности циљних протеина. То подразумева развој инхибитора који окупирају везујућа места директно повезана са функцијама протеина. Стога, протеини који немају таква везујућа места се генерално сматрају фармаколошки недодирљивим. Осим тога, лекови који делују на овакав начин морају се примењивати у режимима дозирања који често доводе до претеране системске изложености леку ради одржања довољне инхибиције протеина. Дакле, постоји ризик од појаве везивања лека ван свог примарног места дејства и нежељених ефеката. Окосница развоја лекова је значајно измењена откако су се појавили PROTAC (енг. *proteolysis targeting chimera*) молекули пре двадесет година као део фармаколошког модела заснованог на покретању догађаја који доводе до разградње циљних протеина. Ово су бифункционални молекули који користе убиквитин-протеазом систем, а састоје се од лиганда који се везује за протеин од интереса (POI), лиганда који регрутује Е3 убиквитин лигазу (E3UL) и линкера који повезује ова два дела. Фармаколошки, PROTAC молекули доводе POI и E3UL у близину, што води формирању функционалног тернарног комплекса POI–PROTAC–E3UL. Овај догађај води полиубиквитинацији и следственој деградацији POI 26S протеазомом. Развој и изузетна својства PROTAC молекула која су их довела до клиничких студија дискутовани су овом раду.

(Примљено 9. децембра 2021, ревидирано 9. марта, прихваћено 14. марта 2022)

REFERENCES

1. I. Churcher, *J. Med. Chem.* **61** (2018) 444 (http://dx.doi.org/10.1021/acs.jmedchem.7b01272)
2. L. E. Limbird, *Mol. Interv.* **4** (2004) 326 (http://dx.doi.org/10.1124/mi.4.6.6)
3. M. Benchekroun, *Future Drug. Discov.* **1** (2019) FDD16 (http://dx.doi.org/10.4155/fdd-2019-0019)
4. M. Rask-Andersen, M. S. Almén, H. B. Schiöth, *Nat. Rev. Drug Discov.* **10** (2011) 579 (http://dx.doi.org/10.1038/nrd3478)
5. T. K. Neklesa, J. D. Winkler, C. M. Crews, *Pharmacol. Ther.* **174** (2017) 138 (http://dx.doi.org/10.1016/j.pharmthera.2017.02.027)
6. J. Campbell, C. J. Ryan, R. Brough, I. Bajrami, H. N. Pemberton, I. Y. Chong, S. Costa-Cabral, J. Frankum, A. Gulati, H. Holme, R. Miller, S. Postel-Vinay, R. Rafiq, W. Wei, C. T. Williamson, D. A. Quigley, J. Tym, B. Al-Lazikani, T. Fenton, R. Natrajan, S. J. Strauss, A. Ashworth, C. J. Lord, *Cell Rep.* **14** (2016) 2490 (http://dx.doi.org/10.1016/j.celrep.2016.02.023)
7. G. S. Cowley, B. A. Weir, F. Vazquez, P. Tamayo, J. A. Scott, S. Rusin, A. East-Seletsky, L. D. Ali, W. F. Gerath, S. E. Pantel, P. H. Lizotte, G. Jiang, J. Hsiao, A. Tsherniak, E. Dwinell, S. Aoyama, M. Okamoto, W. Harrington, E. Gelfand, T. M. Green, M. J. Tomko, S. Gopal, T. C. Wong, H. Li, S. Howell, N. Stransky, T. Liefeld, D. Jang, J. Bistline, B. Hill Meyers, S. A. Armstrong, K. C. Anderson, K. Stegmaier, M. Reich, D. Pellman, J. S. Boehm, J. P. Mesirov, T. R. Golub, D. E. Root, W. C. Hahn, *Sci. Data* **1** (2014) 140035 (http://dx.doi.org/10.1038/sdata.2014.35)
8. T. Wang, K. Birsoy, N. W. Hughes, K. M. Krupczak, Y. Post, J. J. Wei, E. S. Lander, D. M. Sabatini, *Science* **350** (2015) 1096 (http://dx.doi.org/10.1126/science.aac7041)
9. J. Barretina, G. Caponigro, N. Stransky, K. Venkatesan, A. A. Margolin, S. Kim, C. J. Wilson, J. Lehár, G. V. Kryukov, D. Sonkin, A. Reddy, M. Liu, L. Murray, M. F. Berger, J. E. Monahan, P. Morais, J. Meltzer, A. Korejwa, J. Jané-Valbuena, F. A. Mapa, J. Thibault, E. Bric-Furlong, P. Raman, A. Shipway, I. H. Engels, J. Cheng, G. K. Yu, J. Yu, P. Aspesi, M. de Silva, K. Jagtap, M. D. Jones, L. Wang, C. Hatton, E. Palescandolo, S. Gupta, S. Mahan, C. Sougnez, R. C. Onofrio, T. Liefeld, L. MacConaill, W. Winckler, M. Reich, N. Li, J. P. Mesirov, S. B. Gabriel, G. Getz, K. Ardlie, V. Chan, V. E. Myer, B. L. Weber, J. Porter, M. Warmuth, P. Finan, J. L. Harris, M. Meyerson, T. R. Golub, M. P.

Morrissey, W. R. Sellers, R. Schlegel, L. A. Garraway, *Nature* **483** (2012) 603 (http://dx.doi.org/10.1038/nature11003)

10. A. L. Hopkins, C. R. Groom, *Nat. Rev. Drug Discov.* **1** (2002) 727 (http://dx.doi.org/10.1038/nrd892)
11. A. C. Lai, C. M. Crews, *Nat. Rev. Drug Discov.* **16** (2017) 101 (http://dx.doi.org/10.1038/nrd.2016.211)
12. M. Toure, C. M. Crews, *Angew. Chem. Int. Ed. Engl.* **55** (2016) 1966 (http://dx.doi.org/10.1002/anie.201507978)
13. J. S. Lazo, E. R. Sharlow, *Annu. Rev. Pharmacol. Toxicol.* **56** (2016) 23 (http://dx.doi.org/10.1146/annurev-pharmtox-010715-103440)
14. L. Jin, W. Wang, G. Fang, *Annu. Rev. Pharmacol. Toxicol.* **54** (2014) 435 (http://dx.doi.org/10.1146/annurev-pharmtox-011613-140028)
15. A. A. Adjei, *J. Clin. Oncol.* **24** (2006) 4054 (http://dx.doi.org/10.1200/JCO.2006.07.4658)
16. S.-L. Paiva, C. M. Crews, *Curr. Opin. Chem. Biol.* **50** (2019) 111 (http://dx.doi.org/10.1016/j.cbpa.2019.02.022)
17. S. An, L. Fu, *EBioMedicine* **36** (2018) 553 (http://dx.doi.org/10.1016/j.ebiom.2018.09.005)
18. D. Leiser, B. Pochon, W. Blank-Liss, P. Francica, A. A. Glück, D. M. Aebersold, Y. Zimmer, M. Medová, *FEBS Lett.* **588** (2014) 653 (http://dx.doi.org/10.1016/j.febslet.2013.12.025)
19. J. Spiegel, P. M. Cromm, G. Zimmermann, T. N. Grossmann, H. Waldmann, *Nat. Chem. Biol.* **10** (2014) 613 (http://dx.doi.org/10.1038/nchembio.1560)
20. S. Dogan, R. Shen, D. C. Ang, M. L. Johnson, S. P. D'Angelo, P. K. Paik, E. B. Brzostowski, G. J. Riely, M. G. Kris, M. F. Zakowski, M. Ladanyi, *Clin. Cancer Res.* **18** (2012) 6169 (http://dx.doi.org/10.1158/1078-0432.CCR-11-3265)
21. K. Eisermann, D. Wang, Y. Jing, L. E. Pascal, Z. Wang, *Transl. Androl. Urol.* **2** (2013) 137 (http://dx.doi.org/ 10.3978/j.issn.2223-4683.2013.09.15)
22. C. M. Crews, *Chem. Biol.* **17** (2010) 551 (http://dx.doi.org/10.1016/j.chembiol.2010.05.011)
23. J. P. Overington, B. Al-Lazikani, A. L. Hopkins, *Nat. Rev. Drug Discov.* **5** (2006) 993 (http://dx.doi.org/10.1038/nrd2199)
24. J. S. Duncan, M. C. Whittle, K. Nakamura, A. N. Abell, A. A. Midland, J. S. Zawistowski, N. L. Johnson, D. A. Granger, N. V. Jordan, D. B. Darr, J. Usary, P.-F. Kuan, D. M. Smalley, B. Major, X. He, K. A. Hoadley, B. Zhou, N. E. Sharpless, C. M. Perou, W. Y. Kim, S. M. Gomez, X. Chen, J. Jin, S. V. Frye, H. S. Earp, L. M. Graves, G. L. Johnson, *Cell* **149** (2012) 307 (http://dx.doi.org/10.1016/j.cell.2012.02.053)
25. T. Visakorpi, E. Hyytinen, P. Koivisto, M. Tanner, R. Keinänen, C. Palmberg, A. Palotie, T. Tammela, J. Isola, O. P. Kallioniemi, *Nat. Genet.* **9** (1995) 401 (http://dx.doi.org/10.1038/ng0495-401)
26. G. Hatzivassiliou, K. Song, I. Yen, B. J. Brandhuber, D. J. Anderson, R. Alvarado, M. J. C. Ludlam, D. Stokoe, S. L. Gloor, G. Vigers, T. Morales, I. Aliagas, B. Liu, S. Sideris, K. P. Hoeflich, B. S. Jaiswal, S. Seshagiri, H. Koeppen, M. Belvin, L. S. Friedman, S. Malek, *Nature* **464** (2010) 431 (http://dx.doi.org/10.1038/nature08833)
27. S. J. Heidorn, C. Milagre, S. Whittaker, A. Nourry, I. Niculescu-Duvas, N. Dhomen, J. Hussain, J. S. Reis-Filho, C. J. Springer, C. Pritchard, R. Marais, *Cell* **140** (2010) 209 (http://dx.doi.org/10.1016/j.cell.2009.12.040)

28. P. I. Poulikakos, C. Zhang, G. Bollag, K. M. Shokat, N. Rosen, *Nature* **464** (2010) 427 (http://dx.doi.org/10.1038/nature08902)
29. J. Rauch, N. Volinsky, D. Romano, W. Kolch, *Cell Commun. Signal.* **9** (2011) 23 (http://dx.doi.org/10.1186/1478-811X-9-23)
30. X. Tan, N. Thapa, Y. Sun, R. A. Anderson, *Cell* **160** (2015) 145 (http://dx.doi.org/10.1016/j.cell.2014.12.006)
31. I. Vivanco, Z. C. Chen, B. Tanos, B. Oldrini, W.-Y. Hsieh, N. Yannuzzi, C. Campos, I. K. Mellinghoff, *Elife* **3** (2014) e03751 (http://dx.doi.org/10.7554/eLife.03751)
32. Z. Weihua, R. Tsan, W.-C. Huang, Q. Wu, C.-H. Chiu, I. J. Fidler, M.-C. Hung, *Cancer Cell* **13** (2008) 385 (http://dx.doi.org/10.1016/j.ccr.2008.03.015)
33. P. M. Cromm, C. M. Crews, *Cell Chem. Biol.* **24** (2017) 1181 (http://dx.doi.org/10.1016/j.chembiol.2017.05.024)
34. A. M. Giannetti, in *Methods Enzymol.*, L. C. Kuo (Ed.), Academic Press, Cambridge, MA, 2011, p. 169 (http://dx.doi.org/10.1016/B978-0-12-381274-2.00008-X)
35. S. B. Shuker, P. J. Hajduk, R. P. Meadows, S. W. Fesik, *Science* **274** (1996) 1531 (http://dx.doi.org/10.1126/science.274.5292.1531)
36. E. H. Mashalidis, P. Śledź, S. Lang, C. Abell, *Nat. Protoc.* **8** (2013) 2309 (http://dx.doi.org/10.1038/nprot.2013.130)
37. D. A. Erlanson, S. W. Fesik, R. E. Hubbard, W. Jahnke, H. Jhoti, *Nat. Rev. Drug Discov.* **15** (2016) 605 (http://dx.doi.org/10.1038/nrd.2016.109)
38. J.-P. Renaud, C. Chung, U. H. Danielson, U. Egner, M. Hennig, R. E. Hubbard, H. Nar, *Nat. Rev. Drug Discov.* **15** (2016) 679 (http://dx.doi.org/10.1038/nrd.2016.123)
39. K. H. Bleicher, H.-J. Böhm, K. Müller, A. I. Alanine, *Nat. Rev. Drug Discov.* **2** (2003) 369 (http://dx.doi.org/10.1038/nrd1086)
40. R. Macarron, M. N. Banks, D. Bojanic, D. J. Burns, D. A. Cirovic, T. Garyantes, D. V. S. Green, R. P. Hertzberg, W. P. Janzen, J. W. Paslay, U. Schopfer, G. S. Sittampalam, *Nat. Rev. Drug Discov.* **10** (2011) 188 (http://dx.doi.org/10.1038/nrd3368)
41. I. Kola, J. Landis, *Nat. Rev. Drug Discov.* **3** (2004) 711 (http://dx.doi.org/10.1038/nrd1470)
42. M. Zengerle, K.-H. Chan, A. Ciulli, *ACS Chem. Biol.* **10** (2015) 1770 (http://dx.doi.org/10.1021/acschembio.5b00216)
43. M. Pettersson, C. M. Crews, *Drug Discov. Today Technol.* **31** (2019) 15 (http://dx.doi.org/10.1016/j.ddtec.2019.01.002)
44. T. Ishida, A. Ciulli, *SLAS Discov.* **26** (2021) 484 (http://dx.doi.org/10.1177/2472555220965528)
45. M. J. Bond, C. M. Crews, *RSC Chem. Biol.* **2** (2021) 725 (http://dx.doi.org/10.1039/D1CB00011J)
46. Z. S. Hann, C. Ji, S. K. Olsen, X. Lu, M. C. Lux, D. S. Tan, C. D. Lima, *Proc. Natl. Acad. Sci. U.S.A.* **116** (2019) 15475 (http://dx.doi.org/10.1073/pnas.1905488116)
47. D. P. Bondeson, A. Mares, I. E. D. Smith, E. Ko, S. Campos, A. H. Miah, K. E. Mulholland, N. Routly, D. L. Buckley, J. L. Gustafson, N. Zinn, P. Grandi, S. Shimamura, G. Bergamini, M. Faelth-Savitski, M. Bantscheff, C. Cox, D. A. Gordon, R. R. Willard, J. J. Flanagan, L. N. Casillas, B. J. Votta, W. den Besten, K. Famm, L. Kruidenier, P. S. Carter, J. D. Harling, I. Churcher, C. M. Crews, *Nat. Chem. Biol.* **11** (2015) 611 (http://dx.doi.org/10.1038/nchembio.1858)
48. L.-W. Xia, M.-Y. Ba, W. Liu, W. Cheng, C.-P. Hu, Q. Zhao, Y.-F. Yao, M.-R. Sun, Y.-T. Duan, *Future Med. Chem.* **11** (2019) 2919 (http://dx.doi.org/10.4155/fmc-2019-0159)

49. K. M. Sakamoto, K. B. Kim, A. Kumagai, F. Mercurio, C. M. Crews, R. J. Deshaies, *Proc. Natl. Acad. Sci. U.S.A.* **98** (2001) 8554 (http://dx.doi.org/10.1073/pnas.141230798)
50. K. M. Sakamoto, K. B. Kim, R. Verma, A. Ransick, B. Stein, C. M. Crews, R. J. Deshaies, *Mol. Cell. Proteomics* **2** (2003) 1350 (http://dx.doi.org/10.1074/mcp.T300009-MCP200)
51. D. Zhang, S.-H. Baek, A. Ho, K. Kim, *Bioorg. Med. Chem. Lett.* **14** (2004) 645 (http://dx.doi.org/10.1016/j.bmcl.2003.11.042)
52. J. S. Schneekloth, F. N. Fonseca, M. Koldobskiy, A. Mandal, R. Deshaies, K. Sakamoto, C. M. Crews, *J. Am. Chem. Soc.* **126** (2004) 3748 (http://dx.doi.org/10.1021/ja039025z)
53. H. Lee, D. Puppala, E.-Y. Choi, H. Swanson, K.-B. Kim, *Chembiochem* **8** (2007) 2058 (http://dx.doi.org/10.1002/cbic.200700438)
54. A. Rodriguez-Gonzalez, K. Cyrus, M. Salcius, K. Kim, C. M. Crews, R. J. Deshaies, K. M. Sakamoto, *Oncogene* **27** (2008) 7201 (http://dx.doi.org/10.1038/onc.2008.320)
55. D. L. Buckley, C. M. Crews, *Angew. Chem. Int. Ed. Engl.* **53** (2014) 2312 (http://dx.doi.org/10.1002/anie.201307761)
56. A. R. Schneekloth, M. Pucheault, H. S. Tae, C. M. Crews, *Bioorg. Med. Chem. Lett.* **18** (2008) 5904 (http://dx.doi.org/10.1016/j.bmcl.2008.07.114)
57. L. T. Vassilev, B. T. Vu, B. Graves, D. Carvajal, F. Podlaski, Z. Filipovic, N. Kong, U. Kammlott, C. Lukacs, C. Klein, N. Fotouhi, E. A. Liu, *Science* **303** (2004) 844 (http://dx.doi.org/10.1126/science.1092472)
58. K. Sekine, K. Takubo, R. Kikuchi, M. Nishimoto, M. Kitagawa, F. Abe, K. Nishikawa, T. Tsuruo, M. Naito, *J. Biol. Chem.* **283** (2008) 8961 (http://dx.doi.org/10.1074/jbc.M709525200)
59. Y. Itoh, M. Ishikawa, M. Naito, Y. Hashimoto, *J. Am. Chem. Soc.* **132** (2010) 5820 (http://dx.doi.org/10.1021/ja100691p)
60. K. Okuhira, N. Ohoka, K. Sai, T. Nishimaki-Mogami, Y. Itoh, M. Ishikawa, Y. Hashimoto, M. Naito, *FEBS Lett.* **585** (2011) 1147 (http://dx.doi.org/10.1016/j.febslet.2011.03.019)
61. D. L. Buckley, I. Van Molle, P. C. Gareiss, H. S. Tae, J. Michel, D. J. Noblin, W. L. Jorgensen, A. Ciulli, C. M. Crews, *J. Am. Chem. Soc.* **134** (2012) 4465 (http://dx.doi.org/10.1021/ja209924v)
62. J. Hines, J. D. Gough, T. W. Corson, C. M. Crews, *Proc. Natl. Acad. Sci. U.S.A.* **110** (2013) 8942 (http://dx.doi.org/10.1073/pnas.1217206110)
63. D. L. Buckley, K. Raina, N. Darricarrere, J. Hines, J. L. Gustafson, I. E. Smith, A. H. Miah, J. D. Harling, C. M. Crews, *ACS Chem. Biol.* **10** (2015) 1831 (http://dx.doi.org/10.1021/acschembio.5b00442)
64. R. F. Ohana, L. P. Encell, K. Zhao, D. Simpson, M. R. Slater, M. Urh, K. V. Wood, *Protein Expr. Purif.* **68** (2009) 110 (http://dx.doi.org/10.1016/j.pep.2009.05.010)
65. G. E. Winter, D. L. Buckley, J. Paulk, J. M. Roberts, A. Souza, S. Dhe-Paganon, J. E. Bradner, *Science* **348** (2015) 1376 (http://dx.doi.org/10.1126/science.aab1433)
66. G. Ermondi, D. Garcia Jimenez, M. Rossi Sebastiano, G. Caron, *ACS Med. Chem. Lett.* **12** (2021) 1056 (http://dx.doi.org/10.1021/acsmedchemlett.1c00298)
67. H. Lebraud, D. J. Wright, C. N. Johnson, T. D. Heightman, *ACS Cent. Sci.* **2** (2016) 927 (http://dx.doi.org/10.1021/acscentsci.6b00280)
68. B. Zhou, J. Hu, F. Xu, Z. Chen, L. Bai, E. Fernandez-Salas, M. Lin, L. Liu, C.-Y. Yang, Y. Zhao, D. McEachern, S. Przybranowski, B. Wen, D. Sun, S. Wang, *J. Med. Chem.* **61** (2018) 462 (http://dx.doi.org/10.1021/acs.jmedchem.6b01816)

69. ClinicalTrials.gov, http://clinicaltrials.gov/ct2/show/NCT03888612 (accessed Nov 18, 2021)
70. ARVINAS, http://ir.arvinas.com/static-files/1667ba5f-46b6-4c6c-a868-bc1a306fdaad (accessed Nov 22, 2021)
71. Clinicaltrials.gov, http://clinicaltrials.gov/ct2/show/NCT04072952 (accessed Nov 18, 2021)
72. C. A. Lipinski, F. Lombardo, B. W. Dominy, P. J. Feeney, *Adv. Drug Deliv. Rev.* **46** (2001) 3 (http://dx.doi.org/ 10.1016/s0169-409x(00)00129-0)
73. C. A. Lipinski, *Drug Discov. Today Technol.* **1** (2004) 337 (http://dx.doi.org/10.1016/j.ddtec.2004.11.007)
74. H. J. Maple, N. Clayden, A. Baron, C. Stacey, R. Felix, *Medchemcomm* **10** (2019) 1755 (http://dx.doi.org/10.1039/C9MD00272C)
75. T. Neklesa, L. B. Snyder, R. R. Willard, N. Vitale, J. Pizzano, D. A. Gordon, M. Bookbinder, J. Macaluso, H. Dong, C. Ferraro, G. Wang, J. Wang, C. M. Crews, J. Houston, A. P. Crew, I. Taylor, *J. Clin. Oncol.* **37** (2019) 259 (http://dx.doi.org/10.1200/JCO.2019.37.7_suppl.259)
76. ARVINAS, http://ir.arvinas.com/node/7136/pdf (accessed Nov 22, 2021)
77. Y. Zhang, C. Loh, J. Chen, N. Mainolfi, *Drug Discov. Today Technol.* **31** (2019) 53 (http://dx.doi.org/10.1016/j.ddtec.2019.01.001)
78. B. C. Doak, B. Over, F. Giordanetto, J. Kihlberg, *Chem. Biol.* **21** (2014) 1115 (http://dx.doi.org/10.1016/j.chembiol.2014.08.013)
79. D. A. DeGoey, H.-J. Chen, P. B. Cox, M. D. Wendt, *J. Med. Chem.* **61** (2018) 2636 (http://dx.doi.org/10.1021/acs.jmedchem.7b00717)
80. E. A. Villar, D. Beglov, S. Chennamadhavuni, J. A. Porco, D. Kozakov, S. Vajda, A. Whitty, *Nat. Chem. Biol.* **10** (2014) 723 (http://dx.doi.org/10.1038/nchembio.1584)
81. M. Rossi Sebastiano, B. C. Doak, M. Backlund, V. Poongavanam, B. Over, G. Ermondi, G. Caron, P. Matsson, J. Kihlberg, *J. Med. Chem.* **61** (2018) 4189 (http://dx.doi.org/10.1021/acs.jmedchem.8b00347)
82. B. Kuhn, P. Mohr, M. Stahl, *J. Med. Chem.* **53** (2010) 2601 (http://dx.doi.org/10.1021/jm100087s)
83. R. I. Troup, C. Fallan, M. G. J. Baud, *Explor. Target. Antitumor Ther.* **1** (2020) 273 (http://dx.doi.org/10.37349/etat.2020.00018)
84. C. Qin, Y. Hu, B. Zhou, E. Fernandez-Salas, C.-Y. Yang, L. Liu, D. McEachern, S. Przybranowski, M. Wang, J. Stuckey, J. Meagher, L. Bai, Z. Chen, M. Lin, J. Yang, D. N. Ziazadeh, F. Xu, J. Hu, W. Xiang, L. Huang, S. Li, B. Wen, D. Sun, S. Wang, *J. Med. Chem.* **61** (2018) 6685 (http://dx.doi.org/10.1021/acs.jmedchem.8b00506)
85. X. Han, C. Wang, C. Qin, W. Xiang, E. Fernandez-Salas, C.-Y. Yang, M. Wang, L. Zhao, T. Xu, K. Chinnaswamy, J. Delproposto, J. Stuckey, S. Wang, *J. Med. Chem.* **62** (2019) 941 (http://dx.doi.org/10.1021/acs.jmedchem.8b01631)
86. H. C. Kolb, M. G. Finn, K. B. Sharpless, *Angew. Chem. Int. Ed. Engl.* **40** (2001) 2004 (http://dx.doi.org/10.1002/1521-3773(20010601)40:11<2004::AID-ANIE2004>3.0.CO;2-5)
87. J. E. Moses, A. D. Moorhouse, *Chem. Soc. Rev.* **36** (2007) 1249 (http://dx.doi.org/10.1039/B613014N)
88. M. Schiedel, D. Herp, S. Hammelmann, S. Swyter, A. Lehotzky, D. Robaa, J. Oláh, J. Ovádi, W. Sippl, M. Jung, *J. Med. Chem.* **61** (2018) 482 (http://dx.doi.org/10.1021/acs.jmedchem.6b01872)

89. M. Schiedel, T. Rumpf, B. Karaman, A. Lehotzky, S. Gerhardt, J. Ovádi, W. Sippl, O. Einsle, M. Jung, *Angew. Chem. Int. Ed. Engl.* **55** (2016) 2252 (http://dx.doi.org/10.1002/anie.201509843)
90. X. Sun, J. Wang, X. Yao, W. Zheng, Y. Mao, T. Lan, L. Wang, Y. Sun, X. Zhang, Q. Zhao, J. Zhao, R.-P. Xiao, X. Zhang, G. Ji, Y. Rao, *Cell Discov.* **5** (2019) 10 (http://dx.doi.org/10.1038/s41421-018-0079-1)
91. R. J. Deshaies, *Nat. Chem. Biol.* **11** (2015) 634 (http://dx.doi.org/10.1038/nchembio.1887)
92. X. Sun, H. Gao, Y. Yang, M. He, Y. Wu, Y. Song, Y. Tong, Y. Rao, *Signal Transduct. Target. Ther.* **4** (2019) 64 (http://dx.doi.org/10.1038/s41392-019-0101-6)
93. C. E. Nelson, C. H. Hakim, D. G. Ousterout, P. I. Thakore, E. A. Moreb, R. M. C. Rivera, S. Madhavan, X. Pan, F. A. Ran, W. X. Yan, A. Asokan, F. Zhang, D. Duan, C. A. Gersbach, *Science* **351** (2016) 403 (http://dx.doi.org/10.1126/science.aad5143)
94. G. A. Collins, A. L. Goldberg, *Cell* **169** (2017) 792 (http://dx.doi.org/10.1016/j.cell.2017.04.023).

Journal of the Serbian Chemical Society
JSCS@tmf.bg.ac.rs • www.shd.org.rs/JSCS
J. Serb. Chem. Soc. 87 (7–8) S249–S262 (2022)
Supplementary material

SUPPLEMENTARY MATERIAL TO

Protein degradation induced by PROTAC molecules as an emerging drug discovery strategy

MLADEN KORAVOVIĆ[1]*, BOJAN MARKOVIĆ[2], MILENA KOVAČEVIĆ[3], MILENA RMANDIĆ[4] and GORDANA TASIĆ[1]**

[1]University of Belgrade – Faculty of Pharmacy, Department of Organic Chemistry, Vojvode Stepe 450, 11221 Belgrade, Serbia, [2]University of Belgrade – Faculty of Pharmacy, Department of Pharmaceutical Chemistry, Vojvode Stepe 450, 11221 Belgrade, Serbia, [3]University of Belgrade – Faculty of Pharmacy, Department of Pharmacokinetics and Clinical Pharmacy, Vojvode Stepe 450, 11221 Belgrade, Serbia and [4]University of Belgrade – Faculty of Pharmacy, Department of Drug Analysis, Vojvode Stepe 450, 11221 Belgrade, Serbia

J. Serb. Chem. Soc. 87 (7–8) (2022) 785–811

S-1. METHODS TO MANIPULATE PROTEINS OF INTEREST

One method for modulating intracellular proteins is through agents based on nucleic acids, such as antisense oligonucleotides (ASOs), as well as by using agents that exploit RNA interference (RNAi) such as small interfering RNAs (siRNAs). Agents based on nucleic acids have proved themselves to be useful in research, but their development toward potential medicines has faced many challenges: unmodified nucleotides are unstable in serum,[1] while modified ones tend to accumulate in the kidneys[2,3] and can be immunogenic,[4,5] Furthermore, agents based on nucleic acids encapsulated by nanoparticles to improve the distribution are sequestrated in the liver.[6–9] On the other hand, RNAi can recruit off-target messenger ribonucleic acid (mRNA), which leads to undesired effects.[10–12]

Innovative CRISPR-Cas9 genetic engineering technology performs direct genome modification to achieve gene knockout,[13,14] *i.e.* to make the targeted gene inoperative. Although CRISPR-Cas9 is very useful in research, its path toward clinical application is questionable.[15]

The efficacy of these approaches is strongly dependent on the target protein half-life – the long-lived ones are less affected.

---

*,** Corresponding authors. E-mail: (*)mladen.koravovic@pharmacy.bg.ac.rs; (**)gordana.tasic@pharmacy.bg.ac.rs

S-2. UBIQUITIN-PROTEASOME SYSTEM (UPS)

The UPS is the primary pathway for intracellular protein degradation in eukaryotic cells[16] (Fig. S-1). In this process, ubiquitin, evolutionary conserved 76 amino acid polypeptide, is used to mark proteins for degradation. After labeling with ubiquitin, proteins are recognized and degraded by the 26S proteasome. Mechanistically, protein ubiquitination occurs through a three-step enzymatic reaction.[17]

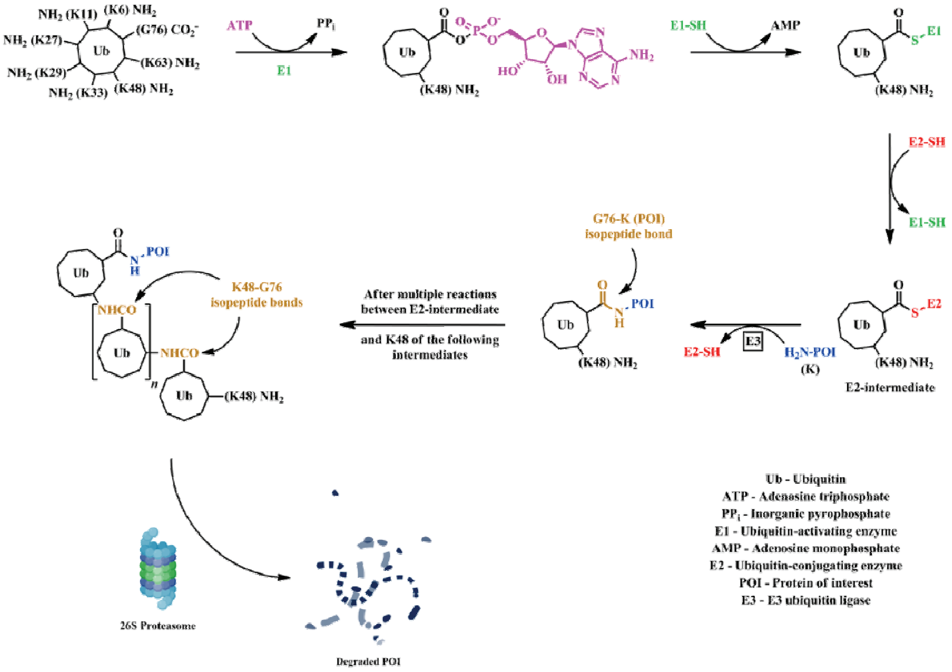

Fig. S-1. Ubiquitin-proteasome system.[18]
(K-residues on all ubiquitins except on the first one were omitted for clarity)

First, the ubiquitin-activating enzyme (E1) creates a thioester bond *via* an ATP-dependent mechanism between the *C*-terminal glycine-76 (G76) residue of ubiquitin and a cysteine residue in its active site. The thioesterified ubiquitin is then transferred from the E1 active site to the ubiquitin-conjugating enzyme (E2) *via* a transthioesterification reaction. Finally, the E3 ubiquitin ligase (E3) binds to both E2-bound ubiquitin and the protein intended for degradation promoting the transfer of ubiquitin onto the protein. After this last step, an isopeptide bond is formed between the carboxyl group of the last amino acid of ubiquitin– G76 and the ε-amino group of the substrate protein's lysine (K). Ubiquitin itself contains seven lysine residues at positions 6, 11, 27, 29, 33, 48 and 63 all of which can serve as acceptors for the second ubiquitin molecule, thus leading to the polyubiquitination of the substrate protein after multiple runs of ubiquitination.[19–21] Interestingly, organization of the polyubiquitination enzymatic cascade follows a hierarchical order. Namely, the human genome encodes two E1 enzymes, 38 E2 enzymes and more than 600 E3 enzymes.[21–25] It is important to say that some proteins can be ubiquitinated with only one ubiquitin on a single lysine residue, which is known as monoubiquitination, as well as on multiple lysine residues, which is known as multi-monoubiquitination. However, only polyubiquitination of proteins can lead to their degradation. Depending on the mode by which ubiquitins are attached in the polyubiquitin chain, the outcome for polyubiquitinated proteins can be different. Proteins marked with K48- or K11-linked polyubiquitin chains are predominantly targeted for recognition and degradation by the 26S proteasome, whereas the K63-linked polyubiquitination or monoubiquitination alters the function of the protein and their subcellular localization. Thus, proteins marked in this way are not intended for degradation but to participate in protein-protein interactions (PPIs), DNA damage responses and signal transduction.[26–31]

S-3. DYNAMICS OF PROTAC-MEDIATED INDUCED PROTEIN DEGRADATION (IPD)

The mechanism of IPD depends on the formation of a ternary complex (TC) that enables the protein of interest (POI) polyubiquitination and proteasomal degradation. Some mathematical models describing TC formation have already been established[32,33] and they predict a bell-shaped dependency between the concentrations of TC and PROTAC (Fig. S-2).[34]

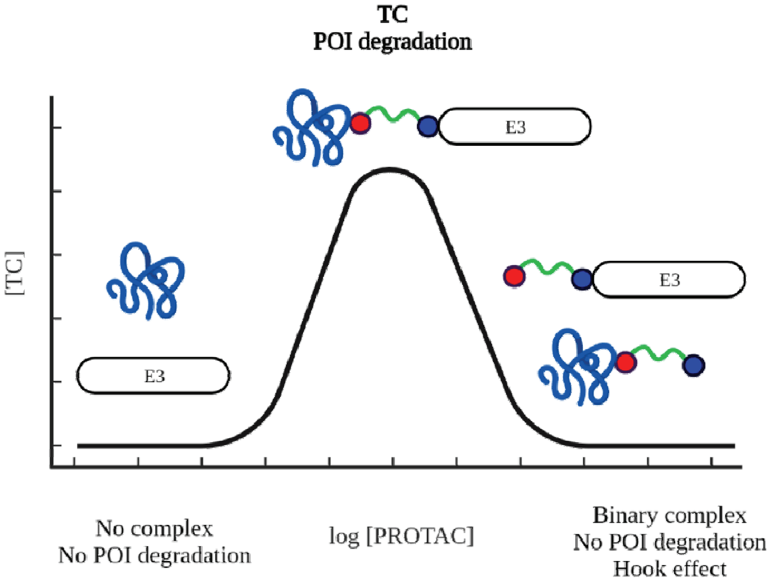

Fig. S-2. Kinetics of ternary complex formation.[35]

Therefore, when the concentration of PROTAC molecules is significantly higher than the DC_{50} (concentration at which the target protein is degraded by 50 %), autoinhibition of TC formation occurs due to increased concentration of PROTAC:E3 ubiquitin ligase and PROTAC:POI binary non-functional complexes.[36] This phenomenon is called "the hook effect"[37] and in the case of PROTACs can be defined as the reduced degradation of POI at high concentrations of small-molecule PROTACs. This phenomenon commonly occurs with three-component systems.[36]

Moreover, attractive or repulsive interactions between the POI and E3 ubiquitin ligase may affect TC formation (Fig. S-3). The term "cooperativity" (α) is used to describe these interactions. More precisely, positive cooperativity (*i.e.* $\alpha > 1$) occurs when PPIs between POI and E3 ubiquitin ligase leads to TC formation. Conversely, negative cooperativity (*i.e.* $\alpha < 1$) occurs when the before-mentioned PPIs revoke TC formation. Positive cooperativity minimizes the extent of the hook effect, thus resulting in increased productive TC formation.[38]

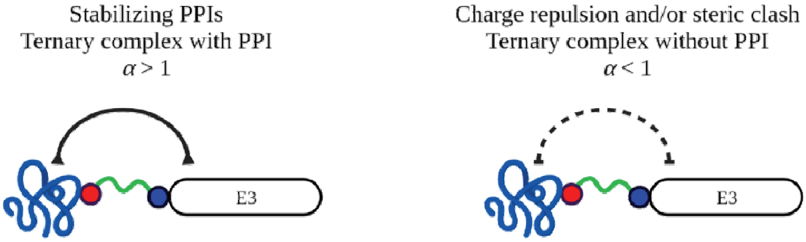

Fig. S-3. Positive and negative cooperativity.[35]

The first crystal structure of TC composed of the MZ1 PROTAC molecule **14**, BRomoDomain-containing protein (BRD) 4 protein and von Hippel-Lindau tumor suppressor (VHL) E3 ubiquitin ligase was reported in 2017 by Ciulli.[39] The crystal structure disclosed the interactions between BRD4 and VHL E3 ubiquitin ligase as well as interactions between the linker and BRD4. The presence of positive cooperativity, as evaluated by isothermal titration calorimetry studies, supported by surface mutagenesis and proximity assays, resulted in higher PROTAC potency and selectivity toward individual members of the BET family proteins.

Further research demonstrated that TC formation can be more important for IPD than binary affinity of POI ligand or complete PROTAC toward the corresponding biological target. For example, foretinib-based PROTAC that possesses relatively low binary affinity toward p38α (K_d = 11 μM) can nevertheless induce the degradation of this POI (DC_{50} = 210 nM, D_{max} (maximum content of target protein degraded) = 91 %).[40] It was noticed that this PROTAC induce the TC formation *via* stabilizing PPIs between p38α and VHL

E3 ubiquitin ligase. It compensated low PROTAC binary affinity for p38α and ultimately led to POI degradation. Therefore, even low-affinity interactions between PROTACs and the corresponding POIs may be stabilized by high-affinity interactions within TC, leading to efficient POI degradation. In accordance with this finding, high affinity POI ligand is not sufficient to obtain potent PROTACs.[41]

Given that PROTACs are a part of the event-driven pharmacology (EDP), it provides additional selectivity toward homologous biological targets when compared to traditional inhibitors. The above mentioned foretinib is a promiscuous kinase ligand that can bind more than 130 kinases. The Crews laboratory demonstrated that foretinib-based PROTAC has a greater binary affinity compared to foretinib itself, because it binds to more than 50 kinases, but induces the degradation of less than 10.[40] In addition, depending on which E3 ubiquitin ligase (cereblon (CRBN) or VHL) was recruited, different degradation profiles were observed. The basis of such selectivity lies in PPIs between E3 ubiquitin ligases and POIs. This conclusion was proved by the existence of proteins that interacted with PROTAC, but remained undegraded because of unstable TCs constructed with recruited E3 ubiquitin ligases.[40] Hence, it could be concluded that simple binding of PROTAC for POI does not necessarily induce degradation. This illustrates the importance of stable TCs formation.

In contrast with this finding, using high-affinity ligands for POIs in PROTAC design is not always sufficient for a biological effect. Namely, despite incorporating high-affinity ligand for BRD4 denoted as I-BET726 (K_d = 4 nM), the PROTAC molecule which contains a lower affinity ligand, denoted as JQ1 (K_d = 100 nM), was more efficient in BRD4 degradation. Such a result is the consequence of the ability of JQ1-based PROTAC to promote TC formation *via* positive cooperativity.[41] However, there are examples of PROTACs where cooperativity is less important for POI degradation.[42,43] For example, CRBN-based potent PROTACs targeting BTK (Bruton's tyrosine kinase) (DC_{50} = 1-40 nM) and BRD4 (DC_{50} = 5–50 nM) showed very little to no cooperativity.

Phillips and Fisher described PROTACs as "programmable essential activators of ubiquitin ligase enzymes":[44] *programmable*, since they can be designed to target any POI; *essential*, since ubiquitin transfer will not occur in their absence; *activators*, since they act as recyclable catalysts that mediate the formation of a catalytically active complex (*i.e.* TC). Therefore, perceiving PROTACs as activators, more precisely as catalysts for POI degradation, gives an outline to better understand PROTAC pharmacology.

Briefly, it is important to consider TC formation during the development of PROTAC molecules. It has already been stated that reliance on binary affinities of either POI ligands incorporated in PROTACs or complete PROTACs can misguide the development of potent degraders. In addition, the importance of cooperativity in TC formation is different for individual E3 ubiquitin ligases and POIs. Hence, it is difficult to suggest some general rules at the molecular level regarding interactions within TCs. In summary, when considering PROTAC design, the main aim should be the formation of functional TCs.

S-4. INFLUENCE OF LINKERS ON PHARMACODYNAMICS OF PROTACS

The degradation efficacy of PROTACs is not only dependent on the affinity of incorporated ligands toward POIs and E3 ubiquitin ligases, but on the combination of those mentioned as well as on the properties of linkers, which ultimately leads to TC formation, POI polyubiquitination and degradation.[45,46] In fact, it is known nowadays that both the chemical composition and length of the linker have great impacts on TC formation, degradation activity and selectivity. Besides, linkers perform specific interactions inside TCs and therefore play an important role in positive cooperativity on TC formation.[39,47] These findings could be useful in the design of PROTACs that display isoform selectivity across structurally related POIs.[42] Additionally, as already stated above, linker-mediated binding cooperativity could be a source of binding affinity toward POIs for PROTACs based on low-affinity POI ligands.[47] However, the chemical compositions of linkers, particularly their lengths and attachment points within PROTACs, have to be optimized for every pair of POI and E3 ubiquitin ligase with which they interact. This should not come as a surprise if TC structural complexity and dynamics are taken into account. Hence, it is very challenging to anticipate which combination of POI/E3 ubiquitin ligase ligands and linker will induce optimal POI degradation. Since the literature does not provide any specific guidelines regarding linkers or any strategy for their design, achieving and optimization of biological activity has been performed through iterative linker modification, where PEG- or alkyl-based linkers are commonly used first.

S-5. PROTAC TECHNOLOGY ADVANTAGES

A detailed presentation of the advantages of PROTAC technology over the other pharmacological approaches can be summarized as follows:

The possibility to tackle pharmacologically intractable proteome

About 20-25 % of therapeutically relevant biological targets are susceptible to conventional drug discovery strategies. Some of those are kinases, G protein-coupled receptors, nuclear hormone receptors and ion channels.[48,49] The proteins with no catalytic activity and/or catalytic-independent functions are still considered as undruggable biological targets.[50] There are several reasons for this, but the most important is that current therapeutic modalities are unable to tackle those potentially therapeutically relevant proteins. Some biological targets that belong to undruggable proteome are transcription factors (c-Myc,[51] β-catenin[52]) and scaffold proteins (BCL10,[53] β-arrestin[54]). These POIs are attractive biological targets and progress in this field has been made by blocking the binding of specific interaction partners of these proteins. Furthermore, aggregated proteins common in neurodegenerative disorders, such as Alzheimer's[55] or Huntington's[56] disease, are especially convenient to be degraded using PROTACs. Although some steps toward blocking PPIs using small-molecule-based inhibitors have been made, this medicinal chemistry field remains challenging since small molecules are directed to inhibit interactions occurring on large PPI surfaces.[57] As already stated, the possibility of PROTACs to interact with any suitable binding site on POIs and perform biological effects is a very prominent feature. More precisely, it is not necessary to either block catalytic functions of POIs or PPIs – any POI ligand is suitable to design a POI degrader. It means that PROTAC , *i.e.* incorporated POI ligand can interact with any part of the biological target and be operative if it induces POI polyubiquitination and subsequent proteasomal degradation. Such theoretical increase in the binding sites of POIs that are suitable for interaction with PROTACs gives the opportunity for pharmacological interventions on the proteome currently considered as pharmacologically intractable using traditional approaches. Hence, the development of new pharmacological modalities that can tackle therapeutically relevant proteins using small-molecule ligands is a priority.

The possibility to overcome pharmacoresistance in cancer

This phenomenon can be explained by the example of kinase inhibitors that have been extensively developed in recent decades.[58] Although this class of drugs has been shown to be very effective in cancer treatment, pharmacoresistant cancers can frequently be seen in patients who thus develop disease recurrence. In this case, PROTAC molecules have been shown to be useful due to the degradation of the whole target proteins. For example, the L18I PROTAC molecule, which degrades mutated BTK, can overcome a form of lymphoma resistant to ibrutinib resulting from the C481S mutation.[59]

The possibility to overcome the accumulation of biological targets

It has been observed that some drugs after binding to the corresponding biological targets can cause their accumulation, even after a short period of time, and this could be explained in two ways. First, drug binding can stabilize the protein and thus prolong its half-life.[60] Such protein stabilization was seen with HER2 inhibitor lapatinib, BRD4 inhibitor JQ1, as well as MCL-1 inhibitor A-1210477.[61–63] Second, under certain circumstances, antagonism may cause compensatory upregulation of POI at the transcriptional level. For example, AR is a transcriptional repressor of its own transcript.[64] After the repression of AR *via* inhibitors, mRNA that codes AR increases, which ultimately leads to higher AR levels and sensitization to relatively low androgen levels. Thus, all the mechanisms for upregulation of biological targets may deteriorate the efficacy of applied inhibitor. The elimination of POIs using PROTAC molecules is expected to be very useful in the case of proteins that may become insensitive to inhibitors either by a stabilization or upregulation mechanism.[65] For example, it has been shown that in the case of BRD4, the inhibitors of which rapidly lose efficacy due to upregulation, PROTAC molecules achieve the degradation of this protein as well as its transcriptional repression.[61]

The possibility to act on biological targets altered by mutations or interactions with binding partners

The appearance of point mutations is a common mechanism of acquired pharmacoresistance. After a certain time of drugging biological target, the appearance of its mutations is inevitable. This phenomenon can be seen with anti-HIV drugs,[66] as well as with drugs inhibiting cancer-related targets such as Bcr-Abl, EGFR, ALK, BTK.[65,67] The emergence of mutations in biological targets diminishes the affinities of their inhibitors, hence limiting their efficacy. However, changes in biological targets that are not the result of mutations can also occur. Namely, the appearance of resistance to Type I Janus kinase (JAK) 2 inhibitors can be attributed to the shift from JAK2:JAK2 homodimerization toward JAK1:JAK2/Tyrosine Kinase 2 (TYK2) heterodimerization.[68] Due to the formation of heterodimers, both JAK1 and TYK2 can perform the phosphorylation of JAK2, thus restarting downstream signaling even in the presence of JAK2 inhibitors. Induced protein degradation using PROTAC molecules is able to tackle these resistance mechanisms, since PROTAC molecules can degrade mutated biological targets. On the other hand, the degradation of therapeutically relevant proteins would prevent inhibitor-induced interactions with auxiliary proteins, which, as already stated, result in biological targets resistant to the applied inhibitors.[65]

Selectivity advancement

The ideal small-molecule antagonist inhibits only pathogenic proteins and does not act on the rest of the proteome. Often, the therapeutic index is limited by the difference in the drug potencies toward the disease-related protein and its wild-type variety. In general, selectivity toward disease-causing proteins (*e.g.* mutated ones) is difficult to achieve and only a few drugs are more active against them compared to the physiological forms of the proteins.[65] For example, dabrafenib has a higher affinity toward mutated BRAF-V600E protein associated with melanoma than for the non-mutated one.[69] Performing pharmacological effects on mutated proteins over closely related wild-type ones is very demanding. It could be assumed that PROTAC technology is a unique opportunity to improve the selectivity of therapeutics. Namely, PROTACs lead to the IPD through two steps: first, the PROTAC molecule binds to the biological target, and then E3 ubiquitin ligase transfers ubiquitin to the exposed lysine residue of the biological target. While the first step is limited by the ability to design a selective ligand for POI, the second step, depending on the position of the exposed lysine relative to the E3 ubiquitin ligase, could be modulated to achieve selectivity even among analogous proteins.[65] For example, the JQ1-based PROTAC molecule, which binds both BRD2 and BRD4 while recruiting VHL, has been shown to have about 10-fold greater potency in BRD4 degradation, although JQ1 has almost the same affinities toward BRD2 and BRD4.[61,70] Thus, a POI bound to a PROTAC molecule does not necessarily have to be degraded. Protein degradation can only occur after its polyubiquitination and this fact should be kept in mind when considering the activity and selectivity of PROTAC molecules. In other words, different proteins with very similar catalytic sites may differ both in amino acid sequences and spatial conformations. Thus, differences within catalytic sites are not necessary to exist, but outside of them they can be very significant. This observation should be perceived as weak points of therapeutically relevant proteins to be exploited using PROTAC molecules.[65]

PROTACs' catalytic MOA

Molecules performing catalytic MOA can be applied at sub-stoichiometric amounts compared to their biological targets, resulting in smaller amounts of such molecules being required to achieve the appropriate pharmacological effects. The fact that has already been stated before is that as long as the POI ligands within the PROTAC molecules do not covalently bind to the biological targets, these molecules perform catalytic MOA.[71] The catalytic nature of PROTAC molecules is manifested by their drastic increase in potency. For example, comparative studies of a PROTAC molecule and a corresponding inhibitor have shown a more significant effect of the former on cell proliferation and apoptosis initiation compared to the latter.[61] Thus, it could be concluded that PROTAC molecules can achieve and maintain the degradation of biological targets even in small quantities. In addition, the ability of these molecules to achieve an appropriate level of protein degradation at relatively low exposures may provide a better therapeutic index since the potential to perform effects outside the desired biological targets is reduced, and thus the toxicity.[65]

EDP framework and prolonged biological effect

When small-molecule, non-covalent inhibitors are no longer present at the site of action, signaling pathways are being restored and thus, the efficacy of these types of drugs is being compromised. On the other hand, the formation of covalent bonds between covalent inhibitors and biological targets may produce pharmacological effects that, in pharmacokinetic terms, exceed exposure to the inhibitors.[72] This phenomenon can be illustrated by the example of ibrutinib. Namely, this drug covalently binds to the cysteine in the active site of BTK. With a dosing regimen of 560 mg once daily, the drug could not be found in plasma within 24 h, but almost complete BTK occupancy was shown at that timepoint.[73] Due to their ability to induce protein degradation, PROTAC molecules may perform a similar pharmacological pattern as covalent inhibitors. In other words, PROTAC molecules can degrade a certain amount of protein, so the resulting pharmacodynamic profiles of PROTACs do not have to correlate with their pharmacokinetic profiles.[74] This loss of the link between pharmacodynamics and pharmacokinetics is especially pronounced for long-lived proteins, because it takes time to resynthesize the requisite amount of them within cells. In the case of short-lived proteins (*i.e.* proteins with a high turnover rate), this advantage is lost and continuous exposure of such biological targets to PROTAC molecules is required.[65] Thus, the concept of EDP differs significantly from the concept of ODP, because within the latter, drugs must constantly inhibit (*i.e.* occupy) their corresponding targets. Thus, three positive aspects of EDP can be stated:[65] a) Exposure to EDP-derived drugs does not have to be continuously above a certain, efficacious level; b) Lower exposure to EDP-derived drugs reduces the risk of side effects and toxicity due to off-target binding, since the selectivity diminishes at high concentrations of ODP-derived drugs; c) PROTAC molecules can cause degradation of POIs even in the presence of higher affinity ligands or in the case of POI interaction with binding partners. For example, if a ligand such as ATP (in the case of kinases) or a natural hormone such as dihydrotestosterone (in the case of AR) has a high affinity for the corresponding target and the PROTAC molecule is designed to bind to the same binding site, it still has the ability to cause degradation of the target, because only its transient binding and subsequent formation of TC is required for a biological effect. In addition to this, the ability of small molecules to interfere with high-affinity PPIs requires a high affinity of such molecules for this kind of biological targets.[75] However, the transfer of ubiquitin onto POIs occurs very rapidly and, once polyubiquitinated, biological targets are intended for proteasomal degradation. If the potency of the ligand is not sufficient to interfere with high-affinity PPIs, it is possible that the incorporation of such ligand into PROTAC may, ultimately, lead to the degradation of POI performing such PPIs. Thus, the concept of EDP may utilize ligands that have not been shown to be good inhibitors on their own, but that could be utilized as ligands for biological targets within the following PROTAC molecules.[65]

REFERENCES

1. P. C. de Smidt, T. L. Doan, S. de Falco, T. J. C. van Berkel, *Nucleic Acids Res.* **19** (1991) 4695 (http://dx.doi.org/10.1093/nar/19.17.4695)
2. R. S. Geary, T. A. Watanabe, L. Truong, S. Freier, E. A. Lesnik, N. B. Sioufi, H. Sasmor, M. Manoharan, A. A. Levin, *J. Pharmacol. Exp. Ther.* **296** (2001) 890 (http://jpet.aspetjournals.org/content/296/3/890.long)

3. B. M. McMahon, D. Mays, J. Lipsky, J. A. Stewart, A. Fauq, E. Richelson, *Antisense Nucleic Acid Drug Dev.* **12** (2002) 65 (http://dx.doi.org/10.1089/108729002760070803)
4. J. T. Marques, B. R. G. Williams, *Nat. Biotechnol.* **23** (2005) 1399 (http://dx.doi.org/10.1038/nbt1161)
5. A. M. Krieg, *Annu. Rev. Immunol.* **20** (2002) 709 (http://dx.doi.org/10.1146/annurev.immunol.20.100301.064842)
6. J. E. Dahlman, K. J. Kauffman, R. Langer, D. G. Anderson, *Chapter Three - Nanotechnology for In vivo Targeted siRNA Delivery*, in *Adv. Genet.*, L. Huang, D. Liu, E. Wagner (Eds.), Academic Press, Cambridge, MA, USA, 2014, p. 37 (http://dx.doi.org/10.1016/B978-0-12-800148-6.00003-1)
7. K. A. Whitehead, R. Langer, D. G. Anderson, *Nat. Rev. Drug Discov.* **8** (2009) 129 (http://dx.doi.org/10.1038/nrd2742)
8. S. Wilhelm, A. J. Tavares, Q. Dai, S. Ohta, J. Audet, H. F. Dvorak, W. C. W. Chan, *Nat. Rev. Mater.* **1** (2016) 16014 (http://dx.doi.org/10.1038/natrevmats.2016.14)
9. D. Peer, J. Lieberman, *Gene Ther.* **18** (2011) 1127 (http://dx.doi.org/10.1038/gt.2011.56)
10. Y. Fedorov, E. M. Anderson, A. Birmingham, A. Reynolds, J. Karpilow, K. Robinson, D. Leake, W. S. Marshall, A. Khvorova, *RNA* **12** (2006) 1188 (http://dx.doi.org/10.1261/rna.28106)
11. A. L. Jackson, S. R. Bartz, J. Schelter, S. V. Kobayashi, J. Burchard, M. Mao, B. Li, G. Cavet, P. S. Linsley, *Nat. Biotechnol.* **21** (2003) 635 (http://dx.doi.org/10.1038/nbt831)
12. S. Qiu, C. M. Adema, T. Lane, *Nucleic Acids Res.* **33** (2005) 1834 (http://dx.doi.org/10.1093/nar/gki324)
13. M. Jinek, K. Chylinski, I. Fonfara, M. Hauer, J. A. Doudna, E. Charpentier, *Science* **337** (2012) 816 (http://dx.doi.org/10.1126/science.1225829)
14. L. Cong, F. A. Ran, D. Cox, S. Lin, R. Barretto, N. Habib, P. D. Hsu, X. Wu, W. Jiang, L. A. Marraffini, F. Zhang, *Science* **339** (2013) 819 (http://dx.doi.org/10.1126/science.1231143)
15. K. G. Coleman, C. M. Crews, *Annu. Rev. Cancer Biol.* **2** (2018) 41 (http://dx.doi.org/10.1146/annurev-cancerbio-030617-050430)
16. D. Nandi, P. Tahiliani, A. Kumar, D. Chandu, *J. Biosci.* **31** (2006) 137 (http://dx.doi.org/10.1007/BF02705243)
17. A. Ciechanover, *EMBO J.* **17** (1998) 7151 (http://dx.doi.org/10.1093/emboj/17.24.7151)
18. Z. S. Hann, C. Ji, S. K. Olsen, X. Lu, M. C. Lux, D. S. Tan, C. D. Lima, *Proc. Natl. Acad. Sci. U S A* **116** (2019) 15475 (http://dx.doi.org/10.1073/pnas.1905488116)
19. M. Sadowski, R. Suryadinata, A. R. Tan, S. N. A. Roesley, B. Sarcevic, *IUBMB Life* **64** (2012) 136 (http://dx.doi.org/10.1002/iub.589)
20. D. Komander, *Biochem. Soc. Trans.* **37** (2009) 937 (http://dx.doi.org/10.1042/BST0370937)
21. Y. Ye, M. Rape, *Nat. Rev. Mol. Cell Biol.* **10** (2009) 755 (http://dx.doi.org/10.1038/nrm2780)
22. R. J. Deshaies, C. A. P. Joazeiro, *Annu. Rev. Biochem.* **78** (2009) 399 (http://dx.doi.org/10.1146/annurev.biochem.78.101807.093809)
23. C. Michelle, P. Vourc'h, L. Mignon, C. R. Andres, *J. Mol. Evol.* **68** (2009) 616 (http://dx.doi.org/10.1007/s00239-009-9225-6)
24. G. Markson, C. Kiel, R. Hyde, S. Brown, P. Charalabous, A. Bremm, J. Semple, J. Woodsmith, S. Duley, K. Salehi-Ashtiani, M. Vidal, D. Komander, L. Serrano, P.

Lehner, C. M. Sanderson, *Genome Res.* **19** (2009) 1905 (http://dx.doi.org/10.1101/gr.093963.109)
25. M. Groettrup, C. Pelzer, G. Schmidtke, K. Hofmann, *Trends Biochem. Sci.* **33** (2008) 230 (http://dx.doi.org/10.1016/j.tibs.2008.01.005)
26. Z. J. Chen, L. J. Sun, *Mol. Cell* **33** (2009) 275 (http://dx.doi.org/10.1016/j.molcel.2009.01.014)
27. L. Deng, C. Wang, E. Spencer, L. Yang, A. Braun, J. You, C. Slaughter, C. Pickart, Z. J. Chen, *Cell* **103** (2000) 351 (http://dx.doi.org/10.1016/S0092-8674(00)00126-4)
28. Z. J. Chen, *Nat. Cell Biol.* **7** (2005) 758 (http://dx.doi.org/10.1038/ncb0805-758)
29. C. M. Pickart, *Trends Biochem. Sci.* **25** (2000) 544 (http://dx.doi.org/10.1016/S0968-0004(00)01681-9)
30. J. Spence, S. Sadis, A. L. Haas, D. Finley, *Mol. Cell. Biol.* **15** (1995) 1265 (http://dx.doi.org/10.1128/MCB.15.3.1265)
31. P. Xu, D. M. Duong, N. T. Seyfried, D. Cheng, Y. Xie, J. Robert, J. Rush, M. Hochstrasser, D. Finley, J. Peng, *Cell* **137** (2009) 133 (http://dx.doi.org/10.1016/j.cell.2009.01.041)
32. E. F. Douglass, C. J. Miller, G. Sparer, H. Shapiro, D. A. Spiegel, *J. Am. Chem. Soc.* **135** (2013) 6092 (http://dx.doi.org/10.1021/ja311795d)
33. C. Lu, Z.-X. Wang, *Anal. Chem.* **89** (2017) 6926 (http://dx.doi.org/10.1021/acs.analchem.7b01274)
34. S. J. Hughes, A. Ciulli, *Essays Biochem.* **61** (2017) 505 (http://dx.doi.org/10.1042/EBC20170041)
35. M. Pettersson, C. M. Crews, *Drug Discov. Today Technol.* **31** (2019) 15 (http://dx.doi.org/10.1016/j.ddtec.2019.01.002)
36. S. An, L. Fu, *EBioMedicine* **36** (2018) 553 (http://dx.doi.org/10.1016/j.ebiom.2018.09.005)
37. L. E. M. Miles, *Ric. Clin. Lab.* **5** (1975) 59 (http://dx.doi.org/10.1007/BF02910016)
38. R. D. Roy, C. Rosenmund, M. I. Stefan, *BMC Syst. Biol.* **11** (2017) 74 (http://dx.doi.org/10.1186/s12918-017-0447-8)
39. M. S. Gadd, A. Testa, X. Lucas, K.-H. Chan, W. Chen, D. J. Lamont, M. Zengerle, A. Ciulli, *Nat. Chem. Biol.* **13** (2017) 514 (http://dx.doi.org/10.1038/nchembio.2329)
40. D. P. Bondeson, B. E. Smith, G. M. Burslem, A. D. Buhimschi, J. Hines, S. Jaime-Figueroa, J. Wang, B. D. Hamman, A. Ishchenko, C. M. Crews, *Cell Chem. Biol.* **25** (2018) 78 (http://dx.doi.org/10.1016/j.chembiol.2017.09.010)
41. K.-H. Chan, M. Zengerle, A. Testa, A. Ciulli, *J. Med. Chem.* **61** (2018) 504 (http://dx.doi.org/10.1021/acs.jmedchem.6b01912)
42. A. Zorba, C. Nguyen, Y. Xu, J. Starr, K. Borzilleri, J. Smith, H. Zhu, K. A. Farley, W. Ding, J. Schiemer, X. Feng, J. S. Chang, D. P. Uccello, J. A. Young, C. N. Garcia-Irrizary, L. Czabaniuk, B. Schuff, R. Oliver, J. Montgomery, M. M. Hayward, J. Coe, J. Chen, M. Niosi, S. Luthra, J. C. Shah, A. El-Kattan, X. Qiu, G. M. West, M. C. Noe, V. Shanmugasundaram, A. M. Gilbert, M. F. Brown, M. F. Calabrese, *Proc. Natl. Acad. Sci. U S A* **115** (2018) E7285 (http://dx.doi.org/10.1073/pnas.1803662115)
43. R. P. Nowak, S. L. DeAngelo, D. Buckley, Z. He, K. A. Donovan, J. An, N. Safaee, M. P. Jedrychowski, C. M. Ponthier, M. Ishoey, T. Zhang, J. D. Mancias, N. S. Gray, J. E. Bradner, E. S. Fischer, *Nat. Chem. Biol.* **14** (2018) 706 (http://dx.doi.org/10.1038/s41589-018-0055-y)
44. S. L. Fisher, A. J. Phillips, *Curr. Opin. Chem. Biol.* **44** (2018) 47 (http://dx.doi.org/10.1016/j.cbpa.2018.05.004)

45. X. Sun, H. Gao, Y. Yang, M. He, Y. Wu, Y. Song, Y. Tong, Y. Rao, *Signal Transduct. Target. Ther.* **4** (2019) 64 (http://dx.doi.org/10.1038/s41392-019-0101-6)
46. G. M. Burslem, C. M. Crews, *Chem. Rev.* **117** (2017) 11269 (http://dx.doi.org/10.1021/acs.chemrev.7b00077)
47. M. J. Roy, S. Winkler, S. J. Hughes, C. Whitworth, M. Galant, W. Farnaby, K. Rumpel, A. Ciulli, *ACS Chem. Biol.* **14** (2019) 361 (http://dx.doi.org/10.1021/acschembio.9b00092)
48. J. A. Wells, C. L. McClendon, *Nature* **450** (2007) 1001 (http://dx.doi.org/10.1038/nature06526)
49. J. Kim, H. Kim, S. B. Park, *J. Am. Chem. Soc.* **136** (2014) 14629 (http://dx.doi.org/10.1021/ja508343a)
50. H. Gao, X. Sun, Y. Rao, *ACS Med. Chem. Lett.* **11** (2020) 237 (http://dx.doi.org/10.1021/acsmedchemlett.9b00597)
51. S. K. Madden, A. D. de Araujo, M. Gerhardt, D. P. Fairlie, J. M. Mason, *Mol. Cancer* **20** (2021) 3 (http://dx.doi.org/10.1186/s12943-020-01291-6)
52. H. Zhang, Y. Bao, C. Liu, J. Li, D. Zhu, Q. Zhang, *Future Med. Chem.* **13** (2021) 927 (http://dx.doi.org/10.4155/fmc-2020-0357)
53. D. Vucic, V. M. Dixit, *J. Exp. Med.* **206** (2009) 2309 (http://dx.doi.org/10.1084/jem.20092160)
54. A. Beautrait, J. S. Paradis, B. Zimmerman, J. Giubilaro, L. Nikolajev, S. Armando, H. Kobayashi, L. Yamani, Y. Namkung, F. M. Heydenreich, E. Khoury, M. Audet, P. P. Roux, D. B. Veprintsev, S. A. Laporte, M. Bouvier, *Nat. Commun.* **8** (2017) 15054 (http://dx.doi.org/10.1038/ncomms15054)
55. W. Wang, Q. Zhou, T. Jiang, S. Li, J. Ye, J. Zheng, X. Wang, Y. Liu, M. Deng, D. Ke, Q. Wang, Y. Wang, J.-Z. Wang, *Theranostics* **11** (2021) 5279 (http://dx.doi.org/10.7150/thno.55680)
56. R. J. Harding, Y.-F. Tong, *Acta Pharmacol. Sin.* **39** (2018) 754 (http://dx.doi.org/10.1038/aps.2018.11)
57. M. C. Smith, J. E. Gestwicki, *Expert Rev. Mol. Med.* **14** (2012) e16 (http://dx.doi.org/10.1017/erm.2012.10)
58. P. Wu, T. E. Nielsen, M. H. Clausen, *Trends Pharmacol. Sci.* **36** (2015) 422 (http://dx.doi.org/10.1016/j.tips.2015.04.005)
59. Y. Sun, N. Ding, Y. Song, Z. Yang, W. Liu, J. Zhu, Y. Rao, *Leukemia* **33** (2019) 2105 (http://dx.doi.org/10.1038/s41375-019-0440-x)
60. D. Martinez Molina, P. Nordlund, *Annu. Rev. Pharmacol. Toxicol.* **56** (2016) 141 (http://dx.doi.org/10.1146/annurev-pharmtox-010715-103715)
61. J. Lu, Y. Qian, M. Altieri, H. Dong, J. Wang, K. Raina, J. Hines, J. D. Winkler, A. P. Crew, K. Coleman, C. M. Crews, *Chem. Biol.* **22** (2015) 755 (http://dx.doi.org/10.1016/j.chembiol.2015.05.009)
62. J. D. Leverson, H. Zhang, J. Chen, S. K. Tahir, D. C. Phillips, J. Xue, P. Nimmer, S. Jin, M. Smith, Y. Xiao, P. Kovar, A. Tanaka, M. Bruncko, G. S. Sheppard, L. Wang, S. Gierke, L. Kategaya, D. J. Anderson, C. Wong, J. Eastham-Anderson, M. J. C. Ludlam, D. Sampath, W. J. Fairbrother, I. Wertz, S. H. Rosenberg, C. Tse, S. W. Elmore, A. J. Souers, *Cell Death Dis.* **6** (2015) e1590 (http://dx.doi.org/10.1038/cddis.2014.561)
63. M. Scaltriti, C. Verma, M. Guzman, J. Jimenez, J. L. Parra, K. Pedersen, D. J. Smith, S. Landolfi, S. Ramon y Cajal, J. Arribas, J. Baselga, *Oncogene* **28** (2009) 803 (http://dx.doi.org/10.1038/onc.2008.432)

64. C. Cai, H. H. He, S. Chen, I. Coleman, H. Wang, Z. Fang, S. Chen, P. S. Nelson, X. S. Liu, M. Brown, S. P. Balk, *Cancer Cell* **20** (2011) 457 (http://dx.doi.org/10.1016/j.ccr.2011.09.001)
65. T. K. Neklesa, J. D. Winkler, C. M. Crews, *Pharmacol. Ther.* **174** (2017) 138 (http://dx.doi.org/10.1016/j.pharmthera.2017.02.027)
66. E. Ramon, L. Belanche-Muñoz, M. Pérez-Enciso, *BMC Bioinformatics* **20** (2019) 410 (http://dx.doi.org/10.1186/s12859-019-2991-2)
67. C. M. Lovly, A. T. Shaw, *Clin. Cancer Res.* **20** (2014) 2249 (http://dx.doi.org/10.1158/1078-0432.CCR-13-1610)
68. P. Koppikar, N. Bhagwat, O. Kilpivaara, T. Manshouri, M. Adli, T. Hricik, F. Liu, L. M. Saunders, A. Mullally, O. Abdel-Wahab, L. Leung, A. Weinstein, S. Marubayashi, A. Goel, M. Gönen, Z. Estrov, B. L. Ebert, G. Chiosis, S. D. Nimer, B. E. Bernstein, S. Verstovsek, R. L. Levine, *Nature* **489** (2012) 155 (http://dx.doi.org/10.1038/nature11303)
69. A. J. King, M. R. Arnone, M. R. Bleam, K. G. Moss, J. Yang, K. E. Fedorowicz, K. N. Smitheman, J. A. Erhardt, A. Hughes-Earle, L. S. Kane-Carson, R. H. Sinnamon, H. Qi, T. R. Rheault, D. E. Uehling, S. G. Laquerre, *PLoS One* **8** (2013) e67583 (http://dx.doi.org/10.1371/journal.pone.0067583)
70. M. Zengerle, K.-H. Chan, A. Ciulli, *ACS Chem. Biol.* **10** (2015) 1770 (http://dx.doi.org/10.1021/acschembio.5b00216)
71. D. P. Bondeson, A. Mares, I. E. D. Smith, E. Ko, S. Campos, A. H. Miah, K. E. Mulholland, N. Routly, D. L. Buckley, J. L. Gustafson, N. Zinn, P. Grandi, S. Shimamura, G. Bergamini, M. Faelth-Savitski, M. Bantscheff, C. Cox, D. A. Gordon, R. R. Willard, J. J. Flanagan, L. N. Casillas, B. J. Votta, W. den Besten, K. Famm, L. Kruidenier, P. S. Carter, J. D. Harling, I. Churcher, C. M. Crews, *Nat. Chem. Biol.* **11** (2015) 611 (http://dx.doi.org/10.1038/nchembio.1858)
72. J. M. Strelow, *SLAS Discov.* **22** (2017) 3 (http://dx.doi.org/10.1177/1087057116671509)
73. R. H. Advani, J. J. Buggy, J. P. Sharman, S. M. Smith, T. E. Boyd, B. Grant, K. S. Kolibaba, R. R. Furman, S. Rodriguez, B. Y. Chang, J. Sukbuntherng, R. Izumi, A. Hamdy, E. Hedrick, N. H. Fowler, *J. Clin. Oncol.* **31** (2013) 88 (http://dx.doi.org/10.1200/JCO.2012.42.7906)
74. A. Mares, A. H. Miah, I. E. D. Smith, M. Rackham, A. R. Thawani, J. Cryan, P. A. Haile, B. J. Votta, A. M. Beal, C. Capriotti, M. A. Reilly, D. T. Fisher, N. Zinn, M. Bantscheff, T. T. MacDonald, A. Vossenkamper, P. Dace, I. Churcher, A. B. Benowitz, G. Watt, J. Denyer, P. Scott-Stevens, J. D. Harling, *Commun. Biol.* **3** (2020) 140 (http://dx.doi.org/10.1038/s42003-020-0868-6)
75. D. Rognan, *Medchemcomm* **6** (2015) 51 (http://dx.doi.org/10.1039/C4MD00328D).

Journal of the Serbian Chemical Society
JSCS@tmf.bg.ac.rs • www.shd.org.rs/JSCS

J. Serb. Chem. Soc. 87 (7–8) 813–827 (2022)
JSCS–5559

Original scientific paper
Published 4 May 2022

Microwave assisted synthesis of novel spiro diarylidenes and their antimicrobial assay

SABITA SHROFF[1], PRAJNA PARIMITA MOHANTA[1], ISWAR BAITHARU[2], BHAWANI PRASAD BAG[3] and AJAYA KUMAR BEHERA[1]*

[1]Organic Synthesis Lab, School of Chemistry, Sambalpur University, Jyoti Vihar Odisha-768019, India, [2]Toxicology Lab, P.G. Department of Environmental Sciences, Sambalpur University, Jyoti Vihar, Odisha-768019, India and [3]Department of Biotechnology and Bioinformatics , Sambalpur University, Jyoti Vihar, Odisha-768019, India

(Received 23 January 2021, revised 20 February, accepted 30 March 2022)

Abstract: A rapid and high yield microwave assisted synthesis of a series of novel 7,9-bis-(arylidene)-4-methyl-2,6,10-triphenyl-2,3-diazaspiro[4,5]dec-3-ene-1,8-dione has been explored. The spiro diarylidene derivatives having nitrogen atom and *α*,*β*-unsaturated ketone moiety were synthesized by aldol condensation between 4-methyl-2,6,10-triphenyl-2,3-diazaspiro[4,5]dec-3-ene-1,8-dione and corresponding aryl aldehydes followed by dehydration. The synthesized series of novel spirodiarylidene derivatives were characterized using IR, ^{1}H- and ^{13}C-NMR and mass spectra. Density functional theory (DFT) study was performed by Gaussian 09 software. The antimicrobial activities of the synthesized derivatives were evaluated against two pathogenic Gram-positive and Gram-negative bacterial strain and three pathogenic fungal species by disk diffusion method. The minimum inhibitory concentration was determined by the microbroth dilution technique. The results of the present study demonstrated that the examined compounds marked **5a** and **5c**, possessing 4-NO_2 and 5-Br-2-OH substituents, are found to be more active against Gram-positive bacterium *Staphylococcus aureus*, 8 and 16 μg mL^{-1}, respectively, and moderately active against Gram-negative bacteria *Pseudomonas aeruginosa* and *Escherichia coli*, compared to other synthetic derivatives. However, none of the synthesized derivatives showed any activity against *Streptococcus pyrogenes*. Compound **5e**, possessing 2,4,6-$(OCH_3)_3C_6H_3$ moiety, exhibited broad spectrum activity against all fungal strains under study, but showed no antibacterial activity.

Keywords: pyrazolone; Michaelis addition; aldol condensation; antibacterial activity; irradiation; antifungal activity.

---

* Corresponding author. E-mail: ajayakumar.behera@suniv.ac.in

https://doi.org/10.2298/JSC210123031S

INTRODUCTION

The development of resistance among pathogenic microbial strains against existing antimicrobial agents is increasing day by day and has become a major concern for public health over the last few decades.[1] There is an utter necessity to develop effective antimicrobial agents with novel modes of action and a broad spectrum of activities to keep pace with evolving pathogenic microbial strains. Number of phytochemicals has been demonstrated to pose robust broad spectrum antimicrobial activity with minimal side effects.[2] Spirocyclic compounds that are found abundantly in plants and animals draw special attention because of their wide applications in medicinal chemistry.[3] Some of them are found to have remarkable biological activities and have been reported to act as antibacterial,[4] antifungal,[5] anti-inflammatory,[6] antimalarial[7] and anticancer agents. The cyclic structures in the spiro compounds, fused at a central carbon, play a very significant role in numerous biological activities of molecules which possess them.[9,10]

Pharmacological activities of several spiro compounds and their derivatives are widely investigated to develop therapeutics against microbial as well as numerous metabolic diseases. The presence of the reactive carbonyl functionalized heterocycles in spiro framework has been shown to exhibit anti-HIV[11] and anti-inflammatory[12] effect. Spiro [indolo-3,10'-indeno[1,2-*b*]quinolin]-2,4,11'-triones and their derivatives have been reported as a new class of antifungal and antimicrobial agents.[13] Besides their antimicrobial activities, the literature reveals that spiro compounds like 7-(3-pyridinyl)-1,7-diazaspiro[4.4]nonane analogue (I)[14] and spirocyclic pyrrolidines (II)[15], Fig. 1, are also used for the treatment of central and autonomic nervous systems dysfunctions and various neurological and psychiatric disorders, as potential drug candidates. Spiro compounds containing heteroatoms in the exo-olefinic scaffold (III) and (IV) are found to have significant antitumor[16] and antibacterial activities,[17] respectively. However, pharmacological activities of spirodiarylidenes are poorly examined so far.

Though spiro compounds and their derivatives possess promising therapeutic potentials, their synthesis using conventional methods are very time consuming and tedious.[18] Microwave irradiation dramatically reduces the reaction times by choosing lower energy pathways, minimizing the number of steps, and reducing energy usage by providing uniform heating. Further microwave assisted synthesis is a greener route of organic synthesis as it ensures minimum use of organic solvents and subsequent generation of waste.[19] Numerous studies have explored the synthesis of spiro compounds, such as novel dispiro-oxindolopyrrolizidines and pyrrolidines, in good yield using microwave assisted organic synthesis methods.[20,21] However, the synthesis of spirodiarylidene derivatives using microwave irradiation is not yet explored. In this paper, we highlight the application of microwave methodology in the synthesis of diarylidenes of spiro compounds from pyrazolone and dibenzalacetone precursors. A series of novel spiro derivatives synthesized are further evaluated for their antibacterial and antifungal activities against a panel of bacterial strains and fungal species.

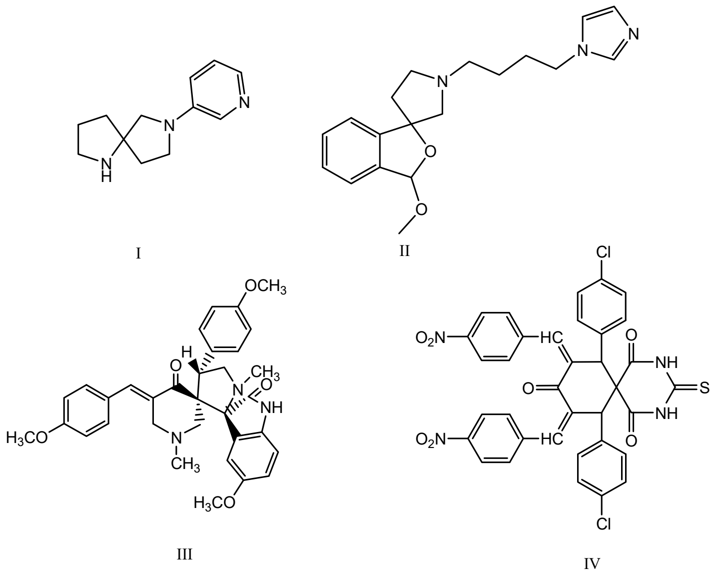

Fig. 1. Bioactive spiro compounds for the treatment of dysfunction of central and autonomic nervous systems (I),[14] neurological and psychiatric disorders (II),[15] as well as antitumor (III)[16] and antibacterial (IV)[17] agents.

EXPERIMENTAL

General procedure

All the reagents and solvents used were analytical grade and were purchased from Merck, Sigma Aldrich and Finar (India). The reactions were performed in Sineo Mas II microwave synthesizer in sealed reaction vessels, power voltage: AC 220 V (±10 %), 50 Hz, rated input power: 1360 W, rated high frequency output power: 1000 W, operating frequency: 2450 MHz. The reaction conditions are optimized by changing different temperatures, time, and power under solvent medium.

Melting points were taken in open capillaries using sulphuric acid-bath and were uncorrected. Reactions were monitored by thin-layer chromatography (TLC) using Merck silica gel 60 F254 precoated plates (0.25 mm) in an appropriate mixture of ethyl acetate and hexane and observed using UV-lamp of 365 nm. IR spectra were obtained on Bruker Alpha-II. ^{1}H- and ^{13}C-NMR spectra were recorded on a Bruker Avance III spectrometer (at 400 and 100 MHz, respectively). Chemical shifts were expressed in parts per million downfield from tetramethylsilane (TMS) dissolved in $CDCl_3$ as an internal standard.[22]

LC–MS analysis was performed with an Agilent 6110 LC–MS instrument with Mercury Luna 3 μ C18 column-attached mass spectrometer with ESC ionisation source in ESI mode. Water:acetonitrile (50:50) containing 0.1 % formic acid was used as the mobile phase. Sample preparation was made using acetonitrile as the diluent. Flow rate was maintained at 1.0 ml/min. The nebulizer pressure ESI mass spectrometer was maintained at 413.7 kPa, vaporizer temp

150 °C, drying gas flow 5 ml/min and drying gas temperature 300 °C. The voltage capacity of single ion polarity was 2000 V, polarity switching 1000v and charging electrode capacity was maintained at 2000 V.

Analytical and spectral data of the compounds are given in Supplementary material to this paper.

Density function theory (DFT) study was performed using Gaussian 09 programme and the calculation was done by applying DFT B3LYP/6-31++g(d,p).[23] Elemental analyses were performed by Flash2000 elemental analyzer and were in agreement with the calculated values within ±0.4 %. The physical, analytical and spectral data for the compounds are given in the Supplementary material to this paper.

Synthetic procedures

*Synthesis of 3-methyl-1-phenyl-1*H*-pyrazol-5(4*H*)-one (1).* A mixture of ethyl acetoacetate (12.76 mL, 100 mmol) and freshly distilled phenylhydrazine (9.8 mL, 100 mmol) was heated at 120 °C in an oil bath for 1 h. The resulting red oil was cooled and stirred with diethyl ether until solidification occurred. The colourless solid thus obtained was filtered and finally recrystallized with ethanol. Yield: 78 %, m.p. 124 °C (lit. m.p. 127 °C).[24]

Synthesis of dibenzalacetone (2). To a solution of 10 % NaOH and ethyl alcohol (80 mL), acetone (3.7 mL, 50 mmol) was added and stirred for 15 min. Then, benzaldehyde (10.19 mL, 100 mmol) was added in two phases and stirred for two hours at 25 °C. Yellow crystals thus separated were filtered, washed with water, and crystallized from ethyl acetate. Yield: 73.2 %, m.p. 112 °C (lit. m.p. 112 °C)[25].

Synthesis of 4-methyl-2,6,10-triphenyl-2,3-diaza-spiro[4.5]dec-3-ene-1,8-dione (3)

Conventional method. A mixture of 3-methyl-1-phenyl-1*H*-pyrazol-5(4*H*)-one (**1**, 0.87 g, 5 mmol) and dibenzalacetone (**2**, 1.17 g, 5 mmol) in 15 ml ethanol in presence of 5 drops of triethanolamine was refluxed for 16 h. The completion of the reaction was monitored by TLC. The reaction mixture was allowed to cool at room temperature. The solution was poured onto ice cold water. The brown solid formed was filtered, dried, and recrystallized from rectified spirit to obtain **3**.[17]

Microwave-assisted (MW) method. A mixture of 3-methyl-1-phenyl-1*H*-pyrazol-5(4*H*)-one (**1**, 0.87 g, 5 mmol) and dibenzalacetone (**2**, 1.17 g, 5 mmol) in 15 mL ethanol in the presence of 5 drops of triethanolamine were irradiated in the microwave at 300 W and 80 °C for 10 min. The reaction mixture was allowed to cool at room temperature. The solution was poured onto ice cold water. The brown solid formed was filtered, dried, and recrystallized from rectified spirit to obtain **3.**

*General procedure for the formation of arylidene derivatives of 4-methyl-2,6,10-triphenyl-2,3-diaza-spiro[4.5]dec-3-ene-1, 8-dione (**5a–f**)*

Conventional method. A mixture of spiro compound **3** (0.2 g, 0.5 mmol) and substituted aryl aldehydes **4a**–**f** (1 mmol) was refluxed for 10 h in the presence of sodium ethoxide (1 mmol) in 10 mL ethanol. The completion of the reaction was monitored by TLC. The reaction mixture was allowed to cool at room temperature. The solution was poured onto ice cold water. The solid formed was filtered, dried, and recrystallized from the rectified spirit to obtain the compounds **5a**–**f**.

MW-assisted method. A mixture of spiro compound **3** (0.2 g, 0.5 mmol) and substituted aryl aldehydes **4a**–**f** (1 mmol) in the presence of sodium ethoxide (1mmol) in 10 mL ethanol was irradiated in microwave at 300 W and 80 °C for 7 min. The reaction mixture was allowed to cool at room temperature. The solution was poured onto ice cold water. The solid formed was filtered, dried, and recrystallized from the rectified spirit to obtain the compounds **5a**–**f**.

Assessment of antimicrobial activity

Test microorganisms. The selection of seven different microbial species was done based on their pathogenic activities and clinical importance to human health. Two Gram-positive bacteria (*Staphylococcus aureus (*MTCC 3615) and *Streptococcus pyrogenes (*MTCC 442), two Gram-negative bacteria (*Escherichia coli* (MTCC 443) and *Pseudomonas aeruginosa* (MTCC 424) and three fungi *Candida albicans (*MTCC 227), *Aspergillus niger (*MTCC 282), and *Aspergillus clavatus (*MTCC 1327) were chosen for assessing the antibacterial and antifungal activity of the synthesized compounds. All the microbial cultures were obtained from Microbial Type Culture Collection (MTCC), Institute of Microbial Technology (IMTECH), Chandigarh, India. While the bacteria were further sub cultured on Nutrient agar, fungi were grown on Sabourauds dextrose agar.

Assessment of antibacterial activity using agar well diffusion method. All the microbial cultures were adjusted to 0.5 McFarland standard, which is visually comparable to a microbial suspension of approximately 1.5×10^8 CFU mL^{-1}. 20 mL of agar medium, was poured into each petri plate and plates were swabbed with 100 mL inocula of the test microorganisms and kept for 15 min for adsorption. Using sterile cork borer of 8 mm diameter, wells were bored into the seeded agar plates, and these were loaded with a 100 mL volume with a concentration of 8.0 mg mL^{-1} of each compound reconstituted in the dimethyl sulphoxide. All the plates were incubated at 37 °C for 24 h. The antimicrobial activity of each compound was evaluated by measuring the zone of growth inhibition against the test organisms. DMSO was used as a negative control, whereas Ciprofloxacin was used as a positive control for bacteria and amphotericin-B for fungi. This procedure was performed in three replicate plates for each organism.[13]

*Determination of minimum inhibitory concentration (*MIC*) of the spiro compounds*

MIC is the lowest concentration of an antimicrobial compound that will inhibit the visible growth of a microorganism after overnight incubation. The antimicrobial potential of the synthesized compounds was evaluated by determining the *MIC* values by the microdilution method. The *MIC*s were determined by measuring the absorbance of microtiter plates at 570 nm for bacteria and 530 nm for fungi. The optical density from each well was compared with the optical density from the positive control wells, the lowest concentration with optical density <0.1 signifies inhibition and considered as *MIC* value.[4]

Antibacterial susceptibility testing by microbroth dilution method

The pure bacterial culture of each microorganism was adjusted to 0.5 in Mueller–Hinton broth (MHB). To avoid bacterial duplication, the suspension of bacterial cells was used immediately within 30 min of turbidity adjustment. All the spiro diarylidene derivatives were dissolved in 1 mL of dimethyl sulfoxide (DMSO) to prepare a stock solution of 1 mg. In this method, a two-fold serial dilution of each chemically synthesized compound was prepared by reconstituting the compound in DMSO first, followed by dilution in sterile distilled water to achieve a decreasing concentration range of 512–1 μg mL^{-1}. Ten different concentrations were prepared from each stock with the medium (1, 2, 4, 8, 16, 32, 64, 128, 256, 512 μg mL^{-1}). A total of 50 μL of each compound concentration was added to sterile 96-well microtiter plates. After that, 50 μL of diluted bacterial inoculums were added to each well including the negative control lane, and 100 μL of broth was added to the positive control lane. The plates were then incubated at 37 °C for 18–24 h. The inhibition of growth was determined by measuring the absorbance at 570 nm using an enzyme-linked immunosorbent assay (ELISA) reader. Ciprofloxacin and all the spirodiarylidene derivatives were dissolved in 1 mL of dimethyl sulfoxide (DMSO) to prepare a stock solution of 1 mg. Amphotericin-B was used as a positive control while DMSO as a negative control.[26]

Antifungal susceptibility testing by microbroth dilution method

The Sabouraud's dextrose agar slant was used for subculturing the fungal strains. Freshly grown pure fungal culture was obtained after incubating the slant for 24–48 h at 35 °C. The fungal suspension was further adjusted to make it equivalent to 0.5 McFarland standards unit of turbidity and the size of the fungal population maintained to 0.5×10^5 or 2.5×10^5. The Sabor and dextrose agar slant culture was incubated for 5 days at 35 °C to obtain the suspension of conidia of the mold. The colonies were covered with 5 mL of sterile distilled water supplemented with Tween 20. The number of conidia in the suspension was counted using a hemocytometer and diluted at a ratio of 1:10 with RPMI to obtain final inoculums of $2–5\times10^5$ conidia mL^{-1}. A total of 50 μL of each compound concentration and 50 μL of fungal suspension were added to each well for the negative control lane and 100 μL of broth was added to the positive control lane. The plate was sealed with aluminum foil and incubated at 35 °C for 24–48 h in a humid atmosphere. The absorbance was determined using an ELISA reader at 530 nm for the yeast species and visually for mold species after 48 hours of incubation.[27,4]

RESULTS AND DISCUSSION

Chemistry

4-methyl-2,6,10-triphenyl-2,3-diaza-spiro[4,5]dec-3-ene-1,8-dione (**3**) and their diarylidene derivatives **5a**–**f** were synthesized by both conventional and microwave-mediated method from the synthetic precursors pyrazol-5-one (**1**) and dibenzalacetone (**2**). The synthetic pathway of 4-methyl-7,9-bis-(arylidene)-2,6,10-triphenyl-2,3-diazaspiro[4,5]dec-3-ene-1,8-diones (**5a**–**f**) is described in Scheme 1.

The equimolar mixture of **1** and **2** was refluxed in an ethanolic medium to furnish **3** in good yield. Alternatively, the same reaction was carried out under microwave (MW) irradiation at 300 W and 80 °C for 10 min to get the same desired compound **3** in better yield. The experimental results in the present study revealed that in the case of microwave heating, better yield (82 *vs*. 70 %) of the desired products was achieved in shorter reaction time (7 min *vs*. 10 h) compared to the conventional method. The MW heating is known to promote rapid molecular mixing of the reactants which increases the intimate contact between the reactant molecules and accelerates the reaction kinetics to afford higher yields in lesser reaction time.[28] The comparison of reaction time and yields between conventional and microwave assisted synthetic routes of the synthesized compounds has been summarized in (Table I).

From the experimental results, it is observed that electron withdrawing substituents on the phenyl ring enhance the yield of the products whereas electron donating groups comparatively reduce it. In the present study, the mixture of **3** and different substituted aryl aldehydes **4a**–**f** was refluxed for 10 h in ethanol to produced **5a**–**f** (68–76 % yield) and enhancement in the yield of the products **5a**–**f** (80–87 % yield) was achieved by irradiating the same under MW radiation at 300 W and 80 °C for 7 min. The final yield percentage of the target products were calculated by:[29]

$$\text{Yield} = 100\frac{\text{Content of the product yielded}}{\text{Content of the product expected}} \tag{1}$$

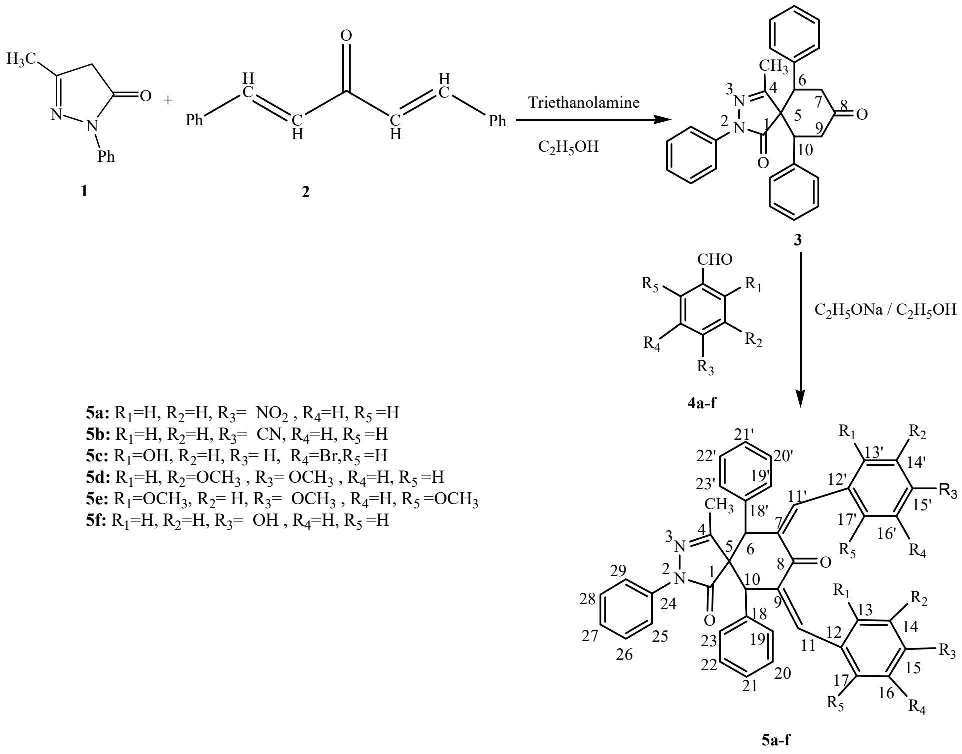

5a: R_1=H, R_2=H, R_3= NO_2 , R_4=H, R_5 =H
5b: R_1=H, R_2=H, R_3= CN, R_4=H, R_5 =H
5c: R_1=OH, R_2=H, R_3= H, R_4=Br,R_5 =H
5d: R_1=H, R_2=OCH_3 , R_3= OCH_3 , R_4=H, R_5 =H
5e: R_1=OCH_3, R_2= H, R_3= OCH_3 , R_4=H, R_5 =OCH_3
5f: R_1=H, R_2=H, R_3= OH , R_4=H, R_5 =H

Scheme 1. Synthetic pathway of **5a**–**f**.

TABLE I. Comparison between conventional and microwave assisted synthetic protocols for compounds **5a**–**f** (reaction time: conventional, 10 h, MW, 7 min)

Compd.	R_1	R_2	R_3	R_4	R_5	Yield, %	
						Conventional	MW
5a	H	H	NO_2	H	H	76	84
5b	H	H	CN	H	H	75	87
5c	OH	H	H	Br	H	72	85
5d	H	OCH_3	OCH_3	H	H	68	81
5e	OCH_3	H	OCH_3	H	OCH_3	70	82
5f	H	H	OH	H	H	69	80

IR spectrum of **5a** ($R_1 = R_2 = R_4 = R_5 = H$, $R_3 = p\text{-}NO_2$) spectrum reveals two characteristic peaks at 1733 and 1691 cm^{-1} corresponding to amidic carbonyl function of pyrazolone moiety and carbonyl function of cyclohexanone scaffold, which is in conjugation with two exocyclic double bonds. The azomethine linkage C=N streching vibrations appears at 1533 cm^{-1} whereas the olefinic stretching vibrations are observed at 1525 cm^{-1}. The band appearing at 1380 cm^{-1} is attributed to symmetric stretching of $ArNO_2$ group.

^1H-NMR spectrum of compound **5a** recorded in $CDCl_3$ exhibited a singlet for methyl protons at $\delta = 1.8$ ppm, and another singlet for two proton methine protons (H-6 and H-10) at $\delta = 3.06$ ppm. The disappearance of the complex pattern of ^1H-NMR spectrum in the target molecule and the appearance of a sharp singlet for two olefinic protons (H-11 and H-11') at $\delta = 7.45$ ppm ensure the incorporation of the double bond at C-7 and C-9 position. In addition, two separate doublets at $\delta = 8.27$ ($J = 8.0$ Hz) and $\delta = 7.79$ ($J = 8.0$ Hz) for the protons of the phenyl group attached to olefinic carbon C-11 and C-11' confirm the formation of diarylidene derivative. A doublet of doublet at $\delta = 7.47$ ($J = 4.0$ Hz, 1.2 Hz) attributed to the ortho protons of the N-phenyl ring of amidic nitrogen of pyrazolone scaffold.

^{13}C-NMR spectrum of compound **5a** gives signals resonating at $\delta = 17.8$, 158.7 and 189.9 ppm, attributed to the respective methyl carbon, azomethine carbon, and amidic carbonyl carbon of pyrazolone ring, whereas the signals at δ 48.5, 63.6, 141.2, 142.9 and 179.9 ppm correspond to the respective methine carbons at C-6 and C-10, spiro carbon C-5, exo-olefinic carbons C-11 and C-11', olefinic carbons in conjugation with carbonyl function and carbonyl carbon of cyclohexanone ring. The signals at δ 111.8 and 121.7 ppm are attributed to C-14, C-14', C-16, C-16' and C-13, C-13', C-17, C-17', signals at δ 137.9 and 143.9 ppm correspond to C-12, C-12' and C-15, C-15' of the phenyl rings attached to exo- olefinic carbons respecttively. The signals at $\delta = 127.3$ ppm corresponds to C-21, C-21', $\delta = 127.8$ ppm to C-19, C-19', C-23, C-23', δ 128.4 to C-20, C-20', C-22, C-22' and $\delta = 133.8$ ppm to C-18, C-18' of the phenyl rings attached to methine carbons at C-6 and C-10. Further, the signals at $\delta = 124.8$ ppm are attributed to C-25, C-29, $\delta = 125.9$ ppm to C-27, $\delta = 129.9$ ppm to C-26, C-28, $\delta =$ $= 137.5$ ppm to C-24 of the phenyl ring attached to pyrazolone ring.

The pyrazol-3-one anion **6** was formed by deprotonation of the active methylene group of pyrazol-3-one **2** in the presence of triethanolamine which generates the enolate intermediate **7**, Scheme 2. Then, the enolate intermediate **7** was added to dibenzalacetone **2** *via* Michael addition. The first Michael adduct thus formed underwent second intramolecular Michael addition under a similar reaction path to obtain the spiro intermediate **3**. Thereafter, the isolated spiro intermediate **3** reacted with two equivalents of aryl aldehydes, in the presence of sodium ethoxide, through Aldol condensation to produce the diarylidene derivative **5**.

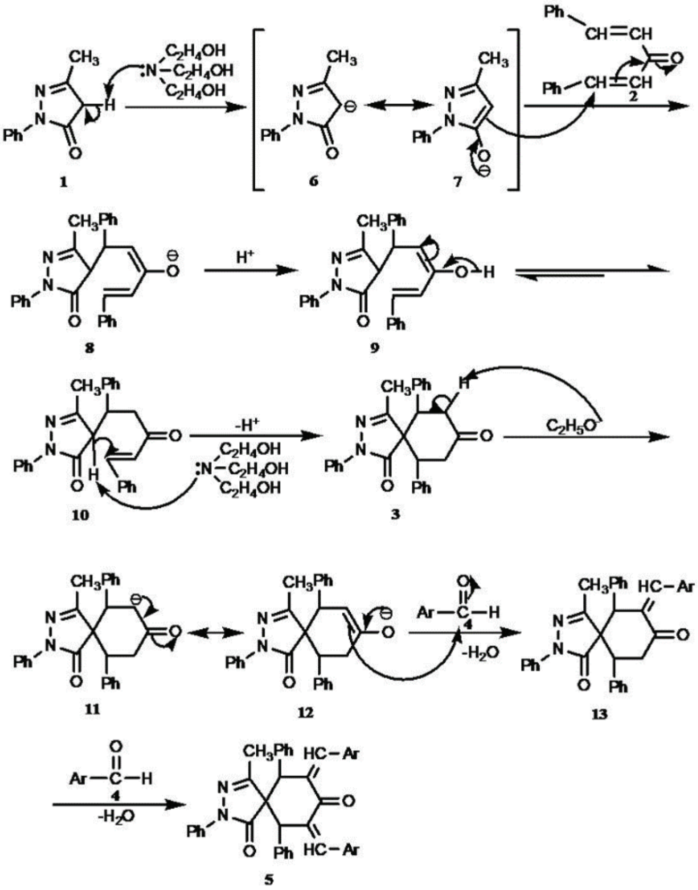

Scheme 2. Plausible mechanism of the synthesized compounds.

DFT study was performed for compound **3** and **5b** using DFT B3LYP/6-31++g(d,p). The optimized structures of compound **3** and **5b** are given. The optimized parameters of structure **3** and **5b** are provided in the Supplementary material.

The optimized structure of compound **3** based on DFT study reveals that N-phenyl, C-6 phenyl and C-10 phenyl rings are in propeller shape (Fig. 2).

In compound **5b**, the bond angles A (2,1,5), A (1,2,3),A (2,3,12), A (2,3,4), A (5,4,6), A (5,4,10), A (7,8,16), A (7,8,9), A (7,53,64), A (9,52,54), A (4,10,15), A (10,9,52) and A (6,7,53) are 108.7814, 112.0698,127.6833, 105.8661, 110.69, 116.1912, 123.1589, 114.7374, 132.4845, 133.5168, 113.1059, 133.2194 and 133.0574°, respectively (provided in Supplementary material).

In the arylidene derivative 4-methyl-(7*E*,9*E*)-7,9-bis-(4-cyano-benzylidene)-2,6,10-triphenyl-2,3-diazaspiro[4,5]dec-3-ene-1,8-dione (**5b**) with the minimum energy of –55133.6 eV, both *p*-CN phenyl groups and the carbonyl function are *trans* to each other across the double bonds (Fig. 2).

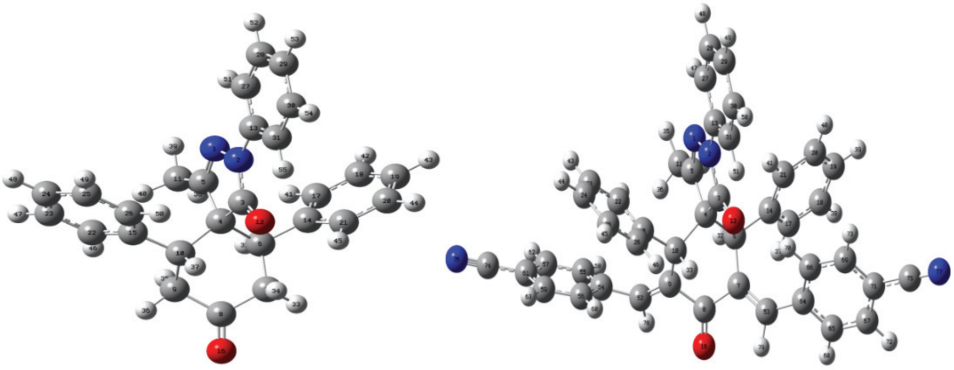
Energy = –35465.9 eV Energy = –55133.6 eV

Fig. 2. Optimizedstructure of compound **3** and **5b**.

Microbial test

All the synthesized compounds **5a–f** were analyzed for their antibacterial and antifungal activity. All compounds showed variable antibacterial activity against the Gram-negative bacteria (*Pseudomonas aeruginosa* and *Escherichia coli)* and Gram-positive bacterium (*Staphylococcus aureus*). However, none of the compounds showed activity against *Streptococcus pyrogene*s. Two compounds, **5a** and **5c**, were found to be most effective against *S. aureus* with a zone of inhibition of 25.2 and 24.1 mm, respectively. Compounds **5a** and **5c** showed higher inhibitory effect with the respective zone of inhibition of 23.7 and 22.1 mm against Gram-negative bacteria *P. aeruginosa* and 22.8 and 20.4 mm, respectively, against *E. coli* (Table II).

TABLE II. Antibacterial activity of novel siro derivatives through agar well diffusion method

Compound	Diameter of the zone of inhibition[a], mm			
	Gram-positive		Gram-negative	
	S. aureus MTCC (3615)	*S. pyrogenes* MTCC (442)	*P. aeruginosa* MTCC (424)	*E. coli* MTCC (443)
5a	**25.2**	–[b]	**23.7**	**22.8**
5b	18.6	–	14.1	13.4
5c	**24.1**	–	**22.1**	**20.4**
5d	16.2	–	16.1	14.9
5e	13.2	–	15.3	12.3
5f	14.7	–	**22.9**	17.5
Ciprofloxacin	**26.7**	**24.3**	**25.0**	**26.3**

[a]Values including diameter of the well (8 mm) and are mean of the three replicates; [b]no activity

However, in the case of fungi, two compounds, **5c** and **5e**, were found to be very effective against *Candida albicans* with the zone of inhibition of 15.8 and 15.1 mm, respectively. Two compounds, **5d** and **5e**, were found to be most effective against *Aspergillus niger and Aspergillus clavatus* with the zone of inhibition of 18.6 and 18.8, and 16.9 and 17.1 mm, respectively (Table III).

TABLE III. Antifungal activity of spiro derivatives through agar well diffusion method

Compound	Diameter of the zone of inhibition[a], mm		
	C. albicans MTCC (227)	*A. niger* MTCC (282)	*A. clavatus* MTCC (1327)
5a	13.1	10.8	14.3
5b	–[b]	–	–
5c	15.9	10.1	11.3
5d	11.6	18.6	16.9
5e	15.1	18.8	17.1
5f	12.3	12.8	13.1
Amphotericin B	16.6	19.3	17.2

[a]Values including diameter of the well (8 mm) and are mean of the three replicates; [b]no activity

The *MIC* of tested compounds ranged between 8 and 512 μg mL^{-1} against bacteria and ranged between 16 and 512 μg mL^{-1} against fungal strains. Compound **5a** was found to be the most effective synthetic derivative having the lowest *MIC* value and the widest spectrum of antibacterial activity as compared to the other tested compounds. The *MIC* value for compound **5a** was 8 μg mL^{-1} against *S. aureus*, 16 μg mL^{-1} against *P. aeruginosa* and 32 μg mL^{-1} aagainst *E. coli*. Compound **5c** also showed remarkable broad spectrum antibacterial activity against both Gram-positive and Gram-negative bacteria except *S. pyrogene*s. The *MIC* value for compound **5c** was 16 μg mL^{-1} against *S. aureus*, 32 μg mL^{-1} against *P. aeruginosa*, and 64 μg mL^{-1} against *E. coli*. Besides, compound **5f** showed strong antibacterial effect against *P. aeruginos*a with the *MIC* value of 32 μg mL^{-1} but showed poor and non-detectable antibacterial activity against *E. coli* and *S. aureus* (Table IV).

Based on the *MIC* calculated for pathogenic fungi, compound **5e** displayed broad spectrum antifungal activity with the *MIC* value of 16 μg mL^{-1} against *C. albicans*, 16 μg mL^{-1} against *A. niger* and 16 μg mL^{-1} against *A. clavatus.* Compound **5c** showed promising antifungal activity against *C. albicans* with the *MIC* of 16 μg mL^{-1} but was observed to be ineffective against *A. clavatus* and *A. niger.* Compound **5d** showed strong antifungal activity against *A. clavatus* and *A. niger* with the *MIC* of 16 and 32 μg mL^{-1}, respectively, but showed no activity against *C. albicans* (Table V).

The results obtained in the present study are in line with our previous report showing the promising antimicrobial activity of diazaspiroundecanetetraone derivatives against *E. coli*, *B. cirroflagellosus*, *A. niger* and *C. albicans*.[17] Several studies show that the antifungal activity of compounds depends on the presence of electron donating or withdrawing substituent in para position in aromatic scaffold.[30] The antibacterial activity of the compounds **5a** and **5c** could therefore be attributed to the present electron withdrawing group such as the bromo group and nitro group, surrounded by high electron density.[4] However, the cellular mechanism underlying the bactericidal and antifungal action of nitro, bromide, and methyl substituted spiro diarylidene derivatives need further investigation.

TABLE IV. Minimum inhibitory concentration (μg mL^{-1}) of spiro diarylidene derivatives against bacterial species using microbroth dilution method

Compound	Bacteria			
	Gram positive		Gram negative	
	S. aureus MTCC (3615)	*S. pyrogenes* MTCC (442)	*P. aeruginosa* MTCC (424)	*E. coli* MTCC (443)
5a	8	16	32	128
5b	256	256	512	–
5c	16	32	64	16
5d	256	128	128	256
5e	512	512	512	16
5f	512	32	128	128
Ciprofloxacin	8	8	16	Nt

TABLE V. Minimum inhibitory concentration (μg mL^{-1}) of spiro diarylidene derivatives against fungal species using microbroth dilution method

Compound	Fungi		
	C. albicans MTCC (227)	*A. niger* MTCC (282)	*A. clavatus* MTCC (1327)
5a	13.1	10.8	14.3
5b	–	–	–
5c	15.9	10.1	11.3
5d	11.6	18.6	16.9
5e	15.1	18.8	17.1
5f	12.3	12.8	13.1
Amphotericin B	16.6	19.3	17.2

CONCLUSION

The present study demonstrates a rapid and novel microwave assisted method for synthesis of a series of pharmacologically important spiro diarylidene compounds from 4-methyl-2,6,10-triphenyl-2,3-diaza-spiro[4,5]dec-3-ene-1,8-dione in high yield in comparison to conventional methods. The study further establishes antimicrobial and antifungal behaviour of some of the synthetic derivatives which could have significant clinical application in developing better antibiotics against infectious organisms. The obtained results indicate that 4-NO_2 derivative (compound **5a**) and 2,4,6-$(OCH_3)_3$ derivative (compound **5e**) may have considerable potential for therapeutic application as a novel wide spectrum drug candidate against bacterial and fungal infections respectively**.** However, further studies are needed to evaluate their efficacy as drug candidates.

SUPPLEMENTARY MATERIAL

Additional data and information are available electronically at the pages of journal website: https://www.shd-pub.org.rs/index.php/JSCS/article/view/10319, or from the corresponding author on request.

Acknowledgments. This work was supported by the UGC (DRS-SAP), New Delhi, under Grant No. F.540/14/DRS/2013/SAP-I. The authors thank FIST-DST under Grant No. SR/FST/ /CSII-021/2012(C) for providing infrastructural research facility. The author, Sabita Shroff is thankful to UGC-BSR for providing fellowship under Grant (F. NO. 25-1/2014-15 (BSR)/7- -166/2007/(BSR)) for smooth conduction of research work. The authors acknowledge National Institute of Technology, Rourkela, Odisha, for recording NMR and Mass spectra.

ИЗВОД

МИКРОТАЛАСНА СИНТЕЗА НОВИХ СПИРО ДИАРИЛЕДЕНА И ИСПИТИВАЊЕ ЊИХОВЕ АНТИМИКРОБНЕ АКТИВНОСТИ

SABITA SHROFF[1], PRAJNA P. MOHANTA[1], ISWAR BAITHARU[2], BHAWANI P. BAG[3] и AJAYA K. BEHERA[1]

[1]*Organic Synthesis Lab, School of Chemistry, Sambalpur University, Jyoti Vihar, Odisha-768019, India,* [2]*Toxicology Lab, P.G. Dept. of Environmental Sciences, Sambalpur University, Jyoti Vihar, Odisha-768019, India и* [3]*Biotechology and Bioinformatics Lab, Sambalpur University, Jyoti Vihar, Odisha-768019, India*

Испитана је брза синтеза серије нових 7,9-бис-(арилиден)-4-метил-2,6,10-трифенил-2,3-диазаспиро[4,5]дец-3-ен-1,8-диона, помогнута микроталасима, са високим приносом. Диспиро диарилиден деривати који садрже азот и α,β-незасићене кето-групе, синтетисани су реакцијама алдолне кондензације, праћене дехидратацијом, између 4-метил-2,6,10-трифенил-2,3-диазаспиро[4,5]дец-3-ен-1,8-диона и одговарајућих арилалдехида. Добијени спироарилиденски деривати окарактерисани су IC, ^{1}H- ^{13}C-NMR и масеним спектрима. DFT (density functional theory) прорачуни извршени су помоћу програма Gaussian 09. Ипитана је антимикробна активност синтетисаних деривата према две Грам-позитивне и две Грам-негативне бактерије и према три врсте гљивица диск-дифузионом методом. Минимална инхибиторна концентација (*MIC*) одређена је микроброт техником разблаживања. На основу добијених резултата показано је да једињења **5a** и **5c** која поседују $4-NO_2$ и 5-Br-2-OH супституенте имају већу активност према Грам-позитивној бактерији *Staphylococcus aureus*, са *MIC* вредностима 8 и 16 μg mL^{-1}, редом, и да су умерено активни према Грам-негативним бактеријама *Pseudomonas aeruginosa* and *Escherichia coli* у поређењу са другим тестираним једињењима. Ипак, ни једно од тестираних једињења не показује активност према *Streptococcus pyrogenes*. Једињење **5e** са 2,4,6-$(OCH_3)_3C_6H_3$ структурним делом показује шири спектар активности према свим сојевима гљивица, али не показује антибактеријску активност.

(Примљено 23. јануара 2021, ревидирано 22. фебруара, прихваћено 30. марта 2022)

REFERENCES

1. M. Grare, M. Mourer, S. Fontanay, J. B. Regnouf-de-Vains, C. Finance, R. E. Duval, *J. Antimicrob. Chemother.* **60** (2007) 575 (https://dx.doi.org/10.1093/jac/dkm244)
2. P. Dahiya, S. Purkayastha, *Indian J. Pharm. Sci.* **74** (2012) 443 (https://dx.doi.org/10.4103/0250-474X.108420)

3. M. Benabdallah, O. Talhi, F. Nouali, N. Choukchou-Braham, K. Bachari, A. M. S. Silva, *Curr. Med. Chem.* **25** (2018) 3748 (https://doi.org/10.2174/0929867325666180309124821)
4. M. A. K. Shakhatreh, M. L. Al-Smadi, O. F. Khabour, F. A. Shuaibu, E. I. Hussein, K. H. Alzoubi, *Drug Des. Devel. Ther.* **10** (2016) 3653 (https://doi.org/10.2147/DDDT.S116312)
5. S. Bag, S. Ramar, M. S. Degani, *Med. Chem. Res.* **18** (2009)309 (https://doi.org/10.1007/s00044-008-9128-x)
6. M. Funakoshi-Tago, K. Nakamura, R. Tsuruya, M. Hatanaka, T. Mashino, Y. Sonoda, T. Kasahara, *Int. Immunopharmacol.* **10** (2010) 562 (https://doi.org/10.1016/j.intimp.2010.02.003)
7. S. J. Yeo, D. X. Liu, H. S. Kim, H. Park, *Malar. J.* **16** (2017)80 (https://doi.org/10.1186/s12936-017-1725-z)
8. W. M. El-Husseiny, M. A. A. El-Sayed, N. I. Abdel-Aziz, A. S. El-Azab, E. R. Ahmed, A. A. M. Abdel-Aziz, *J. Enzyme Inhib. Med. Chem.* **33** (2018) 507 (https://doi.org/10.1080/14756366.2018.1434519)
9. R. Pradhan, M. Patra, A. K. Behera, B. K. Mishra, R. K. Behera, *Tetrahedron* **62** (2006) 779 (https://doi.org/10.1016/j.tet.2005.09.039)
10. P. Saraswat, G. Jeyabalan, M. Z. Hassan, M. U. Rahman, N. K. Nyola, *Synth. Commun.* **46** (2016) 1643 (https://doi.org/10.1080/00397911.2016.1211704)
11. M. Palomba, L. Rossi, L. Sancineto, E. Tramontano, A. Corona, L. Bagnoli, C. Santi, C. Pannecouque, O. Tabarrini, F. Marini, *Org. Biomol. Chem.* **14** (2016)2015 (https://doi.org/10.1039/c5ob02451j)
12. K. Chakraborty, T. Antony, *Nat. Prod. Res.* **35** (2021)1 (https://doi.org/10.1080/14786419.2019.1608545)
13. K. Meena, S. Kumari, J. M. Khurana, A. Malik, C. Sharma, H. Panwar, *Chin. Chem. Lett.* **28** (2017) 136 (https://doi.org/10.1016/j.cclet.2016.06.025)
14. J. P. Strachan, J. J. Farias, J. Zhang, W. S. Caldwell, B. S. Bhatti, *Bioorg. Med. Chem. Lett.* **22** (2012) 5089 (https://doi.org/10.1016/j.bmcl.2012.05.108)
15. A. Jasper, D. Schepmann, K. Lehmkuhl, J. M. Vela, H. Buschmann, J. Holenz, B. Wünsch, *Eur. J. Med. Chem.* **53** (2012) 327 (https://doi.org/10.1016/j.ejmech.2012.04.018)
16. A. S. Girgis, S. S. Panda, I. S. A. Farag, A. M. El-Shabiny, A. M. Moustafa, N. S. M. Ismail, G. G. Pillai, C. S. Panda, C. D. Hall, A. R. Katritzky, *Org. Biomol. Chem.* **13** (2015) 1741 (https://doi.org/10.1039/c4ob02149e)
17. R. K. Behera, A. K. Behera, R. Pradhan, A. Pati, & M. Patra, *Synth. Commun.* **36** (2006) 3729 (https://doi.org/10.1080/00397910600946231)
18. P. Prasanna, K. Balamurugan, S. Perumal, P. Yogeeswari, D. Sriram, *Eur. J. Med. Chem.* **45** (2010) 5663 (https://doi.org/10.1016/j.ejmech.2010.09.019)
19. R. Sakhuja, K. Bajaj, S. M. Abdul Shakoor, & A. Kumar, *Mini. Rev. Org. Chem.* **11** (2014) 55 (https://doi.org/10.2174/1570193x1101140402101513)
20. A. R. Suresh Babu, R. Raghunathan, *Tetrahedron Lett.* **48** (2007) 305 (https://doi.org/10.1016/j.tetlet.2006.11.012)
21. G. Sridhar, T. Gunasundari, R. Raghunathan, *Tetrahedron Lett.* **48** (2007) 319 (https://doi.org/10.1016/j.tetlet.2006.11.002)
22. E. D. Becker, *High resolution NMR Theory and Chemical Applications,* 3rd ed., Academic Press, London, 2000, p. 83 (https://doi.org/10.1016/B978-0-12-084662-7.X5044-3)

23. *Gaussian 16, Rev. C. 01*, Gaussian, Inc., Wallingford, CT, 2016 (https://gaussian.com/)
24. B. S. Furniss, A. J. Hannaford, P. W. Smith, A. R. Tatchell, in *Vogel's Textbook of Practical Organic Chemistry*, 4th ed., ELBS and Longman, London, 1990, p. 143
25. R. Adams, *Organic Synthesis,* John Wiley, London, 1946, p. 22 (https://library.sciencemadness.org/library/books/organic_reactions_v2.pdf)
26. I. Wiegand, K. Hilpert, R. E. W. Hancock, *Nat. Protoc.* **3** (2008) 163 (https://doi.org/10.1038/nprot.2007.521)
27. J. L. Rodriguez-Tudela, *Clin. Microbiol. Infect.* **14** (2008) (https://doi.org/10.1111/j.1469-0691.2007.01935.x)
28. W. S. Bremner, M. G. Organ, *J. Comb. Chem.* **9** (2007) 14 (https://doi.org/10.1021/cc060130p)
29. J. Isac-Garcia, J. A. Dobado, F. G. Calvo-Flores, H. Martinez-Garcia, *Chemistry: Laboratory Manual,* Academic Press, London, 2016, p. 239 (https://doi.org/10.1016/C2015-0-00644-X)
30. S. N. López, M. V. Castelli, S. A. Zacchino, J. N. Domínguez, G. Lobo, J. Charris-Charris, J. C. G. Cortés, J. C. Ribas, C. Devia, A. M. Rodríguez, R. D. Enriz, *Bioorganic Med. Chem.* **9** (2001)1999 (https://doi.org/10.1016/S0968-0896(01)00116-X).

Journal of the Serbian Chemical Society
JSCS@tmf.bg.ac.rs • www.shd.org.rs/JSCS
J. Serb. Chem. Soc. 87 (7–8) S263–S283 (2022)
Supplementary material

SUPPLEMENTARY MATERIAL TO

Microwave assisted synthesis of novel spiro diarylidenes and their antimicrobial assay

SABITA SHROFF[1], PRAJNA PARIMITA MOHANTA[1], ISWAR BAITHARU[2], BHAWANI PRASAD BAG[3] and AJAYA KUMAR BEHERA[1]*

[1]*Organic Synthesis Lab, School of Chemistry, Sambalpur University, Jyoti Vihar Odisha-768019, India,* [2]*Toxicology Lab, P.G. Department of Environmental Sciences, Sambalpur University, Jyoti Vihar, Odisha-768019, India and* [3]*Department of Biotechnology and Bioinformatics , Sambalpur University, Jyoti Vihar, Odisha-768019, India*

J. Serb. Chem. Soc. 87 (7–8) (2022) 813–827

*4-Methyl-2,6,10-triphenyl-2,3-diaza-spiro[4.5]dec-3-ene-1,8-dione (**3**)*

Yield: 285 mg, 70 % (Conventional) and 334 mg, 82 % (MW). M.p. 166––168 °C. ^{1}H-NMR (400 MHz, CDCl$_3$, δ / ppm): 2.12 (*s*, 3H, CH$_3$), 2.60 (*dd*, 2H, J = 14.0 Hz, 3.6 Hz, 7H/9H-equatorial), 3.53 (*dd*, 2H, J = 14.0 Hz, 3.6 Hz, 7H/9H-axial), 4.01–4.08 (*m*, 2H, 2×CH of C-6 & C-10), 7.2–7.3 (*m*, 11H, H-20, H-12, H-13, H14, H-15, H-16, H-12', H-13', H14', H-15', H-16',), 7.34–7.38 (*m*, 2H, H-19 & H-21), 7.42 (*d*, 2H, J = 8.0 Hz, H-18 & H-22). ^{13}C-NMR (100 MHz, CDCl$_3$, δ / ppm): 207.64, 186.52, 160.63, 139.58, 137.97, 129.53, 128.61, 128.11, 127.44, 127.09, 121.29, 63.36, 48.95, 42.96, 16.33. (+) LCMS (*m*/*z*): calculated for [$C_{27}H_{24}N_2O_2$ + H]$^+$ 408.4, observed 409.1.

---

*Corresponding author. E-mail: ajayakumar.behera@suniv.ac.in

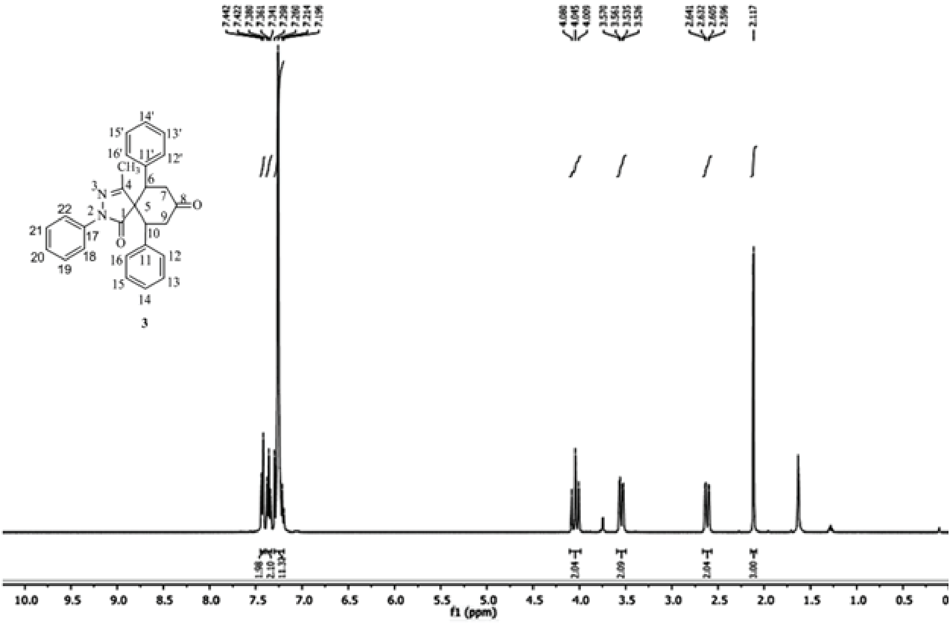

Figure S-1. ^{1}H NMR spectrum of 4-methyl-2,6,10-triphenyl-2,3-diaza-spiro [4.5] dec-3-ene--1,8-dione (**3**) ($CDCl_3$, 400 MHz)

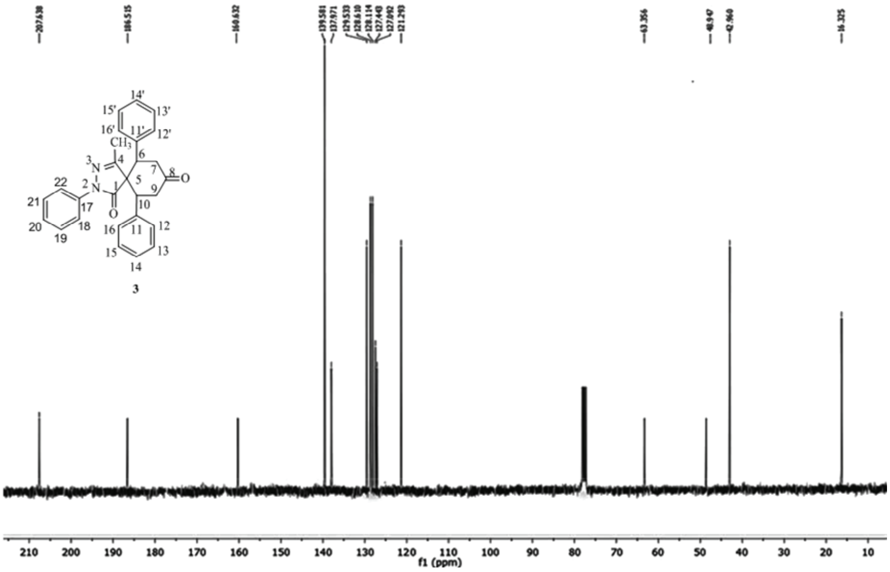

Figure S-2. ^{13}C NMR spectrum of 4-methyl-2,6,10-triphenyl-2,3-diaza-spiro [4.5] dec-3-ene--1,8-dione (**3**) ($CDCl_3$, 100 MHz)

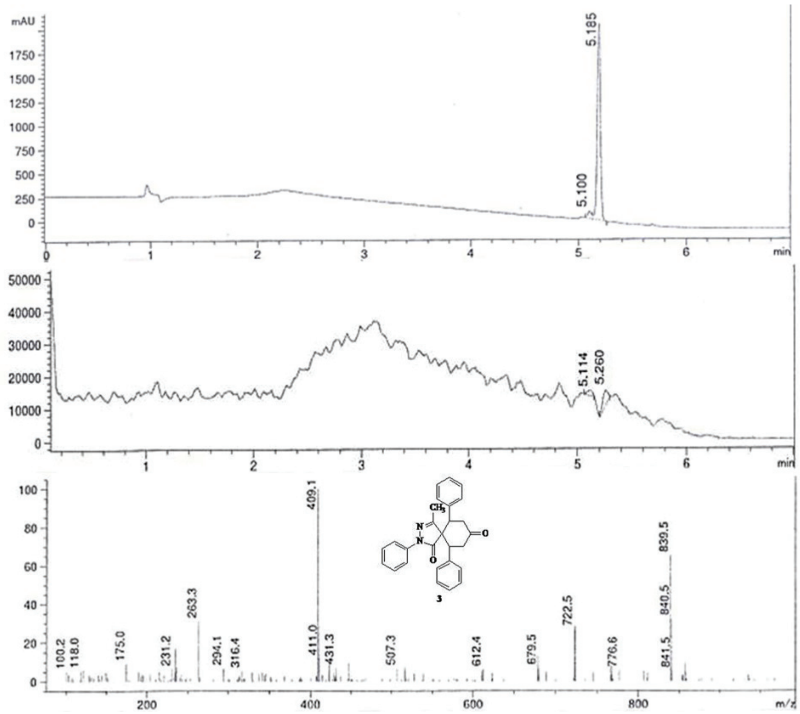

Figure S-3. Mass spectrum of 4-methyl-2,6,10-triphenyl-2,3-diaza-spiro [4.5] dec-3-ene-1,8-dione (**3**)

*4-Methyl-7,9-bis-(4-nitro-benzylidene)-2,6,10-triphenyl-2,3-diaza-spiro[4.5] dec-3-ene-1,8-dione(**5a**)*

Dark brown solid. Yield: 512 mg, 76 % (Conventional) and 566 mg, 84 % (MW). m.p: 80-82 °C, IR (ν_{max}/cm^{-1}):1733, 1691, 1553, 1525,1380. ^{1}H NMR (400 MHz, CDCl$_3$, δ): 1.80 (s, 3H, CH$_3$), 3.10 (s, 2H, 2xCH, H-6 & H-10), 7.20 - 7.23(m, 1H, H-27), 7.24-7.27 (m,6H, H-20,21,22,20',21',22'), 7.38-7.43(m, 4H, H-19,23,19',23'), 7.45(s, 2H, 2x =CH, H-11 & H-11'), 7.47(dd, 2H, *J*=4.0 Hz, 1.2Hz, H-25 & H-29), 7.53-7.56 (m, 2H, H-26,28), 7.79(d, 4H, *J*=8.0 Hz, H-13,17,13',17'), 8.27(d, 4H, *J*=8.0 Hz, H-14,16,14',16'). ^{13}C NMR (100 MHz, CDCl$_3$, δ): 189.91, 179.85, 158.68, 143.86, 142.89, 141.15, 137.97, 137.55, 133.86, 129.91, 128.42, 127.81, 127.34, 125.92, 124.82, 121.7, 111.82, 63.63, 48.54, 17.82. Combustion analysis for $C_{41}H_{30}N_4O_6$: Calculated. C 72.99, H 4.48, N 8.3; found C 72.95, H 4.46, N 8.29. (+) LCMS (*m*/*z*): calculated for $[C_{41}H_{30}N_4O_6 + H]^+$ 674.7, observed 675.6.

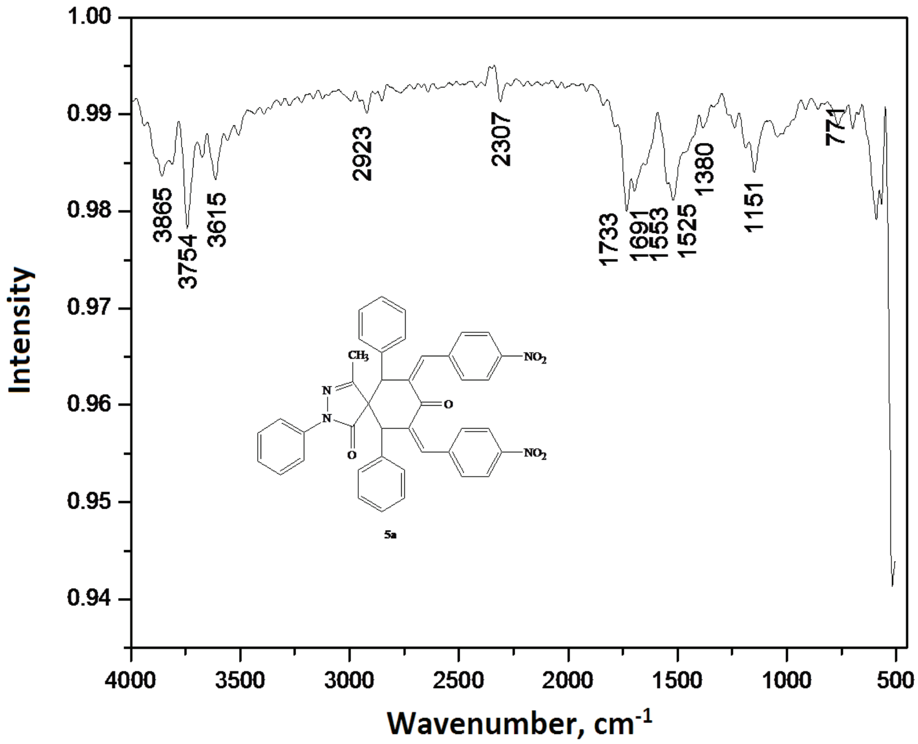

Figure S-4. IR spectrum of 4-methyl-7,9-bis-(4-nitro-benzylidene)-2,6,10-triphenyl-2,3--diaza-spiro[4.5]dec-3-ene-1,8-dione (**5a**)

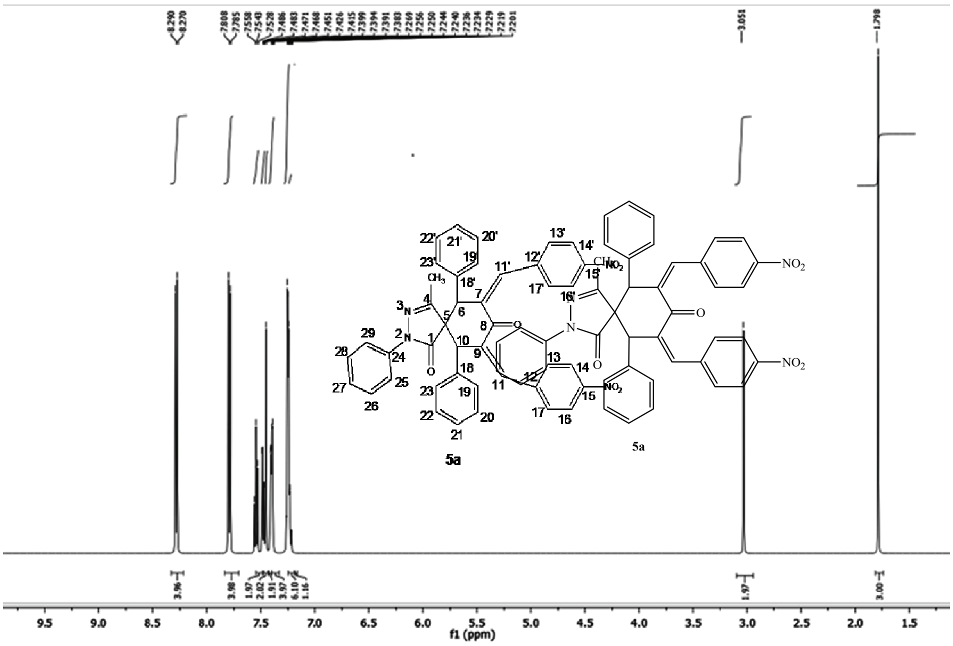

Figure S-5. ^{1}H NMR spectrum of 4-methyl-7,9-bis-(4-nitro-benzylidene)-2,6,10-triphenyl--2,3-diaza-spiro[4.5]dec-3-ene-1,8-dione (**5a**) ($CDCl_3$, 400 MHz)

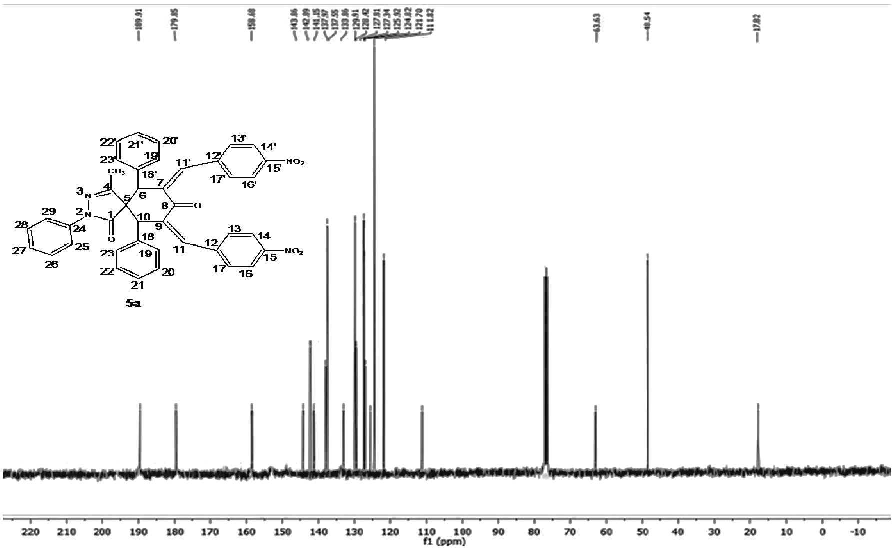

Figure S-6. ^{13}C NMR pectrum of 4-methyl-7,9-bis-(4-nitro-benzylidene)-2,6,10-triphenyl--2,3-diaza-spiro[4.5]dec-3-ene-1,8-dione (**5a**) ($CDCl_3$, 100 MHz)

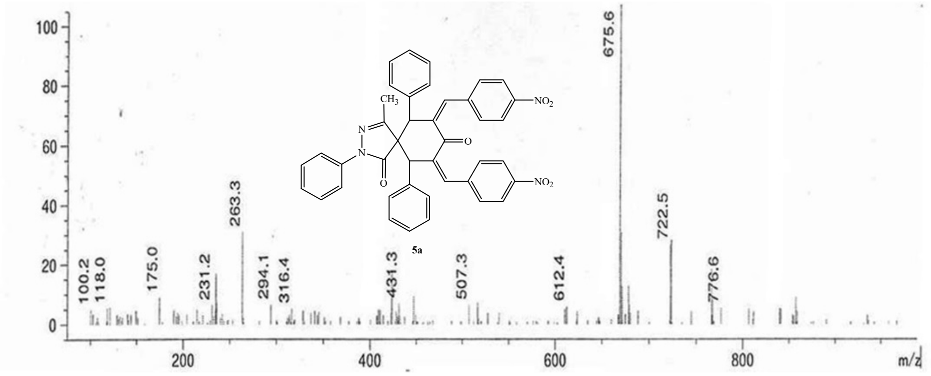

Figure S-7. Mass spectrum of 4-methyl-7,9-bis-(4-nitro-benzylidene)-2,6,10-triphenyl-2,3- -diaza-spiro[4.5]dec-3-ene-1,8-dione (**5a**)

*4-Methyl-7,9-bis-(4-cyano-benzylidiene)-2,6,10-triphenyl-2,3-diazaspiro[4,5]dec-3-ene-1,8-dione(**5b**).* Yellow solid. Yield: 475 mg, 75% (Conventional) and 551 mg, 87 % (MW). m.p.: 110-112 °C, IR (ν_{max}/cm^{-1}):2304, 1730, 1690, 1546, 1512. ^{1}H NMR (400 MHz, $CDCl_3$, δ): 1.90 (s, 3H, CH_3), 3.08(s, 2H, 2xCH, H-6 & H-10), 7.20-7.23 (m, 1H, H-27), 7.25-7.29 (m, 6H, H-20,21,22,20',21',22'), 7.33 (s, 2H,2x =CH, H-11 & H-11'), 7.39-7.43 (m, 4H, H-19,23,19',23'), 7.44 (dd, 2H, *J*=4.0Hz, 1.2Hz, H-25 & H-29), 7.51-7.54 (m, 2H, H-26,28), 7.69 (d, 4H, *J*=8.0 Hz, H-13,17,13',17'), 7.72 (d, 4H, *J*=8.0Hz, H-14,16,14',16'). ^{13}C NMR (100 MHz, $CDCl_3$, δ):189.83, 180.12, 157.34, 143.12, 141.26, 139.76, 137.48, 134.18, 129.53, 128.45, 127.41, 127.09, 125.26, 124.18, 121.29, 119.12, 111.29, 62.83, 48.26, 16.76. Combustion analysis for $C_{43}H_{30}N_4O_2$: Calculated. C, 81.37, H 4.76, N 8.83; found C 81.36, H 4.74, N 8.8. (+) LCMS (*m*/*z*): calculated for $[C_{43}H_{30}N_4O_2 + H]^+$ 634.7, observed 635.4.

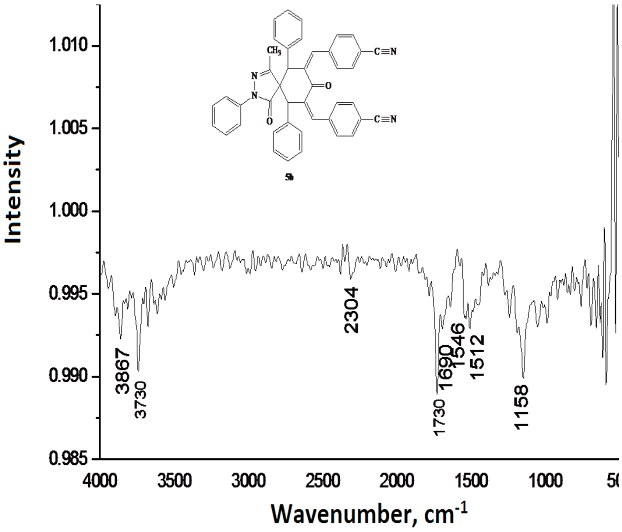

Figure S-8. IR spectrum of 4-methyl-7,9-bis-(4-cyano-benzylidiene)-2,6,10-triphenyl-2,3 diazaspiro[4,5]dec-3-ene-1,8-dione (**5b**)

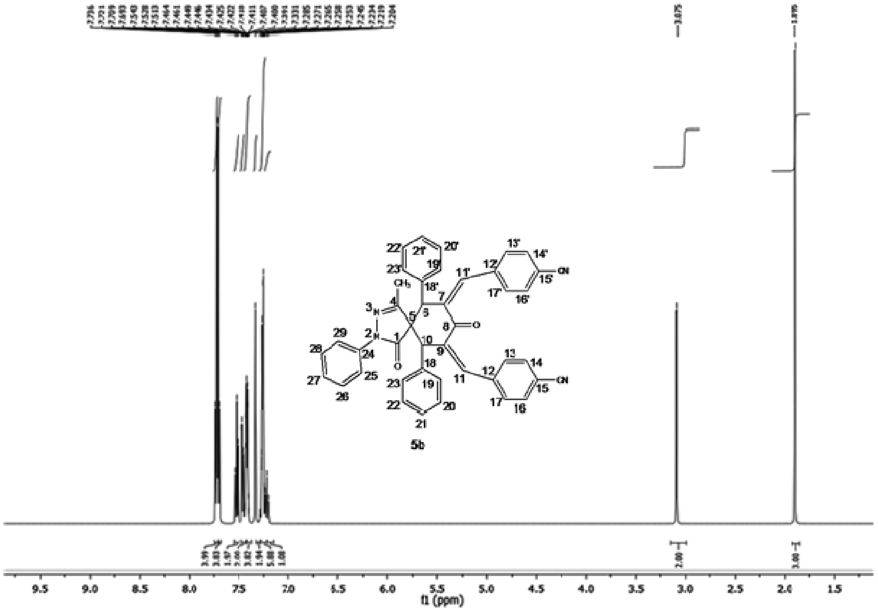

Figure S-9. ^{1}H NMR spectrum of 4-Methyl-7,9-bis-(4-cyano-benzylidiene)-2,6,10-triphenyl--2,3 diazaspiro[4,5]dec-3-ene-1,8-dione (**5b**) ($CDCl_3$, 400 MHz)

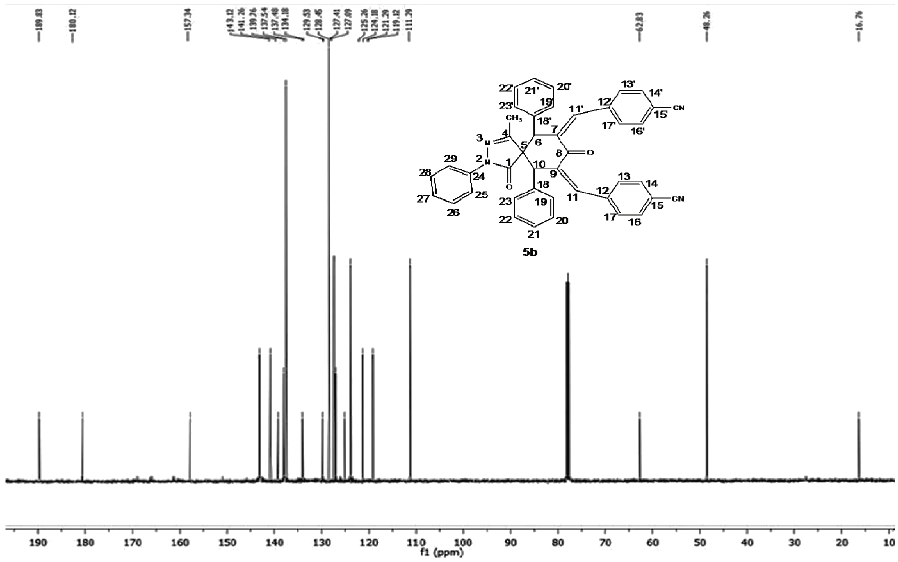

Figure S-10. ^{13}C NMR spectrum of 4-methyl-7,9-bis-(4-cyano-benzylidiene)-2,6,10-triphenyl--2,3-diazaspiro[4,5]dec-3-ene-1,8-dione (**5b**) ($CDCl_3$, 100 MHz).

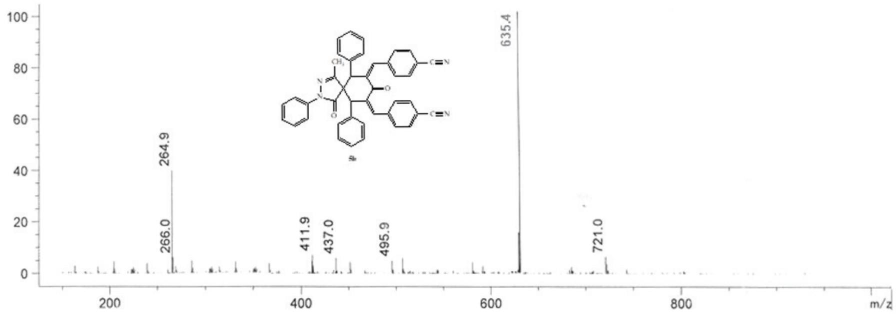

Figure S-11. Mass spectrum of 4-methyl-7,9-bis-(4-cyano-benzylidiene)-2,6,10-triphenyl-2,3-diazaspiro[4,5]dec-3-ene-1,8-dione (**5b**)

*7,9-Bis-(5-bromo-2-hydroxy-benzylidene)-4-methyl-2,6,10-triphenyl-2,3-diazaspiro[4.5] dec-3-ene-1,8-dione(**5c**).* Reddish brown solid. Yield: 557 mg, 72%(Conventional) and 658 mg, 85% (MW). m.p.: 90-92 °C, IR (ν_{max}/cm^{-1}):3614, 1731, 1683, 1546, 1512. ^{1}H NMR (400 MHz, $CDCl_3$ δ): 1.97(s, 3H, CH_3), 3.10 (s, 2H, 2xCH, H-6 & H-10), 6.84(d, 2H, *J*=8.0 Hz, H-16 & 16'), 7.21-7.24(m,1H, H-27), 7.25-7.28(m, 6H, H-20,21,22,20',21',22'), 7.37(d, *J*=8.0 Hz, 2H, H-26 & 28), 7.40-7.43 (m, 4H, H-19,23,19',23'), 7.44(dd, 2H, *J*=4.0 Hz, 1.2Hz, H-25& H-29), 7.50 (s, 2H, 2x =CH, H-11 & H-11'), 7.51-7.54 (m, 2H, H-15&15'), 7.59(s, 2H, H-13 &13'), 9.77(bs, 2H, 2x OH). ^{13}C NMR (100 MHz, $CDCl_3$, δ): 187.02, 177.62, 156.0, 155.26, 145.37, 139.53, 138.9, 137.55, 133.13, 131.39, 129.53, 128.45, 127.41, 127.34, 125.26, 123.13, 121.29, 119.52, 113.18, 63.9, 48.55, 16.33. Combustion analysis for $C_{41}H_{30}Br_2N_2O_4$: Calculated. C 63.58, H 3.9, N 3.62; found C 63.56, H 3.87, N 3.59. (+) LCMS (*m*/*z*): calculated for $[C_{41}H_{30}Br_2N_2O_4 + H]^{2+}$ 774.4, observed 776.1.

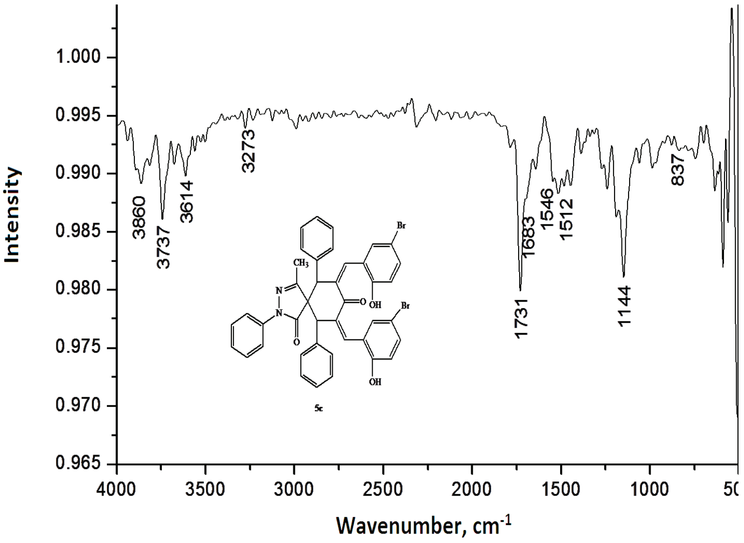

Figure S-12. IR spectrum of 7,9-bis-(5-bromo-2-hydroxy-benzylidene)-4-methyl-2,6,10--triphenyl-2,3-diazaspiro[4.5]dec-3-ene-1,8-dione (**5c**)

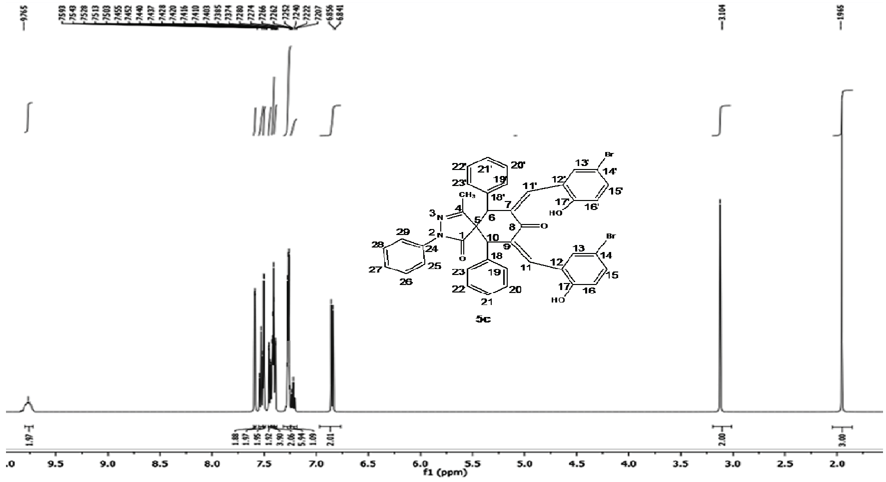

Figure S-13. ^{1}H NMR spectrum of 7,9-bis-(5-bromo-2-hydroxy-benzylidene)-4-methyl--2,6,10-triphenyl-2,3-diazaspiro[4.5]dec-3-ene-1,8-dione (**5c**) ($CDCl_3$, 400 MHz).

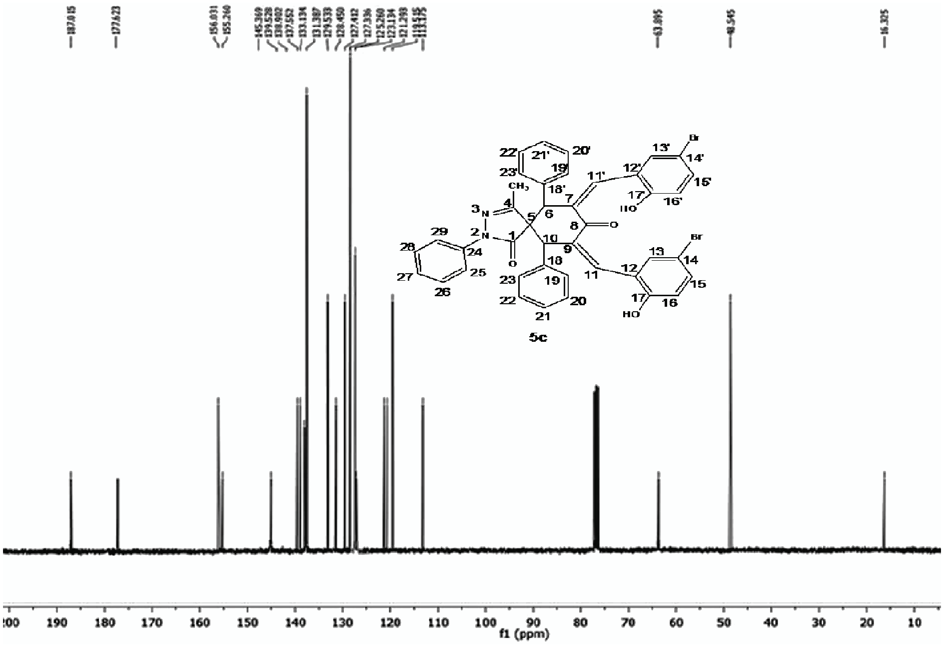

Figure S-14. ^{13}C NMR spectrum of 7,9-bis-(5-bromo-2-hydroxy-benzylidene)-4-methyl--2,6,10-triphenyl-2,3-diazaspiro[4.5]dec-3-ene-1,8-dione (**5c**) ($CDCl_3$, 100 MHz).

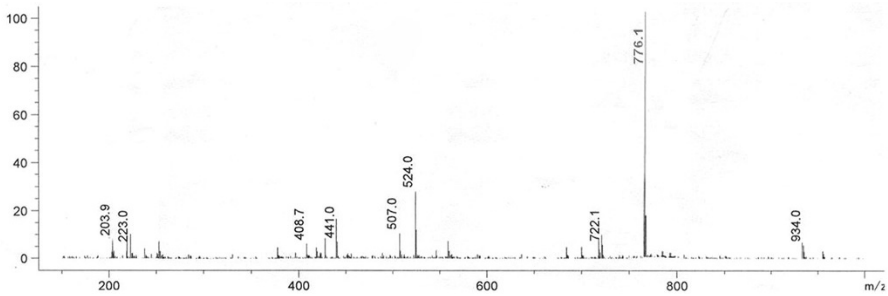

Figure S-15. Mass spectrum of 7,9-bis-(5-bromo-2-hydroxy-benzylidene)-4-methyl-2,6,10--triphenyl-2,3-diazaspiro[4.5]dec-3-ene-1,8-dione (**5c**).

*7,9-Bis-(3,4-dimethoxy-benzylidene)-4-methyl-2,6,10-triphenyl-2,3-diazaspiro[4.5]dec-3-ene-1,8-dione(**5d**).* Pale yellow solid. Yield: 478 mg, 68 % (Conventional) and 570 mg, 81 % (MW). m.p.: 98-101 °C, IR (v_{max}/cm^{-1}):1730, 1690, 1553, 1499, 1144. ^{1}H NMR (400 MHz, $CDCl_3$, δ): 1.96(s, 3H, CH_3), 3.09(s, 2H, 2xCH, H-6 & H-10), 3.82 (s, 12H, 4xOCH_3), 7.09 (d, 2H, *J*=8.0 Hz, H-14 &14'), 7.18-7.21 (m,1H, H-27), 7.22 (s, 2H, H-17&17'), 7.23-7.27(m, 6H, H-20,21,22,20',21',22'), 7.31 (s, 2H, 2x =CH, H-11 & H-11'), 7.36 (dd, 2H, *J*=4.0 Hz, 1.2Hz, H-13 & H-13'), 7.41-7.44 (m, 4H, H-19,23,19',23'), 7.45 (d, 2H, *J*=8.0 Hz, H-25 & 29), 7.51-7.54 (m,2H, H-26 & 28), ^{13}C NMR (100 MHz, $CDCl_3$, δ): 187.07, 176.26, 155.45, 144.92, 140.43, 150.94, 150.04, 140.26, 137.92, 137.51, 129.42, 128.26, 127.41, 127.03, 126.41, 123.57, 121.23, 113.34, 112.51, 64.62, 56.78, 48.5, 16.35. Combustion analysis for $C_{45}H_{40}N_2O_6$: Calculated. C 76.68, H 5.72, N 3.97; found C 76.65, H 5.69, N 3.95. (+) LCMS (*m*/*z*): calculated for $[C_{45}H_{40}N_2O_6 + H]^{2+}$ 704.8, observed 706.5.

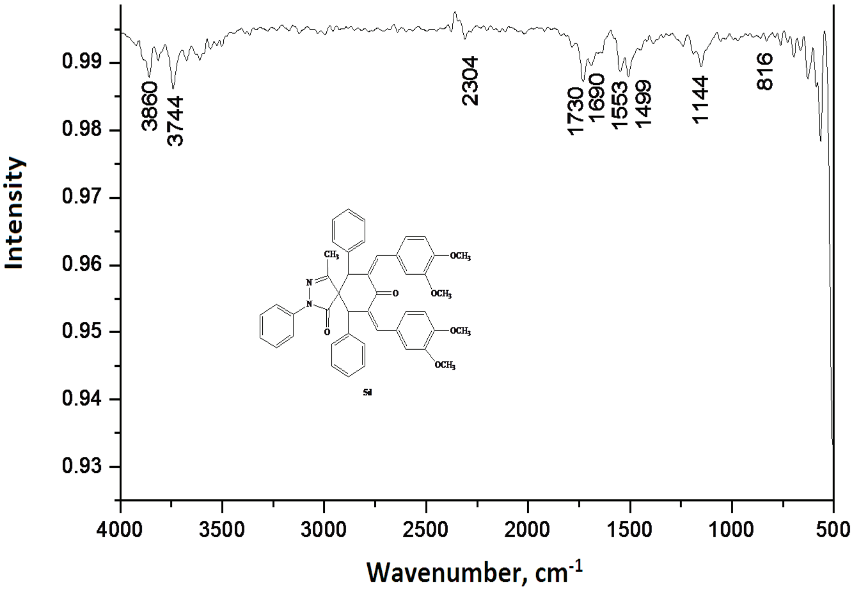

Figure S-16. IR spectrum of 7,9-bis-(3,4-dimethoxy-benzylidene)-4-methyl-2,6,10-triphenyl--2,3-diaza-spiro[4.5]dec-3-ene-1,8-dione (**5d**).

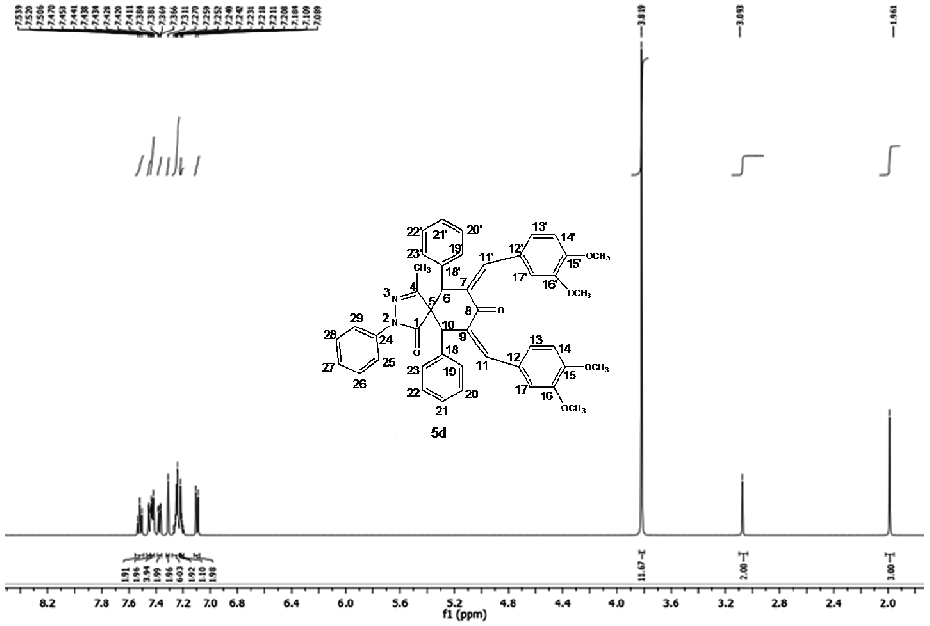

Figure S-17. ^{1}H NMR spectrum of 7,9-bis-(3,4-dimethoxy-benzylidene)-4-methyl-2,6,10--triphenyl-2,3-diaza-spiro[4.5]dec-3-ene-1,8-dione (**5d**) (CDCl$_3$, 400 MHz).

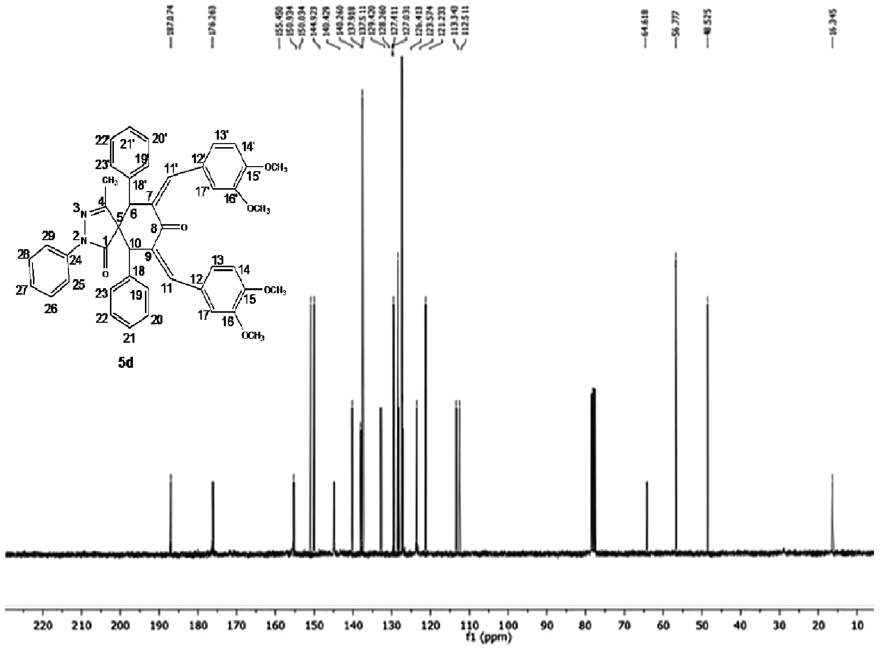

Figure S-18. ^{13}C NMR spectrum of 7,9-bis-(3,4-dimethoxy-benzylidene)-4-methyl-2,6,10--triphenyl-2,3-diaza-spiro[4.5]dec-3-ene-1,8-dione (**5d**) (CDCl$_3$, 100 MHz).

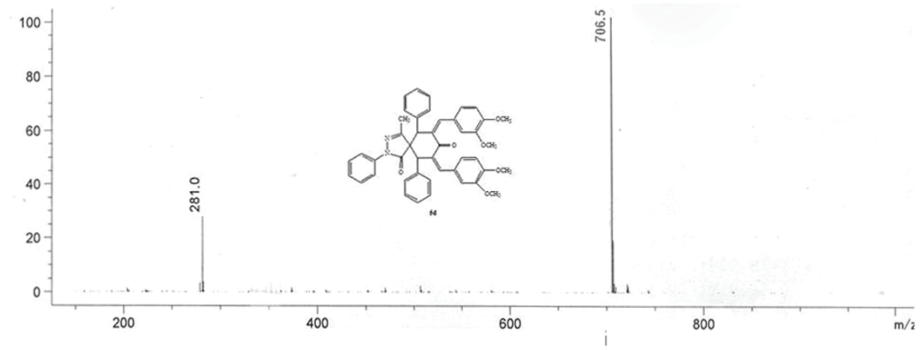

Figure S-19. Mass spectrum of 7,9-bis-(3,4-dimethoxy-benzylidene)-4-methyl-2,6,10--triphenyl-2,3-diaza-spiro[4.5]dec-3-ene-1,8-dione (**5d**).

*4-Methyl-2,6,10-triphenyl-7,9-bis-(2,4,6-trimethoxybenzylidene)-2,3-diazaspiro[4.5]dec-3-ene-1,8-dione (5e).*Pale yellow solid. Yield: 534 mg, 70% (Conventional) and 626 mg, 82% (MW). m.p.: 85-87 °C, IR (ν_{max}/cm^{-1}):1751, 1683, 1546, 1505, 1096. ^{1}H NMR (400 MHz, $CDCl_3$, δ): 1.88 (s, 3H, CH_3), 3.11 (s, 2H, 2xCH, H-6 & H-10), 3.81 (s, 12H, 4xOCH_3), 3.83 (s, 6H, 2xOCH_3), 6.40 (s, 4H, H-14,16,14',16'), 7.21-7.24 (m, 1H, H-27), 7.25-7.28 (m, 6H, H-20,21,22,20',21',22'), 7.36 (s, 2H,2x =CH, H-11 & H-11'), 7.40-7.44 (m, 4H, H-19,23,19',23'), 7.48 (dd, 2H, *J*=4.0Hz, 1.2Hz, H-25 & H-29), 7.53-7.56 (m, 2H, H-26 & 28). ^{13}C NMR (100 MHz, $CDCl_3$, δ): 187.07, 177.55, 160.62, 158.95, 155.45, 144.07, 141.55, 139.54, 137.29, 129.53, 128.09, 127.41, 127.29, 127.06, 121.49, 107.73, 90.97, 64.62, 56.78, 56.03, 48.42, 16.34. Combustion analysis for $C_{47}H_{44}N_2O_8$: Calculated. C 73.8, H 5.8, N 3.66; found C 73.78, H 5.77, N 3.62. (+) LCMS (*m*/*z*): calculated for $[C_{47}H_{44}N_2O_8 + H]^+$ 764.8, observed 765.9.

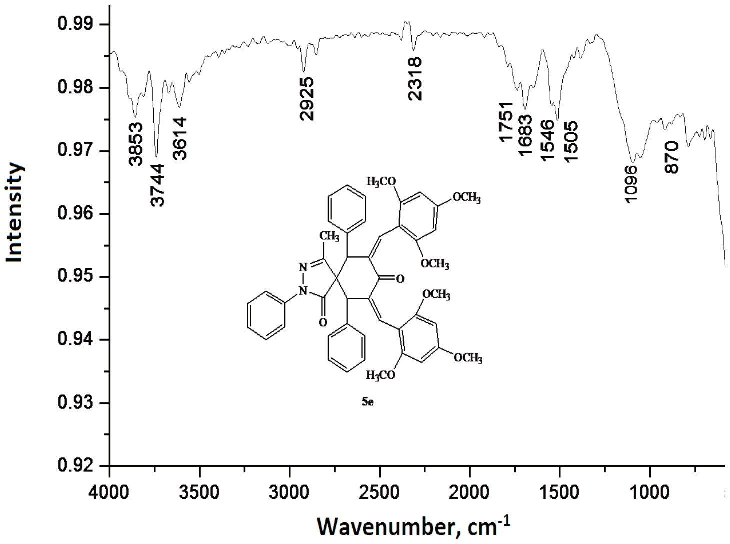

Figure S-20. IR spectrum of 4-methyl-2,6,10-triphenyl-7,9-bis-(2,4,6-trimethoxy--benzylidene)-2,3-diazaspiro[4.5]dec-3-ene-1,8-dione (**5e**).

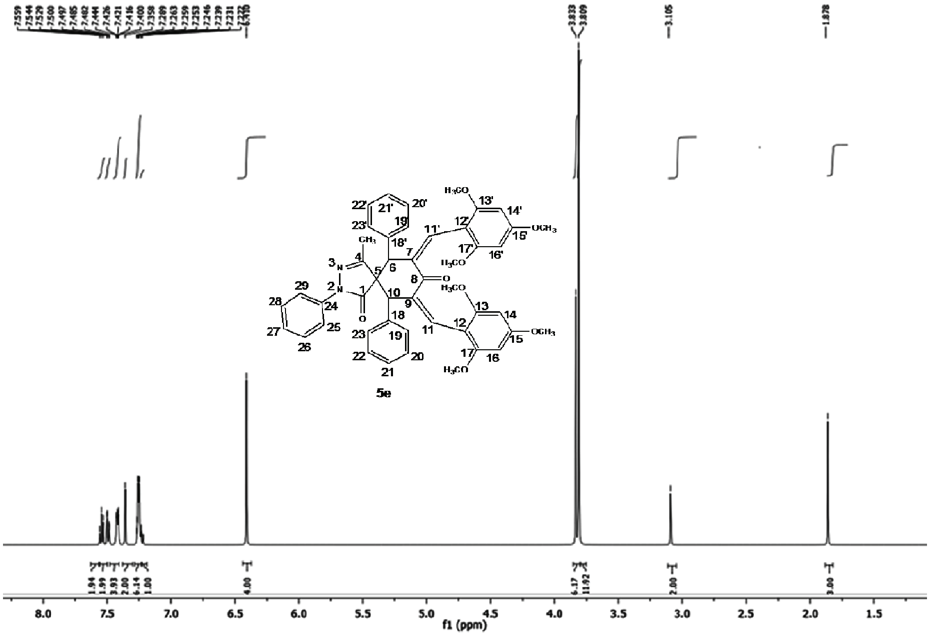

Figure S-21. ^{1}H NMR spectrum of 4-methyl-2,6,10-triphenyl-7,9-bis-(2,4,6-trimethoxy-
-benzylidene)-2,3-diazaspiro[4.5]dec-3-ene-1,8-dione (**5e**) ($CDCl_3$, 400 MHz).

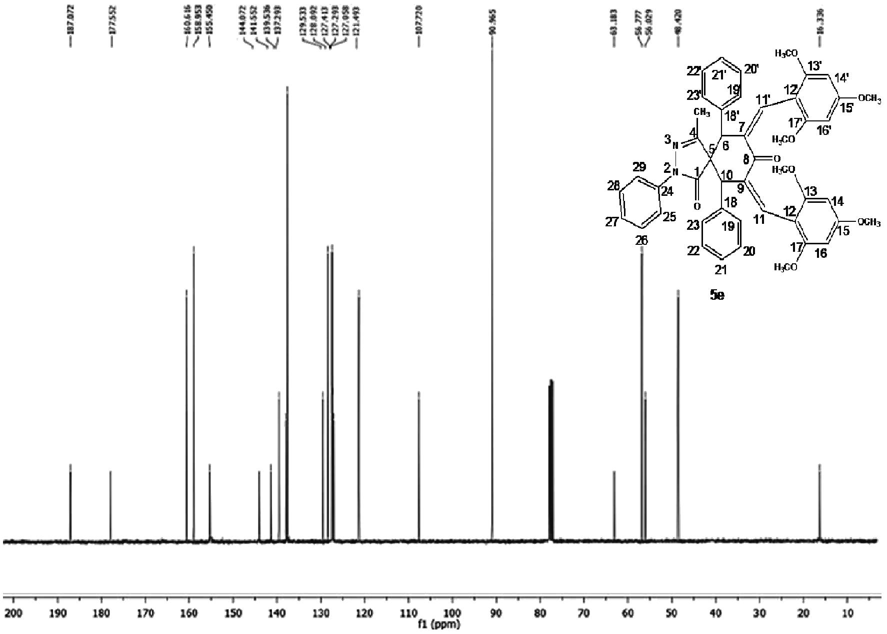

Figure S-22. ^{13}C NMR spectrum of 4-methyl-2,6,10-triphenyl-7,9-bis-(2,4,6-trimethoxy-benzylidene)-2,3-diazaspiro[4.5]dec-3-ene-1,8-dione (**5e**) ($CDCl_3$, 100 MHz).

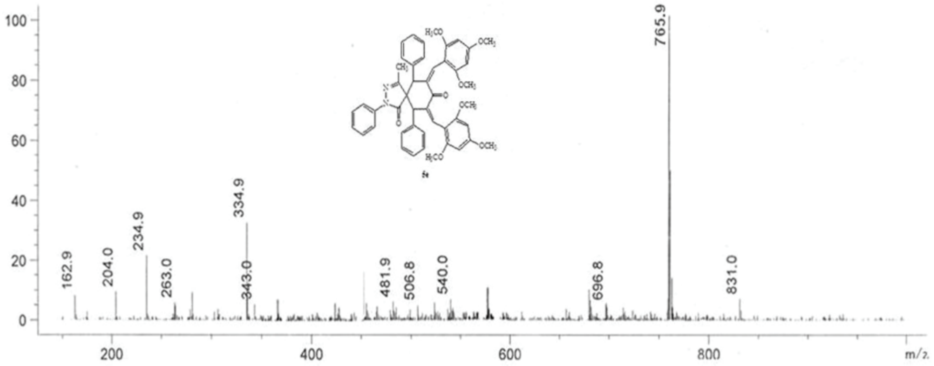

Figure S-23. Mass spectrum of 4-methyl-2,6,10-triphenyl-7,9-bis-(2,4,6-trimethoxy--benzylidene)-2,3-diazaspiro[4.5]dec-3-ene-1,8-dione (**5e**).

*7,9-Bis-(4-hydroxy-benzylidene)-4-methyl-2,6,10-triphenyl-2,3-diazaspiro [4.5]dec-3-ene-1,8-dione(**5f**).* Reddish brown solid. Yield: 425 mg, 69 % (Conventional) and 493 mg, 80 % (MW). m.p.: 104-106 °C, IR (ν_{max}/cm^{-1}):3608, 1751, 1696, 1560, 1505. ^{1}H NMR (400 MHz, CDCl$_3$, δ): 2.02 (s, 3H, CH$_3$), 3.05 (s, 2H, 2xCH, H-6 & H-10), 6.86 (d, 4H, *J*=8.0 Hz, H-14,16,14',16'), 7.21-7.24 (m, 1H, H-27),7.25 (s,2H,2x =CH, H-11&H-11'), 7.26-7.29(m, 6H, H-20,21, 22,20',21', 22'), 7.35(d, 4H, *J*=8.0 Hz, H-13,17,13',17'), 7.40-7.44 (m, 4H, H-19,23,19',23'), 7.47 (dd, 2H, *J*= 4.0 Hz, 1.2Hz, H-25 & H-29), 7.52-7.55 (m, 2H, H-26 &28), 9.59 (bs, 2H, 2xOH). ^{13}C NMR (100 MHz, CDCl$_3$, δ): 187.04, 177.54, 155.26, 145.36, 141.12, 140.43, 137.97, 137.55, 130.65, 129.53, 128.45, 127.41, 127.34, 126.57, 121.29, 116.11, 63.51, 48.95, 16.42. Combustion analysis for $C_{41}H_{32}N_2O_4$: Calculated. C 79.85, H 5.23, N 4.54; found. C 79.81, H 5.2, N 4.51. (+) LCMS (*m*/*z*): calculated for [$C_{41}H_{32}N_2O_4$ + H]$^+$ 616.7, observed 617.2.

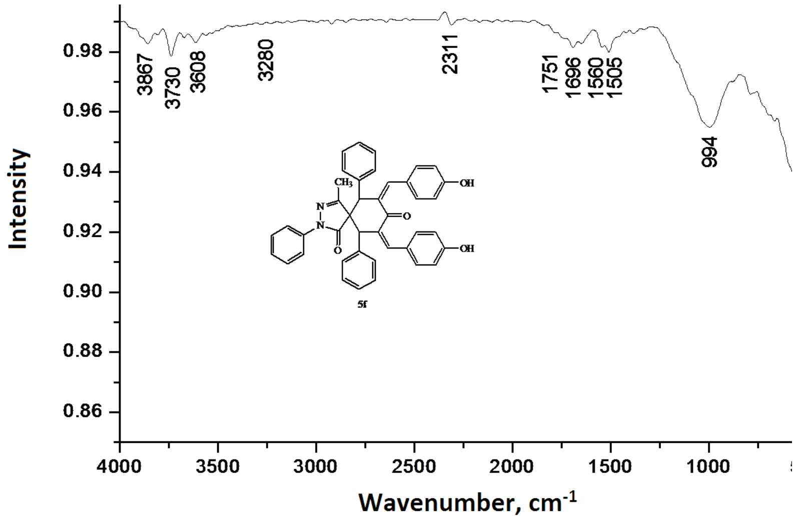

Figure S-24. IR spectrum of 7,9-bis-(4-hydroxy-benzylidene)-4-methyl-2,6,10-triphenyl-2,3--diazaspiro[4.5]dec-3-ene-1,8-dione (**5f**).

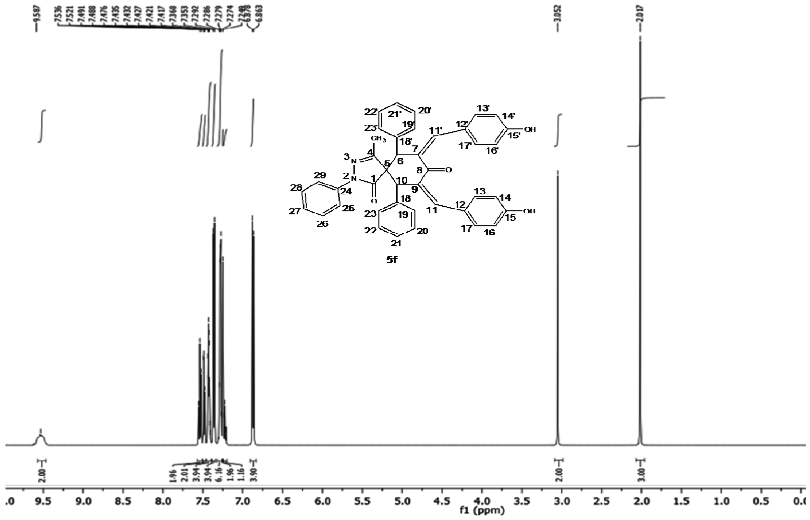

Figure S-25. ^{1}H NMR spectrum of 7,9-bis-(4-hydroxy-benzylidene)-4-methyl-2,6,10--triphenyl-2,3-diazaspiro[4.5]dec-3-ene-1,8-dione (**5f**) ($CDCl_3$, 400 MHz).

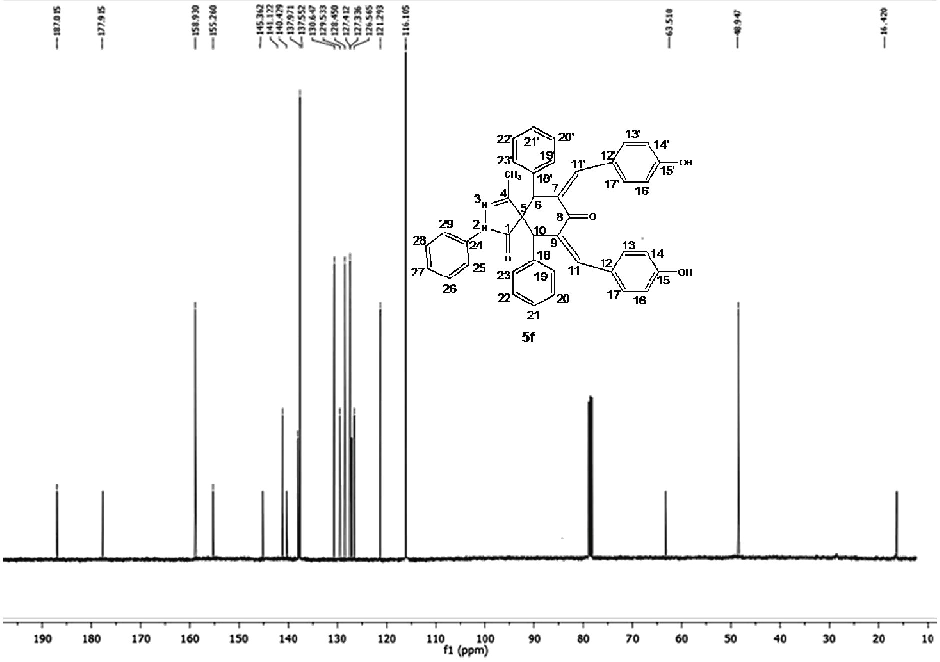

Figure S-26. ^{13}C NMR spectrum of 7,9-bis-(4-hydroxy-benzylidene)-4-methyl-2,6,10--triphenyl-2,3-diazaspiro[4.5]dec-3-ene-1,8-dione (**5f**) ($CDCl_3$, 100 MHz).

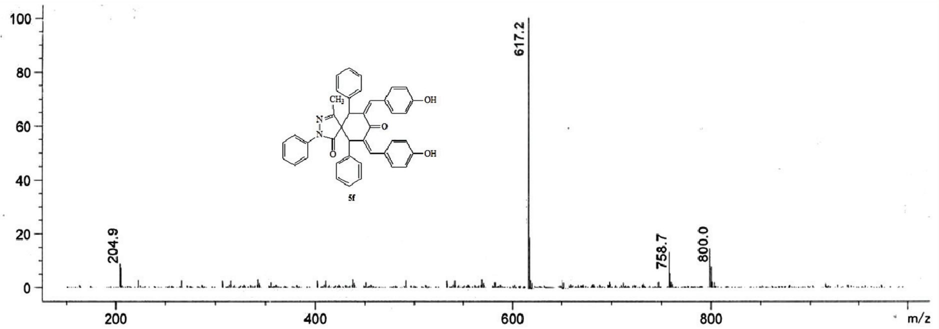

Figure S-27. Mass spectrum of 7,9bBis-(4-hydroxy-benzylidene)-4-methyl-2,6,10-triphenyl--2,3-diazaspiro[4.5]dec-3-ene-1,8-dione (**5f**).

TABLE S-I. Bond length and bond angle of compound 3 after Optimization using DFT

Parameters	Bond length, Å	Parameters	Bond angle, °
N1-N2	1.4034	A (2,1,5)	108.907
N1-C5	1.2876	A (1,2,3)	111.9807
N2-C3	1.3782	A (1,2,13)	118.6363
N2-C13	1.4202	A (3,2,13)	129.3763
C3-C4	1.537	A (2,3,4)	106.2208
C3-O12	1.2264	A (2,3,12)	127.7026
C4-C5	1.5158	A (4,3,12)	126.0575
C4-C6	1.5877	A (3,4,5)	99.9198
C4-C10	1.5842	A (3,4,6)	111.219
C5-C11	1.495	A (5,4,6)	110.2337
C6-C7	1.5429	A (5,4,10)	116.6476
C6-C14	1.525	A (6,4,10)	110.582
C6-H32	1.0966	A (1,5,4)	112.8982
C7-C8	1.5193	A (1,5,11)	120.0156
C7-H33	1.0933	A (4,5,11)	127.0484
C7-H34	1.0978	A (4,6,7)	110.9684
C8-C9	1.5236	A (4,6,14)	114.5591
C8-O16	1.2175	A (4,6,32)	105.0213
C9-C10	1.5393	A (7,6,14)	113.1489
C9-H35	1.0991	A (7,6,32)	106.4349
C9-H36	1.0935	A (14,6,32)	105.8892
C10-C15	1.5267	A (6,7,8)	110.6872
C10-H37	1.0972	A (6,7,33)	111.0992
C11-H38	1.0958	A (6,7,34)	110.6249
C11-H39	1.0921	A (8,7,33)	108.6975
C11-H40	1.0944	A (8,7,34)	108.3323
C13-C27	1.404	A (33,7,34)	107.286
C13-C31	1.4049	A (7,8,9)	115.0769
C14-C17	1.4029	A (7,8,16)	122.7311
C14-C21	1.4045	A (9,8,16)	122.1899

Parameters	Bond length, Å	Parameters	Bond angle, º
C15-C22	1.4029	A (8,9,10)	111.1029
C15-C26	1.4052	A (8,9,35)	107.5767
C17-C18	1.397	A (8,9,36)	108.264
C17-H41	1.0871	A (10,9,35)	112.0241
C18-C19	1.3962	A (10,9,36)	111.0201
C18-H42	1.0862	A (35,9,36)	106.6448
C19-C20	1.3973	A (4,10,9)	112.2182
C19-H43	1.086	A (4,10,15)	113.7583
C20-C21	1.3965	A (4,10,37)	103.3626
C20-H44	1.0861	A (9,10,15)	114.1925
C21-H45	1.0846	A (9,10,37)	106.1228
C22-C23	1.3981	A (15,10,37)	106.0509
C22-H46	1.0858	A (5,11,38)	111.6091
C23-C24	1.396	A (5,11,39)	109.4596
C23-H47	1.0863	A (5,11,40)	111.0081
C24-C25	1.3974	A (38,11,39)	108.6075
C24-H48	1.086	A (38,11,40)	107.4932
C25-C26	1.3958	A (39,11,40)	108.5749
C25-H49	1.0861	A (2,13,27)	119.172
C26-H50	1.0865	A (2,13,31)	120.876
C27-C28	1.3944	A (27,13,31)	119.9518
C27-H51	1.0818	A (6,14,17)	119.5823
C28-C29	1.3974	A (6,14,21)	122.2029
C28-H52	1.0862	A (17,14,21)	118.1997
C29-C30	1.3964	A (10,15,22)	122.6511
C29-H53	1.0858	A (10,15,26)	119.3265
C30-C31	1.3963	A (22,15,26)	118.0131
C30-H54	1.0863	A (14,17,18)	121.2142
C31-H55	1.0809	A (14,17,41)	119.5772
		A (18,17,41)	119.2071
		A (17,18,19)	119.9803
		A (17,18,42)	119.7536
		A (19,18,42)	120.2656
		A (18,19,20)	119.4519
		A (18,19,43)	120.2837
		A (20,19,43)	120.2641
		A (19,20,21)	120.4235
		A (19,20,44)	120.1077
		A (21,20,44)	119.4688
		A (14,21,20)	120.728
		A (14,21,45)	120.0704
		A (20,21,45)	119.1973
		A (15,22,23)	121.0508
		A (15,22,46)	120.2589
		A (23,22,46)	118.6841

Parameters	Bond length, Å	Parameters	Bond angle, °
		A (22,23,24)	120.248
		A (22,23,47)	119.5832
		A (24,23,47)	120.168
		A (23,24,25)	119.3597
		A (23,24,48)	120.3056
		A (25,24,48)	120.3314
		A (24,25,26)	120.223
		A (24,25,49)	120.1859
		A (26,25,49)	119.5889
		A (15,26,25)	121.0917
		A (15,26,50)	119.5846
		A (25,26,50)	119.3194
		A (13,27,28)	119.7234
		A (13,27,51)	119.5329
		A (28,27,51)	120.7436
		A (27,28,29)	120.7846
		A (27,28,52)	119.0485
		A (29,28,52)	120.1668
		A (28,29,30)	119.1113
		A (28,29,53)	120.4466
		A (30,29,53)	120.4422
		A (29,30,31)	121.0673
		A (29,30,54)	120.1087
		A (31,30,54)	118.8239
		A (13,31,30)	119.3616
		A (13,31,55)	119.9719
		A (30,31,55)	120.6665

TABLE S-II. Bond length and bond angle of compound 5b after optimization using DFT

Parameters	Bond length, Å	Parameters	Bond angle, °
N1-N2	1.4032	A (2,1,5)	108.7814
N1-C5	1.2874	A (1,2,3)	112.0698
N2-C3	1.3801	A (1,2,13)	118.581
N2-C13	1.4222	A (3,2,13)	129.2761
C3-C4	1.538	A (2,3,4)	105.8661
C3-O12	1.2254	A (2,3,12)	127.6833
C4-C5	1.5125	A (4,3,12)	126.3661
C4-C6	1.5714	A (3,4,5)	100.0674
C4-C10	1.6059	A (3,4,6)	116.8856
C5-C11	1.4955	A (3,4,10)	103.9681
C6-C7	1.527	A (5,4,6)	110.69
C6-C14	1.5309	A (5,4,10)	116.1912
C6-H32	1.1008	A (6,4,10)	108.9623
C7-C8	1.501	A (1,5,4)	112.9752
C7-C53	1.3501	A (1,5,11)	120.5944

Parameters	Bond length, Å	Parameters	Bond angle, °
C8-C9	1.5185	A (4,5,11)	126.2983
C8-O16	1.2245	A (4,6,7)	112.0152
C9-C10	1.5278	A (4,6,14)	119.2836
C9-C52	1.35	A (4,6,32)	101.1835
C10-C15	1.5235	A (7,6,14)	116.4093
C10-H33	1.0983	A (7,6,32)	101.5681
C11-H34	1.0969	A (14,6,32)	102.6732
C11-H35	1.0921	A (6,7,8)	110.0794
C11-H36	1.0949	A (6,7,53)	133.0574
C13-C27	1.4038	A (8,7,53)	116.5527
C13-C31	1.4046	A (7,8,9)	114.7374
C14-C17	1.407	A (7,8,16)	123.1589
C14-C21	1.3995	A (9,8,16)	122.0901
C15-C22	1.403	A (8,9,10)	111.5635
C15-C26	1.4045	A (8,9,52)	114.9494
C17-C18	1.3933	A (10,9,52)	133.2194
C17-H37	1.0874	A (4,10,9)	112.304
C18-C19	1.3987	A (4,10,15)	113.1059
C18-H38	1.0861	A (4,10,33)	100.4324
C19-C20	1.3935	A (9,10,15)	119.6461
C19-H39	1.0858	A (9,10,33)	103.5288
C20-C21	1.3997	A (15,10,33)	105.0397
C20-H40	1.086	A (5,11,34)	110.5294
C21-H41	1.0819	A (5,11,35)	109.7297
C22-C23	1.3957	A (5,11,36)	111.7205
C22-H42	1.0833	A (34,11,35)	108.1118
C23-C24	1.397	A (34,11,36)	107.2061
C23-H43	1.086	A (35,11,36)	109.4457
C24-C25	1.3963	A (2,13,27)	119.1241
C24-H44	1.0859	A (2,13,31)	120.8388
C2-C26	1.397	A (27,13,31)	120.0366
C25-H45	1.0861	A (6,14,17)	116.3387
C26-H46	1.0868	A (6,14,21)	125.7841
C27-C28	1.3945	A (17,14,21)	117.8156
C27-H47	1.0818	A (10,15,22)	123.9801
C28-C29	1.3973	A (10,15,26)	117.989
C28-H48	1.0861	A (22,15,26)	118.0046
C29-C30	1.3963	A (14,17,18)	121.4329
C29-H49	1.0857	A (14,17,37)	119.335
C30-C31	1.3963	A (18,17,37)	119.2305
C30-H50	1.0861	A (17,18,19)	120.0581
C31-H51	1.0809	A (17,18,38)	119.6995
C52-C54	1.4798	A (19,18,38)	120.2415
C52-H78	1.0916	A (18,19,20)	119.1928
C53-C64	1.4694	A (18,19,39)	120.3875

Parameters	Bond length, Å	Parameters	Bond angle, °
C53-H79	1.0907	A (20,19,39)	120.4194
C54-C55	1.4071	A (19,20,21)	120.5448
C54-C56	1.4051	A (19,20,40)	120.2345
C55-C57	1.3913	A (21,20,40)	119.2204
C55-H58	1.0864	A (14,21,20)	120.9482
C56-C59	1.3912	A (14,21,41)	121.2696
C56-H60	1.0839	A (20,21,41)	117.7814
C57-C61	1.4059	A (15,22,23)	120.9784
C57-H62	1.0849	A (15,22,42)	120.4495
C59-C61	1.4052	A (23,22,42)	118.5619
C59-H63	1.0847	A (22,23,24)	120.3509
C61-C74	1.4348	A (22,23,43)	119.5321
C64-C65	1.4098	A (24,23,43)	120.116
C64-C66	1.4063	A (23,24,25)	119.4142
C65-C67	1.3893	A (23,24,44)	120.2394
C65-H68	1.0865	A (24,25,26)	120.0172
C66-C69	1.3916	A (24,25,45)	120.2959
C66-H70	1.0835	A (26,25,45)	119.6834
C67-C71	1.4067	A (15,26,25)	121.2324
C67-H72	1.0848	A (15,26,46)	119.3911
C69-C71	1.4054	A (25,26,46)	119.3721
C69-H73	1.0849	A (13,27,28)	119.6648
C71-C75	1.4346	A (13,27,47)	119.6188
C74-N76	1.1641	A (28,27,47)	120.7162
C75-N77	1.1643	A (27,28,29)	120.7765
		A (27,28,48)	119.0551
		A (29,28,48)	120.1683
		A (28,29,30)	119.158
		A (28,29,49)	120.4237
		A (30,29,49)	120.4183
		A (29,30,31)	121.0361
		A (29,30,50)	120.1218
		A (31,30,50)	118.842
		A (13,31,30)	119.3279
		A (13,31,30)	119.3279
		A (13,31,51)	120.0464
		A (30,31,51)	120.6257
		A (9,52,54)	133.5168
		A (9,52,78)	113.1699
		A (54,52,78)	113.2648
		A (7,53,64)	132.4845
		A (7,53,79)	113.4806
		A (64,53,79)	114.0253
		A (52,54,55)	119.2816
		A (52,54,56)	121.8042

Parameters	Bond length, Å	Parameters	Bond angle, °
		A (55,54,56)	118.566
		A (54,55,57)	121.0637
		A (54,55,58)	119.5439
		A (57,55,58)	119.3916
		A (54,56,59)	120.8575
		A (54,56,60)	119.6222
		A (59,56,60)	119.5198
		A (55,57,61)	119.7622
		A (55,57,62)	120.4638
		A (61,57,62)	119.7697
		A (56,59,61)	120.0456
		A (56,59,63)	120.2196
		A (61,59,63)	119.7339
		A (57,61,59)	119.659
		A (57,61,74)	120.1163
		A (59,61,74)	120.2233
		A (53,64,65)	118.0672
		A (53,64,66)	123.2136
		A (65,64,66)	118.6022
		A (64,65,67)	121.1653
		A (64,65,68)	119.381
		A (67,65,68)	119.4469
		A (64,66,69)	120.5948
		A (64,66,70)	119.7266
		A (69,66,70)	119.6186
		A (65,67,71)	119.6505
		A (65,67,72)	120.5281
		A (71,67,72)	119.8191
		A (66,69,71)	120.2362
		A (66,69,73)	120.1135
		A (71,69,73)	119.649
		A (67,71,69)	119.6896
		A (67,71,75)	120.1196
		A (69,71,75)	120.1859

Journal of the Serbian Chemical Society
JSCS-info@shd.org.rs • www.shd.org.rs/JSCS

J. Serb. Chem. Soc. *87* (7–8) 829–843 (2022)
JSCS–5560

Original scientific paper
Published 28 April 2022

Aspirin–hydrogel ocular film for topical delivery and ophthalmic anti-inflammation

ASHIRBAD NANDA[1,2], SHUBHASHREE DAS[2], RUDRA N. SAHOO[1,2], SOUVIK NANDI[1], RAKESH SWAIN[1], SUNIL PATTANAIK[1], DEBAJYOTI DAS[1] and SUBRATA MALLICK[1]*

[1]*School of Pharmaceutical Sciences, Siksha 'O' Anusandhan (Deemed to be University), Bhubaneswar, Odisha, 751003, India and* [2]*Centurion University of Technology and Management, Odisha, India*

(Received 4 May, revised 24 December 2021, accepted 28 February 2022)

Abstract: Ocular drug delivery in hydrogel forming film form has several benefits over conventional dosage forms. An ophthalmic anti-inflammation study was undertaken using topically applied aspirin in a hydrogel film formulation. A hydroxypropyl methylcellulose (HPMC) matrix film formulation was prepared by the solvent casting and evaporation technique by taking triethanolamine (TEA) as a plasticizer. *Ex vivo* corneal permeation as well as anti-inflammatory potential of aspirin was studied on carrageenan induced rabbit eye model. Moisture uptake was found to be in the range of 17.1 and 19.1 % for all the film formulations. The film with the higher HPMC content exhibited both increased moisture uptake and amount of swelling. Among the formulations, the swelling order was found to increase with increasing amount of HPMC in the film. Presence of the hydrogel matrix forming polymer sustained the drug release and corneal permeation for more than 6 h and controlled the process by the diffusion mechanism. The signs of carrageenan induced acute inflammation was inhibited completely within just 2 h of placing the film in the rabbit eye whilst the positive control continued showing redness and increased tear secretion. Aspirin ocular film formulation could be utilized for ocular anti-inflammation for an extended period of time with better patient compliance.

Keywords: non-steroidal anti-inflammatory drug; ocular delivery; HPMC; swelling and erosion.

INTRODUCTION

Hydrogel-based formulations for ocular drug delivery have several benefits over conventional dosage forms, *i.e.*, enhanced probability of delivering drugs at a slow and uniform flow, improved ocular residence time and proper dosing.[1]

---

* Corresponding author. E-mail: profsmallick@gmail.com; subratamallick@soa.ac.in
https://doi.org/10.2298/JSC210504019N

This will also ensure better patient compliance due to the reduced frequency of administration and lowering incidence of side-effects. This ocular film would be retained in the cul-de-sac of the eye for an extended period of time. Thus, a small piece of film will stay in the patient's eye without any kind of discomfort.[2] Acetylsalicylic acid (aspirin), a nonsteroidal anti-inflammatory drug (NSAID) is used as an anti-rheumatic, antipyretic, and anti-thrombotic drug.[3–5] Anti-inflammatory activity on the corneal surface may be possible due to aspirin or its metabolites secretion in the tear fluid in low dose aspirin users of cardiac patients.[4] Cardiac subjects taking 100 mg aspirin orally for antiaggregant purposes have faced less dry eye syndrome without interfering with the tear flow. Internal bleeding, gastrointestinal inflammation, and ulcer are the main dose-dependent adverse effects caused by oral administration of aspirin. The therapeutic drug levels may be obtained in the anterior and posterior segment of the eye by a topical film-type delivery system avoiding systemic distribution and related side effects.[6] Retinal bioavailability of aspirin may not be sufficient after oral administration due to blood eye and blood-retinal barriers.[7] Therefore, an option was developed for topically applied film formulation with increased ocular residence time.[8] Delivery of medication to the human eye is an integral part of medical treatment. Conventional ocular dosage forms, *i.e.*, eye drops and eye ointments, have certain disadvantages such as poor availability, repeated administration and irregular doses and drug loss due to nasolacrimal drainage.[9] Reducing the volume of dose could moderately develop some local action and diminish side effects. As a solid film formulation, this could be one improvement step for ophthalmic delivery of drugs.[10] Ocular bioavailability could be significantly improved by extending residence time in the cul-de-sac rather than losing most of the drug in nasolacrimal drainage. Currently, hydrophilic soft gels are attracting a lot of attention in ophthalmic drug delivery systems.[11] These provide a uniform store of the drug at the place of administration after being exposed to the watery biological fluid. The solid matrix hydrogel swells and produces a transparent viscous gel layer, facilitating distribution of drug in a controlled process.[12] *In situ* gel loaded with a hydrogel forming agent may be a potential tool for improving the bioavailability by extending the ocular residence time.[13] In ophthalmic drug delivery systems, mucoadhesive biodegradable polymer can adhere to the conjunctival mucosa for an extended period of time and the drug releases *via* erosion from the place of its administration.[14] HPMC is drawing considerable attention in the field of controlled release drug delivery systems for the formation of a hydrogel in the presence of water and is popularly employed in mucoadhesive ocular drug delivery.[15,16] The present work was undertaken for the development of ocular mucoadhesive hydrogel film by embedding the drug in an HPMC matrix. HPMC is reported to show cytoprotection against thimerosal induced DNA damage in Chang conjunctival cells.[17] Moreover, HPMC is able to provide protection to aspirin from hydrolytic degradation.[18,19] Aspirin in the presence of HPMC K100 polymer has shown significant stability after 5 weeks of exposure to 40 °C and 75 % RH.[20] The ocular anti-inflammatory activity of aspirin has been investigated in the carrageenan induced rabbit eye model. Analytical characterizations were conducted in order to understand the drug excipient interaction and stability of the film formulation.

MATERIALS AND METHODS

Aspirin was obtained from Himedia Laboratory Pvt. Ltd., Nashik, India. Hydroxypropyl methylcellulose (HPMCK100M: 100,000 cPs) was locally purchased from Burgoyne and Co (Mumbai, India) and triethanolamine (TEA) was procured from Merck Pvt. Ltd. (Mumbai, India).

Animal

Male New Zealand rabbits of 1.5–2.0 kg and albino rats of 150–250 g were obtained from the institutional animal house for *in vivo* and histological study. All the animals and handling protocols were reviewed and approved by the animal ethical committee of the institute. The animals were approved by CPCSEA of SOADU (IAEC/SPS/SOA/04/2019) before starting the study.

Aspirin film formulation

Aspirin films (Table I) were prepared by the casting and solvent evaporation method. HPMC was weighed and sprinkled in about 40 ml of water contained in a 100 ml beaker. The beaker was then placed in the refrigerator below 10 °C for 2 days for complete swelling. Accurate amount of triethanolamine (plasticizer) was added to HPMC swelled gel with continuous stirring for 24 h at laboratory ambient condition.[21] Aspirin (200 mg) solution was prepared in another 100 ml beaker with a small amount of ethanol (10 ml), and HPMC swelled gel was added over it with continuous stirring for 12 h (Table I). The transparent polymeric mass was spread onto the petri dish uniformly (casting) and placed in the hot air oven at 40 °C until constant weight of prepared film was obtained. Prepared films were separated from the Petri dish and packed in the zip lock Tarson pouch and preserved in a wide mouth airtight plastic container until further studies.

TABLE I. Aspirin film formulations and physicochemical characteristics for ocular delivery

Film code	$m_{\text{HPMC 100K}}$[a] / mg	Triethanolamine[b] / mg	Thickness[c] / μm	Moisture content[c] / %	Moisture uptake[c], % *RH* / %			Surface pH	Assay value[c], %
					65	74	85		
AH1	900	135 (15 %)	210±8.3	8.42±0.92	14.5±0.15	17.10±1.61	18.3±0.2	7.4	16.02±0.24
AH2	1000	120 (12 %)	231±5.5	10.97±0.88	14.51±0.08	17.47±1.25	18.5±0.15	7.5	14.98±0.19
AH3	1100	100 (9 %)	244±3.3	11.94±1.13	16.8±0.1	18.80±1.29	19.7±0.2	7.3	14.04±0.28
AH4	1200	110 (9.17 %)	260±5.1	11.99±1.16	18.8±0.05	19.14±0.80	20.4±0.2	7.6	12.75±0.42

[a]Hydrogel forming agent; [b]plasticizer, aspirin was given 200 mg for each of the formulations, value in brackets represents the amount of triethanolamine based on the HPMC content; [c]mean±*SD*, *n* = 3

Physicochemical characteristics

The thickness measurement of the film formulations was realized utilizing a Mitutoyo digital micrometer (Japan). Random 10 cut portions of the film were measured and the average values were recorded.[18,22] Folding endurance of the film formulations was determined by continually folding a 2 cm×2 cm of the formulated film at a particular portion. This action was continued until the film broke at the point of folding. The number of times the film could be folded was considered as the folding endurance value.[23] For moisture content determination, a cut piece of the prepared film was weighed and put into an airtight desiccator containing activated silica gel. The film was then removed after 24 h or until it reached to constant weight. The difference between the initial and final weight gave the moisture content. For the determination of moisture uptake, a preweighed cut piece of film was placed under 65, 74 and 85 % relative humidity (*RH*) by using saturated solutions of KCl, NaCl and $AlCl_3$, respectively. The film was then placed in a desiccator containing activated silica gel and weighed after it achieved a constant dry weight. The difference between the initial and final weight gave the moisture uptake at various relative humidity conditions. A small piece of the film was allowed to swell up for 2 h in distilled water under ambient laboratory condition for the determination of the surface pH. The surface pH was measured using pH meter by dipping the electrode into the swollen mass of the film.[24] Three observations were recorded for each formulation to calculate the mean value. The assay of aspirin was performed by taking a preweighed cut piece of film and dissolving it in water by continuous stirring and gentle boiling with the addition of 1 M HCl.[25] After hydrolysis, salicylic acid was produced that forms violet-blue complexes with Fe^{3+}. The intensity of the colour depends on the salicylic acid concentration in a sample. Ferric nitrate (Fe^{3+}) was added for colour development and then the salicylic acid content was determined by UV–Vis spectroscopy, at 561 nm (Jasco, V-630 spectrophotometer).[26-29]

Swelling behaviour of the films

The swelling properties were estimated after determining the percent swelling and erosion of the film formulations. The swelling profile of the formulations (≈1 cm×1 cm) was evaluated by placing them in Petri dishes with approximately 40 ml of phosphate buffer (pH 6.8).[22] The excess water in the Petri dish was removed after careful swabbing with tissue paper without disturbing the swollen film and the weight gain by the film was measured at different time intervals.[30] The dry weight of the swollen film was determined after drying at 60 °C overnight in a hot air oven and preserved in a desecrator for a furtherr 24 h. The swelling rate (K_s) was determined from the slope of the initial linear region of percentage swelling *vs*. time plot:[31]

$$\text{Swelling}=100\frac{\text{Weight of swollen mass}\ -\ \text{Dry weight before swelling}}{\text{Dry weight of film before swelling}} \tag{1}$$

$$\text{Matrix erosion}=100\frac{\text{Dry weight of film}\ -\ \text{Dried weight after swelling}}{\text{Dry weight of film before swelling}} \tag{2}$$

Scanning electron microscopy (SEM)

SEM was performed to study the morphology of the film formulation. Pieces of the film formulations were examined at various magnifications to observe the surface morphology using a scanning electron microscope (JEOL, JSM-6510).

Fourier transform infrared (FTIR) spectroscopy

Powder sample of the drug and formulations were estimated with Bruker FTIR spectrophotometer. The samples were placed on the attenuated total reflectance (ATR) with ZnSe (zinc selenide) crystals and pressed using the integrated pressure application device.

X-Ray diffractometry

The of X-ray diffraction patterns of the crystalline aspirin, film formulations and a placebo film were measured using an X-ray diffractometer (Rigaku, Ultima IV) applying 40 kV voltage and 15 mA current. CuKα (radiation 1.5406 Å) was used as the source of X-rays anode material and the diffraction was measured at a scan speed of 1° per min for 2θ 5–70°.

Differential scanning calorimetry (DSC)

DSC data of aspirin, matrix films and placebo films was obtainrd using a differential scanning calorimeter (Mettler Toledo; DSC 1, Switzerland) in the temperature range from 30 to 300 °C to understand the drug excipient interaction. Aspirin and film sample were taken in aluminium crucible and examined under a dynamic nitrogen atmosphere (50 mL min^{-1}) at a heating rate of 10 °C min^{-1}.

In vitro *dissolution of the drug*

In vitro dissolution of aspirin from the films was performed in a USP type II dissolution apparatus (Electolab, TDT06L, India) utilizing 200 mL phosphate buffer (pH 6.8) as the dissolution medium at 34.0±0.2 °C and 50 rpm for 6 h.[18,31-33] A piece of film, weighing between 55–72 mg, was cut and attached to a glass slide using cyanoacrylate glue and carefully placed at the bottom of a vessel containing the dissolution medium. At different time intervals, 10 ml samples were withdrawn through a membrane filter (0.45 µm, syringe driven) and the same volume of fresh medium was placed in each vessel. The evaluation of the aspirin contents was then performed by UV–Vis spectroscopy at 561 nm following the above given method. Conversion factor of 1.3004 was used to estimate aspirin content from salicylic acid produced. The dissolution data of the film formulations were reported as the mean of minimum 3 determinations. The kinetics of drug release from the matrix film formulations were elucidated using different kinetic models such as the first order, Higuchi, Korsmeyer–Peppas and Peppas–Sahlin models.

The mathematical equations used for describing kinetics of drug release and corneal permeation were:[19]

First order:

$$\log C = \log C_0 + K_1 t/2.303 \tag{3}$$

Higuchi model:

$$C = K\sqrt{t} \tag{4}$$

where C_0 = initial drug content; C = cumulative amount of drug release/permeating per unit area of the film; K_1 = First order release rate constant; K = Higuchi release/permeation rate constant.

Korsmeyer–Peppas model (this power law model describes drug release from a polymeric matrix):

$$C_t/C_\infty = Ktn \tag{5}$$

where C_t/C_∞ = fraction of release/permeation of drug at time t; K = Peppas release/permeation rate constant; n = release/permeation exponent.

Peppas–Sahlin model:

$$M_t/M_\infty = k_1 t^m + k_2 t^{2m} \tag{4}$$

were M_t/M_∞ = Fraction dissolved, %; k_1 = the constant related to the Fickian kinetics; k_2 = the constant related to Case II relaxation kinetics; m = the diffusional exponent.

Ex vivo *corneal permeation*

The *ex vivo* corneal permeation study was performed using fresh, undamaged whole goat eyes, collected from a local slaughterhouse within one hour after sacrifice.[34] The whole eyes were washed in distilled water followed by rinsing with phosphate buffer (pH 6.8). About 5 to 6 mm sclera of the cornea were removed from the whole eye. Pieces of films weight ranging from 42.8–72 mg were employed at the centre of the cornea on the modified Franz diffusion apparatus and the diffusion of drug testing was performed for 6 h at 34±0.2 °C and 50 rpm in triplicate. The epithelium of the cornea was facing vertically tonthe donor compartment with an effective area of 1.4 cm^2 and 200 ml of phosphate buffer (pH 6.8) medium as the diffusion media taken in the receptor chamber. Samples were withdrawn from the receptor chamber at regular intervals using syringe driven membrane filter (0.45 μm). Absorbance data at 561 nm were obtained using a UV–Vis spectrophotometer.[31] The steady state flux (Jss) of the drug was measured from the slope of the linear regression line of the cumulative amount of drug in the receptor chamber (Q_f) *vs*. time plot.[35]

Effect of aspirin on ocular inflammation

The effect of aspirin on ocular inflammation was studied in rabbits. Food and water were made accessible to the animals *ad libitum*. Acute conjunctival inflammation was induced in the rabbit eye by injecting (Dispo Van 30 G, India) carrageenan (100 μl, 3 %) to the upper palpebral region.[18,36] Proparacaine hydrochloride ophthalmic solution USP (0.5 %) was used for anesthetizing rabbit eye prior to the injection. Signs of inflammation and redness were recognized 1 h after the injection. A small piece of film (AH4) was placed in the cul-de-sac region after sterilizing it by UV exposure[18,22] at a distance of 25 cm from the UV light source for 10 min just before the anti-inflammatory study (UV wavelength at 277 nm using Phillips TUV 30w, India) under ambient laboratory condition. Images were captured and all the signs and symptoms were visualized.

RESULTS AND DISCUSSION

Physicochemical characteristics of film formulations

The mean thickness and the standard deviation of the films were determined. The thickness of all the film formulations was found to be in the range of 210.0±8.3 to 260.0±5.1 μm. A gradually increased content of HPMC in the formulation increased the thickness of the film. The films have exhibited good folding-endurance (more than 200) showing sufficient strength and flexibility but not fragility.[18,22] Under ambient laboratory conditions, the moisture content of the film formulations ranged from 8.42 (AH1) to 12 % (AH4). The film formulations remained stable without being fully dried and fragile due to the presence of moisture in the films. The significant increase in moisture content was observed owing to the increased content of HPMC (P < 0.01). Among the films tested, AH1 and AH4 showed the minimum and maximum moisture uptake, *i.e.*, 17.097 and 19.139 %, respectively, at RH 74 %. The maximum moisture uptake was found in the film containing the highest concentration of HPMC, which readily absorbs moisture when exposed to the atmosphere. The pH of the film surface was found in the range as 7.4 to 7.6, which are assumed to give no irritation to the mucosal tissues. The film formulations and physical characteristics of aspirin film formulations are given in Table I.

Swelling and erosion study

Hydration and swelling behaviour followed by matrix erosion studies were performed for understanding drug residence time and drug release dynamics due to its great significance related to dose, dosage form and effect. When the hydrophilic polymeric (HPMC) matrix film comes in contact with water it begins to swell.[16] The erosion is accompanied with hydration and degradation of the hydrophilic matrix film. The hydration and swelling increased and the increase in hydration as the function of time was recognized from the swelling profile of the films (Fig. 1A). AH4 showed the highest percentage swelling (2216 %) than the other formulations owing to its high content of HPMC polymer. The order was: AH1 < AH2 < AH3 < AH4. In another report, the swelling of hydrogel transdermal films were found to be about 2000 % after 13 h.[37] All the film formulations were almost transparent and the writing background was clearly seen through the film (Fig. 1C). AH4 exhibited least erosion (13.7 %) among the film formulations owing to the presence of high content of polymer (Fig. 1B).

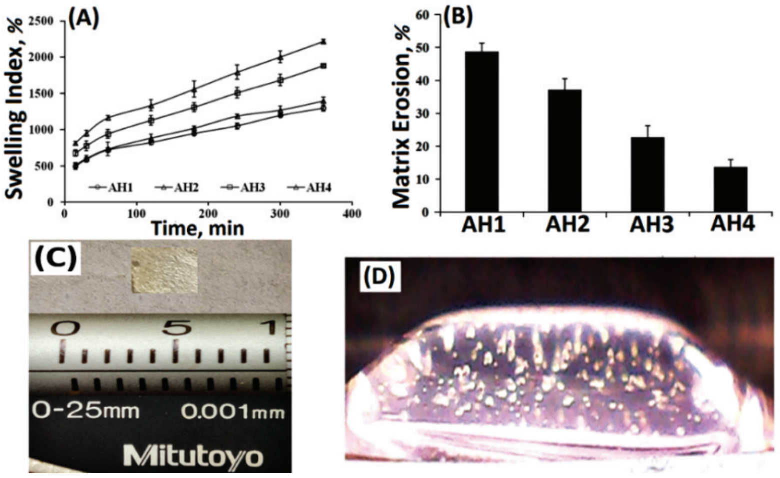

Fig. 1. A) Swelling behaviour of aspirin film formulation; B) matrix erosion of the film formulations after 6 h; C) digital image of films before swelling; D) after swelling.

Scanning electron microscopy

Scanning electron microscopy was used for examining crystal morphology of aspirin and the surface morphology of aspirin containing film formulations (Fig. 2). Distinctive geometric crystals (brick-shaped) with or without twinning was observed in the photomicrographs of pure aspirin (1000×).[38,39] On the other hand, the crystal geometry disappeared in the photomicrographs of the films. The smooth and non-porous surface of the film formulations confirmed the almost homogenous mixing and uniform distribution of the drug. Uniform solubility of aspirin in the HPMC matrix of the films was probably due to the drug amorphization decreasing the crystalline intensity.

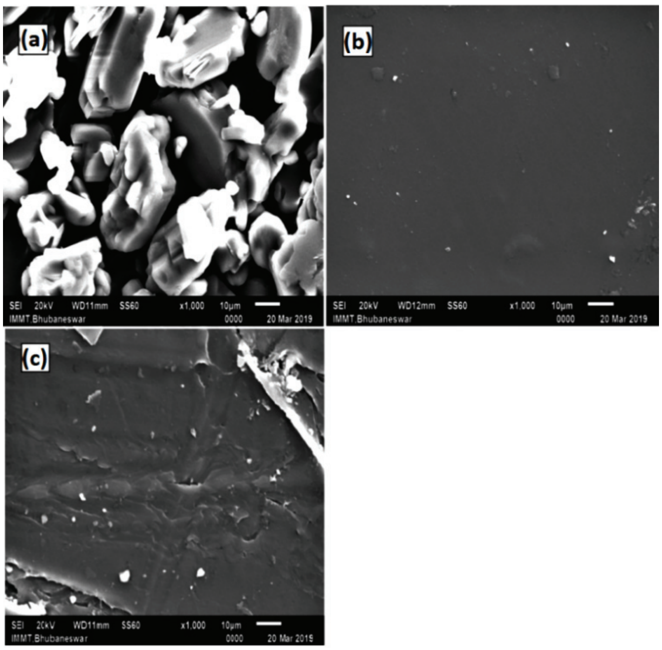

Fig. 2. Scanning electron micrographs of: a) crystalline aspirin; b) AH1; c) AH4.

Fourier transformation infrared spectroscopy

The Fourier transform infrared spectra of aspirin and the formulations are shown in Fig. 3A.

Aspirin exhibits characteristic peaks due to the presence of benzene ring, carboxylic acid and ester groups. The bands in between 2800 to 3000 cm^{-1} (narrow absorptions) represents the interactions with C–H bonds (O–H stretch from CO–OH vibration). The peak at 1678 cm^{-1} is due to stretching of carbonyl groups (C=O), C=O stretch at 1750 cm^{-1} indicates the presence of ester groups.[40] All formulations showed decreased intensity of the peak and a shifting of the broad band in the spectral region 4000–3000 cm^{-1} of O–H stretching vibrations was observed. This was again due to the intramolecular hydrogen bonding between the polymer and the drug, which confirms the drug is completely incorporated within the polymeric matrix.

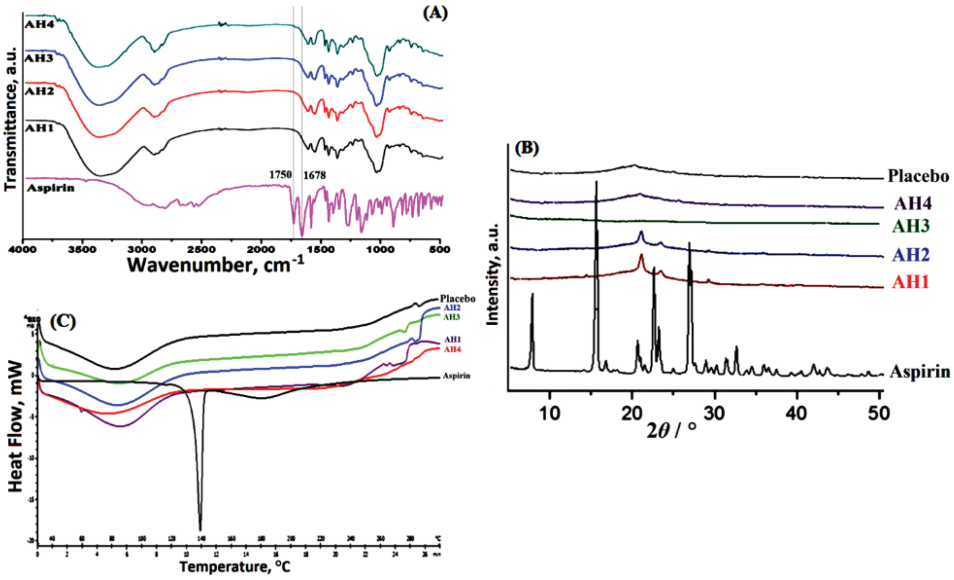

Fig. 3. A) FTIR spectra of aspirin and the film formulations; B) XRD patterns of aspirin and the film formulations; C) DSC thermograms of aspirin and the film formulations.

X-ray diffractometry

The powder X-ray diffraction patterns of pure aspirin and the films are presented in Fig. 3B. The diffractogram of aspirin showed a series of intense peaks at 2θ of 15, 20, 23 and 27° indicating its own crystalline pattern.[41] These characteristic peaks were not observed in the diffraction patterns of the AH1, AH2, AH3 and AH4 films. This result indicated the occurrence of a true drug–polymer solid solution and the amorphization of aspirin to a great extent in the films was confirmed. It is understood that a major part of the drug exists as a solid-solid solution in the HPMC matrix, and a minor part is probably present in the semi-crystalline or microcrystalline form. The HPMC polymers formed solid solutions with the drug by forming an amorphous polymeric network. HPMC film plasticized by triethanolamine also offered a considerable performance in the significant inhibition of drug crystal growth. HPMC as the matrix polymer inhibited crystal growth the drug in the film.[18,19] This is the very reason that greater HPMC amorphized the drug relatively more in the respective film formulation containing increased amount of HPMC. Accordingly, the XRD peaks are relatively more intense in AH1 and AH2 compared to AH3 and AH4.

Differential scanning calorimetry

The results of thermal analysis of pure aspirin and the formulations by DSC are shown in Fig. 3C. Aspirin showed a characteristic sharp melting endothermic peak at 138.53 °C.[39] In the range of about 60–110 °C, the appearance of a broad endothermic signal may be an indication of moisture removal from the HPMC.[15,38] The absence of an endothermic peak observed with the film formulation indicating significant amorphization of aspirin.

In vitro *release of drug*

Drug release profiles of various formulations are shown in Fig. 4A. The aspirin-in-HPMC film formulation showed the sustained effect of release of aspirin. HPMC as the hydrophilic matrix polymer in the film formulation inhibited the crystal growth in general and maintained aspirin in the amorphous state.[18] The high viscosity grade of HPMC (K100M) extended the drug release in a controlled manner over a period of 6 h. The percent release of drug from film AH1, AH2, AH3 and AH4 was found to be 92.0, 83.75, 77.1 and 67.4 %, respectively, at the end of 6 h as shown in Fig. 4A. Formulation AH1 showed the highest (92.0 %), and formulation AH4 showed the lowest (67.4 %) drug release after 6 h due to the presence of HPMC in highest amount in the film and consequently, the highest percentage swelling (2216.5 %) rather than the other formulations. Maximum erosion of the formulation AH1 exhibited relatively the highest release of aspirin. With increasing content of HPMC, as the polymer matrix in the film formulation, the drug release was gradually sustained at 6 h ($P < 0.02$).

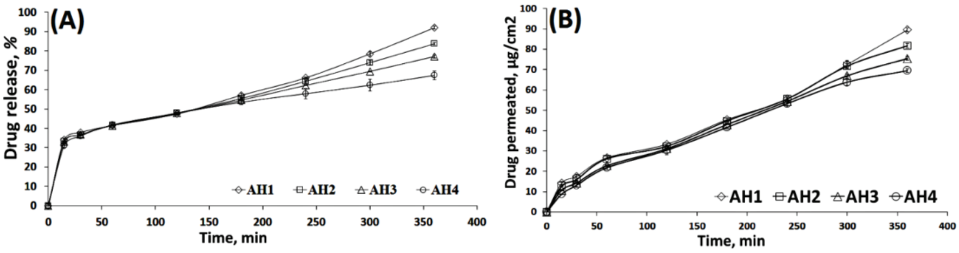

Fig. 4. A) *In-vitro* drug release profile of the film formulations; B) *ex-vivo* corneal permeation of the films.

Ex vivo *permeation study*

Ex vivo permeation profiles of aspirin through the corneal mucosa are shown in Fig. 4B. The amount of drug permeated for formulation AH1, AH2, AH3 and AH4 was found to be 89.59, 81.82, 75.48 and 69.51 % respectively. The amount of drug permeated after 6 h was highest in the case of AH1 relative to the other formulations.

The fact that AH4 showed the lowest amount of drug permeation after 6 h may be due to higher concentration of HPMC compared to the other formulations. Drug permeation was observed to be more sustained with the increasing content of HPMC in the film formulations, drug release was gradually sustained at 6 h ($P < 0.01$).

Korsmeyer–Peppas power law fits well with the permeation pattern. The r^2 value ranged from 0.964 to 0.996 and the permeation exponent (n) value was closer to 0.5 (0.561 to 0.654), the mechanism of permeation could be a diffusion-controlled process (Table II). According to the Peppas–Sahlin model, the k_1 value is greater than the k_2 value in both the cases of drug release and permeation confirming the drug release from the hydrogel matrix to be by the Fickian diffusion mechanism (Table III). Flux of the film was decreased with increasing content of HPMC and found in the order: AH1 > AH2 > AH3 > AH4 (13.0, 12.9, 12.6 and 12.2 μg min^{-1}, respectively, Table II).[16,18]

Anti-inflammatory activity of aspirin

The anti-inflammatory action is depicted in Fig. 5. In a variety of animal models, carrageenan is commonly used for inducing cytokine mediated acute inflammation.[42]

Freund's adjuvant used for inducing chronic inflammation may last for more than 14 days, whereas carrageenan induced inflammation can be recovered within 24 h.[43] Carrageenan was injected in the upper palpebral conjunctiva of the right rabbit eye for induction of inflammation. The normal eye was used as control where no signs of inflammation were seen. Watery eye with continuous lacrimation, redness and swelling of the conjunctiva (as signs and symptoms of inflamemation) were observed after 1 h of the injection. AH4 was hydrated by the tear fluid and resulted in continuous release of drug just after application of the film in the cul-de-sac of the rabbit eye. Reduced inflammation was noticed within 2 h and the redness had also almost vanished.[15,20] Thus, aspirin-in-HPMC formulation could be explored in ophthalmic anti-inflammation. Embedding the drug in the HPMC matrix also made it more tolerable to the ocular environment.[36] A similar anti-inflammatory study was performed by Nandi *et al.* 2021 by administering vildagliptin film formulation in the eye for reduction of inflammation by inhibiting DPP-4.[36]

CONCLUSION

Aspirin-in-HPMC film formulations were successfully prepared with sufficient flexibility and swelling property for better patient comfort. Both the drug release and corneal permeation were sustained for more than 6 h and exhibited a diffusion-controlled mechanism. The signs of acuteness of inflammation induced by carrageenan were alleviated within 2 h of placing the film indicating ocular anti-inflammatory activity. Aspirin-in-HPMC film formulation could be a better option for controlling ocular anti-inflammation for an extended period of time with better patient compliance.

TABLE II. The rate of swelling and the release/permeation kinetics of the prepared film formulations

Film code	K_s min^{-1}	Release					Permeation					
		First order	Higuchi		Peppas		First order	Higuchi		Peppas		Jss^a
		r^2	K / % min$^{-1/2}$	r^2	n	r^2	r^2	K / % min$^{-1/2}$	r^2	n	r^2	µg min^{-1}
AH1	2.19±0.23	0.878	3.566	0.925	0.292	0.892	0.874	4.645	0.935	0.561	0.964	15.84±0.87
AH2	2.47±0.16	0.936	3.188	0.957	0.279	0.927	0.952	4.463	0.959	0.580	0.976	14.29±0.37
AH3	3.36±0.08	0.935	2.816	0.976	0.259	0.947	0.980	4.282	0.975	0.619	0.988	12.78±0.49
AH4	3.88±0.06	0.878	2.301	0.997	0.236	0.991	0.993	4.090	0.986	0.654	0.996	10.88±0.88

[a]Mean±*SD*; $n = 3$

TABLE III. Peppas–Sahlin model parameters

Formulation code	Drug release			Permeation		
	k_1 / min^{-m}	k_2 / min^{-2m}	m	k_1 / min^{-m}	k_2 / min^{-2m}	m
AH1	9.683	1.375	0.273	1.813	0.068	0.545
AH2	1.968	0.083	0.520	1.968	0.083	0.520
AH3	11.893	2.181	0.219	1.823	0.082	0.518
AH4	13.571	2.929	0.184	1.060	0.575	0.447

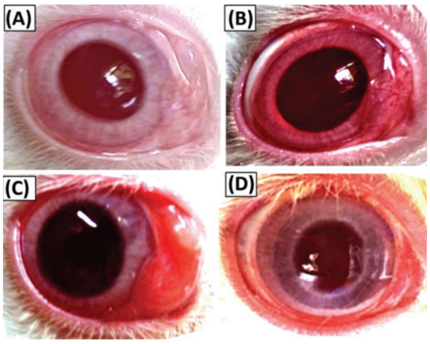

Fig. 5. Anti-inflammatory activity study: A) normal eye; B) inflamed eye 1 h after carrageenan injection; C) application of film formulation 1 h after inflammation; D) revival to the normal eye 2 h after application of the film formulation.

Acknowledgment. The authors are very thankful to the honourable President Professor Manojranjan Nayak, Siksha 'O' Anusandhan (Deemed to be University) for his encouragement and institutional facilities.

ИЗВОД

ОКУЛАРНИ ФИЛМ АСПИРИН–ХИДРОГЕЛ ЗА ПОВРШИНСКО НАНОШЕЊЕ У ЛЕЧЕЊУ ОЧИЈУ И ПРОТИВ УПАЛЕ

ASHIRBAD NANDA[1,2], SHUBHASHREE DAS[2], RUDRA N SAHOO[1,2], SOUVIK NANDI[1], RAKESH SWAIN[1], SUNIL PATTANAIK[1], DEBAJYOTI DAS[1] и SUBRATA MALLICK[1]

[1]*School of Pharmaceutical Sciences, Siksha 'O' Anusandhan (Deemed to be University), Bhubaneswar, Odisha, India, 751003 и* [2]*Centurion University of Technology and Management, Odisha, India*

Примена лекова у облику хидрогел филмова за лечење очију има неколико предности у поређењу са уобичајеним начинима примене. Извршена су испитивања површинске примене аспирина за третман против-упалних офталмолошких процеса. Припремљен је хидрогел матрикс од хидроксипропил-метилцелулозе (HPMC) методом додавања и упаравња растварача, уз додатак триетаноламин (TEA) за повећање еластичности. Испитивана је пропустност рожњаче као и потенцијал анти-упалног ефекта аспирина на моделу зечијег ока иритираног карагенином. Утврђено је да је апсорпција влаге у опсегу 17,097 и 19,139 % за све формулације филмова. Висок садржај HPMC у филму повећава апсорпцију влаге и оток. Присуство полимера за формирање матрице подржава отпуштање лека и пропустност рожњаче више од 6 сати у контролисаном процесу према дифузионом механизму. Акутна упала изазаване карагенином је инхибирана потпуно у току 2 сата након постављања филма на зечије око, док у позитивној контролној групи постоји континуитет црвенила и лучења суза. Окуларна формулација која садржи аспирин може се применити за анти-инфламаторно дејство на очима у продуженом периоду са бољим утицајем.

(Примљено 5. маја, ревидирано 24. децембра 2021, прихваћено 28. фебруара 2022)

REFERENCES

1. G. Fang, Q. Wang, X. Yang, Y. Qian, G. Zhang, Q. Zhu, B. Tang, *Colloids Surfaces,. A* **627** (2021) 127187 (https://doi.org/10.1016/j.colsurfa.2021.127187)
2. G. Fan, G. Li-li, W. Yan-rong, Q.I. Wang, *Int. Eye Sci.* **17** (2017) 2359 (https://doi.org/10.3980/j.issn.1672-5123.2017.12.45)

3. M. T. Kralinger, M. Voigt, G. F. Kieselbach, D. Hamasaki, B. C. Hayden, J. M. Parel, *Ophthalmic Res.* **35** (2003) 102 (https://doi.org/10.1159/000069129)
4. S. Das, J. R. Bellare, R. Banerjee, *Colloids Surfaces, B* **93** (2012) 161 (https://doi.org/10.1016/j.colsurfb.2011.12.033)
5. A. Yazici, E. Sarı, E. Ayhan, *J. Ocul. Pharmacol. Ther*. **34** (2018) 256 (https://doi.org/10.1089/jop.2017.0064)
6. Ameeduzzafar, J. Ali, M. Fazil, M. Qumbar, N. Khan, A. Ali, *Drug Deliv*. **23** (2016) 700 (https://doi.org/10.3109/10717544.2014.923065)
7. L. Battaglia, M. Gallarate, L. Serpe, F. Foglietta, E. Muntoni, A. P. Rodriguez, M. Angeles, S. Aspiazu, in *Lipid Nanocarriers for Drug Targeting*, A. M. Grumezescu, Ed., William Andrew Applied Science Publishers, Norwich, NY, 2018, pp. 269–312 (https://doi.org/10.1016/B978-0-12-813687-4.00007-4)
8. A. Pramanik, R. N. Sahoo, S. K. Pradhan, S. Mallick, *Indian J. Pharm. Sci.* **83** (2021) 794-807 (https://doi.org/10.36468/pharmaceutical-sciences.831)
9. R. Swain, S. Nandi, R. N. Sahoo, S. S. Swain, S. Mohapatra, S. Mallick. *J. Drug Deliv. Sci. Technol.* **67** (2021) 102956 (https://doi.org/10.1016/j.jddst.2021.102956)
10. Z. Jafariazar, N. Jamalinia, F. Ghorbani-Bidkorbeh, S. A. Mortazavi, *Iran. J. Pharm. Sci*. **14** (2015) 23 (https://doi.org/10.22037/ijpr.2015.1709)
11. G. Fang, X. Yang, Q. Wang, A. Zhang, B. Tang, *Mater. Sci. Eng., C* **127** (2021) 112212 (https://doi.org/10.1016/j.msec.2021.112212)
12. N. Kavanagh, O. I. Corrigan, *Int. J. Pharm.* **279** (2004) 141 (https://doi.org/10.1016/j.ijpharm.2004.04.016)
13. B. Vigani, S. Rossi, G. Sandri, M. C. Bonferoni, C. M. Caramella, F. Ferrari, *Pharmaceutics* **12** (2020) 859 (https://doi.org/10.3390/pharmaceutics1209085)
14. A. A. El-Bary, H. K. Ibrahim, B. S. Haza'a, I. A. Sharabi, *Pharm. Dev. Technol*. **24** (2019) 824 (https://doi.org/10.1080/10837450.2019.1602631)
15. M. Mansour, S. Mansour, N. D. Mortada, S. S. Abd El-Hady, *Drug. Dev. Ind. Pharm*. **34** (2008):744 (https://doi.org/10.1080/03639040801926030)
16. M. Tighsazzadeh, J. C. Mitchell, J. S. Boateng, *Int. J. Pharm*. **566** (2019) 111 (https://doi.org/10.1016/j.ijpharm.2019.05.059).
17. J. Ye, H. Zhang, H. Wu, C. Wang, X. Shi, J. Xie, J. He, J. Yang, *Graefes Arch. Clin.* **250** (2012) 1459 (https://doi.org/10.1007/s00417-012-2087-4)
18. A. Nanda, R. N. Sahoo, A. Pramanik, *Colloids Surfaces, B* **172** (2018) 555 (https://doi.org/10.1016/j.colsurfb.2018.09.011)
19. M. R. Abbaspour, B. S. Makhmalzadeh, S. Jalali, *Jundishapur J. Nat. Pharm. Prod.* **5** (2010) 6 (https://brief.land/jjnpp/articles/72379.html)
20. P. Talik, J. Piotrowska, U. Hubicka, *AAPS Pharm. Sci. Tech*. **20** (2019) 187 (https://doi.org/10.1208/s12249-019-1406-z)
21. R. Mohapatra, S. Senapati, C. Sahoo, S. Mallick, *Colloids Surfaces, B* **123** (2014)170 (https://doi.org/10.1016/j.colsurfb.2014.09.012)
22. A. Pramanik, R. N. Sahoo, A. Nanda, *Curr. Eye Res*. **43** (2018) 828 (https://doi.org/10.17344/acsi.2019.5139)
23. K. N. Priya, S. Bhattacharyya, P. R. Babu, *Dhaka Univ. J. Pharm. Sci*. **13** (2014) 75 (https://doi.org/10.3329/dujps.v13i1.21866)
24. B. Panda, R. Subhadarsini, S. Mallick, *Expert Opin. Drug Deliv.* **13** (2016) 633 (https://doi.org/10.1517/17425247.2016.1154038)

25. M. J. Habib, J. A. Rogers, *Int. J. Pharm.* **44** (1988) 235 (https://doi.org/10.1016/0378-5173(88)90120-2)
26. J. T. Mitchell-Koch, K. R. Reid, M. E. Meyerhoff, *J. Chem. Educ.* **85** (2008) 1658 (https://doi.org/10.1021/ed085p1658)
27. N. A. Farid, G. S. Born, W. V. Kessler, S. M. Shaw, W. E. Lange*, Clin. Chem*. **21** (1975) 1167 (https://doi.org/10.1093/clinchem/21.8.1167)
28. W. J. Keller Jr., *Am. J. Clin. Pathol.* **17** (1947) 415 (https://doi.org/10.1093/ajcp/17.5_ts.415)
29. W. A. McBryde, J. L. Rohr, J. S. Penciner, J. A. Page, *Can. J. Chem.* **48** (1970) 2574 (https://doi.org/10.1139/v70-433)
30. A. Pramanik, R. N. Sahoo, S. Nandi, A. Nanda, S. Mallick, *Acta Chim. Slov.* **68** (2021) 159-69 (http://dx.doi.org/10.17344/acsi.2020.6298)
31. P. W. Morrison, C. J. Connon, V. V. Khutoryanskiy, *Mol. Pharm*. **10** (2013) 756 (https://doi.org/10.1021/mp3005963)
32. R. N. Sahoo, B. S. Satapathy, S. Mallick, *J. Serb. Chem. Soc.* **86** (2021) 571 (https://doi.org/10.2298/JSC201209021N)
33. B. S. Satapathy, A. Patel, R. N. Sahoo, S. Mallick, *J. Serb. Chem. Soc*. **86** (2021) 51 (https://doi.org/10.2298/JSC200705049S)
34. P. K. Pawar, D. K. Majumdar, *AAPS Pharm. Sci. Tech*. **7** (2006) 13 (https://doi.org/10.1208/pt070113)
35. M. F. Sohail, G. Shahnaz, F. ur Rehman, A. ur Rehman, N. Ullah, U. Amin, G. M. Khan, K. U. Shah, *AAPS Pharm. Sci. Tech*. **20** (2019) 288 (https://doi.org/10.1208/s12249-019-1484-y)
36. S. Nandi, A. Ojha, A. Nanda, R. N. Sahoo, R. Swain, K. P. Pattnaik, S. Mallick, *Z. Phys. Chem.* **236** (2021) 275 (https://doi.org/10.1515/zpch-2021-3081)
37. E. Larraneta, R. E. Lutton, A. J. Brady, E. M. Vicente-Pérez, A. D. Woolfson, R. R. Thakur, R.F. Donnelly, *Macromol. Mater. Eng.* **300** (2015) 586 (https://doi.org/10.1002/mame.201500016)
38. A. Semalty, M. Semalty, D. Singh, M. S. Rawat, *Int. J. Pharm. Sci. Nanotechnol*. **3** (2010) 940 (https://doi.org/10.37285/ijpsn.2010.3.2.7)
39. S. Farias, J. S. Boateng, *Int. J. Pharm*. **553** (2018) 65 (https://doi.org/10.1016/j.ijpharm.2018.10.025)
40. R. Mohanty, S. K. Das, N. R. Singh, M. Patri, *Zebrafish*. **13** (2016) 188 (https://doi.org/10.1089/zeb.2015.1215)
41. J. A. Castro-Hermida, H. GóMez-Couso, M. E. Ares-Mazás, M. M. Gonzalez-Bedia, N. CastañEda-Cancio, F. J. Otero-Espinar, J. Blanco-Mendez, *J. Pharm. Sci*. **93** (2004) 197 (https://doi.org/10.1002/jps.10528)
42. T. Oka, T. Shearer, M. Azuma, *Curr. Eye Res*. **29** (2004) 27 (https://doi.org/10.1080/02713680490513164)
43. J. C. Fehrenbacher, M. R. Vasko, D. B. Duarte, *Curr. Protoc. Pharmacol*. **56** (2012) 541 (https://doi.org/10.1002/0471141755.ph0504s56).

Journal of
the Serbian
Chemical Society

JSCS-info@shd.org.rs • www.shd.org.rs/JSCS

J. Serb. Chem. Soc. 87 (7–8) 845–856 (2022)
JSCS–5561

Original scientific paper
Published 23 March 2022

Glycerol and malonic acid as corrosion inhibitors as seen through the density functional theory perspective

LUIS DIAZ-BALLOTE[1]*, LUIS MALDONADO-LOPEZ[1], LILIANA SAN-PEDRO[2],
EMANUEL HERNÁNDEZ-NUÑEZ[3] and JUAN GENESCA[4]

[1]Departamento de Física Aplicada, CINVESTAV-Unidad, km 6 antigua carr. a Progreso, Mérida, Yuc., 97310, México, [2]Facultad de Ingeniería, Universidad Autónoma de Yucatán Av. Industrias no contaminantes por Periférico norte, P.O. Box 150 Cordemex, Mérida, Yucatán, México, [3]Departamento de Recursos del Mar, CINVESTAV-Unidad, km 6 antigua carr. a Progreso, Mérida, Yuc., 97310, México and [4]Polo Universitario de Tecnología Avanzada, Facultad Química, Universidad Nacional Autónoma de México, UNAM, 66629 Apodaca Nuevo León, México

(Received 1 December 2021, accepted 17 February 2022)

Abstract: Glycerol (G) is the major co-product in the transesterification process of biodiesel. As clean energy demand increases, the production of G also increases and new ways of re-using it are needed. In the last decade, some experimental studies claimed that G and its derivative, malonic acid (MA), could be used as corrosion inhibitors. Yet, presently, there is little evidence of it and more studies are needed to confirm that G and MA could have a good performance in metal protection. The present work aims to study the reactivity of G and MA, since reactivity and inhibition are intimately linked. The density functional theory (DFT) at the B3YLP/6-31G** level of theory was used to study the reactivity of both molecules. The global and local quantum parameters derived were used to assess the reactivity of both molecules. Analysis of the calculated reactivity descriptors suggest that G and MA should exhibit an acceptable corrosion efficiency, but MA showed have a greater potential as a corrosion inhibitor.

Keywords: reactivity; DFT; Fukui functions; Orca software; global descriptors; anticorrosive method; computational chemistry.

INTRODUCTION

Glycerol (G) is generated during bioethanol and biodiesel production.[1] Approximately 10 % of G is produced as triacyl to mono alkyl esters (biodiesel) conversion, in the transesterification process.[1] In the USA alone, the biodiesel production in 2020 was 1,817 million of gallons, which approximately represents

---

* Corresponding author. E-mail: luisdiaz@cinvestav.mx

https://doi.org/10.2298/JSC211201012D

a G amount of 181.7 millions of gallons.[2] Although, such a biodiesel production represents an important amount, in the last three years the production of biodiesel has stagnated.[2,3] Glycerol is a key compound to increase the biodiesel production profit, since it is a valuable co-product that could increase the attention in the production of the biofuel. Various attempts to convert G into a value-added product, through novel applications, can be found in the literature.[1] It was reported elsewhere[4] that G could be used as environmentally friendly corrosion inhibitor for copper exposed to alkali media. The results were based on electrochemical measurements such as impedance and linear polarization. The corrosion inhibitor efficiency of G was found to be up to 83 %. Glycerol has also been proposed for simultaneous dual action: functioning as gas hydrate and corrosion inhibitor, for which an inhibitor efficiency of 66 % was reported.[5] Malonic acid (MA), a derivative of G combined with Zn^+, has also been reported as corrosion inhibitor for carbon steel in various solutions. According to the authors, a corrosion efficiency of 85 % was reached.[6] Malonic acid has also been reported as corrosion inhibitor to protect aluminium in contact with alkali solutions.[7] In this case, the efficiency was more encouraging (95 %). In addition, according to Sagoe *et al.*,[8] reinforced steel could also be protected by MA. Despite the experimental evidence, studies focused on the inhibition performance of G and MA are scarce. The low interest suggests the need for better understanding 0f G and MA reactivity as corrosion inhibitors. In this sense, the density functional theory (DFT) has demonstrated itself to be very helpful in the investigation and design of corrosion inhibitors.[9] The quantum key parameters obtained from DFT could be used to better understand the reactivity of the studied molecules. The global and local descriptors calculated from DFT are directly related to the reactivity of the molecule and are a valuable tool to predict new sustainable corrosion inhibitors.[10,11] This encourages the use of DFT to achieve better comprehension of the reactivity of the G and MA molecules. The present work aims to study the reactivity of both, G and MA, using DFT through an analysis of various global and local quantum parameters. Specifically, by studying the reactivity of the molecules, it is expected to obtain insight into the performance of G and MA as corrosion inhibitors.

DETAILS OF THE THEORETICAL CALCULATIONS

Glycerol and MA were studied in the liquid and gas phases using DFT. The starting structures were downloaded from the webpage of Pubchem[12] in sdf format (PubChem CID: 753, PubChem CID: 867; for G and MA respectively). Conformers with the lowest energy of G and MA were found using the systematic rotor conformer method and the MMFF94 force field of the Avogadro software.[13] Gabedit[14] was used as user interface of the ORCA program (version 4.0.1.2), in which the structures were optimized using the hybrid functional B3LYP and the basis 6-31G** implemented in ORCA.[15] The absence of imaginary frequencies in the output results was confirmed to ensure that the equilibrium point corresponded to a minimum of the potential energy. The effect of water on the quantum properties was calculated using the polarizable continuum model (CPMC)[16] and the dielectric constant of water ($\varepsilon = 80.4$). Again

ORCA and the same B3LYP/6-31G** energy level were used to determine the effect of water. From the calculations, the highest occupied molecular orbital (HOMO) and the lowest unoccupied molecular orbital (LUMO) levels were determined, as well as the total dipole moment of the molecule. The HOMO and LUMO levels were used to calculate the global reactivity descriptors. With the aid of the auxiliar program ORCA plot, cube files format containing the electronic density were generated for the neutral, anionic, and cationic forms of both molecules. These files were subsequently used for math operation between electronic density plots and were performed with the aid of Chemcraft,[17] according to expressions (1) and (2):

$$f^{+}(r) = \rho_{\mathrm{N+1}}(r) - \rho_{\mathrm{N}}(r) \tag{1}$$

$$f^{-}(r) = \rho_{\mathrm{N}}(r) - \rho_{\mathrm{N-1}}(r) \tag{2}$$

where, f^{+} stands for the Fukui function, the maximum value of which shows the reactive region of the molecule that is more susceptible to nucleophilic attack; f^{-} stands for the Fukui function, maximum value of which shows the reactive region of the molecule that is more susceptible to electrophilic attack; $\rho_{\mathrm{N}}(r)$ stands for the electronic density of the optimized molecule; $\rho_{\mathrm{N+1}}(r)$ stands for the electronic density of the anionic form of the molecule and $\rho_{\mathrm{N-1}}(r)$ stands for the electronic density of the cationic form of the molecule.

RESULTS AND DISCUSSION

The optimized molecules of G and MA are shown in Fig. 1. Each atom in the molecules is labelled for its identification and the bond lengths between atoms are provided. The G bond lengths calculated in this study are given in the second column of Table I. For comparison, the bond lengths calculated in other theoretical studies are also provided. The results demonstrate that the optimized geometry of G has bond lengths that are in good agreement with those reported in the literature. The bond lengths between atoms in the MA molecule are given in Table II. Again, previously reported data of the bond lengths are included and an acceptable agreement is also observed.

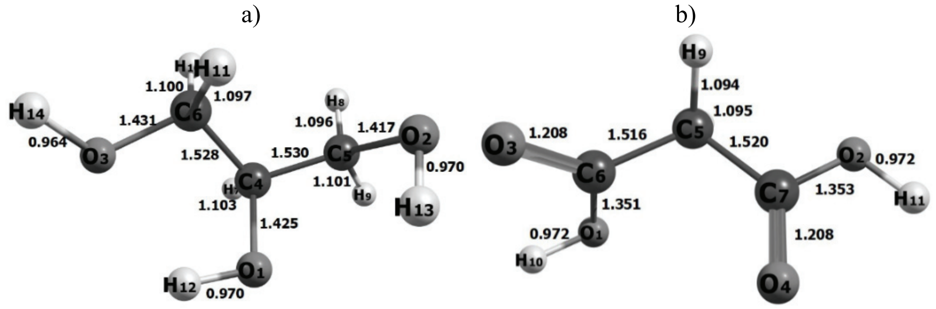

Fig. 1. Optimized geometries of: a) glycerol and b) malonic acid molecules with their bond lengths in Å.

HOMO, LUMO, dipole moment and total energy

The energies of the HOMO and LUMO levels (E_{HOMO} and E_{LUMO}, respectively), were obtained from the theoretical results. The same theoretical results pro-

TABLE I. Molecular bonds of glycerol (G) calculated with B3LYP hybrid functional and 6-31G** basis set, and comparison to molecular bonds calculated in other studies

Bond	Bond length, Å		
	This work	Callam[18]	Tereshchuk[23]
O_1–H_{12}	0.97	0.97	0.98
O_1–C_4	1.43	1.43	1.44
H_{10}–C_6	1.10	1.10	1.10
H_{11}–C_6	1.10	1.10	1.10
C_4–C_5	1.53	1.53	1.53
C_4–C_6	1.53	1.53	1.53
H_7–C_4	1.10	1.10	1.10
C_6–O_3	1.43	1.43	1.44
H_8–C_5	1.10	1.10	1.11
H_9–C_5	1.10	1.10	1.10
C_5–O_2	1.42	1.42	1.43
O_2–H_{13}	0.97	0.97	0.98
O_3–H_{14}	0.96	0.97	9.97

TABLE II. Molecular bonds of malonic acid calculated at the B3LYP/6-31G** level, and comparison to molecular bonds obtained in other studies (theoretical and experimental)

Bond	Bond length, Å		
	This work	Merchán[19]	Maçôas[20]
O_1–H_{10}	0.97	0.99	098
C_7–O_2	1.35	1.37	1.34
C_6–O_1	1.35	1.37	1.33
C_5–C_6	1.52	1.55	1.53
C_5–C_7	1.52	1.54	1.50
C_6–O_3	1.21	1.22	1.20
H_8–C_5	1.09	1.09	1.09
H_9–C_5	1.09	1.09	1.09
C_7–O_4	1.21	1.22	1.22
O_2–H_{11}	0.97	0.98	0.97

vided the dipole moment and the total molecule energy. The numerical values of these parameters are given in Table III. Frequently, E_{HOMO} is related to the reactivity of the molecule,[21] given that this orbital contains the electrons farthest from the nucleus and, therefore, easily donated or shared. In this context, electrons from the HOMO level are more likely to be transferred to the empty orbitals (d-orbitals) at the metal surface. On the other hand, electrons from the metal surface could be transferred towards the LUMO level of the inhibitor. Interestingly, a lower value of the E_{LUMO} favors a better inhibition effect. Perhaps, the most relevant parameter derived from the frontier molecular orbitals (HOMO, and LUMO) is the value of the energy gap (ΔE) between them. Several studies have demonstrated that the reactivity of a molecule increases with a decreasing value of ΔE.[22] Therefore, the best inhibition effect is expected from molecules with lower ΔE. In Table III, it is observed that MA has a lower energy gap (ΔE = = 7.60 eV), which suggests that it would present a better inhibition effect efficiency with respect to G (ΔE = 8.65 eV). The dipole moment is another relevant parameter involved in the reactivity of a molecule since it provides a measure of the polarizability of the molecule.[23] A positive correlation has been frequently reported between dipole moment and the inhibitor adsorption on the metal surface. Therefore, it is expected that higher values of dipole moment would lead to better adsorption of the inhibitor molecules on the metal surface and to higher inhibition efficiency.[24] In the present study, the found values of the dipole moment were similar for both molecules.

TABLE III. HOMO level energy (E_{HOMO}), LUMO level energy (E_{LUMO}), energy gap (ΔE), Dipole moment, and total energy (E_{T}) of G and MA, calculated at the B3LYP/6-31G** level of energy. Values of the parameters that include the solvent effect are given in parenthesis

Quantum parameter	G	MA
E_{LUMO} / eV	1.657 (2.202)	–0.014 (0.014)
E_{HOMO} / eV	–6.993 (–7.160)	–7.620 (–7.707)
ΔE / eV	8.65 (9.362)	7.606 (7.721)
Dipole moment, D[a]	2.35 (2.85)	2.27 (3.23)
E_{T} / Ha	–344.601 (–344.615)	–417.445 (–417.466)

[a] 1 D = 3.335×10^{30} C m

Furthermore, the total energy (E_{T}) is associated with the stability of a molecule. The total energy is associated with the electron donation ability, which in turn relates to the reactivity of a molecule. Specifically, a less reactive molecule would have a higher E_{T}, while a highly reactive molecule would have a lower E_{T}. The values given in Table III suggest that MA (E_{T} = –417.445 Ha) is more reactive than G (E_{T} = –344.601 Ha).[25,26]

HOMO and LUMO orbitals

The optimized geometry of the G and MA molecules along with their corresponding HOMO and LUMO levels are shown in Fig. 2. It could be seen that the HOMO and LUMO levels coverer practically the whole molecule. However, a closer inspection shows a slight preference to cover the oxygen atoms. The latter suggests that these atoms are likely the most reactive sites in both molecules and, therefore, responsible for the inhibition of the corrosion process. This result is consistent with various studies that pointed to oxygen, nitrogen, sulfur, and phosphorus as the main heteroatoms responsible for the inhibition efficiency.[9] In addition, molecules with multiple bonds have been associated with effective corrosion inhibition.[27]

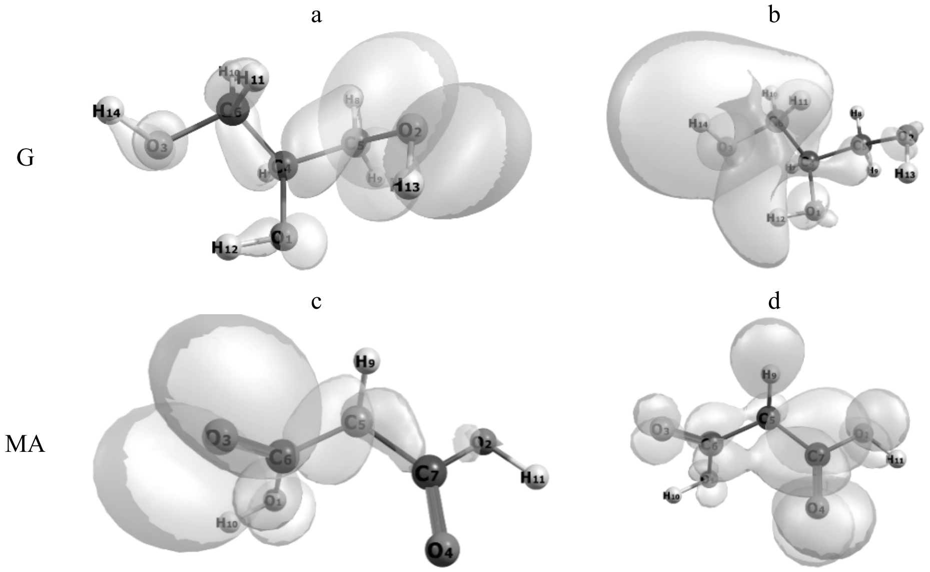

Fig. 2. HOMO and LUMO orbitals on glycerol (a and b) and malonic acid c and d).

Descriptors of reactivity

In this work, some global descriptors of reactivity (Table IV) were derived from the frontier molecular orbitals (HOMO, and LUMO). Initially, the ionization energy (I) and the affinity (A) were calculated. In agreement with the Koopman theorem,[28] these parameters could be approximated to the negative of the energies of the HOMO ($I = -E_{\mathrm{HOMO}}$) and the LUMO ($A = -E_{\mathrm{LUMO}}$) levels. I is a measure of the energy required to remove an electron from the molecule, *i.e.*, a molecule with higher values of ionization potential would be less reactive because it is harder to remove electrons from it.[29] A is related to the negative of the unoccupied orbital (LUMO). Thus, it represents the ability of the molecule to

TABLE IV. Global reactivity descriptors for G and MA calculated at the B3LYP/6-31G** energy level. The values calculated including the solvent effect are given within parenthesis. Experimental results of corrosion inhibition efficiency are given in the last row

Global descriptor	G	MA
I / eV	6.993 (7.16)	7.62 (7.707)
A / eV	–1.657 (–2.202)	0.014 (–0.014)
μ / eV	–2.668 (–2.479)	–3.817 (–3.846)
χ / eV	2.668 (2.469)	3.817 (3.846)
η / eV	4.325 (4.681)	3.803 (3.860)
S /eV	0.23 (0.21)	0.26 (0.26)
ω / eV	0.823 (0.651)	1.91 (1.92)
ΔN	0.500 (0.484)	0.418 (0.408)
Corrosion inhibition efficiency, %	66,[5] 84[4]	85,[6] 95[7]

accept electrons.[10] For higher values of A, the reactivity increases because the electron is easily transferred to the inhibitor. In other words, the molecule is more susceptible to nucleophilic attack,[30] in this case MA (see Table IV).

The chemical potential (μ) is a descriptor that represents the trend of an electron to escape from the electronic cloud of an atom or molecule.[31] The chemical potential is calculated inserting I and A in the expression (3):

$$\mu = 1/2(I + A) \tag{3}$$

μ is useful to explore the global nucleophilic or electrophilic behavior of the molecule. Higher values of μ indicate higher propensity of the electrons to escape from the electronic cloud and, thus, the molecule is more susceptible to electrophile attack. A more susceptible molecule is also more reactive, and a more efficient corrosion inhibition is expected. G in Table IV has a higher value of μ with respect to MA. Hence, a better inhibition efficiency would be expected when using G as a corrosion inhibitor. The next descriptor is the Mulliken electronegativity, defined as the negative of the chemical potential ($\chi = -\mu$). This descriptor is a measure of the ability of a molecule to attract electrons, *i.e.*, the higher the ability to attract electrons, the more reactive is the molecule. Consequently, the inhibition efficiency increases with increasing Mulliken electronegativity. It can be seen in Table IV that MA has a higher value of χ and should exhibit better inhibition efficiency than G.

Hardness (η) and softness (S) are parameters connected to the electron flow resistance. The hardness value can be obtained using expression (4):

$$\eta = 1/2(I - A) \tag{4}$$

For example, η has been pointed out as a measure of the opposition to electron flow. The global effect is a reduction in the adsorption the inhibitor or a decrease of the inhibition efficiency. The results suggest that MA should exhibit a better performance as corrosion inhibitor than G. S provides another insight to η, *i.e.*, it measures how easily electrons flow between the inhibitor and the metal surface. It can be calculated through the following relation:

$$S = 1/2\eta \tag{5}$$

A high S value denotes good flow of electrons and, thus, better adsorption of the species at the metal surface. Generally, it has been reported that a highly reactive molecule has low energy gap, low hardness, and high softness values.[32] Moreover, a molecule with these features will also have a good performance as corrosion inhibitor. It can be observed in Tables III and IV that MA has the lower energy gap, lower hardness, and higher softness, which suggests that MA would have better performance than G.

The electrophilicity (ω) was define in 1999 by Parr *et al.*[33] It combines the electronegativity and the hardness into the following expression:

$$\omega = \chi^2/2\omega \tag{6}$$

χ represents the capacity of a molecule for electron acceptance. From the relation (6), it can be observed that when the χ value rises or the η value decreases, ω increases. In other words, a good electrophile can accept electrons from the "d" orbitals and form feedback bonds, which improves the adsorption and, in turn, the inhibition efficiency. Zhang *et al.*,[34] found a good correlation between ω and the inhibition efficiency. The authors found that the highest value of ω is correlated with the best inhibition efficiency. MA exhibited the higher value of ω, which indicates to MA being a better corrosion inhibitor when compared to G.

Another routinely employed indicator of the ability of a molecule to donate electrons is called the transferred electron fraction ΔN, given by the following relation:

$$\Delta N = \frac{\chi_{\text{met}} - \chi_{\text{inh}}}{2(\eta_{\text{met}} + \eta_{\text{inh}})} \tag{7}$$

where χ_{met} and χ_{inh} are the electronegativities of the metal and inhibitor molecules, respectively, and η_{met} and η_{inh} are the corresponding hardness values. The inhibition efficiency increases with the ability to transfer electrons.[10] Interestingly, no significant differences between the ΔN values for G and MA were observed.

Possible solvent effects were evaluated by comparing the results obtained for the gas and liquid phases, listed in Table IV, and no significant difference was observed. This result demonstrates that the solvent has no considerable impact in the calculations. The values obtained for many the global reactivity descriptors presented in this work (E_{LUMO}, ΔE, A, χ, η and S) indicate that MA should present better behavior than G, as a corrosion inhibitor. This observation is in accordance with experimental results of the corrosion inhibition efficiency, shown in Table IV.

Electrostatic potential

The electrostatic potential reveals the presence of electrical charge. Both, the nucleus and the electrons contribute to the electrostatic potential (positive charge from the nucleus and negative from the electrons). Mapping the iso-surface of the electrostatic potential regions around a molecule allows the determination of the dominant type of charge at a specific region. Commonly, positive regions are represented in blue, while negative regions are represented in red.[35] The electrostatic potential provides similar information to that obtained from the dipole moment, but in a graphical form. Blue regions are susceptible to nucleophilic attack, while red regions are susceptible to electrophilic attack. The electrostatic potential of G and MA are shown in Fig. 3. The graphics show that the positive regions cover mainly the hydrogen atoms, and the negative regions cover the oxygen atoms, suggesting a high electron density around the oxygen atoms. These results are in good agreement with those reported by Thakur *et al.*[36] Furthermore, they are consistent with the previous observation that oxygen atoms have high electronegativity values.[37]

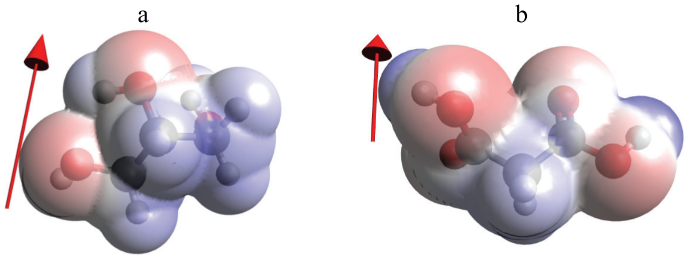

Fig. 3. Electrostatic potential and dipole moment of a) glycerol, and b) malonic acid.

Fukui functions

The Fukui function is understood as a variation in the chemical potential due to an external disturbance or due to a change in the electron density function, caused by a variation in the number of electrons.[38] The Fukui function, f^+, reveals the local region (or atom) of the molecule prone to nucleophilic attack, which means that the molecule accepts electrons in that site. On the other hand, the Fukui function, f^-, reveals the local region prone to electrophilic attack (the molecule donates electrons in that region).[39] The Fukui functions are valuable local descriptors that allow the identification of the reactive regions in a molecule. Graphical representation of the Fukui functions of G and MA are shown in Fig. 4. It was observed that in G, the susceptible atomic sites for nucleophilic/electrophilic attack are O_1, O_3/O_2, while in MA, they are C_7/O_3, O_4.

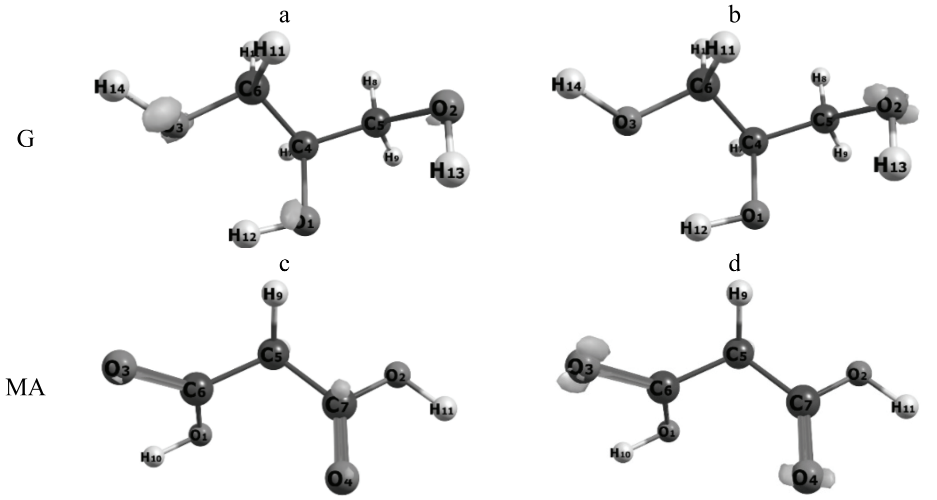

Fig. 4. Graphical representation of the Fukui functions f^+ and $f^-$of: glycerol (a and b) and malonic acid (c and d).

CONCLUSIONS

To gain insight into the potential application of G and MA as corrosion inhibitors, their reactivity was studied using DFT at the B3LYP/6-31G** level of theory. The bond lengths obtained from the optimized molecular geometries show quite similar dimensions to those reported in other theoretical studies. Global descriptors of reactivity were calculated from the theoretical results. Based on the quantum parameters and their analysis, the following conclusions were derived.

– No significant difference was observed between the same descriptors for the gas and liquid phases of G and MA.

– The results found suggest that MA would be a more promising compound as a corrosion inhibitor than G.

The Fukui functions and the electrostatic potential maps suggest that the adsorption of G and MA is mainly through the oxygen atoms.

ИЗВОД

ГЛИЦЕРОЛ И МАЛОНСКА КИСЕЛИНА КАО ИНХИБИТОРИ КОРОЗИЈЕ САГЛЕДАНИ ИЗ ПЕРСПЕКТИВЕ ТЕОРИЈЕ ФУНКЦИОНАЛА ГУСТИНЕ

LUIS DIAZ-BALLOTE[1], LUIS MALDONADO-LOPEZ[1], LILIANA SAN-PEDRO[2], EMANUEL HERNÁNDEZ-NUÑEZ[3] и JUAN GENESCA[4]

[1]*Departamento de Física Aplicada, CINVESTAV-Unidad, km 6 antigua carr. a Progreso, Mérida, Yuc., 97310, México,* [2]*Facultad de Ingeniería, Universidad Autónoma de Yucatán Av. Industrias no contaminantes por Periférico norte, P.O. Box 150 Cordemex, Mérida, Yucatán, México,* [3]*Departamento de Recursos del Mar, CINVESTAV-Unidad, km 6 antigua carr. a Progreso, Mérida, Yuc., 97310, México u* [4]*Polo Universitario de Tecnología Avanzada. Facultad Química. Universidad Nacional Autónoma de México, UNAM. 66629 Apodaca, Nuevo León, México*

Глицерол (G) је главни споредни производ процеса трансестерификације биодизела. Како се повећава потражња за чистом енергијом, повећава се и производња G и траже се нови начини за његову даљу употребу. У последњој деценији, неке експерименталне студије тврде да G и његов дериват, малонска киселина (MA), могу да се користе као инхибитори корозије. Ипак, до сада, мало је доказа за то и више студија је потребно да се потврди да би G и MA имали добро дејство у заштити метала. Овај рад тежи да проучи реактивност G и MA, пошто су реактивност и инхибиција блиско повезани. Коришћена је теорија функционала густине (DFT) на B3YLP/6-31G** нивоу теорије за проучавање реактивности оба молекула. Изведени глобални и локални квантни параметри коришћени су за оцену реактивности оба молекула. Анализа израчунатих дескриптора реактивности сугерише да би G и MA требали да испоље прихватљиву ефикасност код корозије, али MA показује већи потенцијал као инхибитор корозије.

(Примљено 1. децембра 2021, прихваћено 17. фебруара 2022)

REFERENCES

1. S. A. N. M. Rahim, C. S. Lee, F. Abnisa, M. K. Aroua, W. A. W. Daud, P. Cognet, Y. Pérès, *Sci. Total Environ.* **705** (2020) 1 (http://dx.doi.org/10.1016/j.scitotenv.2019.135137)

2. U.S. Energy Information Administration, https://www.eia.gov/petroleum/reports.cfm (accessed August 30, 2021)
3. OECD-FAO Agricultural Outlook, https://stats.oecd.org/index.aspx?queryid=84952 (accessed August 30, 2021)
4. S. L. Chi-Ucán, A. Castillo-Atoche, P. Castro Borges, J. A. Manzanilla-Cano, G. González-García, R. Patiño, L. Díaz-Ballote, *J. Chem.* **2014** (2014) 1 (http://dx.doi.org/10.1155/2014/396405)
5. V. Sivabalan, B. Walid, Y. Madec, A. Qasim, B. Lal, *Malaysian J. Anal. Sci.* **24** (2020) 62 (https://mjas.analis.com.my/mjas/v24_n1/pdf/Sivabalan_24_1_7.pdf)
6. A. Jayashree, F. R. Selvarani, J. W. Sahayaraj, A. J. Amalraj, S. Rajendran, *Port. Electrochim. Acta* **27** (2009) 23 (http://dx.doi.org/10.4152/pea.200901023)
7. P. S. S. Rajendran, *Int. J. Sci. Res.* **6** (2017) 2692 https://www.ijsr.net/archive/v6i6/ART20174819.pdf.
8. K. K. Sagoe-Crentsil, V. T. Yilmaz, F. P. Glasser, *Cem. Concr. Res.* **23** (1993) 1380 (http://dx.doi.org/10.1016/0008-8846(93)90075-K)
9. G. Gece, *Corros. Sci.* **50** (2008) 2981 (http://dx.doi.org/10.1016/j.corsci.2008.08.043)
10. I. B. Obot, D. D. Macdonald, Z. M. Gasem, *Corros. Sci.* **99** (2015) 1 (http://dx.doi.org/10.1016/j.corsci.2015.01.037)
11. D. K. Verma, *Adv. Eng. Test.* (2018) (http://dx.doi.org/10.5772/intechopen.78333)
12. National Library of Medicine, https://pubchem.ncbi.nlm.nih.gov/ (accessed August 30, 2021)
13. M. D. Hanwell, D. E. Curtis, D. C. Lonie, T. Vandermeerschd, E. Zurek, G. R. Hutchison, *J. Cheminform.* **4** (2012) 1 (http://dx.doi.org/10.1186/1758-2946-4-17)
14. A.-R. Allouche, *J. Comput. Chem.* **32** (2011) 174 (https://doi.org/10.1002/jcc.21600)
15. F. Neese, *Wiley Interdiscip. Rev. Comput. Mol. Sci.* **2** (2012) 73 (https://dx.doi.org/10.1002/wcms.81)
16. M. Cossi, V. Barone, *J. Chem. Phys.* **109** (1998) 6246 (http://dx.doi.org/10.1063/1.47765)
17. G. Zhurko, D. Zhurko, http://www.chemcraft.com/ (accessed August 27, 2021)
18. C. S. Callam, S. J. Singer, T. L. Lowary, C. M. Hadad, *J. Am. Chem. Soc.* **123** (2001) 11743 (http://dx.doi.org/10.1021/ja011785r)
19. M. Merchán, F. Tomás, I. Nebot-Gil, *J. Mol. Struct. THEOCHEM* **109** (1984) 51 (http://dx.doi.org/10.1016/0166-1280(84)80134-7)
20. E. M. S. Maçôas, R. Fausto, J. Lundell, M. Pettersson, L. Khriachtchev, M. Räsänen, *J. Phys. Chem. A* **104** (2000) 11725 (http://dx.doi.org/10.1021/jp002853j)
21. N. V. P. Rangel, L. P. da Silva, V. S. Pinheiro, I. M. Figueredo, O. S. Campos, S. N. Costa, F. M. T. Luna, C. L. Cavalcante, E. S. Marinho, P. de Lima-Neto, M. A. S. Rios, *Fuel* **289** (2021) (http://dx.doi.org/10.1016/j.fuel.2020.119939)
22. J. Fang, J. Li, *J. Mol. Struct. THEOCHEM* **593** (2002) 179 (http://dx.doi.org/10.1016/S0166-1280(02)00316-0)
23. N. F. El Boraei, S. A. Halim, M. A. M. Ibrahim, *Anti-Corrosion Methods Mater.* **65** (2018) 626 (http://dx.doi.org/10.1108/ACMM-04-2018-1927)
24. A. Zarrouk, B. Hammouti, A. Dafali, M. Bouachrine, H. Zarrok, S. Boukhris, S. S. Al-Deyab, *J. Saudi Chem. Soc.* **18** (2014) 450 (http://dx.doi.org/10.1016/j.jscs.2011.09.011)
25. A. M. Al-Sabagh, N. M. Nasser, A. A. Farag, M. A. Migahed, A. M. F. Eissa, T. Mahmoud, *Egypt. J. Pet.* **22** (2013) 101 (http://dx.doi.org/10.1016/j.ejpe.2012.09.004)

26. R. Padash, M. Rahimi-Nasrabadi, A. Shokuhi Rad, A. Sobhani-Nasab, T. Jesionowski, H. Ehrlich, *Appl. Phys. A Mater. Sci. Process.* **125** (2019) 1 (http://dx.doi.org/10.1007/s00339-018-2376-9)
27. A. Döner, R. Solmaz, M. Özcan, G. Kardaş, *Corros. Sci.* **53** (2011) 2902 (http://dx.doi.org/10.1016/j.corsci.2011.05.027)
28. T. Koopmans, *Physica* **1** (1934) 104 (http://dx.doi.org/10.1016/S0031-8914(34)90011-2)
29. E. A. M. Gad, E. M. S. Azzam, S. A. Halim, *Egypt. J. Pet.* **27** (2018) 695 (http://dx.doi.org/10.1016/j.ejpe.2017.10.005)
30. X. Liao, Y. Zhu, S. G. Wang, H. Chen, Y. Li, *Appl. Catal., B* **94** (2010) 64 (http://dx.doi.org/10.1016/j.apcatb.2009.10.021)
31. L. E. Gómez-Pineda, C. M. Quiroa-Montalván, *Rev. Mex. Ing. Quim.* **15** (2016) 667 (http://dx.doi.org/10.24275/rmiq/sc1244)
32. N. Ammouchi, H. Allal, Y. Belhocine, S. Bettaz, E. Zouaoui, *J. Mol. Liq.* **300** (2020) (http://dx.doi.org/10.1016/j.molliq.2019.112309)
33. R. G. Parr, L. V. Szentpály, S. Liu, *J. Am. Chem. Soc.* **121** (1999) 1922 (http://dx.doi.org/10.1021/ja983494x)
34. J. Zhang, G. Qiao, S. Hu, Y. Yan, Z. Ren, L. Yu, *Corros. Sci.* **53** (2011) 147 (http://dx.doi.org/10.1016/j.corsci.2010.09.007)
35. X. Cao, *Chem. Phys.* **311** (2005) 203 (http://dx.doi.org/10.1016/j.chemphys.2004.09.037)
36. S. Thakur, S. M. Borah, N. C. Adhikary, *Optik (Stuttg).* **168** (2018) 228 (http://dx.doi.org/10.1016/j.ijleo.2018.04.099)
37. A. H. Radhi, E. A. B. Du, F. A. Khazaal, Z. M. Abbas, O. H. Aljelawi, S. D. Hamadan, H. A. Almashhadani, M. M. Kadhim, *NeuroQuantology* **18** (2020) 37 (http://dx.doi.org/10.14704/nq.2020.18.1.NQ20105)
38. R. Mejia-Urueta, F. Nuñez-Zarur, R. Vivas-Reyes, *Int. J. Quantum Chem.* **112** (2012) 2808–2815 (http://dx.doi.org/10.1002/qua.24008)
39. E. F. Blanco-Acuña, L. Pérez-Hincapié, A. Pérez-Gamboa, G. Castellar-Ortega, M. Cely--Bautista, *Rev. ION* **31** (2019) 51 (http://dx.doi.org/10.18273/revion.v31n2-2018004).

Journal of the Serbian Chemical Society
JSCS@tmf.bg.ac.rs • www.shd.org.rs/JSCS

J. Serb. Chem. Soc. 87 (7–8) 857–865 (2022)
JSCS–5562

Original scientific paper
Published 28 April 2022

Theoretical study on the insertion reaction of the phosphenium cation and azirane

JINSONG GU, XIAODONG ZHAO, SHANKUI LIU and XIAOJUN TAN*

College of Biological Science and Technology, University of Jinan, Jinan, Shandong, 250022, People's Republic of China

(Received 2 January, revised 22 February, accepted 7 March 2022)

Abstract: The mechanism of the insertion reaction between the phosphenium cation and azirane has been investigated theoretically in order to better understand the reactivity for the valence isoelectronic of carbene. The phosphenium cation acts as an electrophilic reagent and accepts the σ electrons of azirane to form a complex in the first combination step. The greater the positive charge on the phosphorus in the phosphenium cation, the more stable is the formed complex. Introduction of substituents will decrease the positive charge on the phosphorus in the phosphenium cation. The order of positive charge on phosphorus is $HP^+–F > HP^+–OH > HP^+–NH_2$, which is consistent with their Lewis acidities. The complex transforms to a four-membered ring product *via* a transition state in the second insertion step. The product is more stable than the complex due to the decrease of the ring extension.

Keywords: electrophilic reagent; carbene; silylene.

INTRODUCTION

The phosphenium cation (R_2P^+) is valence isoelectronic and isolobal with carbene (R_2C), silylene (R_2Si) and the nitrenium cation (R_2N^+).[1,2] The simplest phosphenium cation is H_2P^+, which contains a positive charged phosphorus center and two hydrogens. H_2P^+ is detected through photoionization of PH_3 and other phosphorus-bearing compounds.[3] The ground state of H_2P^+ is a singlet, the energy gap of singlet–triplet is about 67 kJ m^{-1}.[4] The hybridization of the central phosphorous atom can be regarded as being sp^2, with a lone electron pair in the filled sp^2 orbital and a vacant p orbital.[5] Introduction of a variety of substituents has been used to prepare and isolate stable phosphenium cations. The diaminomethylphosphenium cation, $(NMe_2)_2P^+$, is the first stable, isolable cation in low-coordinated phosphorus chemistry.[6] Later, other stable phosphenium cations

---

* Corresponding author. E-mail: chem.2001@163.com
https://doi.org/10.2298/JSC220103021G

have been characterized successively, for example the phosphanetriylammonium cation ($MeN=P^+$)[7] and methylenephosphenium cation ($Me_2C=P^+$).[8]

The chemistry of different species tends to be dominated by their electrophilic behaviour, a key concern is their Lewis acidities. The fluoride ion affinities (FIAs) can act as a measure of the Lewis acidities of phosphenium cations.[9] Slattery *et al*. calculated the FIAs of 33 phosphenium cations with a range of substituents. The results demonstrated that phosphenium cations are often stronger Lewis acids than neutral species, but in many cases are less Lewis acidic than highly electrophilic cations such as $[Me_3C]^+$ or $[Me_3Si]^+$.[10] The dipole moments of PH_2^+ and other compounds containing silicon or phosphorus have been computed to evaluate the intensities of rotational transitions and reactivity.[11]

The chemical reactions of the phosphenium cation are similar to its carbon--based and silicon-based analogues, including cycloaddition reaction, C–H insertion reaction, *etc.*, making them versatile reagents in some kinds of transformations and reactions.[12–14] The phosphenium cation can be applied as ligands in coordination chemistry, acting as the building blocks in phosphorus-bearing compounds.[15] In addition, as a class of strongly π-accepting ligands, phosphenium cation can be used in homogeneous catalytic systems.[16]

The reactions of carbene and silylene have been extensively investigated. The reactions of the phosphenium cation have also attracted attentions.[17,18] Since the phosphenium cations have a vacant p orbital and a filled sp^2 orbital, they can act as both Lewis acids and Lewis bases, respectively. Phosphenium cation can participate in complexation reactions with metals where it acts as a Lewis base,[19,20] or in cycloaddition reactions with alkynes where it acts as a Lewis acid.[21] In the present study, we performed a comprehensive theoretical investigation of the reaction between phosphenium cation and azirane was performed. The reaction mechanism has been described and the effects of a variety of substituents in phosphenium cation have been evaluated. The present results will enrich the available data for the relevant phosphenium cation chemistry and will provide more information for expanding its application in coordination chemistry and catalytic systems.

CALCULATION METHOD

For the reaction between phosphenium cation and azirane, the popular hybrid density functional (B3LYP)[22,23] with 6-311++G** and aug-cc-pVTZ basis sets were employed to locate all the stationary points along the reaction pathway without imposing any symmetry constraints. The reliability and efficiency of this method in predicting the geometries and properties have been verified by a number of investigations.[24,25] Frequency analyses was conducted to confirm the nature of the minima and transition state. Moreover, intrinsic reaction coordinate (IRC) calculations were also performed to further validate the calculated transition state connecting reactant and product. Additionally, the relevant energy quantities, such as reaction energies and barrier heights, were corrected with zero-point vibrational energy (ZPVE) corrections.

To further refine the calculated energy parameters, single-point energy calculations were performed at the CCSD(T)/6-311++G** level of theory based on the stationary points optimized by the corresponding B3LYP method. As described below in Fig. 1 and Table I, several kinds of computational levels can give approximately consistent results for the optimized structures and the calculated reaction profile of the reaction between H_2P^+ and azirane. Therefore, for the reaction of substituted phosphenium cation (HXP^+) and azirane, the B3LYP method in conjunction with the 6-311++G** basis set was performed to confirm the nature of the minima and transition state as well as the energy parameters. For the sake of simplicity, for all the reactions, the energy results at the B3LYP/6-311++G** level were mainly discussed below if not noted otherwise.

All the calculations were performed using the Gaussian 09 program.[26] Matrixes of whole optimized structures are given in Supplementary material to this paper.

RESULTS AND DISCUSSIONS

For the insertion reaction of phosphenium cation and azirane, the first step was the formation of a complex (Com) without barrier. The second step was the isomerization of Com to a product (Pro) *via* a transition state (TS). The geometric parameters for the reactants (R1-H_2P^+ and R2-azirane), Com, TS and Pro involved insertion reaction are displayed in Fig. 1. The corresponding energies are listed in Table I.

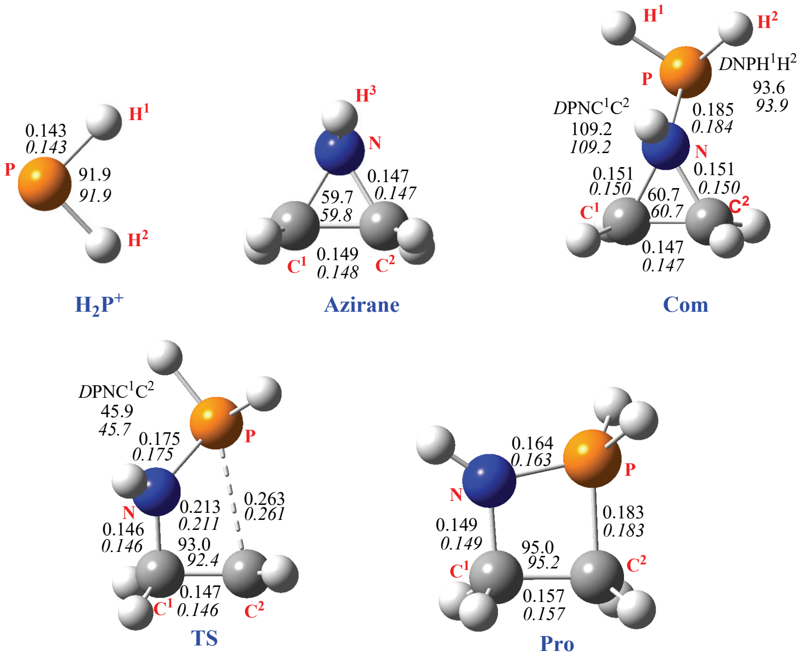

Fig. 1. Optimized structures of the reactants (H_2P^+, azirane), complex (Com), transition state (TS), and product (Pro) in the insertion reaction at the B3LYP/6-311++G** (first line) and B3LYP/aug-cc-pVTZ (second line, *italic*) level of theory, where the bond length and bond angle (and dihedral angle) are in nm and degree, respectively.

TABLE I. The calculated relative energies (kJ mol^{-1}) in the reaction of phosphenium cation (H_2P^+) and azirane with respect to the isolated reactants at the three calculated levels of theory considering the ZPVE corrections

Species	B3LYP/6-311++G**	CCSD(T)//B3LYP/6-311++G**	B3LYP/aug-cc-pVTZ
Com	–405.8	–407.0	–424.6
TS	–242.6	–246.0	–230.0
Pro	–425.7	–437.3	–435.4

When phosphenium cation approaches to the N atom of azirane, it can form a complex (Com) with azirane, which is a barrier-free process. In the Com, the configuration of azirane fragment changed slightly compared with that in isolated azirane. The bond length of C^2–N in the Com prolonged slightly by 0.003 nm than that in isolated azirane, denoting a weakening of the C^2–N bond. To investigate the combination process of phosphenium cation and azirane, the potential energy curve for the Com was constructed along the distance between the two fragments. As displayed in Fig. 2, the energy of the system decreases continuously before the combination of PH_2^+ and azirane. After the equilibrium point (here the N–P bond is 0.185 nm), the energy will be increased rapidly as PH_2^+ and azirane approach each other.

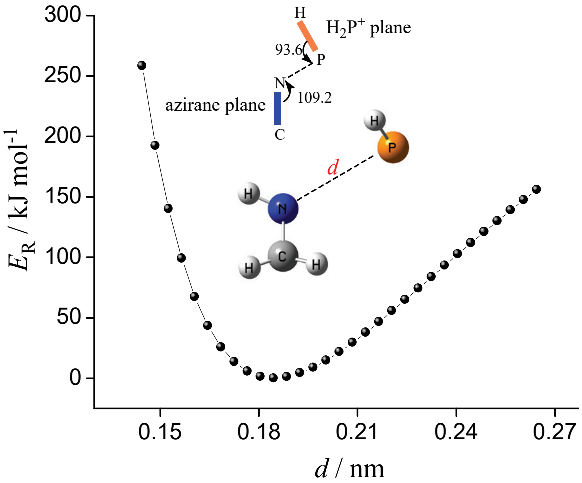

Fig. 2. Energy changes in the combined process of complex along with the distance between two fragments at the B3LYP/6-311++G** level of theory.

The combination process can be understood through interaction of the frontier molecular orbital theory. As displayed in Fig. 3, the frontier orbitals for LUMO of H_2P^+ and HOMO of azirane are symmetrically matching. As H_2P^+ initially interacts with azirane, the 3p unoccupied orbital of phosphorus in H_2P^+ inserts into the sp^3 orbital of azirane to form a σ→p donor–acceptor bond, resulting in the formation of the Com. The dihedral angle of PNC^1C^2 (109.2°) is identical with the angle of normal sp^3 orbitals (109.28°), which proves the mechanism described above. As an electrophilic reagent, H_2P^+ accepts σ electrons from azirane in the combination process. The greater the positive charge on phosphorus atom in H_2P^+, the easier the formation of the σ→p donor–acceptor bond will be and therefore, the more stable will the formed complex be.

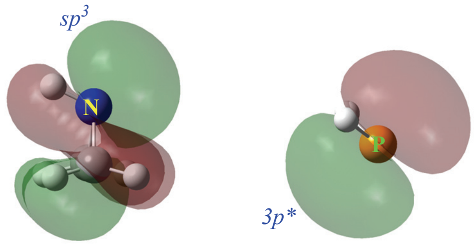

HOMO of azirane LUMO of H_2P^+

Fig. 3. The calculated LUMO orbital for H_2P^+ and the HOMO orbital for azirane.

For the sake of better understanding the combination process of phosphenium cation and azirane, the effect of variety of substituents was considered, which are marked with superscript "X". The geometric parameters for the ^{X}Com, ^{X}TS, and ^{X}Pro are listed in Table II, The corresponding energies are listed in Table III.

TABLE II. The geometric parameters for the species involved in the insertion reaction of substituted phosphenium cation (HXP^+) and azirane

Geometry	X	Bond length, nm						Bond angle, °	
		P–X	N–P	C^1N	C^2N	C^1C^2	C^2P	$\angle NC^1C^2$	$DPNC^1C^2$
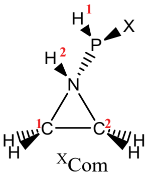 ^{X}Com	F	0.161	0.184	0.151	0.151	0.147	0.292	61.0	109.6
	CH_3	0.184	0.186	0.150	0.150	0.147	0.292	60.7	109.2
	OH	0.163	0.187	0.150	0.151	0.147	0.295	60.8	109.6
	OCH_3	0.162	0.189	0.150	0.150	0.147	0.296	60.7	109.2
	NH_2	0.166	0.193	0.150	0.150	0.148	0.297	60.7	108.6
	$NHCH_3$	0.165	0.196	0.149	0.150	0.148	0.300	60.6	108.2
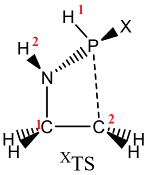 ^{X}TS	F	0.160	0.173	0.147	0.210	0.147	0.261	90.9	50.2
	CH_3	0.183	0.176	0.147	0.209	0.147	0.263	90.9	48.2
	OH	0.163	0.175	0.147	0.209	0.147	0.262	90.5	49.6
	OCH_3	0.162	0.175	0.147	0.208	0.147	0.263	90.2	50.4
	NH_2	0.167	0.175	0.147	0.211	0.147	0.268	91.9	52.1
	$NHCH_3$	0.167	0.175	0.147	0.212	0.147	0.271	92.1	53.4
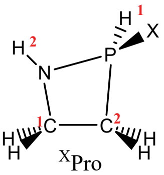 ^{X}Pro	F	0.157	0.161	0.150	0.226	0.157	0.181	94.7	5.2
	CH_3	0.180	0.165	0.149	0.226	0.157	0.183	95.0	–9.2
	OH	0.159	0.163	0.150	0.225	0.157	0.181	94.7	2.9
	OCH_3	0.157	0.163	0.149	0.225	0.157	0.181	94.7	3.3
	NH_2	0.163	0.164	0.149	0.225	0.156	0.183	94.7	–6.9
	$NHCH_3$	0.163	0.164	0.149	0.225	0.156	0.184	94.8	–7.3

TABLE III. The calculated Mulliken charge of the phosphorus atom in HXP^+ and the relative energies in the reaction of substituted phosphenium cation and azirane at the B3LYP/6-311++G** level of theory considering the ZPVE corrections

Species (HXP^+)	Mulliken charge of P in $^{X}R1$	Relative energy, kJ mol^{-1}		
		^{X}Com	^{X}TS	^{X}Pro
$H–P^+–H$	0.955	–405.8	–242.6	–425.7
$H–P^+–F$	0.914	–373.1	–235.7	–427.4
$H–P^+–CH_3$	0.807	–325.8	–173.4	–382.0
$H–P^+–OH$	0.751	–289.7	–146.1	–346.5
$H–P^+–OCH_3$	0.672	–248.1	–105.5	–312.4
$H–P^+–NH_2$	0.644	–210.8	–59.8	–265.2
$H–P^+–NHCH_3$	0.555	–174.8	–24.9	–230.9

As displayed in Table III, for the substituted HXP^+, the greater the positive charge on phosphorus in phosphenium cation, the more stable the formed complex will be. Take the substituted $HP^+–OH$ as an example, both the phosphorus and oxygen are in sp^2 hybridization. The unoccupied p orbital of phosphorus and occupied p orbital of oxygen are in parallel. The two p orbitals overlap to form a π bond, in which some electrons on oxygen transferred to phosphorus, resulting in a decrease in the positive charge of phosphorus in $HP^+–OH$. The greater the electronegativity, the greater is the ability of bounding electron, therefore, the less the electrons are transferred to phosphorus. The electronegativity order of elements in the second period is F > O > N > C, therefore, the order of positive charge on phosphorus should be $HP^+–F > HP^+–OH > HP^+–NH_2 > HP^+–CH_3$, which is in good agreement with the calculated results, with an exception of $HP^+–CH_3$. The reason is that the carbon in the $–CH_3$ group is in sp^3 hybridization and hence, cannot form a π bond with the unoccupied p orbital of phosphorus, which limits the transfer of electron from C to P. In addition, the fluorine in $HP^+–F$ is also in sp^3 hybridization. The sp^3 hybridization combined with highest electronegativity, the electron on fluorine can't transfer to phosphorus, which results in highest positive charge on the fluorine in $HP^+–F$. As shown in Fig. 4, there is a simple linear relationship between relative energy of ^{X}Com and positive charge on phosphorus of HXP^+.

The order of the positive charge density in the substituted phosphenium cation is consistent with the order of their Lewis acidities reported by the Slattery group.[10]

The Com transforms to the Pro *via* a ring-expanding process with a barrier of 163.2 kJ mol^{-1}. The unique imaginary frequency calculated for the corresponding TS is 512i cm^{-1} at the B3LYP/6-311++G** level of theory.

As shown in Fig. 1, the distance of $C^2–P$ in TS is 0.263 nm, indicating the new bond of $C^2–P$ is to be formed. Simultaneously, the $C^2–N$ distance in the R2 fragment of TS reached 0.213 nm, which is greatly elongated than that in Com.

Therefore, based on the bond length data, the single bond of C^2–N in Com is to be broken *via* TS. The formation of the new σ bond of C^2–P and the break of σ bond of C^2–N occurred simultaneously. The Pro is a four-membered ring compound, bearing phosphorus and nitrogen, which is stabilized by 19.9 kJ mol^{-1} compared to the three-membered Com.

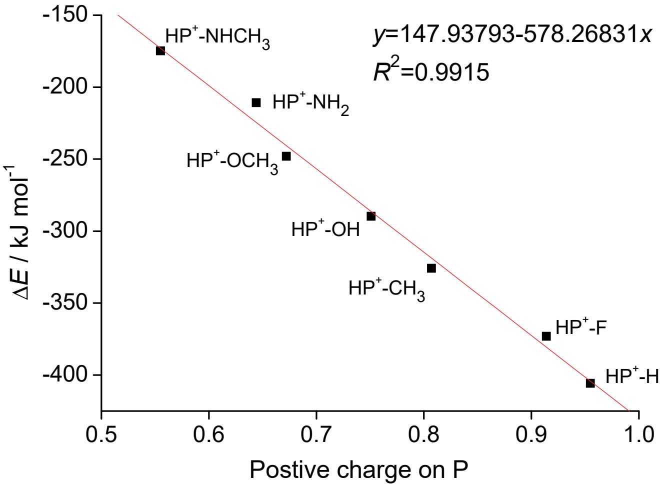

Fig. 4. The relationship between relative energy of ^{X}Com and the positive charge on the phosphorus of HXP^+.

CONCLUSIONS

In the present study, the insertion reaction between the phosphenium cation and azirane has been comprehensively investigated employing the B3LYP theoretical method with 6-311++G** and aug-cc-pVTZ basis sets. The first step of the reaction is the formation of a complex without barrier. H_2P^+ acts as an electrophilic reagent and accepts the σ electrons of azirane in the combination process. The greater the positive charge on the phosphorus in the phosphenium cation, the more stable is the formed complex. Introduction of substituents will decrease the positive charge on the phosphorus in the phosphenium cation. The order of positive charge of phosphorus is HP^+–F > HP^+–OH > HP^+–NH_2, which is consistent with their Lewis acidities. Therefore, introduction of substituents will decrease the stability of the complex. The complex transforms to a four-membered ring product *via* a transition state. The product is more stable than the complex due to the decreased ring-tension.

SUPPLEMENTARY MATERIAL

Matrixes of whole optimized structures are available electronically at the pages of journal website: https://www.shd-pub.org.rs/index.php/JSCS/article/view/11539, or from the corresponding author on request.

Acknowledgments. This work was supported by the Nature Science Foundation of Shandong Province (ZR2020MC004), and Focus on Research and Development Plan in Shandong Province (2019JZZY011116).

ИЗВОД

ТЕОРИЈСКО ПРОУЧАВАЊЕ РЕАКЦИЈЕ УГРАДЊЕ ФОСФЕНИЈУМ КАТЈОНА НА АЗИРАН

JINSONG GU, XIAODONG ZHAO, SHANKUI LIU и XIAOJUN TAN

College of Biological Science and Technology, University of Jinan, Jinan, Shandong, 250022, People's Republic of China

Механизам реакције уградње фосфенијум катјона у азирен проучен је теоретски како би се боље разумела реактивност интермедијера валентно изоелектронским са карбеном. Фосфенијум катјон делује као електрофилни реагенс и прихвата σ електроне азирана формирајући комплекс у првом ступњу комбиновања. Што је веће позитивно наелектрисање на фосфору у фосфенијум катјону, то је формирани комплекс стабилнији. Увођење супституената ће смањити позитивно наелектрисање на фосфору у фосфенијум катјону. Редослед позитивних наелектрисања на фосфору је $HP^+–F > HP^+–OH > HP^+–NH_2$, што се слаже са Лусовим киселостима. Комплекс се трансформише у производ са четворочланим прстеном преко прелазног стања у другом ступњу уградње. Производ је стабилнији од комплекса због смањења напона у прстену.

(Примљено 3. јануара, ревидирано 22. фебруара, прихваћено 7. марта 2022)

REFERENCES

1. J. F. Harrison, R. C. Liedtke, J. F. Liebman, *J. Am. Chem. Soc.* **101** (1979) 162 (https://doi.org/10.1021/ja00518a006)
2. D. E. Falvey, C. J. Cramer, *Tetrahedron Lett.* **33** (1992) 1705 (https://doi.org/10.1016/S0040-4039(00)91711-8)
3. J. Berkowitz, L. A. Curtiss, S. T. Gibson, J. P. Greene, *J. Chem. Phys.* **84** (1986) 375 (https://doi.org/10.1063/1.450147)
4. J. F. Harrison, *J. Am. Chem. Soc.* **103** (1981) 7406 (https://doi.org/10.1021/ja00415a002)
5. H. M. Cheng, C. F. Lin, S. Y. Chu, *J. Phys. Chem., A* **111** (2007) 6890 (https://doi.org/10.1021/jp070812i)
6. M. G. Thomas, C. W. Schultz, R. W. Parry, *Inorg. Chem.* **16** (1977) 994 (https://doi.org/10.1021/ic50171a005)
7. J. C. Clyburne, M. J. Schriver, *Inorg. Chem.* **35** (1996) 3062 (https://doi.org/10.1021/ic951132+)
8. G. David, E. Niecke, M. Nieger, J. Radseck, W. W. Schoeller, *J. Am. Chem. Soc.* **116** (1994) 2191 (https://doi.org/10.1021/ja00084a088)
9. J. W. Larson, T. B. McMahon, *Inorg. Chem.* **26** (1987) 4018 (https://doi.org/10.1021/ic00271a011)
10. J. M. Slattery, S. Hussein, *Dalton Trans.* **41** (2012) 1808 (https://doi.org/10.1039/c1dt11636c)
11. H. P. Műller, D. E. Woon, *J. Phys. Chem., A* **117** (2013) 13868 (https://doi.org/10.1021/jp4083807)
12. C. A. Dyker, N. Burford, *Chem. Asian J.* **3** (2008) 28 (https://doi.org/10.1002/asia.200700229)
13. N. Burford, P. J. Ragogna, R. McDonald, M. J. Ferguson, *J. Am. Chem. Soc.* **125** (2003) 14404 (https://doi.org/10.1021/ja036649w)

14. J. J.Weigand, M. Holthausen, R. Fröhlich, *Angew. Chem. Int. Ed*. **48** (2009) 295 (https://doi.org/10.1002/anie.200804903)
15. N. E. Brasch, I. G. Hamilton, E. H. Krenske, S. Bruce, *Organometallics* **23** (2004) 299 (https://doi.org/10.1021/om030607z)
16. B. Breit, *J. Mol. Catal., A* **143** (1999) 143 (https://doi.org/10.1016/S1381-1169(98)00377-X)
17. A. H. Cowley, R. A. Kemp, *Chem. Rev*. **85** (1985) 367 (https://doi.org/10.1021/cr00069a002)
18. T. Krachko, J. C. Slootweg, *Eur. J. Inorg. Chem*. **24** (2018) 2734 (https://doi.org/10.1002/ejic.201800459)
19. M. B. Abrams, B. L. Scott, R. T. Baker, *Organometallics* **19** (2000) 4944 (https://doi.org/10.1021/om0005351)
20. D. Gudat, A. Haghverdi, M. Nieger, *J. Organomet. Chem*. **617** (2001) 383 (https://doi.org/10.1016/S0022-328X(00)00624-0)
21. S. Burck, D. Gudat, *Inorg. Chem*. **47** (2008) 315 (https://doi.org/10.1021/ic7017049)
22. S. G. He, B. S. Tackett, D. J. Clouthier, *J. Chem. Phys.* **121** (2004) 257 (https://doi.org/10.1063/1.1758699)
23. C. Lee, W. Yang, R.G. Parr, *Phys. Rev., B* **37** (1988) 785 (https://doi.org/10.1103/PhysRevB.37.785)
24. Y. Zhao, W. H. Wang, W. L. Feng, W. L. Wang, P. Li, *J. Phys. Chem., A* **122** (2018) 7312 (https://doi.org/10.1021/acs.jpca.8b04775)
25. K. Xu, W. W. Wang, W. J. Wei, W. L. Feng, Q. Sun, P. Li, *J. Phys. Chem., A* **121** (2017) 7236 (https://doi.org/10.1021/acs.jpca.7b05858)
26. Gaussian 09, Gaussian, Inc., Wallingford, CT, 2010 (https://gaussian.com/g09citation/).

Journal of the Serbian Chemical Society
JSCS@tmf.bg.ac.rs • www.shd.org.rs/JSCS
J. Serb. Chem. Soc. 87 (7–8) S284–S294 (2022)
Supplementary material

SUPPLEMENTARY MATERIAL TO

Theoretical study on the insertion reaction of the phosphenium cation and azirane

JINSONG GU, XIAODONG ZHAO, SHANKUI LIU and XIAOJUN TAN*

College of Biological Science and Technology, University of Jinan, Jinan, Shandong, 250022, People's Republic of China

J. Serb. Chem. Soc. 87 (7–8) (2022) 857–865

TABLE S-I. The Cartesian coordinates of the optimized specie (H_2P^+) at the B3LYP/6-311++G** level

Atoms	*x*	*y*	*z*
P	0.000000	0.000000	0.117031
H	0.000000	1.028323	-0.877732
H	0.000000	-1.028323	-0.877732

TABLE S-II. The Cartesian coordinates of the optimized specie (Azirane) at the B3LYP/6-311++G** level

Atoms	*x*	*y*	*z*
C	0.741742	-0.400099	0.023277
C	-0.743412	-0.397661	0.023314
H	1.250532	-0.564422	0.968543
H	1.281447	-0.749939	-0.849746
H	-1.252006	-0.559948	0.969008
H	-1.284617	-0.746014	-0.849376
N	0.001642	0.857569	-0.171807
H	0.003166	1.403901	0.684676

---

* Corresponding author. E-mail: chem.2001@163.com

TABLE S-III. The Cartesian coordinates of the optimized specie (Com) at the B3LYP/6-311++G** level

Atoms	*x*	*y*	*z*
C	1.390212	-0.736451	-0.183067
C	1.390209	0.736453	-0.183066
H	1.077243	-1.264291	-1.075583
H	2.046946	-1.276269	0.487167
H	1.077238	1.264290	-1.075583
H	2.046941	1.276275	0.487166
P	-1.429443	0.000000	-0.201659
H	-1.876090	-1.041582	0.653840
H	-1.876091	1.041581	0.653840
N	0.273532	-0.000001	0.509470
H	0.348207	-0.000003	1.524545

TABLE S-IV. The Cartesian coordinates of the optimized specie (TS) at the B3LYP/6-311++G** level

Atoms	*x*	*y*	*z*
C	1.415938	-0.442804	-0.271250
C	1.245202	0.960660	0.125210
H	1.525773	-0.626935	-1.339146
H	2.208595	-0.952693	0.282116
H	1.095917	1.769950	-0.581719
H	1.275264	1.202579	1.182388
P	-1.259765	0.200692	-0.141597
H	-2.272124	-0.753888	-0.411500
H	-1.719094	0.590118	1.137307
N	0.104851	-0.829833	0.249967
H	0.081342	-1.537811	0.980975

TABLE S-V. The Cartesian coordinates of the optimized specie (Pro) at the B3LYP/6-311++G** level

Atoms	*x*	*y*	*z*
C	-1.372724	-0.168360	-0.000024
C	-0.506694	1.143060	-0.000046
H	-1.985654	-0.275448	0.894407
H	-1.985767	-0.275432	-0.894378
H	-0.599089	1.760085	0.892044
H	-0.599005	1.759957	-0.892234
P	0.961782	0.051518	0.000070
H	1.825563	0.098572	1.115273
H	1.825871	0.098545	-1.114890
N	-0.203552	-1.097173	-0.000115
H	-0.207288	-2.107042	-0.000049

TABLE S-VI. The Cartesian coordinates of the optimized specie (^{F}Com) at the B3LYP/6-311++G** level

Atoms	*x*	*y*	*z*
C	-1.571281	0.847820	-0.368340
C	-1.962415	-0.520618	0.045588
H	-1.228251	1.020943	-1.382417
H	-1.991919	1.709705	0.136837
H	-1.900794	-1.331099	-0.672455
H	-2.667016	-0.665781	0.856368
P	1.025955	-0.609931	-0.273374
H	1.341834	-1.372098	0.923966
N	-0.602234	0.031351	0.487848
H	-0.533991	0.328042	1.463551
F	1.889846	0.808510	0.144038

TABLE S-VII. The Cartesian coordinates of the optimized specie (^{F}TS) at the B3LYP/6-311++G** level

Atoms	*x*	*y*	*z*
C	1.645019	-0.681656	-0.296516
C	1.806735	0.772512	-0.130054
H	1.513614	-1.042014	-1.315123
H	2.405603	-1.269555	0.221424
H	1.683061	1.484090	-0.939373
H	2.103810	1.147085	0.843691
P	-0.789141	0.511332	0.032328
H	-1.178379	0.903212	1.335945
N	0.401782	-0.655585	0.482915
H	0.352927	1.228620	1.325750
F	-2.062946	-0.402247	-0.308691

TABLE S-VIII. The Cartesian coordinates of the optimized specie (^{F}Pro) at the B3LYP/6-311++G** level

Atoms	*x*	*y*	*z*
C	1.692775	-0.073138	-0.372355
C	0.848860	1.166327	0.095717
H	1.899693	-0.067830	-1.443888
H	2.616120	-0.203074	0.194102
H	0.589584	1.895141	-0.673536
H	1.203510	1.665706	0.998564
P	-0.579872	-0.042717	0.441952
H	-1.281020	-0.318798	1.650189
N	0.667036	-1.104494	0.013421
H	0.708850	-2.107238	-0.110688
F	-1.884191	0.105464	-0.630905

TABLE S-IX. The Cartesian coordinates of the optimized specie (^{CH3}Com) at the B3LYP/6-311++G** level

Atoms	*x*	*y*	*z*
C	-1.654878	0.829411	-0.451344
C	-2.016190	-0.463603	0.181458
H	-1.366702	0.844464	-1.496084
H	-2.060621	1.754853	-0.059354
H	-1.986423	-1.370308	-0.411686
H	-2.683469	-0.480972	1.035388
P	0.920773	-0.667524	-0.302207
H	1.116771	-1.521771	0.852501
N	-0.643475	0.140001	0.457957
H	-0.531379	0.562315	1.380599
C	2.159272	0.698945	0.160146
H	3.159677	0.299245	-0.038547
H	2.007987	1.564075	-0.488336
H	2.107667	0.992436	1.211362

TABLE S-X. The Cartesian coordinates of the optimized specie (^{CH3}TS) at the B3LYP/6-311++G** level

Atoms	*x*	*y*	*z*
C	-1.740183	0.701994	-0.292454
C	-1.899376	-0.738489	-0.064024
H	-1.668630	1.019353	-1.331189
H	-2.460311	1.318890	0.247740
H	-1.812362	-1.481483	-0.847727
H	-2.138566	-1.075702	0.938232
P	0.721672	-0.550098	-0.033755
H	0.901348	-1.177198	1.220726
N	-0.450676	0.692535	0.404181
H	-0.376153	1.254324	1.251116
C	2.303769	0.361036	-0.174695
H	2.455634	1.019880	0.685752
H	3.121379	-0.364766	-0.204313
H	2.322047	0.943178	-1.096241

TABLE S-XI. The Cartesian coordinates of the optimized specie ($^{\mathrm{CH_3}}$Pro) at the B3LYP/6-311++G** level

Atoms	*x*	*y*	*z*
C	-1.787417	-0.122079	0.332778
C	-0.926324	1.159308	0.045537
H	-2.124577	-0.190537	1.369537
H	-2.645716	-0.208879	-0.338216
H	-0.690265	1.769372	0.917884
H	-1.271982	1.788543	-0.774460
P	0.522601	0.016415	-0.450546
H	0.849663	0.010278	-1.844452
N	-0.706425	-1.105898	0.016724
H	-0.758318	-2.112273	-0.014723
C	2.122124	0.022829	0.501442
H	2.691110	-0.883039	0.273904
H	2.705135	0.899811	0.203831
H	1.900623	0.061437	1.569286

TABLE S-XII. The Cartesian coordinates of the optimized specie ($^{\mathrm{OH}}$Com) at the B3LYP/6-311++G** level

Atoms	*x*	*y*	*z*
C	-1.695852	0.763021	-0.471553
C	-1.971841	-0.509306	0.244245
H	-1.473340	0.735657	-1.532326
H	-2.113749	1.692326	-0.102057
H	-1.949100	-1.442866	-0.307205
H	-2.586103	-0.510032	1.137192
P	1.005391	-0.588565	-0.334955
H	1.148602	-1.461795	0.807123
N	-0.612040	0.157905	0.406718
H	-0.437178	0.636995	1.293815
O	2.021057	0.662487	0.322249
H	2.451984	1.250670	-0.333391

TABLE S-XIII. The Cartesian coordinates of the optimized specie (^{OH}TS) at the B3LYP/6-311++G** level

Atoms	*x*	*y*	*z*
C	1.692162	-0.680690	-0.294859
C	1.826598	0.771648	-0.117195
H	1.587856	-1.036542	-1.317971
H	2.445899	-1.263996	0.236926
H	1.701297	1.485828	-0.922511
H	2.108074	1.144366	0.861184
P	-0.778849	0.502415	0.002067
H	-1.068812	0.997248	1.289859
N	0.431890	-0.670072	0.458816
H	0.387669	-1.221003	1.317023
O	-2.154086	-0.353768	-0.149948
H	-2.382341	-0.667218	-1.035320

TABLE S-XIV. The Cartesian coordinates of the optimized specie (^{OH}Pro) at the B3LYP/6-311++G** level

Atoms	*x*	*y*	*z*
C	1.707575	0.014783	-0.379042
C	0.786996	1.169056	0.156139
H	1.917175	0.104814	-1.446714
H	2.637951	-0.091922	0.181078
H	0.460459	1.904437	-0.580542
H	1.124071	1.656822	1.070888
P	-0.564671	-0.125277	0.439795
H	-1.142846	-0.528675	1.681885
N	0.748829	-1.097490	-0.062340
H	0.848426	-2.081689	-0.267612
O	-1.865110	0.229451	-0.601463
H	-2.663523	-0.340835	-0.650405

TABLE S-XV. The Cartesian coordinates of the optimized specie (^{OCH_3}Com) at the B3LYP/6-311++G** level

Atoms	*x*	*y*	*z*
C	-1.873640	1.086102	-0.350917
C	-2.498523	-0.181116	0.109292
H	-1.581682	1.183915	-1.390361
H	-2.090556	2.013294	0.166738
H	-2.654169	-0.984232	-0.602569
H	-3.165381	-0.179826	0.963635
P	0.417048	-0.908645	-0.378200
H	0.232469	-1.975755	0.580613
N	-1.037731	0.092331	0.437031
H	-0.824842	0.350912	1.403660
O	1.666956	-0.130823	0.539836
C	2.588591	0.834682	-0.110134
H	3.351987	1.022333	0.642771
H	3.041797	0.399095	-1.003238
H	2.064571	1.762195	-0.355604

TABLE S-XVI. The Cartesian coordinates of the optimized specie (^{OCH_3}TS) at the B3LYP/6-311++G** level

Atoms	*x*	*y*	*z*
C	-1.903391	0.974604	-0.030631
C	-2.295116	-0.328828	-0.581776
H	-1.539492	1.712024	-0.743075
H	-2.644536	1.418816	0.635555
H	-2.115927	-0.619451	-1.609776
H	-2.826637	-1.019245	0.062866
P	0.256434	-0.753654	-0.088419
H	0.189468	-1.832447	0.818046
N	-0.837689	0.329805	0.749472
H	-0.890346	0.398644	1.766666
O	1.741692	-0.281282	0.336903
C	2.500409	0.732865	-0.376814
H	3.510074	0.678516	0.021305
H	2.510335	0.516959	-1.446734
H	2.079430	1.720765	-0.184775

TABLE S-XVII. The Cartesian coordinates of the optimized specie (^{OCH_3}Pro) at the B3LYP/6-311++G** level

Atoms	x	y	z
C	-2.143774	0.188350	-0.488199
C	-1.414850	-1.112924	-0.000728
H	-2.268121	0.219998	-1.572649
H	-3.102885	0.356365	0.004913
H	-1.113058	-1.814759	-0.779236
H	-1.888455	-1.635560	0.830555
P	0.048359	-0.029187	0.522437
H	0.526095	0.190643	1.854529
N	-1.097067	1.140550	0.010227
H	-1.067740	2.143923	-0.100942
O	1.420689	-0.439430	-0.388438
C	2.768215	0.188152	-0.239896
H	3.440278	-0.527337	-0.708845
H	2.782811	1.139612	-0.772583
H	3.022095	0.315037	0.816555

TABLE S-XV. The Cartesian coordinates of the optimized specie (^{NH_2}Com) at the B3LYP/6-311++G** level

Atoms	*x*	*y*	*z*
C	-1.723613	0.816451	-0.411983
C	-2.019364	-0.524470	0.157517
H	-1.431472	0.895187	-1.452950
H	-2.190809	1.697296	0.012567
H	-1.938832	-1.398925	-0.478796
H	-2.697714	-0.620162	0.997156
P	0.992646	-0.564238	-0.333020
H	1.137399	-1.470578	0.785332
N	-0.690912	0.142008	0.469879
H	-0.595095	0.531589	1.409286
N	2.147628	0.599330	0.189984
H	2.591006	0.605631	1.098890
H	2.496678	1.282277	-0.468429

TABLE S-XVI. The Cartesian coordinates of the optimized specie (^{NH2}TS) at the B3LYP/6-311++G** level

Atoms	*x*	*y*	*z*
C	1.710735	-0.690565	-0.287556
C	1.911635	0.745586	-0.069940
H	1.616525	-1.013806	-1.322520
H	2.429086	-1.319169	0.242482
H	1.818443	1.485114	-0.856297
H	2.180080	1.082357	0.924569
P	-0.759200	0.511430	-0.042677
H	-1.018858	1.117213	1.205301
N	0.434414	-0.673560	0.442253
H	0.348943	-1.275734	1.262683
N	-2.191729	-0.339102	-0.172709
H	-2.940078	-0.262809	0.503537
H	-2.479151	-0.726108	-1.061439

TABLE S-XVII. The Cartesian coordinates of the optimized specie (^{NH2}Pro) at the B3LYP/6-311++G** level

Atoms	*x*	*y*	*z*
C	-1.775432	-0.100882	0.302593
C	-0.901995	1.158938	-0.011682
H	-2.124990	-0.136896	1.336756
H	-2.623395	-0.203915	-0.377976
H	-0.689952	1.812706	0.835544
H	-1.211652	1.751119	-0.873638
P	0.558127	-0.007588	-0.404628
H	1.048259	-0.103510	-1.739038
N	-0.701248	-1.105180	0.023541
H	-0.756590	-2.112333	0.065506
N	2.006609	0.059340	0.483108
H	2.902338	-0.112083	0.044132
H	2.011112	0.191279	1.486125

TABLE S-XVIII. The Cartesian coordinates of the optimized specie (^{NHCH3}Com) at the B3LYP/6-311++G** level

Atoms	x	y	z
C	-1.892170	1.137037	-0.206584
C	-2.545124	-0.191151	-0.065733
H	-1.452606	1.411128	-1.158817
H	-2.216227	1.963719	0.414769
H	-2.569210	-0.861745	-0.917703
H	-3.338725	-0.330295	0.658950
P	0.426751	-0.867474	-0.377522
H	0.250910	-2.001483	0.504899
N	-1.159155	0.025662	0.515934
H	-1.111892	0.118153	1.532046
N	1.788858	-0.199328	0.427825
H	2.081794	-0.550901	1.332029
C	2.614210	0.887424	-0.135677
H	2.490447	1.815654	0.431475
H	3.668046	0.596552	-0.118527
H	2.326789	1.067133	-1.174634

TABLE S-XIX. The Cartesian coordinates of the optimized specie (^{NHCH3}TS) at the B3LYP/6-311++G** level

Atoms	*x*	*y*	*z*
C	-1.934062	0.970953	-0.009008
C	-2.413656	-0.314598	-0.522559
H	-1.590538	1.688653	-0.751337
H	-2.621087	1.449088	0.691755
H	-2.284910	-0.627085	-1.551756
H	-2.923802	-0.984227	0.159633
P	0.237707	-0.739795	-0.143335
H	0.153834	-1.889625	0.672519
N	-0.839505	0.326912	0.737620
H	-0.824018	0.449380	1.751720
N	1.779940	-0.280490	0.305571
H	2.297778	-0.865615	0.949493
C	2.571057	0.755911	-0.372834
H	2.939006	1.485174	0.351271
H	3.419283	0.314733	-0.900672
H	1.945777	1.277902	-1.098544

TABLE S-XX. The Cartesian coordinates of the optimized specie (^{NHCH3}Pro) at the B3LYP/6-311++G** level

Atoms	*x*	*y*	*z*
C	-2.275046	0.143762	-0.294408
C	-1.442024	-1.131860	0.058020
H	-2.632665	0.152604	-1.326677
H	-3.114264	0.298697	0.387417
H	-1.265501	-1.826137	-0.764994
H	-1.760468	-1.678805	0.946249
P	0.068649	-0.008026	0.385198
H	0.582534	0.155809	1.704254
N	-1.168302	1.120204	-0.056285
H	-1.193140	2.125805	-0.142115
N	1.506309	-0.229079	-0.500661
H	1.419218	-0.485880	-1.477926
C	2.870556	0.094833	-0.019267
H	2.863691	0.226537	1.066309
H	3.537650	-0.737383	-0.254543
H	3.246247	1.010851	-0.483389

Journal of the Serbian Chemical Society
JSCS@tmf.bg.ac.rs • www.shd.org.rs/JSCS

J. Serb. Chem. Soc. 87 (7–8) 867–877 (2022)
JSCS–5563

Original scientific paper
Published 19 July 2022

Supercapacitive properties of the alkali metal hydroxides--activated carbons obtained from sucrose•

MILICA G. KOŠEVIĆ[1*#], SANJA S. KRSTIĆ[2], VLADIMIR V. PANIĆ[1,3,4#]
and BRANISLAV Ž. NIKOLIĆ[5#]

[1]Institute of Chemistry, Technology and Metallurgy, National Institute of the Republic of Serbia, University of Belgrade, Belgrade, Serbia, [2]University of Belgrade, Vinča Institute of Nuclear Sciences, Belgrade, Serbia, [3]Centre of Excellence in Environmental Chemistry and Engineering – ICTM, University of Belgrade, Belgrade, Serbia, [4]State University of Novi Pazar, Department of Natural and Mathematical Sciences, Novi Pazar, Serbia and [5]Faculty of Technology and Metallurgy, University of Belgrade, Belgrade, Serbia

(Received 30 June, revised and accepted 18 July 2022)

Abstract: The influence of different hydroxides, applied to activate carbon black, on the electrochemical properties of activated carbon was investigated. The carbon material was prepared by hydrothermal treatment of sucrose and afterwards thermally activated using KOH, NaOH and LiOH. The electrochemical properties of the obtained samples were examined by cyclic voltammetry and electrochemical impedance spectroscopy and correlated to their physicochemical properties. All samples showed characteristic capacitor-like behaviour. The highest specific capacitance was obtained for the KOH-treated sample, while the increase in capacitance follows the sequence of the growth of ionic radius of a metal from an alkali which is used for activation. It was found that the dependence on the type of hydroxide is due to differences in the radii of a metal. The alkalies of larger radii of metal generated make pores wider and consequently the structure of a porous layer become more accessible to the charge transfer of capacitive response.

Keywords: sucrose-derived carbons; alkali-treated carbon materials; sugar-derived carbons; electrochemical capacitance distribution.

---

[*] Corresponding author. E-mail: milica.kosevic@ihtm.bg.ac.rs
[#] Serbian Chemical Society member.

[•] This paper is dedicated to our distinquished colleagues, Radoslav Atanasoski and Radoslav Adžić, to honour their 80th birthday anniversaries (born in January and February 1942, respectively). Both of them gave outstanding contribution to the contemporary electrochemistry, particularly to electrocatalysis and fuel cell development. During decades, being outstanding scientists, they were our coworkers and teachers, but also exceptionally good friends. We wish to both of these great men all the best for many years to come.

https://doi.org/10.2298/JSC220730059K

INTRODUCTION

Emerging advances in modern electronics have been given rise to increased necessities for highly efficient energy storage systems. As one of the most popular type of electrochemical energy storage systems, supercapacitors recently gained the highest attention owing to the following characteristics: high power density, structure-dependent charge/discharge rate, energy density, environmental friendliness, rentability, long cycle life, *etc.*[1,2] Their superior capacitive properties originate not only from the charge stored in an electrochemical double layer, but also from the fast and highly reversible Faradaic reactions occurring at the electrode/electrolyte interface, which results in the so-called pseudocapacitance.[3,4] These unique performances are obtained from different redox-active and porous electrode materials, especially noble metal oxides,[5] but also from carbon-based materials,[2,6–9] including activated carbons,[10–14] graphene,[4,15–17] carbon nanogels[18] and carbon nanotubes.[19,20] Carbon-based materials are among the most popular for supercapacitor application. They possess the required properties such as high surface area, low specific volume, controllable pore size, good electrical and thermal conductivity, acceptable chemical stability. The most important feature are low synthesis costs, since carbon-based materials can be obtained from a variety of cheap and waste precursor materials.[21,22] Environmentally friendly and economically acceptable precursors are definitely the main advantage of the carbon-based materials of excellent capacitive properties. Numerous studies of waste biomass-derived active carbons demonstrate their high specific surface areas, as well as specific capacitance values. K_2CO_3-activated waste tea-derived carbon can deliver specific capacitance of 123 F g^{-1}.[10] KOH-activated calyx biowaste-derived carbons possesses the specific surface area of 798 m^2 g^{-1} able to release the specific capacitance of 223 F g^{-1} at 1 A g^{-1} discharge current.[11] NaOH-activated carbon materials derived from heavy bio-oils give specific surface area as high as 2826 m^2 g^{-1} and the specific capacitances of 417 F/g at 0.5 A g^{-1} and 334 F g^{-1} at 20 A g^{-1}.[12] Even self-activated wood-derived carbon material delivers specific capacitance of 143.6 F g^{-1} at 1 A g^{-1} with surface area of 1145 m^2 g^{-1}.[13] Charging capability and energy-delivering efficiency in supercapacitor systems request materials with high surface area and pores that fit to the relief of ionic transport throughout. The pore size distribution and its variability are controllable characteristics of the active carbon materials and they depend on different factors. Set of parameters in synthesis and corresponding approach involves the definition of synthesis precursor used and the type of activation method applied subsequently.

The activation method of carbon materials can be chemical or physical. Cai *et al.*[23] investigated the influence of the synthesis and activation conditions on the properties of the KOH-activated carbon. Specific surface area and capacitance of the carbon obtained from the glucose, another common and cheap precursor, significantly varied depending on the activation conditions, *i.e.*, synthesis temperature, sample/activation agent ratio, concentration of the precursor solutions, *etc*. Besides the mentioned synthesis conditions, activation processes are intrinsically governed by the type of activation agent that finally defines the porosity of the active product. Alkalies are widely used agents for chemical activation of carbon materials in the processes where the carbonization of organic precursors and activation process take place simultaneously.[11,12,23,24] These simultaneous processes significantly improve the structure and consequently capacitive properties. For example, the specific capacitance of the NaOH surface-activated commercial carbon cloth arose to 42.2 F g^{-1}, which is almost two orders of magnitude higher than the capacitance of the un-activated sample.[24] Beside alkalies, there are different chemical agents used for carbon activation, such as K_2CO_3,[10] H_3PO_4[10,25] and $ZnCl_2$.[26]

This research involves the influence of the different alkali activation agents on the morphology and consequently the electrochemical properties of the activated carbon materials obtained from sucrose. Considering the aforementioned desired assets of the precursors, sucrose was chosen as a cheap, nontoxic and easily accessible precursor material. The carbon-containing material, which was obtained by hydrothermal method from sucrose, did not possess any remarkable capacitive properties. Hence, the experiment was further performed by chemical activation procedure employing several alkalies, KOH, NaOH and LiOH, in order to find the best capacitive outputs in a term of specific surface area, microporous morphology and finally the correlation between capacitive and physicochemical properties, induced by the activation process.

EXPERIMENTAL

Material synthesis

Synthesis of the activated carbon materials was performed in two steps, as described in our previous work.[27] The first step is the hydrothermal treatment of the sucrose in order to obtain carbon-containing material, while in the second step carbonaceous materials were activated using hydroxides.

The required amount of sucrose was dissolved in the deionised water. The obtained 1.0 mol dm^{-3} solution was placed in an autoclave with polytetrafluoroethylene chamber and kept in an oven under autogenous pressure at 240 °C for 24 h. The activation was performed afterwards by chemical treatment of the obtained sample with KOH, NaOH or LiOH. Activation of the samples was completed in an atmosphere of nitrogen, since the presence of oxygen would result in complete pyrolysis and generation of CO_2, which affects porosity development as well.[28] After the physical mixing of dried selected carbon-containing precursors and a hydroxide in solid state at room temperature in a mass ratio of 1:3, the solid mixtures were thermally treated in a horizontal tube furnace (Protherm Furnaces, model PTF 16/38/250, Turkey) at 750 °C, under 200 cm^3 min^{-1} of nitrogen flow and the heating rate of 5 °C min^{-1}, with the retention time of 1 h. After carbonization and activation, the samples were washed with distilled water till the neutral pH value of effluent.

Electrochemical measurements

Basic electrochemical characteristics of the synthesized samples were investigated using cyclic voltammetry (CV) technique. Depending on the CV response and its stability stages, some of the samples were afterwards subjected to the electrochemical impedance spectroscopy (EIS) to further investigate their capacitive features. All measurements were performed in 0.1 M H_2SO_4 solution at ambient temperature. Cyclic voltammetry was done at the sweep rate of 50 mV s^{-1}. The EIS was recorded in a single sine mode at open circuit potential, with a sinusoidal voltage of 10 mV-amplitude (root mean square).

Electrochemical measurements were recorded in a three-electrode cell with Ag/AgCl reference electrode and platinum plate as a counter electrode on potentiostat/galvanostat Bio-Logic SP200 (Bio-Logic SAS, Grenoble, France). All potentials are referred to Ag/AgCl scale. The working electrode was prepared by pipetting the 0.020 ml of the sample suspension onto a glassy carbon disk (GC, 0.196 cm^2) electrode and dried at room temperature. Sample suspension consisted of 3 mg of alkali-treated carbon and 1 ml H_2O and was ultrasonically treated (40 kHz, 70 W) for 1 h before application. To ensure the adhesion of the dry layer, it was covered by the nafion from appropriate solution (1:100 volume ratio of 10 mass % nafion solution in isopropanol/water and water).

Considering that registered EIS data were of capacitive-like shape, they were fitted into the transmission line equivalent electrical circuit (TLEEC) of time distributed constants using ZView (v. 3.2b, Scribner Associates Inc., Southern Pines, NC, USA). TLEEC consisted of resistors and capacitors in a notation $R_\Omega(C_0(R_{p,1}(C_1(R_{p,2}(...(R_{p,n}C_n)))$, where C_n correlates to the capacitance available behind $\sum_{i=1}^{n} R_{p,i}$ resistances; R_Ω correlates to electrolyte ohmic resistance.

RESULTS AND DISCUSSION

Characteristic cyclic voltammograms (CVs) of the as synthesized and alkali-treated samples are shown in Fig. 1.

All registered CV curves are of typical capacitor-like shape for carbon-based materials.[29] The CV currents of the untreated sample (Fig. 1b) are significantly lower in comparison to those registered for alkali-treated samples (Fig. 1a), which demonstrates excellent activation efficiency. Weakly pronounced anodic peaks around 0.50 (for S) and 0.25 V (for activated samples) appear to be redox ones, since cathodic counterparts are registered during discharging. The LiOH-treated sample shows more than five-fold increase in CV currents with respect to the untreated sample. On the other hand, this increase is more than two orders of magnitude for the KOH- and NaOH-treated samples. The treatment causes a development of a redox transition around 0.25 V, quite close to the typical position of quinonic surface redox response.[30] Fig. 1 clearly shows that the improvements of capacitive properties by alkali treatment are more pronounced for alkalies containing an alkali metal of larger ionic radius. This indicates that the surface states of carbon particles are different if treated by different alkalies, which produces significant varieties in capacitive properties.

The investigation of CV response stability showed that the alkali-treated samples required from several tens up to 200 cycles, depending on alkali used, to reach the highest CV currents. The corresponding changes in capacitance[31] with cycling are shown in Fig. 2 for alkali-treated samples. The CV responses of the highest currents for KOH and LiOH treated samples were found to be unstable, since the currents gradually decreased upon subsequent cycling. This feature of decreasing CV currents was also alkali-dependent, varying from few tens for LiOH-treated sample to more than 100 cycles in a case of the S-KOH sample, for the currents to relax to the values of initial CV response. S-NaOH sample showed quite stable response upon the continuous increase in CV currents.

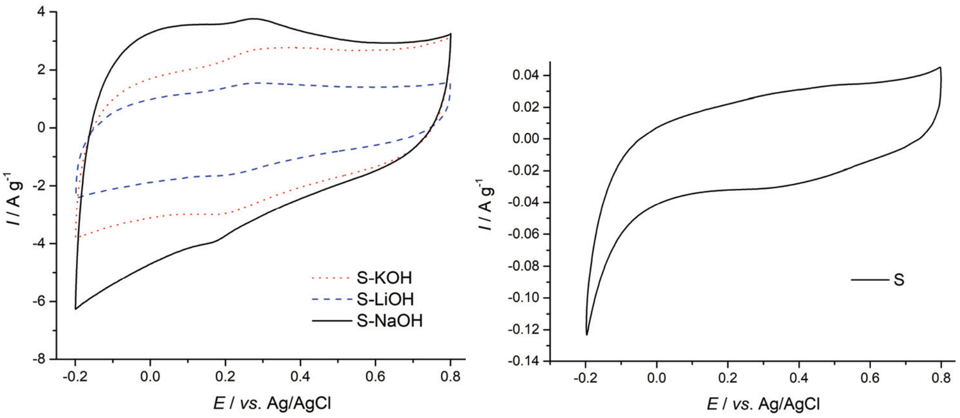

(a) (b)

Fig. 1. Cyclic voltammograms of alkali-treated (a) and as-synthesized (b) carbons. Electrolyte: 0.1 M H_2SO_4, $v = 50$ mV s^{-1}.

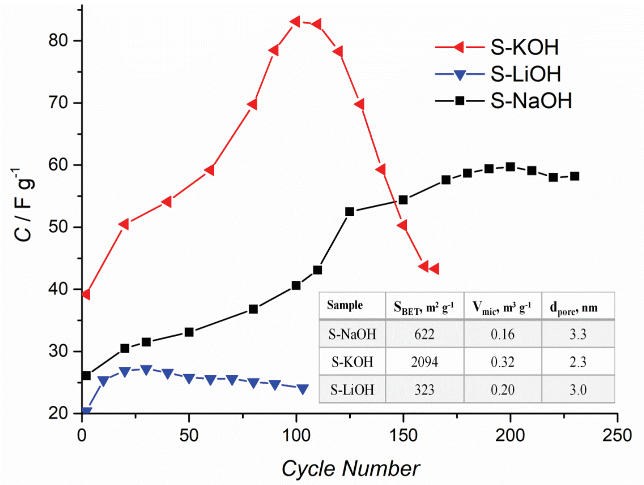

Sample	S_{BET}, m² g⁻¹	V_{mic}, m³ g⁻¹	d_{pore}, nm
S-NaOH	622	0.16	3.3
S-KOH	2094	0.32	2.3
S-LiOH	323	0.20	3.0

Fig. 2. Capacitance of alkali-treated samples during CV measurements. Electrolyte: 0.1 M H_2SO_4, $v = 50$ mV s^{-1}. Inset:[27] morphological properties of activated carbons (S–*X*OH): specific surface areas (S_{BET}), micropore volume (V_{mic}) and average pore width (d_{pore}).

The cycling initially produces the three-fold increase in capacitance upon 100 cycles for S-KOH sample. The highest specific capacitance registered in this most active charging/discharging cycle is around 85 F g^{-1}. However, this curing by cycling does not last, since subsequent cycling has an opposite effect – the capacitance is decreased to the initial values in next 65 cycles. In contrast to this unsteady capacitive behaviour, S-NaOH sample showed lower but stable capacitive response. Its capacitance steadily increases up to ~170 cycle. Once reached, the maximum specific capacitance of 60 F g^{-1} was preserved in the following 50 cycles. Stabilizing influence of NaOH was proved also in other systems requiring modification of solid–liquid interface for coating deposition onto electrified surface.[32],[33] Finally, the capacitance of LiOH-treated sample reached comparatively stable, but the lowest capacitance values of about 25 F g^{-1} during 100 cycles.

The changes from Fig. 2 could be caused by characteristic changes in the layer structures of KOH- and NaOH-treated samples induced by alkalies, and can be related to the samples' morphology parameters from the table shown as the inset of Fig. 2.[27] The values of maximum acquired specific capacitance are in an accordance with the samples' BET surface area. S-KOH exhibited the highest specific capacitance and this sample also possesses the highest specific area as well as the highest volume of micropores. In opposite to these highest values stands S-LiOH sample that exhibited both the lowest specific capacitance and specific area/volume of micropores. However, although samples' BET specific areas are in accordance with their maximum registered specific capacitances, this relation isn't proportional. Namely, the S-KOH surface is about 3.4 and 6.5 times larger than the surfaces of S-NaOH and S-LiOH samples, respectively, while the S-KOH maximum capacitance is only 1.4 and 3.3 times higher than those obtained for the S-NaOH and the S-LiOH, respectively. Moreover, the stable S-KOH specific capacitance is even lower than that of the S-NaOH, suggesting that capacitance isn't controlled solely by the BET surface area. According to the literature,[29,34] higher BET surface usually indicates higher capacitance. However, other parameters, like mesoporous surface and pore diameter, have also an effect on the capacitive behaviour. Although micropores (with pore diameter, d_p<2 nm) should have an essential role in the capacitance, acting as a source of adsorption sites, their small dimension could hinder the ion access to nanoporous structure. Hence, the presence of the mesoporous microporous surface (d_p in the range 2––50 nm) is of essential importance for ion accessibility.[35]

Since CV findings revealed more stable capacitive nature of the NaOH and LiOH-treated samples in comparison to the S-KOH, the S-NaOH and S-LiOH samples were further investigated by EIS measurements. The registered and fitting EIS data of these samples are presented in a capacitive complex plane in Fig. 3.

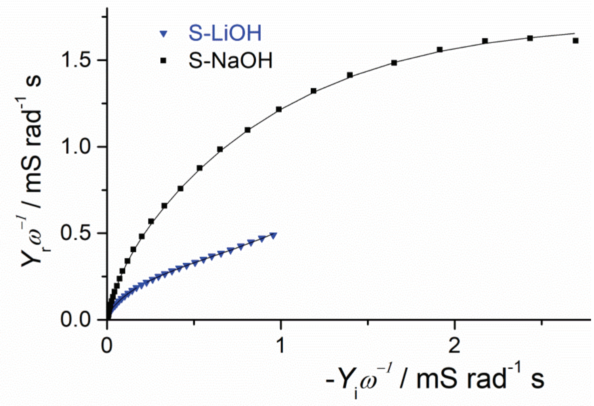

Fig. 3. Registered (symbols) and fitting (lines) EIS data of the S-LiOH and S-KOH samples.

Both samples showed capacitive loops, indicating their capacitive-like behaviour.

The S-NaOH related loop is considerably larger in comparison to the S-LiOH, suggesting its higher capacitance. This is in accordance with the capacitive values obtained from CV results (Fig. 1), where the S-NaOH sample also showed superior capacitive properties.

The differences in the samples' structure, reflected in the impedance characteristics (Fig. 3), are presented in Fig. 4 as the distributions of the pore resistance and the capacitance through a layer of the samples. The data were obtained by fitting the experimental EIS data to an appropriate TLEEC (as explained in Experimental; additional data are given in Supplementary material to this paper).

S-LiOH sample required higher number of the branches (higher *n*) in comparison to the S-NaOH sample, *i.e.*, 5 compared to 2. TLEEC, described in Experimental, required the parallel resistor and capacitor elements in series to TLEEC. This RC circuit can be assigned to the nafion layer at the sample surface, since the capacitance values are at least one order of the magnitude lower in comparison to the capacitances in each individual of TLEEC. On the other hand, *R* values are comparable to those in the branches. Hence, the initial increase in capacitances observed in the Fig. 2 can be attributed to the resistance decrease due to continuous wetting of the nafion layer. As shown in Fig. 2, the S-NaOH sample reached highest capacitance considerably faster. This is in accordance with mentioned *R* values ascribed to the nafion layer. Namely, the resistance of the nafion layer on the top of the S-NaOH sample was considerably higher than that registered for S-LiOH, 62 Ω, in contrast to 16 Ω. It follows that the electrolyte needs longer time to overcome higher resistance of the nafion layer in order to get the full access to the sample's surface. The unexpected difference in the impedance responses of a nafion layer might be due to its different interference with S-LiOH and S-NaOH.[36]

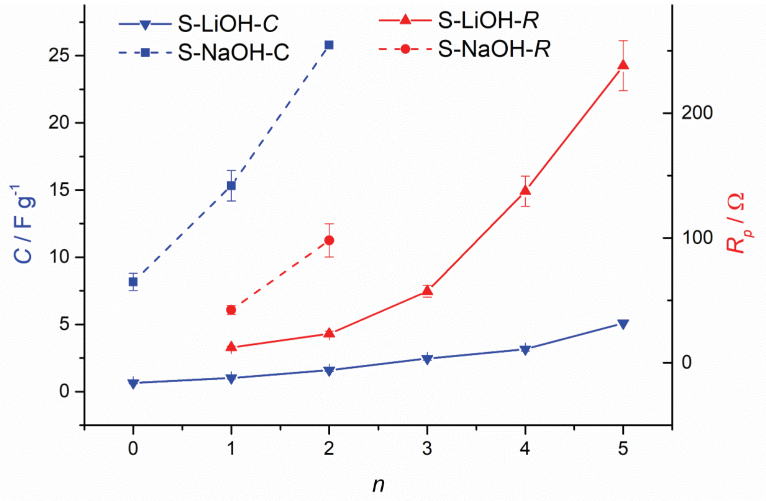

Fig. 4. The pore resistance (R_p) and capacitance (C) distribution throughout the porous structure of S-LiOH and S-NaOH. The values were obtained by fitting the data from Fig. 3 to 5- and 2-branched transmission line equivalent electrical circuits, respectively (the error bars, represent standard deviation of the fitting data).

Higher number of the branches required for the S-LiOH sample indicates its more complex structure, as a consequence of the smaller pore dimension of the S-LiOH in comparison to the S-NaOH (3.0 *vs*. 3.3 nm)[27] and higher micropores' volume (0.20 *vs*. 0.16 $cm^3 g^{-1}$)[27], causing its active sites harder to access. The overall capacitances calculated from the EIS results (Fig. 4) were 49.3 and 14.0 F g^{-1} for S-NaOH and S-LiOH, respectively. These values correlate to the overall pore resistance throughout the branches, *i.e.*, 140 Ω for S-NaOH and 468 Ω for S-LiOH. It can be concluded that S-NaOH sample is of more accessible structure, hence its pore resistance was lower due to the wider pores and consequently its active sites were more accessible to the electrolyte giving higher capacitance values. This is in accordance to CV results, showing that S-NaOH sample is of higer CV currents, *i.e.*, the capacitance values calculated from CV response were higher for this samples too, compared to the S-LiOH.

CONCLUSION

The treatment with alkalies causes a multi-fold increase in the capacitance of carbonaceous materials synthesized by sucrose pyrolysis, but the stability of the capacitive features during continuous charging/discharging is intrinsic. The capacitance during charging/discharging cycles initially increases and afterwards decreases. This feature is found to be caused by the continuous penetration of the electrolyte through the adhesion-ensuring nafion layer at the top of carbon layer.

The carbon layers activated with an alkali of small metal radius are of more developed porous structure, which is analyzed through the distributions of the capacitance and pore resistance, gained by impedance measurements. Although being of the more developed nanoporous structure, more compact layers are less available for charging/discharging processes and hence of modest capacitive characteristics.

The capacitive characteristics are more improved if the alkalies containing metal of the larger ionic radius are used for treatment. The correlation between capacitive features and physical characteristics of the carbon structure is suggested. The alkalies of larger radii of a metal are able to generate wider pores and consequently the structure of a porous layer more accessible for the charge transfer of capacitive response, which appears to be closely related to the degree of modification of the surface carbon particles.

SUPPLEMENTARY MATERIAL

Additional data and information are available electronically at the pages of journal website: https://www.shd-pub.org.rs/index.php/JSCS/article/view/11960, or from the corresponding author on request.

Acknowledgement. This work was funded by the Serbian Ministry of Education, Science and Technological Development Grant No. 451-03-68/2022-14/200026.

ИЗВОД

СУПЕРКАПАЦИТИВНА СВОЈСТВА УГЉЕНИЧНИХ МАТЕРИЈАЛА ДОБИЈЕНИХ ИЗ САХАРОЗЕ И АКТИВИРАНИХ ХИДРОКСИДИМА АЛКАЛНИХ МЕТАЛА

МИЛИЦА Г. КОШЕВИЋ[1], САЊА С. КРСТИЋ[2], ВЛАДИМИР В. ПАНИЋ[1,3,4] и БРАНИСЛАВ Ж. НИКОЛИЋ[5]

[1]Институт за хемију, технологију и металургију, Институт од националног значаја за републику Србију, Универзитет у Београду, Београд, [2]Институт за нуклеарне науке „Винча“, Универзитет у Београду, Београд, [3]Центар изузетних вредности, Институт за хемију, технологију и металургију, Инситут од националног значаја за републику Србију, Универзитет у Београду, Београд, [4]Државни универзитет у Новом Пазару, Департман за природно–математичке науке, Нови Пазар и [5]Технолошко–металуршки факултет, Универзитет у Београду, Београд

Испитиван је утицај различитих активирајућих хидроксида на електрохемијска својства активираних угљеничних материјала. Угљенични материјал је добијен хидротермалним третманом сахарозе, а потом активиран помоћу KOH, NaOH и LiOH. Електрохемијска својства добијених узорака испитивана су цикличном волтаметријом и спектроскопијом електрохемијске импеданције. Синтетизовани материјали показују капацитивна својства. Највећа специфична капацитивност добијена је за узорак третиран помоћу KOH, док капацитивност прати величину пречника јона метала из алкалије којом је активиран угљенични материјал.

(Примљено 30. јуна, ревидирано и прихваћено 18. јула 2022)

REFERENCES

1. B. K. Saikia, S. M. Benoy, M. Bora, J. Tamuly, M. Pandey, D. Bhattachary, *Fuel* **282** (2020) 118796 (https://doi.org/10.1016/j.fuel.2020.118796)
2. A. González, E. Goikolea, J. A. Barrena, R. Mysyk, *Renew. Sustain. Energy Rev*. **58** (2016) 1189 (https://doi.org/10.1016/j.rser.2015.12.249)
3. Y. Liu, S.P. Jiang, Z. Shao, *Mater. Today Adv.* 7 (2020) 100072 (https://doi.org/10.1016/j.mtadv.2020.100072)
4. D. Sačer, M. Kralj, S. Sopčić, M. Košević, A. Dekanski, M. K. Roković, *J. Serb. Chem. Soc.* **82** (2017) 411 (https://doi.org/10.2298/JSC170207027S)
5. G. Šekularac, M. Košević, A. Dekanski, V. Djokić, M. Panjan, V. Panić, *ChemElectroChem* **4** (2017) 2535 (https://doi.org/10.1002/celc.201700609)
6. D. M. Mijailović, M. M. Vukčević, Z. M. Stević, A. M. Kalijadis, D. B. Stojanović, V. V. Panić, Petar S. Uskoković, *J. Electrochem. Soc.* **164** (2017) A1061 (https://doi.org/10.1149/2.0581706jes)
7. V. N. K. S. K. Nersu, B.R. Annepu, S. S. B. Patcha, S. S. Rajaputra, *J. Electrochem. Sci. Eng.* **12** (2022) 451 (http://dx.doi.org/10.5599/jese.1310)
8. A. S. Dobrota, I. A. Pašti, J. *Electrochem. Sci. Eng*. **10** (2020) 141 (https://doi.org/10.5599/jese.742)
9. D. M. Mijailović, V. V. Radmilović, U. Č. Lačnjevac, D. B. Stojanović, V. D. Jović, V. R. Radmilović, P. S.Uskoković, *Appl. Surf. Sci.* **534** (2020) 147678 (https://doi.org/10.1016/j.apsusc.2020.147678)
10. I. I. G. Inal, S. M.Holmes, A. Banford, Z. Aktas, *Appl. Surf. Sci.* **357** (2015) 696 (https://doi.org/10.1016/j.apsusc.2015.09.067)
11. G. Dhakal, D. Mohapatra, Y-Il Kim, J. Lee, W. K. Kim, J-J. Shim, *Renew. Energy* **189** (2022) 587 (https://doi.org/10.1016/j.renene.2022.01.105)
12. Y. Zhu, Z. Li, Y. Tao, J. Zhou, H. Zhang, *J. Energy Storage* **47** (2022) 103624 (https://doi.org/10.1016/j.est.2021.103624)
13. Y. Chen, Y. Yu, X. Zhang, C. Guo, C. Chen, S. Wang, D. Min, *Ind. Crops Prod.* **181** (2022) 114802 (https://doi.org/10.1016/j.indcrop.2022.114802)
14. S. J. Rajasekaran, V. Raghavan, *J. Electrochem. Sci. Eng.* **12** (2022) 545 (http://dx.doi.org/10.5599/jese.1314)
15. G. Radić, I. Šajnović, Ž. Petrović, M.K. Roković, *Croat. Chem. Acta* **91** (2018) 481 (https://doi.org/10.5562/cca3452)
16. D. Sačer, I. Spajić, M. K. Roković, *J. Mater. Sci* **53** (2018) 15285 (https://doi.org/10.1007/s10853-018-2693-6)
17. S. S. Rajaputra, N. Pennada, A. Yerramilli, N. M. Kummara, *J. Electrochem. Sci. Eng*. **11** (2021) 197 (https://doi.org/10.5599/jese.1031)
18. M. Xu, A. Wang, Y. Xiang, J. Niu, *J. Clean. Prod.* **315** (2021) 128110 (https://doi.org/10.1016/j.jclepro.2021.128110)
19. S. Sopčić, N. Šešelj, M. K. Roković, *J. Solid State Electrochem.* **23** (2019) 205 (https://doi.org/10.1007/s10008-018-4122-9)
20. H. Pan, J. Li, Y. Feng, *Nanoscale Res. Lett.* **5** (2010) 654 (https://doi.org/10.1007/s11671-009-9508-2)
21. M. Karnan, A. G. Karthick Raj, K. Subramani, S. Santhoshkumara, M. Sathish, *Sustain. Energy Fuels* **4** (2020) 3029 (https://doi.org/10.1039/C9SE01298B)
22. S. Ahmed, A. Ahmed, M. Rafat, *J. Saudi Chem. Soc.* **22** (2018) 993 (https://doi.org/10.1016/j.jscs.2018.03.002)

23. X. Cai, Y. Xiao, W. Sun, F. Yang, *Electrochim. Acta* **406** (2022) 139861 (https://doi.org/10.1016/j.electacta.2022.139861)
24. S. Pang, L. Lin, Y. Shen, S. Chen, W. Chen, N. Tan, A. Ahmad, A. A. Al-Kahtani, A. M. Tighezza, *Mater. Lett.* **315** (2022) 131985 (https://doi.org/10.1016/j.matlet.2022.131985)
25. J. Xu, L. Chen, H. Qu, Y. Jiao, J. Xie, G. Xing, *Appl. Surf. Sci*. **320** (2014) 674 (https://doi.org/10.1016/j.apsusc.2014.08.178)
26. X. H. P. Ling, M. Yu, X. Wang, X. Zhang, M. Zheng, *Electrochim. Acta* **105** (2013) 635 (https://doi.org/10.1016/j.electacta.2013.05.050)
27. S. S. Krstić, M. M. Kragović, V. M. Dodevski, A. D. Marinković, B. V. Kaluđerović, G. Žerjav , A. Pintar, M. C. Pagnacco , M. D. Stojmenović, *Sci. Sinter.* **50** (2018) 255 (https://doi.org/10.2298/SOS1802255K)
28. B. Zdravkov, J. Čermák, M. Sefara, Josef Janků, *CEJC* **5** (2007) 385 (https://doi.org/10.2478/s11532-007-0017-9)
29. E. Frackowiak, *Phys. Chem. Chem. Phys*. **9** (2007) 1774 (https://doi.org/10.1039/B618139M)
30. M. Quan, D. Sanchez, M. F. Wasylkiw, D. K. Smith, *J. Am. Chem. Soc.* **129** (2007) 12847 (https://doi.org/10.1021/ja0743083)
31. O. Gharbi, M. T. T. Tran, B. Tribollet, M. Turmine, V. Vivier, *Electrochim. Acta* **343** (2020) 136109 (https://doi.org/10.1016/j.electacta.2020.136109)
32. M. R. Pantović Pavlović, M. M. Pavlović, S. Eraković, J. S. Stevanović, V. V. Panić, N. Ignjatović, *Mater. Lett*. **261** (2020) 127121 (https://doi.org/10.1016/j.matlet.2019.127121)
33. S. Kaiser, M. S. Kaiser, *J. Electrochem. Sci. Eng*. **10** (2020) 373 (https://doi.org/10.5599/jese.877)
34. L. Miao, Z. Song, D. Zhu, L. Li, L. Gan, M. Liu, *Mater. Adv.* **1** (2020) 945 (https://doi.org/10.1039/D0MA00384K)
35. H. L. K. S. Mosch, O. Akintola, W. Plass, S. Hoeppener, U. S. Schubert, A. Ignaszak, *Langmuir* **32** (2016) 4440 (https://doi.org/10.1021/acs.langmuir.6b00523)
36. V. V. Panić, A. B. Dekanski, V. B. Mišković-Stanković, B. Ž. Nikolić, *Chem. Biochem. Eng. Q*. **23** (2009) 23.

Journal of the Serbian Chemical Society
JSCS@tmf.bg.ac.rs • www.shd.org.rs/JSCS
J. Serb. Chem. Soc. 87 (7–8) S295–S296 (2022)
Supplementary material

SUPPLEMENTARY MATERIAL TO

Supercapacitive properties of the alkali metal hydroxides-activated carbons obtained from sucrose[•]

MILICA G. KOŠEVIĆ[1]*, SANJA S. KRSTIĆ[2], VLADIMIR V. PANIĆ[1,3,4]
and BRANISLAV Ž. NIKOLIĆ[5]

[1]Institute of Chemistry, Technology and Metallurgy, National Institute of the Republic of Serbia, University of Belgrade, Belgrade, Serbia, [2]University of Belgrade, Vinča Institute of Nuclear Sciences, Belgrade, Serbia, [3]Centre of Excellence in Environmental Chemistry and Engineering – ICTM, University of Belgrade, Belgrade, Serbia, [4]State University of Novi Pazar, Department of Natural and Mathematical Sciences, Novi Pazar, Serbia and [5]Faculty of Technology and Metallurgy, University of Belgrade, Belgrade, Serbia

J. Serb. Chem. Soc. 87 (7–8) (2022) 867–877

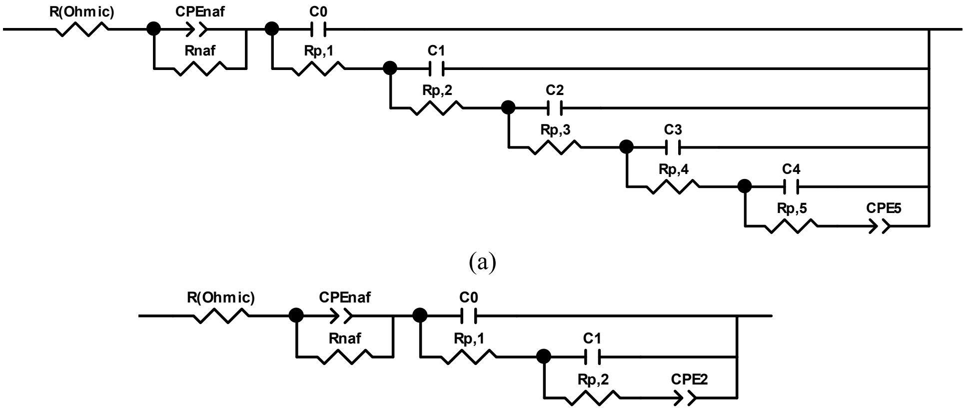

(a)

(b)

Fig. S-1. Transmission line equivalent electrical circuits (TLEECs) used to fit the impedance data of S-LiOH (a) and S-NaOH (b) carbons.

---

* Corresponding author. E-mail: milica.kosevic@ihtm.bg.ac.rs

TABLE S-I. The values of parameters (± absolute error) of TLEEC elements gained by fitting to TLEECs shown in Fig. S-1a and b; type of fitting: complex, type of weighting: calculated modulus; max. iterations: 100

Parameter	S-LiOH	S-NaOH
R(Ohmic) / Ω	20.78±0.03	22.01±0.09
Q_{naf} / 10^{-5} S $\mathrm{s}^{n_{\mathrm{naf}}}$	3.6±0.3	5.1±0.2
n_{naf}	0.721±0.006	0.812±0.006
R_{naf} / Ω	15.6±0.3	62±1
C_0 / 10^{-5} F	3.1±0.3	49±4
$R_{\mathrm{p},1}$ / Ω	12.4±0.9	42±4
C_1 / 10^{-5} F	6.1±0.4	92±7
$R_{\mathrm{p},2}$ / Ω	23±2	98±13
Q_2 / 10^{-5} S s^{n_2}	–	212±6
n_2	–	0.74±0.01
C_2 / 10^{-5} F	9.6±0.5	–
$R_{\mathrm{p},3}$ / Ω	57±5	–
C_3 / 10^{-5} F	14.8±0.8	–
$R_{\mathrm{p},4}$ / Ω	138±12	–
C_4 / 10^{-5} F	19.0±0.9	–
$R_{\mathrm{p},5}$ / Ω	240±20	–
Q_5 / 10^{-5} S s^{n_5}	62.0±0.8	–
n_5	0.634±0.003	–
	Fitting quality	
$\chi^2\times10^5$	1.68	32.3
Weighted sum of squares	1.88×10^{-3}	3.23×10^{-2}

Journal of the Serbian Chemical Society
JSCS-info@shd.org.rs • www.shd.org.rs/JSCS
J. Serb. Chem. Soc. 87 (7–8) 879–889 (2022)
JSCS–5564
Original scientific paper
Published 25 March 2022

Electrochemical reduction of tungsten(VI) oxide from a eutectic melt $CaCl_2$–NaCl under potentiostatic conditions

OLHA BOSENKO[1]*, SERHII KULESHOV[1], VALERII BYKOV[2]
and ANATOLIY OMEL'CHUK[1]

[1]V. I. Vernadsky Institute of General and Inorganic Chemistry of the National Academy of Sciences of Ukraine, 32-34 Acad. Palladina Ave., Kyiv, 03142, Ukraine and [2]Institute of Physics of the NAS of Ukraine, Science Ave., Kyiv, 03028, Ukraine

(Received 5 November 2021, revised 11 February, accepted 14 February 2022)

Abstract: The paper presents results of the study of the electrochemical reduction of tungsten(VI) oxide in a melt of the eutectic composition 52 mol% $CaCl_2$ and 48 mol% NaCl at a liquid gallium electrode. Scanning electron microscopy and X-ray diffraction methods were used to study the microstructures of the obtained powders. The Rietveld method which is based on diffraction patterns were used to calculate the quantitative content of phases in WO_3 reduction products. The thermodynamic properties of the electrolysis process were investigated by voltammetry. It is shown that a necessary condition for the electrochemical reduction of WO_3 is electrolysis at potentials higher than the standard electrode potential of decomposition of calcium tungstate, which is formed by the interaction of tungsten oxide with calcium chloride. The reduction can take place by both electrochemical and metallothermic mechanisms depending on the conditions of electrolysis. The reduction product is fine tungsten with a particle crystallite size of up to 1 μm.

Keywords: reduction of WO_3; potentiostatic electrolysis; tungsten oxide; melts; calcium and sodium chlorides.

INTRODUCTION

Tungsten has a unique physical and chemical properties, that is why alloys and composites based on it are widely used in various fields of modern science and technology such as metallurgy, mechanical and instrument engineering, electrical engineering, structural materials, *etc.*[1–5] Analysis of the scientific and technical literature shows that the demand for tungsten and products made from it is growing, and that the prices for tungsten products are rising accordingly.[6,7] The known methods of producing tungsten by reducing its oxide compounds with

---

[*] Corresponding author. E-mail: olyabosenko@ionc.kiev.ua
https://doi.org/10.2298/JSC211105008B

hydrogen are characterized by high specific energy consumption and require a complex technological equipment.[8,9] Recent studies have shown that a promising method for producing refractory metals can be direct electrochemical reduction of their oxides in melts based on calcium compounds (FFC – Cambridge Process).[10,11]

The articles showed the possibility of electrochemical production of tungsten powder from molten mixtures NaCl–KCl–Na_2WO_4, KCl–NaCl–NaF–Na_2WO_4 and NaCl–KCl–NaF–WO_3.[12–14] The possibility in principle of electrochemical reduction of $CaWO_4$ to tungsten in melts based on calcium chloride in the temperature range of 873–1173 K is shown in.[15,16]

Despite the currently accumulated experimental material, the information on the conditions for the reduction of tungsten oxide in molten electrolytes is extremely limited. For example, according to the research,[16] tungsten trioxide cannot be electrochemically reduced to tungsten metal in the eutectic melt of sodium and calcium chlorides without large losses, while the works-proof that this process can be implemented in molten mixtures of LiCl–KCl and KF–KCl, CsF–CsCl.[17,18] There is no information on large losses of tungsten due to the formation and sublimation of volatile tungsten compounds. Given the above, the study of the processes that occur during the electrochemical reduction of tungsten oxide is an important not only applied but also scientific task.

The aim of this work is to identify the influence of electrolysis conditions on the composition of reduction products, current yield and the degree of extraction of tungsten from dispersed WO_3.

EXPERIMENTAL

The electrochemical reduction of tungsten trioxide was carried out in an argon atmosphere in a quartz reactor (n) with a Teflon lid (e), in which were installed the tubes for argon inlet (a) and outlet (b) by using rubber seals, and also current collectors (c) of tungsten wire with a diameter of 1.0–2.6×10^{-3} m to the graphite anode (f) and liquid gallium cathode (g). The tungsten wires were covered with quartz or corundum tubes (d) to avoid contact with the molten electrolyte. The schematic drawing of the cell assembly is shown in Fig. 1. The reactor was installed in a shaft furnace to ensure the required temperature of electrolysis. Tungsten(VI) oxide (h) was loaded into a corundum crucible (k, outer diameter 37 mm, height 60 mm) on the surface of molten gallium.

About 70.0±0.5 g of a thoroughly dehydrated electrolyte mixture (j) of the composition 52 mol% $CaCl_2$ and 48 mol% NaCl was used in every experiment. This composition has a melting point of 780 K,[19] and it was prepared from analytically pure compounds with a main reagent content of > 99.9 wt.%. Gallium mark GL-1 with a purity of 99.9% was used as the cathode (g). In each experiment, 1.40±0.10 g of gallium was charged into the crucible (m). For the reduction, tungsten (VI) oxide containing at least 99.9999 wt.% WO_3 with a particle size of 30–80 μm was used. The amount of tungsten oxide loaded on the cathode was 0.5 g in each experiment. The anodes were made of low-porosity graphite MPG-7 (f). The working temperature was controlled at 1013±1 K. The electrolysis temperature was monitored using a platinum: platinum–rhodium thermocouple (R-type) thermocouple placed just outside the quartz vessel near the bottom of the reactor (n). Electrochemical reduction was carried out with a stabilized DC source MPS-3010L-1 (Matrix Technology Inc., China, 30 V, 10 A). In each experiment, 0.30±0.05 A·h of electricity was passed through the cell.

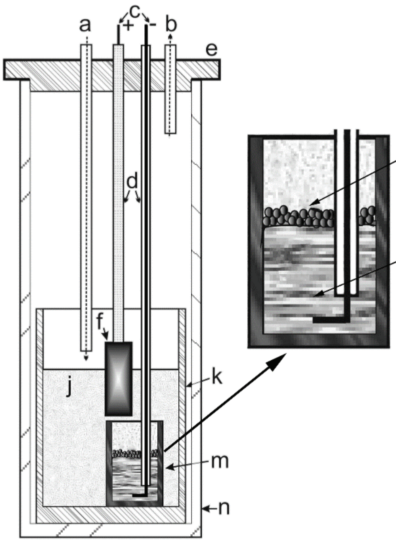

Fig. 1. Schematic diagram of the reactor for the electrochemical reduction of oxygenated tungsten(VI) compounds in molten electrolytes on a liquid gallium cathode.

The lid (e) with the electrodes was removed from the reactor after electrolysis, and the contents of the crucible (m) were poured into a thoroughly dried stainless steel vessel. The salt and metal phases were easily separated from each other due to the large difference in the crystallization temperature of the molten electrolyte (780 K) and gallium (~303 K). The salt phases and the fine powder that remained on the surface of the vessel after the separation of gallium were weighed, transferred to a glass beaker and poured over with an aqueous solution of 0.1 M HCl. The solution and the fine phase were separated by decantation after the complete dissolution of the salt phase. The formed fine phase was washed several times with distilled water until there was no qualitative reaction (with a silver nitrate solution) to the presence of chlorine anions in the decantate.[20] The precipitate was washed free from the electrolyte residues and dried at 393 K to constant weight, and its morphology and phase composition were investigated. The gallium what was unloaded from the crucible (m) and the melt in the crucible (k) were used after weight adjustment to reduce next portions of tungsten oxide.

The X-ray phase analysis (X-ray diffraction) of electrolysis products was performed on a diffractometer DRON-3M with CuKα radiation. The phase composition was identified using the computer software Match! Crystal Impact ver. 3.3 with databases ICDD PDF-2.[19] The Rietveld method using the software Jana 2006 and the database COD (Crystallography Open Database) was used to determine the quantitative content of the phases. Crystallographic data for tungsten (spatial group Im-3m, crystallographic parameters: a = 3.1648 Å) and $CaWO_4$ (spatial group I 41/a:2, crystallographic parameters: a = 5.2429 Å, c = 11.3737) were used in the calculations.[22,23]

The morphology of the reduction products was studied using a scanning electron microscope JEOL JSM-35.

The voltammetric research was performed using a potentiostat PI-50-1 with a programmer PR-8 in a three-electrode cell. The working electrode was a platinum plate with an area of 2.3 cm^2, the auxiliary electrode was a glassy carbon plate with an area of $S \approx 5.3$ cm^2. The potential of the working electrode was recorded and reported relative to the unpolarized platinum reference electrode. The voltammograms were recorded with a two-coordinate self-recording potentiometer LKD-4 and digitized using the software GetData Graph Digitizer 2.26. All electrodes were pre-ground to get a mirror surface before each measurement, then washed with distilled water and dried. The study was performed at a temperature of 1013 K.

RESULTS AND DISCUSSION

To determine the possibility of the direct electrochemical reduction of tungsten trioxide, the values of standard electrode potentials ($E^\ominus$) of reactions that can take place at the cathode were calculated:

$$MCl_n + ne^- \rightarrow M + nCl^-, \text{ where M: Na, Ca} \qquad (1)$$

$$WO_3 + 6e^- \rightarrow W + 3O^{2-} \qquad (2)$$

In addition, it is known that tungsten trioxide interacts with calcium chloride in the molten state to form slightly soluble calcium tungstate and volatile tungsten oxochloride:[9,16]

$$2WO_3 + CaCl_2 \rightarrow CaWO_4 + WO_2Cl_2, \qquad (3)$$

therefore, calcium tungstate may also be involved in the reduction:

$$CaWO_4 + 6e^- \rightarrow W + 4O^{2-} + Ca^{2+} \qquad (4)$$

According to research,[15] the solubility of calcium tungstate at 1025 K is ~0.2 wt.%. This shows in favor of that the predominant amount of calcium tungstate should be reduced in the solid-state. The participation of tungsten oxychloride in electrode processes was not taken into account, because at temperatures above 484 K it turns into a gaseous state and is comes out of the melt.[16,22] The calculations were performed using a well-known relation:

$$E^\ominus = \Delta G^\ominus / nF \qquad (5)$$

where $\Delta G^\ominus$ is the Gibbs energy change of formation of the corresponding component of the reaction mixture, n is the number of electrons participating in the electrode reaction, F is the Faraday constant and thermodynamic data given in the reference book.[24] The results of the calculations are given in Table I.

From the above data it is seen that tungsten trioxide has the lowest standard electrode potential and that in cathodic polarization, it must primarily participate in electrochemical transformations in the molten electrolyte mixture. If the interaction of tungsten oxide with the melt takes place (3), as a result of which calcium tungstate is formed, its reduction should take place in the potential range between the reduction potentials of tungsten trioxide and calcium and sodium chlorides. The reduction of NaCl and $CaCl_2$ should occur at larger values of the electrode potentials in almost the same interval.

Analysis of the results of voltammetric studies confirms this prediction. The nature of the platinum electrode voltammograms in an electrolyte mixture, without tungsten trioxide, indicates that no processes occur in the cathodic region of potentials except for the joint discharge (1) of calcium and sodium cations (Fig. 2, curve 1).

TABLE I. Thermodynamic characteristics of the components of the reaction mixture, ΔG / kJ mol^{-1}; $E^{\ominus}$ / V

Component		Temperature, K			
		700	800	900	1000
WO_3	$\Delta G^{\ominus}$ / kJ mol^{-1}	–660.184	–635.098	–610.269	–585.679
	$-E^{\ominus}$ / V	1.14	1.10	1.05	1.01
NaCl	$\Delta G^{\ominus}$ / kJ mol^{-1}	–346.096	–336.836	–327.722	–318.768
	$-E^{\ominus}$ / V	3.59	3.49	3.40	3.30
$CaCl_2$	$\Delta G^{\ominus}$ / kJ mol^{-1}	–686.518	–671.630	–656.856	–642.183
	$-E^{\ominus}$ / V	3.56	3.48	3.40	3.33
$CaWO_4$	$\Delta G^{\ominus}$ / kJ mol^{-1}	–1397.999	–1363.770	–1329.773	–1295.992
	$-E^{\ominus}$ / V	2.41	2.36	2.30	2.24
CaO	$\Delta G^{\ominus}$ / kJ mol^{-1}	–561.854	–551.594	–541.345	-531.087
	$-E^{\ominus}$ / V	2.91	2.86	2.80	2.75
Na_2O	$\Delta G^{\ominus}$ / kJ mol^{-1}	–322.190	–308.121	–294.253	-280.590
	$-E^{\ominus}$ / V	3.34	3.19	3.05	2.91

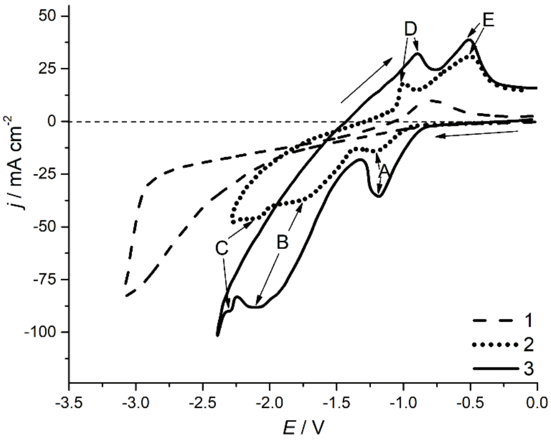

Fig. 2. j–E characteristics of a platinum electrode in the eutectic melt $CaCl_2$– NaCl without tungsten oxide (1) and in its presence: 4.7×10^{-4} (2) and 9.3×10^{-4} mol cm^{-3} (3). The potential scan rate is 0.05 V s^{-1}, the temperature is 1013 K.

On the reverse scan of the voltammogram in the region of potentials close to –1.0 V, the voltammogram exhibits in the anodic region currents that characterize the joint ionization of sodium and calcium. In the presence of tungsten oxide, the voltammograms exhibit in the cathodic region three waves, the height of which increases with increasing its content in the melt. On the reverse scan of the voltammogram, it exhibits in the anodic region only two waves, the height of which also increases with increasing the WO_3 content of the melt. Because tungsten oxide is poorly soluble in a eutectic mixture of sodium and calcium chlorides, argon was bubbled through it to suspend the oxide in the bulk electrolyte before recording the voltammograms. The coordinates of the maximum values of the waves recorded on the voltammograms are given in Table II.

TABLE II. Coordinates of the extreme point of the waves that characterize the electrochemical reduction of WO_3

Wave	Potential, V		Current density, mA cm^{-2}	
	Curve 2	Curve 3	Curve 2	Curve 3
A	–1.2	–1.2	–13.9	–35.2
B	–1.8	–2.1	–37.8	–87.8
C	–2.1	–2.3	–46.1	–90.0
D	–1.0	–0.9	17.8	32.2
E	–0.5	–0.5	30.9	38.7

Considering the values of the standard electrode potentials given in Table I, we can assume that wave A corresponds to process (2), and wave B to process (4).

Wave C characterizes the discharge of calcium cations bound to oxygen anions, which must accumulate in the cathode layer of the molten electrolyte due to the course of processes (2) and (4). This will inevitably lead to the formation of oxides of calcium and sodium, thermodynamic decomposition potentials, which are less than the decomposition potentials of chlorides of these metals (Table I). The increase in current density recorded on voltammograms after peak C is already associated with the discharge of sodium and calcium cations, which are bound to chlorine anions and are part of the basic electrolyte – a molten mixture of calcium and sodium chlorides. It should be noted that in this section of the voltammetry (after peak C) the platinum electrode will be partially covered by calcium. It is known that the discharge of metal cations, on the cathode made of the same metal or partially covered with it, occurs at a much lower overvoltage.[25] Wave D, which is observed on the reverse scan of the voltammograms most likely characterizes the anodic dissolution of sodium and calcium alloy, which is formed during the forward potential scan on the surface of the platinum cathode, and wave E characterizes tungsten dissolution.

In order to identify the products formed during the electrochemical reduction of WO_3, electrolysis was performed under potentiostatic conditions at different potentials, in particular those that are lower than the standard potential of the process (4) and exceed it.

In contrast to the known process (FFC Cambridge process),[26] the electrochemical reduction of tungsten oxide was carried out using a liquid gallium cathode, omitting the stage of preliminary preparation, which includes granulation and sintering. Gallium has a very high boiling point (2477 K) and at the reduction temperature (1013 K) does not evaporate and does not react with the molten electrolyte mixture, tungsten oxide or tungsten. Due to the large difference in the specific mass of gallium and tungsten, W settled to the bottom of the crucible (m, Fig. 1), which protected it from interaction with the components of the molten electrolyte mixture. The liquid gallium cathode not only provides reliable contact with tungsten oxide, but also creates more favorable conditions for its reduction because the area of contact of fine powder with the liquid phase is much larger than that of granulated and sintered WO_3 samples with the solid leads. In addition, it should be noted that the electrolytic reduction of the initial compounds (tungsten oxide, calcium tungstate) in the solid-state is accompanied by a significant decrease in molar volume (almost 5 times in the case when calcium tungstate is reduced to tungsten). The reduction mode proposed by the authors provides uniform polarization of each particle of oxygen-containing tungsten compounds, unimpeded removal of electrolysis products from the reduction zone and avoids blocking the cathode surface by both initial compounds and reduction products. Such electrolysis conditions provide uniform polarization of each tungsten oxide particle, avoid blocking both their surface and the cathode surface by reduction products.

The analysis of the obtained results (Table III, Fig. 3) showed that the reduction products at potentials exceeding the values of the standard potentials of the process (2) at the cathode form a mixture of tungsten and calcium tungstate, the amount of which significantly exceeds the amount of tungsten.

TABLE III. The composition of the products of electrochemical reduction of WO_3 depending on the conditions of electrolysis

Reduction potential, V	Phase content of the formed product, wt. %		Definition error
	W	$CaWO_4$	
–1.3	1.35	98.65	Less than 1.83 %
–2.0	21.20	78.80	Less than 2.60 %
Higher than or equal to –2.4	100.00	–	–

Pure tungsten is formed at the cathode only at potentials exceeding the standard electrode potential of the process (4), Fig. 3d. Tungsten, which does not contain impurity phases, is also formed when electrolysis is carried out at potentials exceeding the standard electrode potential of reaction (1). In this case, metallothermic reduction reactions of tungsten oxide is possible at the cathode:

$$WO_3 + 3nM \rightarrow W + 3M_nO \tag{6}$$

where $n = 2$ when sodium participates in the reduction and $n = 1$ when the reducing agent is calcium. The probability of the process (6) is very high, if we take into account the fact that due to alloy formation, on liquid cathodes, metal cations are discharged at more positive potentials than on solid ones.[25] If we add together Eqs. (1) and (6), we obtain an equation that generally corresponds to the process (2). Thus, the obtained results give grounds to believe that the reduction of tungsten trioxide, depending on the implementation conditions, can occur both by the electrochemical mechanism (processes (2), (4)) and by the metallothermic one (6).

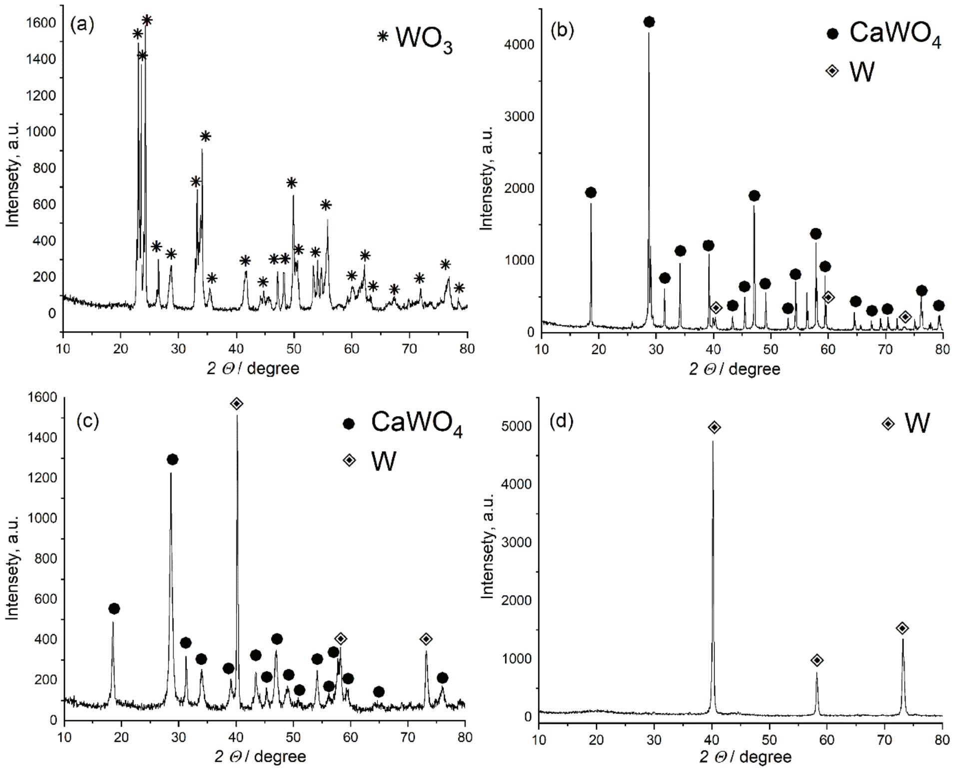

Fig. 3. Typical diffraction patterns of WO_3 before electrolysis (a) and of products obtained after electrolysis at *E* from –1.0 to –1.3 V (b); from –1.4 to –2.3 V (c); negative to –2.4 V (d).

The maximum degree of extraction of tungsten (W) from tungsten oxide was not lower than 58.00±0.01 %. It was calculated from the formula (7):

$$W = 100\frac{m_{\text{pract}}}{m_{\text{theor}}} \tag{7}$$

where m_{pract} is the mass of tungsten obtained by reduction; m_{theor} is the mass of tungsten contained in the weighed amount of WO_3 loaded on the cathode. The current yield did not exceed 57.27±0.01 %.

The course of the processes (3) and (6) may be the cause of low values of the degree of extraction of tungsten from the oxide and current yields. To avoid these undesirable processes, it is advisable to use $CaWO_4$ instead of WO_3 as the initial compound for reduction and to carry out electrolysis under conditions that minimize the contribution of electrochemical decomposition of electrolyte mixture components (1) to the general process of tungsten production. In the case of the use of calcium tungstate it can be represented by the scheme (4).

Fig. 4 shows a SEM image of the original tungsten(VI) oxide (a) and metallic tungsten (b) obtained by electrolysis at a potential of –2.4 V. These results indicate that the electrochemical reduction of tungsten oxide compounds is accompanied by the formation of crystallites of much smaller volume. The size of the formed dendritic groups is several tens of micrometers. The crystallized particles were observed as an individual (less than 1 μm), and as dendrites (average length up to 10 μm).

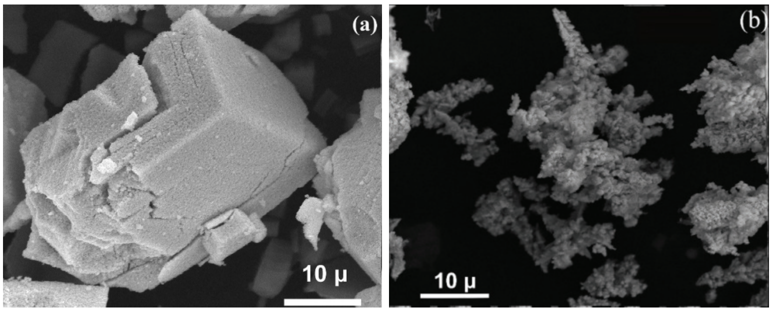

Fig. 4. Typical SEM images: a) WO_3; b) electrolysis product (W).

CONCLUSION

A necessary condition for the electrochemical reduction of tungsten(VI) oxide in a molten eutectic mixture of sodium and calcium chlorides on a liquid gallium electrode is electrolysis at potentials exceeding the standard electrode potential of decomposition of calcium tungstate, which is formed by the interaction of oxide with calcium chloride. The reduction can take place by both electrochemical and metallothermic mechanisms depending on the conditions of potentiostatic electrolysis. The reduction product is fine tungsten with a crystallite size of not larger than 1.00×0.88 μm. The current yield, under conditions that provide pure tungsten is 57.27 %, and the degree of extraction 57.99 %. The reason of the low values of current yield and the degree of extraction may be side processes of interaction of WO_3 with the components of the molten electrolyte mixture, and also the reduction of sodium and calcium at the liquid cathode. It is more expedient for the electrochemical production of tungsten, from a molten eutectic mixture of calcium and sodium chlorides, to use $CaWO_4$ as an initial compound instead of WO_3.

ИЗВОД

ЕЛЕКТРОХЕМИЈСКА РЕДУКЦИЈА ВОЛФРАМ(VI)-ОКСИДА ИЗ ЕУТЕКТИЧКОГ РАСТОПА $CaCl_2$–NACl У ПОТЕНЦИОСТАТСКИМ УСЛОВИМА

OLHA BOSENKO, SERHII KULESHOV, VALERII BYKOV[1] и ANATOLIY OMEL'CHUK

[1]*V.I. Vernadsky Institute of General and Inorganic Chemistry of the National Academy of Sciences of Ukraine, 32-34 Acad. Palladina Ave., Kyiv, 03142, Ukraine и* [2]*Institute of Physics of the NAS of Ukraine, Science Ave., Kyiv, 03028, Ukraine*

У раду су приказани резултати испитивања електрохемијске редукције волфрам(VI)-оксида из растопа еутектичког састава $CaCl_2$–NaCl (52–48 mol%) на електроди од течног галијума. Микроструктура добијених прахова је испитивана методама скенирајуће електронске микроскопије и дифракције X-зрака. Rietveld анализом дифрактограма је одређен квантитативан фазни састав производа редукције WO_3. Термодинамичке карактеристике процеса електролизе су испитиване волтаметријом. Показано је да је неопходан услов за редукцију WO_3 да током електролизе потенцијал катоде буде виши од стандардног електродног потенцијала разлагања калцијум-волфрамата, који је формиран интеракцијом волфрам(VI)-оксида и калцијум-хлорида. Редукција се може одиграти и електрохемијским и металотермијским механизмом у зависности од услова електролизе. Производ редукције је фини прах волфрама величине кристалита до 1 μm.

(Примљено 5. новембра 2021, ревидирано 11. фебруара, прихваћено 14. фебруара 2022)

REFERENCES

1. V. Gavrish, G. Baranov, T. Chayka, N. Derbasova, in *XII International Conference Radiation-thermal Effects and Processes in Inorganic Materials,* Tomsk, Russian Federation, 2016, IOP Conf. Series: Materials Science and Engineering, IOP Publishing, 2017, 012013 (http://dx.doi.org/doi:10.1088/1757-899X/168/1/012013)
2. E. G. Sokolov, A. V. Ozolin, S. A. Arefieva, in *Materials Science Forum,* Trans Tech Publications Ltd., Switzerland, 2020, p. 511 (http://dx.doi.org/10.4028/www.scientific.net/MSF.992.511)
3. V. M. Gavrish, G. A. Baranov, T. V. Chayka, N. M. Derbasova, A. V. Lvov, Y. M. Matsuk, in *International Scientific Conference on Radiation-Thermal Effects and Processes* in *Inorganic Materials,* Tomsk, Russia, 2015, IOP Conf. Ser. Mater. Sci. Eng., IOP Publishing, 2016, 012028 (http://dx.doi.org/10.1088/1757-899X/110/1/012028)
4. E. Lassner, W.-D. Schubert, T*ungsten: properties, chemistry, technology of the element, alloys, and chemical compounds*, Springer, Boston, MA, 1999, p. 422 (http://dx.doi.org/10.1007/978-1-4615-4907-9)
5. R. Sarathi, T. K. Sindhu, S. R. Chakravarthy, A. Sharma, K. V. Nagesh, J. *Alloys Compd.* **475** (2009) 658 (http://dx.doi.org/10.1016/j.jallcom.2008.07.092)
6. U.S. Department of the Interior, U.S. Geological Survey, *Metal prices in the United States through 2010*: U.S. Geological Survey Scientific Investigations Report 2012–5188, Pubs.Usgs.Gov, Reston, VA, 2013
7. E. Lassner, W.-D. Schubert, E. Lüderitz, H. U. Wolf, *Ullmann's Encyclopedia of Industrial Chemistry*, Wiley-VCH Verlag GmbH & Co. KGaA, Weinheim, 2012 (http://dx.doi.org/10.1002/14356007.a27_229)
8. Y. Wu, Z. Lv, H. Sun, and J. Dang, *J. Mater. Res. Technol.* **8** (2019) 4687 (https://doi.org/10.1016/j.jmrt.2019.08.014)

9. N. E. Fouad, K. M. E. Attyia, M. I. Zaki, *Powder Technol.* **74** (1993) 31 (https://doi.org/10.1016/0032-5910(93)80005-U)
10. G. Z. Chen, D. J. Fray, in *Non-Ferrous Metals Processing*, TMS Light Metals, RresearchGate, Charlotte, NC, 2004, p. 881
11. A. M. Abdelkader, K. T. Kilby, A. Cox, D. J. Fray, *Chem. Rev.* **113** (2013) 2863 (https://doi.org/10.1021/cr200305x)
12. L. Zhang, Z. Nie, X. Xi, L. Ma, X. Xiao, M. Li, *Metall. Mater. Trans., B* **49** (2017) 334 (https://doi.org/10.1007/s11663-017-1125-3)
13. J. Li, X. Y. Zhang, Y. Bin Liu, Y. G. Li, R. P. Liu, *Rare Met.* **32** (2013) 512. (https://doi.org/10.1007/s12598-013-0156-4)
14. J. Li, Y. Li, L. Liu, Z. Cai, X. Zhang, R. Liu, *Rare Met. Mater. Eng.* **42** (2013) 2237 (https://doi.org/10.1016/s1875-5372(14)60028-x)
15. D. Tang, W. Xiao, H. Yin, L. Tian, D. Wang, *J. Electrochem. Soc.* **159** (2012) E139 (https://doi.org/10.1149/2.113206jes)
16. M. Erdoğan, I. Karakaya, *Metall. Mater. Trans., B* **41** (2010) 798 (https://doi.org/10.1007/s11663-010-9374-4)
17. R. Abdulaziz, L. D. Brown, D. Inman, S. Simons, P. R. Shearing, D. J. L. Brett, *Electrochem. Commun.* **41** (2014) 44 (https://doi.org/10.1016/j.elecom.2014.01.022)
18. T. Nohira, T. Ide, X. Meng, Y. Norikawa, and K. Yasuda, *J. Electrochem. Soc.* **168** (2021) 046505 (https://doi.org/10.1149/1945-7111/abf266)
19. The Fact™ and FactSage™ databases, http://www.crct.polymtl.ca/fact/documentation/FS_All_PDs.htm (accessed 5.9.21)
20. A. P. Kreshkov, *Fundamentals of Analytical Chemistry*, Chemistry, Moscow, 1970, p. 472 (https://www.twirpx.com/file/379406)
21. H. Putz, *Match! Phase Analysis using powder diffraction*, Crystal impact, Bonn, 2020, p. 143 (http://www.crystalimpact.com/download/match3/Manual.pdf)
22. Crystallographic Computing System for Standard and Modulated Structures Jana 2006, http://jana.fzu.cz (accessed 7.9.21)
23. Crystallography Open Database, http://www.crystallography.net (accessed 7.9.21)
24. I. Barin, *Thermochemical Data of Pure Substances*, VCH Verlagsgesellschaft mbH, Weinheim, 1995, p. 1885 (lSBN 3-527-28745-0)
25. Yu. K. Delimarsky, *Electrochemistry of ionic melts*, Metallurgy, Moscow, 1978, pp. 223––224 (https://ua1lib.org/book/1042044/0e752b)
26. D. J. Fray, G. Z. Chen, T. W. Farthing, (Cambridge University), UK Patent WO 9964638, PCT/GB 99/01781 (1999).

Journal of the Serbian Chemical Society
JSCS-info@shd.org.rs • www.shd.org.rs/JSCS

J. Serb. Chem. Soc. 87 (7–8) 891–898 (2022)
JSCS–5565

Original scientific paper
Published 23 March 2022

Rheological and morphological analysis of irradiated high and low density polyethylene samples

AIDAR KADYIROV[1]*, AYDAR AKHMADIYAROV[2], RUSLAN GARIPOV[3]
and EKATERINA VACHAGINA[1]

[1]Institute of Power Engineering and Advanced Technologies, FRC Kazan Scientific Center, Russian Academy of Sciences, Kazan, Russia, [2]Department of Physical Chemistry, Kazan Federal University, Kazan, Russia and [3]Kazan National Research Technological University, Kazan, Russia

(Received 27 November 2021, revised 14 February, accepted 21 February 2022)

Abstract: The influence of intensity of the γ-irradiation on commercial high and low density polyethylene (LDPE and HDPE) granules (Kazanorgsintez PJSC, Kazan, Tatarstan, Russia) on their rheological and morphological properties at irradiation doses of 5 and 10 kGy was studied. Experiments in the oscillation mode revealed an increase in the dynamic moduli values with increasing radiation dose compared to the initial samples. At the same γ-irradiation doses, the HDPE samples compared to the LDPE ones showed the greatest changes in rheological properties, while the zero shear viscosity of HDPE increased by order of magnitude compared to the initial one at the irradiation dose of 10 kGy. Morphology analysis of supramolecular structures revealed an increase in cob-web-type structures for the irradiated sample in comparison with the initial sample, which may indicate the formation of branched structures under γ-irradiation.

Keywords: polyethylene; γ-irradiation; cobwebs structure.

INTRODUCTION

Polyethylene is the most usedr polymer material on the global market.[1–3] Most of the low-density polyethylene (LDPE) and high-density polyethylene (HDPE) are supplied to end-product manufacturers in the granular form. In comparison with the powdery and flaky forms, it has significant advantages: high bulk density; flowability, *i.e.*, when dosing, packing, moving, it is not accumulated in equipment units and does not form “dead zones” that lead to process instability and shutdowns; minimization of losses, since it is completely removed from feeding devices; less risk of destruction; no dust formation.

---

* Corresponding author. E-mail: aidarik@rambler.ru

https://doi.org/10.2298/JSC211127014K

Due of the growing demand for polymer products, as well as the emergence of new materials with improved characteristics, currently, modification of some properties of polyethylene is required, *i.e.*, improvement of only the necessary features while maintaining the others at the same level.[4–6] γ-Irradiation is one of the known methods for changing the properties of polymers.[7–11] For example,[12] when polypropylene was exposed to a low irradiation dose (up to 200 kGy), it was possible to achieve ~~a~~ higher melt strength and special rheological properties. El-Shamy *et al.* observed an increase in conductivity and improvement in the dielectric properties of polymer films after γ-irradiation.[10] An increase in the viscoelastic properties of polyethylene was observed after γ-irradiation in the range of irradiation doses from 7 to 103 kGy.[13]

As a result of ionizing radiation (irradiation doses of 20, 30 and 35 kGy),[14] some polymers, in particular, polyethylene, are prone to crosslinking, while others (*e.g.*, polypropylene and poly(methyl methacrylate) are more prone to chain breaking and decomposition. It was observed that under certain modes of ionizing radiation, the mechanical strength and hardness of LDPE and HDPE were increase by 40–60 %.[15] In addition, the effects of γ-irradiation on the electric properties of high-pressure polymer films have been studied.[16] The results of experimental studies showed that, after irradiation, cross-connections are formed inside the polyethylene, and carbonyl groups are formed on the surface. This leads to an insignificant increase in the degree of crystallinity and specific volumetric electrical resistance.

As a literature review showed, most of the studies present the results of γ-irradiation of finished polymer products (mainly films). For example, HDPE samples after hydraulic pressing were γ-irradiated in different atmospheres.[17] In another study, small samples were cut from LDPE sheets,[18] their dimensions were 12×50×2.5 mm^3, and then they were processed on industrial equipment; the values of the irradiation dose ranged from 100 to 2000 kGy. Polymer films 40 mm wide,[8] 0.6 and 1.2 mm thick were considered in the study. They were irradiated with a total dose of 25 kGy in a closed glass container. After γ-irradiation, prismatic specimens of 12.5×12.5×25.4 mm^3 for compression testing and specimens of 12.5 mm for tensile testing were extracted from a plate of industrial HDPE.[9]

The present work aims at studying the effect of γ-irradiation intensity on rheological and morphological properties of LDPE and HDPE granules produced by Kazanorgsintez PJSC (Kazan, Russia). Thus, unlike the majority of other authors, the irradiation of granules with subsequent production of disks (diameter 25 mm, thickness 1.2 mm) by pressing was considered. These disks were the objects for investigation in the present study.

EXPERIMENTAL

Materials

LDPE and HDPE granules produced by Kazanorgsintez PJSC, the largest Russian producer of ethylene polymers and copolymers, were taken as the objects of research. LDPE of 15313-003 grade (hereinafter – 153) meets the requirements of GOST 16337-77 (Russia). Technical characteristics of this polyethylene grade: density 0.9185–0.922 kg m^{-3}, melt flow index 0.21–0.39 g per 10 min (measured at the load of 2.16 kg and at the temperature of 463 K); tensile yield limit not less than 9.8 MPa. HDPE of PE2HT76-17 grade (hereinafter referred to as 2HT) corresponds to technical specifications TU 2243-174-00203335-2007 (Russia). Technical characteristics of this polyethylene grade: density 0.955–0.961 kg m^{-3}, melt flow index 2.3–3.3 g per 10 min (measured at a load of 5 kg at a temperature of 463 K); tensile yield limit not less than 26 MPa. For both samples (LDPE and HDPE), the tensile tests were performed using dumbbell-shaped plate specimens with the following dimensions: thickness – 1 mm; the width – 3 mm and length of the narrow part – 40 mm. The dimensions of the current specimens were calculated as the average value of triple measurements.

γ-*Irradiation*

Irradiation of LDPE and HDPE granules was realized using a RV-1200 radiation unit (Russia). The Co^{60} isotope was the source of γ-radiation. The maximum activity of the irradiator was 2.3×1016 Bq (600 kCi). The installation contained a mechanism for rotating tape blocks, an irradiation chamber, extracted irradiator traverse, ~~a~~ feeding device, tubular elements with radiation sources, ~~a~~ plane irradiator, an assembly chamber, a backup storage, an operator's room, an irradiator storage, ~~a~~ transport device for tape blocks, ~~an~~ annular transport channel, and concrete walls. The samples were placed in an RV-1200 chamber at certain distances from the radiation source. Since these distances were different, the dose of irradiation was also different. Thus, polymers with irradiation doses of 5 and 10 kGy were obtained in the course of the irradiation. During irradiation, polyethylene granules were in 2 kg tissue bags; 2 bags, 2 kg each, were exposed to one dose.

Sample preparation

Before pressing, LDPE and HDPE granules weighing 60–70 g were prepared. The process of manufacturing polymer products by pressing was based on filling a mold cavity with a melt, followed by its compaction due to pressure and cooling. The pressed samples were prepared using a YT-30 RS press. Pressing mode: the temperature was 403.15 K for LDPE and 433.15 K for HDPE; pressure – 100 atm.; process duration – 10 min. When preparing the samples, pre-compaction was performed (*i.e.*, when the pressure dropped, it was increased to 9.806 kPa). Cooling time to the temperature of 303.15–313.15 K was 3–4 min. Plates with the size of 150×150 mm^2 and thickness of 1.2 mm were obtained in sets of five.

Morphology observation

The morphology study of the supramolecular structures of the polyethylene samples was performed on cleaved discs. To prepare the cleavage, the specimens (discs with a diameter of 25 mm and a thickness of 1.2 mm) were submerged in liquid nitrogen for 40 s, after which they were removed and cleaved. The samples fixed on the holder were placed in the chamber of a Quorum Q 150T ES vacuum unit (Quorum, Great Britain). The conductive layer was deposited by cathode sputtering of Au/Pd alloy at a ratio of 80/20. The thickness of the applied layer was 10 nm. The morphology of samples was observed with a Merlin field-emission scanning electron microscope (Carl Zeiss, Germany). The surface morphology was surveyed at an accelerating voltage of primary electrons of 5 kV and a probe current of 300 pA for minimal impact on the object of study.

Parallel plate rheology

The frequency sweep and rotary tests were performed to identify the rheological properties through dynamic modulus (G', G'' / Pa), viscosity curve, and 1st normal stress coefficient of pure and γ-irradiated samples. Rheological measurements were made using a Physica MCR-102 (Anton Paar) instrument at 473.15–493.15 K. The study was performed in an inert environment (nitrogen) to avoid polymer destruction. The predetermined temperature of the sample was controlled and maintained by the lower heating system based on Peltier elements P-PTD200 and the active casing based on Peltier elements H-PTD200 (maintenance error – 0.01 K); a P-ETD400 device was used for temperatures above 473.15 K. This method minimizes temperature gradients in the samples (Anton Paar Physical MCR technical specifications). The PP25 “plate-plate” system was used in the studies; the diameters of the upper and lower plates were 25 mm.

RESULTS AND DISCUSSION

Rheological analysis

The curves of effective viscosity (η), storage (G'), and loss (G'') moduli are shown in Fig. 1. The frequency range (ω) of 0.05-200 rad s^{-1} corresponds to the linear viscoelastic regime when the strain is equal to 5 %.

It is noteworthy that with an increase in the absorbed dose of γ-irradiation, the values of the storage modulus and loss modulus increase, including their position relative to each other. Moreover, the influence of γ-irradiation on HDPE is more significant than that on LDPE. For HDPE, the values of G' and G'' at low frequencies increase by an order of magnitude at the irradiation dose of 10 kGy. For the initial unirradiated LDPE sample, the processing of the obtained data revealed that at the temperature of 473.15 K, the cross over point of G' and G'' is $\omega^* = 1.26$ rad s^{-1}, *i.e.*, $G' > G''$ at $\omega > 1.26$ rad s^{-1} and $G' > G''$ at $\omega < 1.26$ rad s^{-1}; for HDPE this value is $\omega^* = 36.75$ rad s^{-1} (Table I), which is different by an order of magnitude. The table shows the angular frequency values corresponding to the cross over points of G' and G'' distribution for the studied samples at 473.15, 483.15 and 493.15 K. According to the table, for HDPE, there is a sharp shift of the cross over point to the region of low angular velocity, *i.e.*, the material acts as elastic over a wider range of angular velocity.

As expected, exposure to γ-irradiation led to an increase in the effective viscosity, in particular η_0 (Fig. 1a and c). Note that the range of shear rates is limited to 0.4 s^{-1} due to extrusion of the sample through the gap at high shear rates. As illustrated in the figure, for HDPE, the increase in the irradiation dose by 10 kGy led to an increase in η_0 by an order of magnitude, compared to LDPE, despite the fact that the viscosity of the initial samples differed insignificantly. Thus, the obtained results indicate that γ-irradiation is more effective for HDPE-type polymers, which is accompanied by a more pronounced increase in both the values of dynamic moduli and the value of the effective viscosity.

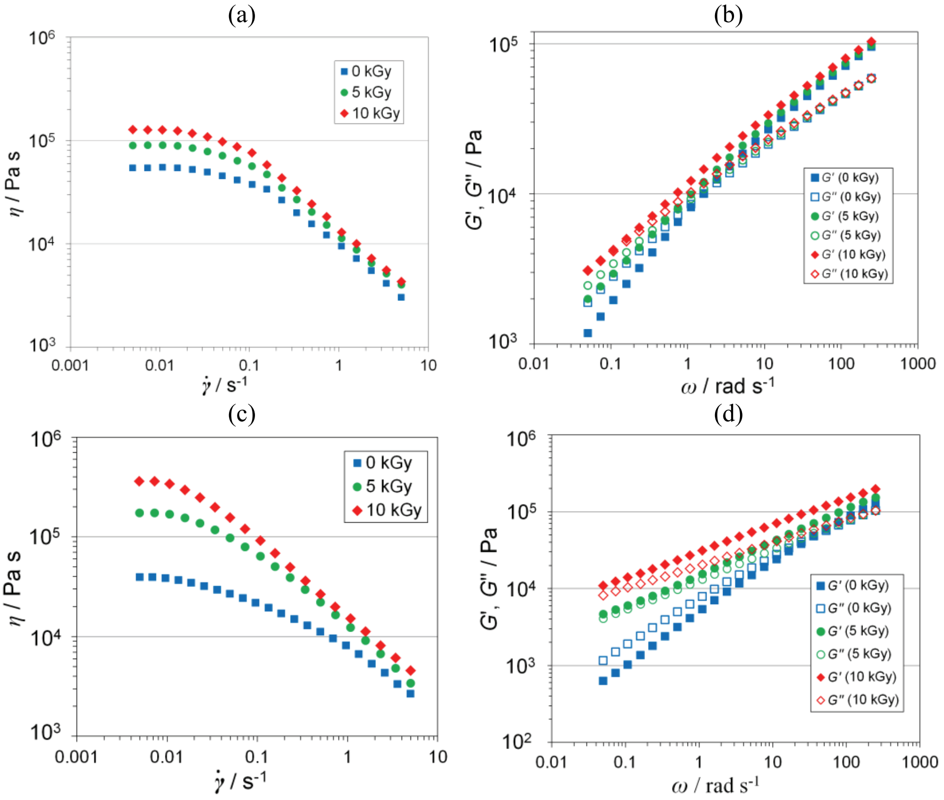

Fig. 1. Viscosity curves (a, c) and dynamic moduli (b, d) for 153 (LDPE, a, b) and 2HT (HDPE, c, d) at a temperature of 473.15 K.

TABLE I. Influence of irradiation dose on cross over point (ω^* / rad s^{-1}) of G' and G''

Sample	Temperature, K	γ / kGy		
		0	5	10
LDPE (153)	473.15	1.26	0.58	0.05
	483.15	1.65	0.59	0.08
	493.15	2.04	0.64	0.13
HDPE (2HT)	473.15	36.75	0.04	$G'>G''$
	483.15	39.5	5.73	0.13
	493.15	46.1	6.27	0.42

Morphological analysis

Changes in the morphology of supramolecular structures after exposure to intense radiation were studied using the HDPE as an example. The photographs were taken at 20000× uniform magnification. The measurements were performed for the cleavages of the initial samples. shows The fibrous objects visible in Fig. 2 could not be attributed to structures such as a mixture of "nodules" and "cobwebs".[19] It was observed that, in the absence of irradiation, during the sample crystallization after pressing, "nodules" and "cobwebs" of a uniform type were formed with an average "cobwebs" diameter of 117.6 nm and a small number of "cobwebs" of small diameter (Fig. 2a). An irradiation dose of 5 kGy leads to the decrease in the average diameter of the "cobwebs" down to 56.4 nm and the increased content of "cobweb" structures. This could be explained by the formation of branched structures on irradiation of polyethylene, which interferes with the structuring of the macromolecules.[20]

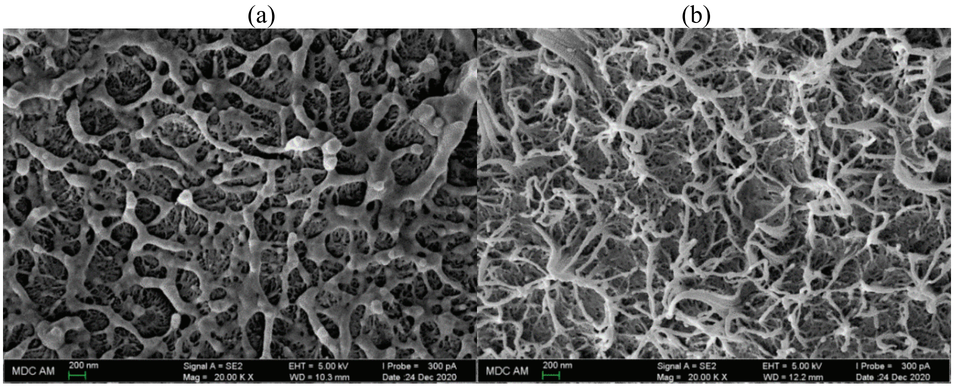

Fig. 2. SEM micrographs of HDPE samples (cleavages) under different irradiation doses: 0 (a) and 5 kGy (b).

CONCLUSIONS

In this work, the rheological and morphological properties of commercial polyethylene samples of LDPE and HDPE grades were analyzed. The studies were performed on samples made by pressing granules that had been exposed to γ-irradiation from the Co^{60} isotope. Experiments in the oscillation mode revealed an increase in storage and loss moduli with increasing radiation dose. The increase in dynamic moduli and effective viscosity for HDPE were more significant, especially at low angular frequencies and shear rates. For both samples (LDPE and HDPE), an increase in the radiation dose was found to lead to a shift in the cross over point for G' and G'' to lower values, *i.e.*, treated samples behave like a solid body at lower angular velocities. Morphology analysis of the supramolecular structures revealed an increase in the cobweb-type structures for the irradiated sample compared to the original one. In this case, the original sample has a structure consisting of nodules and cobwebs. Thus, irradiation of polyethylene granules leads to the formation of branched structures, which seem to interfere with the structuring of the macromolecules on their further path to the final products.

Acknowledgments. The rheological properties were investigated with the financial support from RFBR (Project No. 19-01-00375). Morphological analysis was realized with the financial support from the Russian Science Foundation (Project No. 19-11-00220).

ИЗВОД

РЕОЛОШКА И МОРФОЛОШКА АНАЛИЗА ЗРАЧЕНИХ HDPE И LDPE УЗОРАКА

AIDAR KADYIROV[1], AJDAR AKHMADIYAROV[2], RUSLAN GARIPOV[3] и EKATERINA VACHAGINA[1]

[1]*Institute of Power Engineering and Advanced Technologies, FRC Kazan Scientific Center, Russian Academy of Sciences, Kazan, Russia,* [2]*Department of Physical Chemistry, Kazan Federal University, Kazan, Russia* и [3]*Kazan National Research Technological University, Kazan, Russia*

Проучаван је утицај интензитета зрачења комерцијалних гранула LDPE и HDPE (Kazanorgsintez PJSC, Казан, Татарстан, Русија) на њихова реолошка и морфолошка својства у дозама озрачености од 5 и 10 kGy. Експерименти у режиму осцилација открили су повећање вредности динамичког модула са повећањем дозе радијације у поређењу са почетним узорцима. У истим дозама зрачења, HDPE узорци у поређењу са LDPE показали су највеће промене у реолошким својствима, док се вискозност при малим брзинама смицања HDPE повећала за ред величине у поређењу са почетном са дозом озрачености од 10 kGy. Морфолошка анализа супрамолекуларних структура открила је повећање структура типа паукове мреже за озрачени узорак у поређењу са почетним, што може указивати на формирање разгранатих структура под зрачењем.

(Примљено 27 новембра 2021, ревидирано 14. фебруара, прихваћено 21. фебруара 2022)

REFERENCES

1. R. Geyer, J. R. Jambeck, K. L. Law, *Sci. Adv.* **3** (2017) e1700782 (https://doi.org/10.1126/sciadv.1700782)
2. P. Chalmin, *FACTS Reports* **19** (2019) 6 (https://journals.openedition.org/factsreports/5071)
3. W. Xu, W.-Q. Chen, D. Jiang, C. Zhang, Z. Ma, Y. Ren, L. Shi, *Ecosyst. Health Sustain.* **6** (2020) 1 (https://doi.org/10.1080/20964129.2020.1756925)
4. S. A. Bhusari, V. Sharma, S. Bose, B. Basu, *J. R. Soc. Interface* **16** (2019) 20180273 (https://doi.org/10.1098/rsif.2018.0273)
5. W. Wu, Y. Wang, *J. Macromol. Sci., B* **59** (2020) 213 (https://doi.org/10.1080/00222348.2019.1709710)
6. X. Liu, C. Wang, J. Liu, G. Wang, Z. Yang, F. Chen, J. Song, *J. Appl. Phys.* **125** (2019) 123301 (https://doi.org/10.1063/1.5061751)
7. Sheeja, O. Manaf, A. Sujith, *AIP Conf Proc* **1849** (2017) 020040 (https://doi.org/10.1063/1.4984187).
8. R. Dorati, C. Colonna, C. Tomasi, G. Bruni, I. Genta, T. Modena, B. Conti, *J. Biomater. Sci. Polym. Ed.* **23** (2012) 2223 (https://doi.org/10.1163/156856211X613915)
9. S. S. Cota V. Vasconcelos, M. Senne Jr., L. L. Carvalho, D. B. Rezende, R. F. Côrrea, *Braz. J. Chem. Eng.* **24** (2007) 259 (https://doi.org/10.1590/S0104-66322007000200010)
10. A. G. El-Shamy, W. M. Attia, K. M. Abd El Kader, *Mater. Chem. Phys.* **191** (2017) 225 (https://doi.org/10.1016/j.matchemphys.2017.01.026)

11. S. A. Nouh, B. O. Alsobhi, A. A. Elfadl, A. M. Massoud, *J. Inorg. Organomet. Polym. Mater.* **27** (2017) 1851 (https://doi.org/10.1007/s10904-017-0650-5)
12. A. B. Lugão, B. Hutzler, T. Ojeda, S. Tokumoto, R. Siemens, K. Makuuchi, A. L. Villavicencio, *Radiat. Phys. Chem*. **57** (2000) 389 (https://doi.org/10.1016/S0969-806X(99)00473-9)
13. A. J. Satti, N. A. Andreucetti, R. Quijada, C. Sarmoria, J. M. Pastor, E. M. Valles, *J. Appl. Polym. Sci.* **117** (2010) 290 (https://doi.org/10.1002/app.31983)
14. A. J. Satti, J. A. Ressia, M. L. Cerrada, N. A. Andreucetti, E. M. Vallés, *Radiat. Phys. Chem*. **144** (2018) 298 (https://doi.org/10.1016/j.radphyschem.2017.09.002)
15. G. K. Novikov, V. V. Fedchishin, A. I. Smirnov, *Plast. Massy* **11** (2019) 7 (https://doi.org/10.35164/0554-2901-2019-11-12-7-9)
16. A. A. Guzhova, M. F. Galikhanov, *Surf. Eng. Appl. Electrochem.* **53** (2017) 240 (https://doi.org/10.3103/S106837551703005X)
17. H. F. R. Ferreto, A. C. F. Oliveira, R. Gaia, D. F. Parra, A. B. Lugão, *AIP Conf. Proc.* **1593** (2014) 236 (https://doi.org/10.1063/1.4873771).
18. J. C. M. Suarez, E. E. C. Monteiro, E. B. Mano, *Polym. Degrad. Stab.* **75** (2002) 143 (https://doi.org/10.1016/S0141-3910(01)00213-0).
19. M. Ruff, C. Paulik, *Macromol. React. Eng.* **7** (2013) 71 (https://doi.org/10.1002/mren.201200050)
20. G. H. Michler, V. Seydewitz, M. Buschnakowski, L.P. Myasnikowa, E. M. Ivan’kova,V. A. Marikhin, Y. M. Boiko, S. Goerlitz, *J. Appl. Polym. Sci.* **118** (2010) 866 (https://doi.org/10.1002/app.32346).

Journal of the Serbian Chemical Society
Version electronic
JSCS-info@shd.org.rs • www.shd.org.rs/JSCS

J. Serb. Chem. Soc. 87 (7–8) 899–910 (2022)
JSCS–5566

Original scientific paper
Published 5 May 2022

Determination of the absolute hardness of electrolytically produced copper coatings by application of the Chicot–Lesage composite hardness model

IVANA O. MLADENOVIĆ[1], JELENA S. LAMOVEC[2], DANA VASILJEVIĆ-RADOVIĆ[1], VESNA RADOJEVIĆ[3] and NEBOJŠA D. NIKOLIĆ[1]*#

[1]University of Belgrade, Institute of Chemistry, Technology and Metallurgy, Njegoševa 12, 11000 Belgrade, Serbia, [2]University of Criminal Investigation and Police Studies, Cara Dušana 196, Zemun, 11000 Belgrade, Serbia and [3]University of Belgrade, Faculty of Technology and Metallurgy, Karnegijeva 4, 11001 Belgrade, Serbia

(Received 14 October, revised 6 December, accepted 7 December 2021)

Abstract: In this study, a novel procedure, based on application of the Chicot–Lesage (C–L) composite hardness model, was proposed for the determination of an absolute hardness of electrolytically produced copper coatings. The Cu coatings were electrodeposited on the Si(111) substrate by the pulsating current (PC) regime with a variation of the following parameters: the pause duration, the current density amplitude and the coating thickness. The topography of produced coatings was characterized by atomic force microscope (AFM), while a hardness of the coatings was examined by Vickers microindentation test. Applying the C–L model, the critical relative indentation depth $(RID)_c$ of 0.14 was determined, which is independent of all examined parameters of the PC regime. This *RID* value separated the area in which the composite hardness of the Cu coating corresponded to its absolute hardness ($RID < 0.14$) from the area in which the application of the C–L model was necessary for a determination of the absolute coating hardness ($RID \geq 0.14$). The obtained value was in a good agreement with the value already published in the literature.

Keywords: electrodeposition; the pulsating current; topography; hardness; relative indentation depth.

INTRODUCTION

According to its unique combination of properties, such as high thermal and electrical conductivity, malleability, corrosion resistance, and good adhesiveness with a substrate, copper found wide application in many industrial branches such as aerospace, automotive, electronics and telecommunications.[1] Due to its anti-

---

* Corresponding author. E-mail: nnikolic@ihtm.bg.ac.rs
[#] Serbian Chemical Society active member.
https://doi.org/10.2298/JSC211014105M

microbial characteristics, Cu also found application in a medicine in a control of healthcare-associated infections.[2] The methods including electrodeposition, electroless plating, chemical vapour deposition (CVD), physical vapour deposition (PVD), thermal spray and sputtering techniques are widely used for the production of Cu in a form of coatings on various conductive or non-conductive substrates.[2] The choice of a method for a production of Cu coatings is closely related to a desired application of the coating.

The main advantages of electrodeposition processes over the other production techniques are the obtaining of coatings of desired quality and thickness by an easy control of parameters and regime of electrodeposition.[3] The both constant (galvanostatic) and periodically changing (the PC and the reversing current (RC)) regimes are used in a production of Cu coatings for commercial purposes. The main parameters affecting a quality of coatings are: type and composition of electrolyte, temperature, stirring of electrolyte, the type of cathode, time of electrodeposition, *etc*.[3]

Mechanical properties of metal coatings are closely related with their morphological and structural characteristics determining a quality of any coating. Hardness is one of the most important mechanical properties of coatings, and indentation techniques are widely used to determine it.[4] The main challenge in hardness analysis of any coating is a determination of its absolute (or real) hardness which exclude a contribution of substrate (cathode) in measured hardness value. It can be done either by the use of relatively small indentation loads which enable that a critical indentation depth after which a substrate begins to affect hardness is not exceeded, or by the application of various composite hardness models which in calculations predict contributions from both substrate and coating in measured hardness value. The first way is usually suitable for the thick coatings, because it enables the use of larger indentation loads. The Chicot––Lesage (C–L),[5–8] Chen–Gao (C–G)[9–11] and Korsunsky (K-model)[12–15] are most often used composite hardness models for a determination of an absolute hardness of coating. The choice of models depends on substrate/coating hardness ratio, and some of them give optimum results for „hard film on soft substrate" systems like Korsunsky model,[12–15] while some other models like the Chen––Gao[9–11] and the Chicot–Lesage[5–8] are suitable for the analysis of "soft film on hard substrate" systems.

For a long time was adopted so-called Buckle's one-tenth rule,[4] which predicts that a critical indentation depth above which a substrate begins to affect a coating hardness is 0.1 of a coating thickness value. However, this rule has not an universal character, and the beginning of effect of a substrate on a coating hardness depends on substrate/coating hardness ratio,[4] and it depends on the indenter geometry, plastic pile-up effect, film/substrate adhesion, elastic properties of the film and substrate and the friction between the indenter and film.[4,16–20] For example, for „soft film on hard substrate“ systems, this rule is too strong, while for systems like „hard film on soft substrate“, more restrictive limitations than the one-tenth rule can be valid.

In this study, the try to determine an absolute (or real) hardness of Cu coatings obtained by the PC regime on very hard Si(111) cathodes is made by the analysis of data obtained by applying the C–L model. The idea for this study was based on our recently published results,[8,21] in which extremely high values for the hardness of the Cu coatings on Si(111) were observed using the application of the C–L model.[8] The solution of this problem, through an establishment of the limiting (or critical) relative indentation depth $(RID)_c$ of 0.14 for the Cu coatings of various thicknesses, was obtained the same way, but on the brass cathode.[21] The aim of this study is to resolve some of the main dilemmas related to an application of the C–L model in a determination of absolute (or real) hardness of the Cu coatings on the hard substrates.

EXPERIMENTAL

The copper coatings were electrolytically produced by the electrodeposition of Cu on the Si(111) hard substrate. The electrodeposition of copper was performed by the pulsating current (PC) regime from 240 g L^{-1} $CuSO_4 \cdot 5H_2O$ in 60 g L^{-1} H_2SO_4, at the room temperature in an open cell of a prismatic shape.

The parameters of the applied PC regime for electrodeposition of Cu coatings are given in Table I.

TABLE I. The parameters of the PC regime used for electrodeposition of copper coatings on the Si(111). j_A – the current density amplitude; j_{av} – the average current density; t_p – pause duration; ν – frequency; δ – thickness of coating; deposition pulse, t_c = 5 ms

No.	t_p / ms	j_A / mA cm^{-2}	j_{av} / mA cm^{-2}	ν / Hz	δ / μm
1	5	100	50	100	40
2	7.5	100	40	80	40
3	15	100	25	50	40
4	28.3	100	15	30	40
5	5	120	60	100	40
6	5	140	70	100	40
7	5	100	50	100	20
8	5	100	50	100	60

Analytical grade chemicals (p.a.) and double distilled water were used for a preparation of the electrolyte. The two parallel Cu sheets placed close to the wall of cell were used as the anodes. The Si(111) orientation of (1.0×1.0) cm^2 surface area is used as a cathode, and it was placed in the middle of the cell between two parallel Cu anodes. The preparation of the Si(111) cathodes for electrodeposition was described elsewhere.[8]

Topography of the Cu coatings was examined by the atomic force microscope (AFM) using model auto probe CP research; TM microscopes, Veeco Instruments, in the contact mode. The scan area was (70×70) μm^2. The R_q (root mean square roughness) value of the same coatings was determined using the software WSxM 4.0 beta 9.3 version.[22]

Vickers microhardness tester Leitz Kleinert Prufer DURIMET I was used for the measurements and determination of an absolute (or real) hardness of the Cu coatings. The dwell time of 25 s, and loads in the 0.049–2.942 N range were used for this purpose. The rest of the experimental procedure for a determination of a composite hardness of the Cu coatings is presented in literature.[8]

RESULTS AND DISCUSSION

Basic facts

The regime of pulsating current (PC) is defined by periodic repetitions of current square wave and pause, and it can be presented as:[3]

$$j_{\mathrm{av}} = j_{\mathrm{A}} \frac{t_{\mathrm{c}}}{t_{\mathrm{c}} + t_{\mathrm{p}}} \tag{1}$$

where j_{av} is the average current density, j_{A} is the current density amplitude, and t_{c} and t_{p} are durations of deposition pulse and pause, respectively.

For the PC regime, frequency, ν, is another important parameter, and it is defined as:

$$\nu = \frac{1}{t_{\mathrm{c}} + t_{\mathrm{p}}} \tag{2}$$

The PC regime gives optimum results in the range of frequencies between 10 and 100 Hz, and electrodeposition process in this range of frequency (the ms range) occurs at the average current density.[3]

Topography and roughness of the Cu coatings produced by the various PC regimes

Morphology and roughness of the electrolytically produced Cu coatings were characterized by AFM. Fig. 1 shows the 2D (two dimensional) AFM images of the Cu coatings obtained with various parameters of the PC regime, *i.e.*, at various average current density values.

The decrease of both size and regularity of Cu grains is observed with increasing the j_{av} values. It is necessary to note that the fine-grained coatings were obtained starting from an average current density of 40 mA cm^{-2}. This change in surface morphology can be attributed to a decrease of contribution of the activation control and an increase of contribution of the diffusion control with increasing j_{av} value, since a formation of all these Cu coatings occurred in the mixed activation-diffusion control.[8]

The decrease of grain size was accompanied by an increase of uniformity of the Cu coatings, which is confirmed by roughness analysis of the obtained coatings. The values of R_{q} roughness parameters for the same Cu coatings are given in Table II. The presence of the larger grains in the Cu coatings obtained using j_{av} of 15 and 25 mA cm^{-2} (Fig. 1a and b, respectively) induced an increased nonuniformity, and hence, larger roughness of these coatings relative to those obtained with the larger j_{av} values, when fine-grained coatings are formed. The slight increase in a roughness of the Cu coatings with j_{av} of 60 and 70 mA cm^{-2} is due to a beginning of dominant effect of the diffusion control of the electrodeposition process, characterizing a formation of rougher deposits and the obtaining of various disperse or irregulars forms.[3,8]

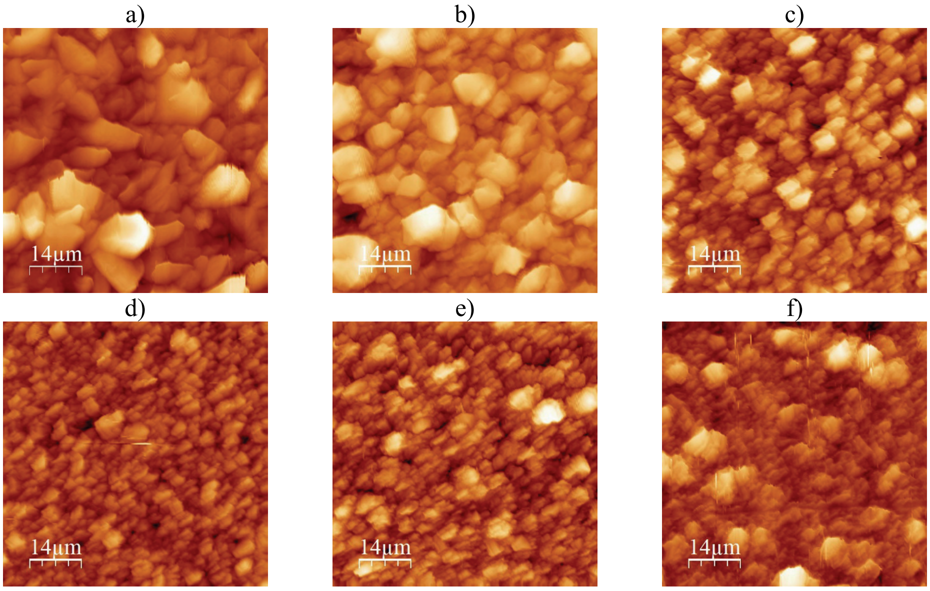

Fig. 1. The 2D AFM images of the Cu coatings obtained by the PC regime at j_{av} of: a) 15, b) 25, c) 40, d) 50, e) 60 and f) 70 mA cm^{-2}. The thickness of coatings, δ= 40 µm.

TABLE II. The values of R_q roughness obtained by application of AFM software from (70×70) µm^2 scan area, and Meyer's index m for the Cu coatings produced by various PC regimes

j_{av} / mA cm^{-2}	15	25	40	50	60	70
R_q / nm	677.2	599.2	490.8	318.0	326.3	359.9
m	0.4288	0.4372	0.4770	0.4979	0.4346	0.3447

The same technique is used to analyse the effect of thickness of coatings on their roughness. Fig. 2 shows 2D AFM images of the Cu coatings, obtained at j_{av} of 50 mA cm^{-2}, with thicknesses of 20 (Fig. 2a) and 60 µm (Fig. 2b). Although the uniform fine-grained coatings were obtained with the both thicknesses, it is necessary to note that size of grains enlarged with increasing the coating thickness. This was in accordance with theory considering a mechanism of electrodeposition by the PC regime on morphology of metal deposits.[3] For the Cu coatings thicknesses from 20 and 60 µm, the values of R_q roughness were 131.1 and

367.2 nm, respectively. This increase in roughness of the coatings is just a consequence of the growing size of grains with the thickness of coating.

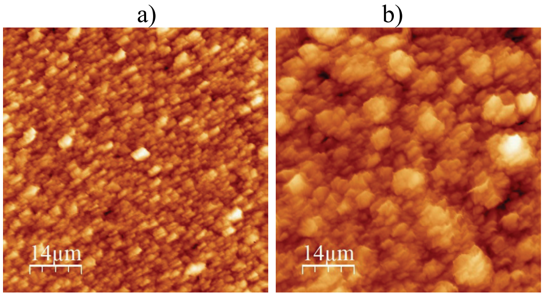

Fig. 2. The 2D AFM images of the Cu coatings obtained by the PC regimes at *j*av of 50 mA cm^{-2}. The thicknesses of coatings, δ, a) 20 and b) 60 µm.

Hardness analysis of the Cu coatings produced by the various the PC regimes

The measured (also known as composite) hardness, H_c / Pa, of any coating depends on applied load, P / N, and size of a diagonal, d / m, made by indenter in a coating, and it is defined as:[8]

$$H_c = 1.8544\frac{P}{d^2} \tag{3}$$

This value often includes a contribution of substrate (cathode), and for that reason, it is necessary to eliminate this contribution in order to obtain absolute (or real) hardness of a coating. The application of various composite hardness models represents valuable way to achieve it.[8,11,14,15,21]

Fig. 3a shows the dependencies of the composite hardness (H_c) on the relative indentation depth (*RID*) for the Cu coatings obtained on the Si(111) cathodes at the various average current densities (*i.e.*, frequencies). *RID* is defined as a ratio between an indentation depth (h) and a thickness of coating (δ) as $RID = h/\delta$, where an indentation depth is related with a diagonal size as $h = d/7$. The indentation depth increases a contribution of a substrate to the measured composite hardness with the growth of *RID* values. At the high *RID* values the composite hardness corresponded to a hardness of substrate.[8] Although there is no precise boundary where a contribution of substrate to measured hardness begins, as well as where measured hardness begins to correspond to a substrate hardness, the *RID* values of 0.1 and 1, respectively, are usually taken as the limiting values for these boundaries.[8] The fact that a significant number of H_c values is situated in a zone where the substrate affects hardness (Fig. 3a) indicated a necessity of application of the composite hardness models in a determination of the absolute hardness of the Cu coatings.

With the hardness of 7.42 GPa,[8] Si(111) belongs to a group of very hard substrates, while the Cu coatings on the Si(111) electrodes belong to a group of "soft film on hard substrate" type of a composite system. The C–L composite model showed as very valuable for a determination of the absolute hardness of such coatings,[8] and the dependencies of the coating hardness, H_{coat} on the *RID*, calculated by this model,for the given Cu coatings, are presented in Fig. 3b. The detailed description of the C–L composite hardness model can be found in literature.[8] At the first sight, it can be noticed that the calculated H_{coat} values were much larger than the measured H_{c} values at the smaller *RID* values. Anyway, it is illogical and an additional analysis of the obtained dependencies was necessary in order to determine the absolute (real) values of the coating hardness in the whole range of the *RID* values.

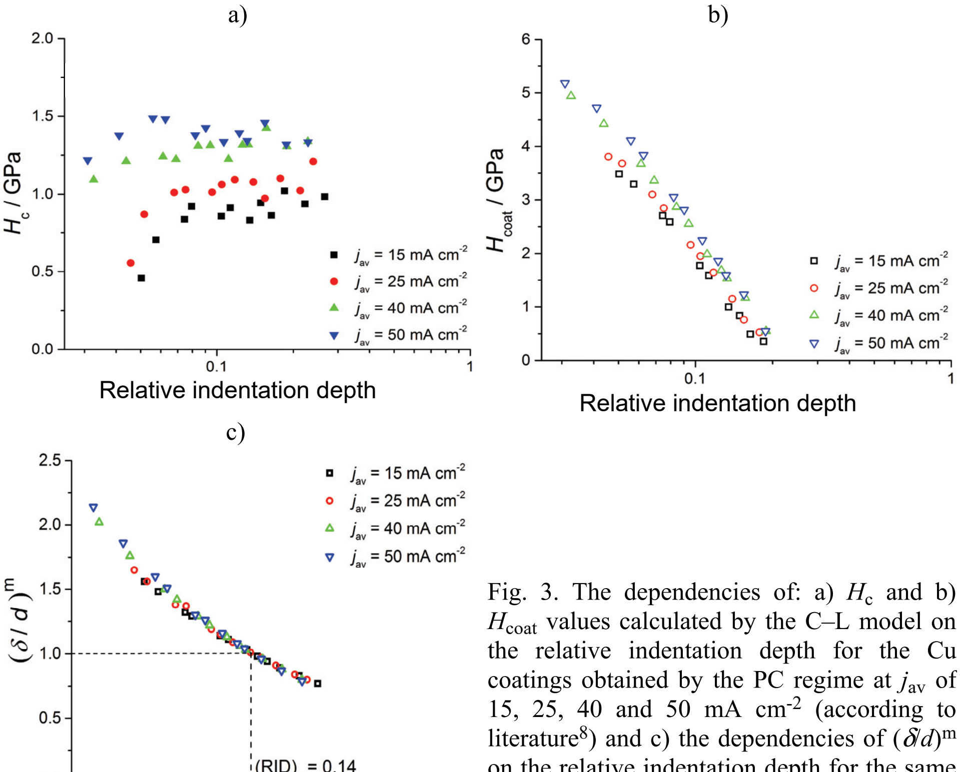

Fig. 3. The dependencies of: a) H_{c} and b) H_{coat} values calculated by the C–L model on the relative indentation depth for the Cu coatings obtained by the PC regime at j_{av} of 15, 25, 40 and 50 mA cm^{-2} (according to literature[8]) and c) the dependencies of $(\delta/d)^{\mathrm{m}}$ on the relative indentation depth for the same Cu coatings. The thickness of coatings, δ = 40 µm.

For that reason, the following analysis of the obtained dependencies was performed using the C–L model. Fig. 3c shows the dependencies of the $(\delta/d)^{\mathrm{m}}$ on the *RID* values for the Cu coatings obtained on the various average current densities (*i.e.*, frequencies). In these dependencies, an exponent *m* is the composite Meyer's index, calculated by a linear regression performed on all experimental points for the given coating–substrate system.[6,14] The values of this exponent calculated for the Cu coatings are given in Table II. The composite Meyer's index defines a way of change of the composite hardness with the applied load. The detailed explanation of the composite Meyer's index can be found in literature.[6,14] The increase of the Meyer's composite index with the increase of j_{av} from 15 to 50 mA cm^{-2} can be explained by the strain hardening effect.

Assuming that the C–L model is valid up to $(\delta/d)^m = 1$,[7] the limiting or critical *RID* value of 0.14 ($(RID)_c = 0.14$) was determined (Fig. 3c). It is clear that for *RID* values larger than 0.14 it is necessary to apply the C–L model in order to determine an absolute hardness of the Cu coatings. On the other hand, for the *RID* values smaller than this value, the measured composite hardness corresponded to the coating hardness. In this way a precise boundary where begins an effect of substrate (cathode) on the measured hardness of Cu coatings is determined. The additional analysis of the data shown in Fig. 3a and b can confirm this assumption. Namely, the careful analysis of these data showed that the *RID* value of 0.14 represents the limiting value after which the measured H_c values become larger than the calculated H_{coat} values. For the *RID* values smaller than 0.14, the calculated H_{coat} values are larger than the measured H_c values, and this difference increased with the decrease of *RID* values, so that at the small *RID* values, they became much larger than the H_c values. It is necessary to note that this critical *RID* value was independent of the applied average current density.

That way was confirmed the *RID* limiting value of 0.14, previously observed for the Cu coatings of various thicknesses, obtained by the same regime on the brass substrate.[21] In the next step, the Cu coatings noted at a frequency of 100 Hz, but at j_{av} of 60 and 70 mA cm^{-2} were analyzed. Simultaneously, the Cu coatings obtained at ν of 100 Hz and j_{av} of 50 mA cm^{-2}, but with the thicknesses of 20 and 60 μm are also analyzed. The H_c and H_{coat} dependencies on the *RID* for these coatings are given in Fig. 4a and b, respectively. These figures also include the same dependencies for the 40 μm thick Cu coating obtained at j_{av} of 50 mA cm^{-2}, which have been already given in Fig. 3.

The dependencies of the $(\delta/d)^m$ on the *RID* for the analyzed Cu coatings are shown in Fig. 4c. The values of *m* exponent for the Cu coatings obtained at j_{av} of 60 and 70 mA cm^{-2} are given in Table II, while *m* values for 20 and 60 μm thick Cu coatings were 0.3591 and 0.4286, respectively. The increase of the Meyer's composite index with the growing coating thickness is due to a decrease of influence of substrate with the thickness of coating.

Applying the same procedure, which takes into consideration of a validity of the C–L model up to $(\delta/d)^m = 1$, the critical *RID* value of 0.14 was also determined for these Cu coatings. The analysis of these dependencies also showed that for $RID < 0.14$ the calculated H_{coat} values were larger than the measured H_c values, strongly proving that *RID* of 0.14 represents the limiting (or critical) value separating an area in which the measured composite hardness can be equal to an absolute hardness of the coating, from that in which the application of the C–L model was necessary for a determination of the absolute hardness. It is very clear that the critical *RID* value is not affected by the average current density and the thickness of coating.

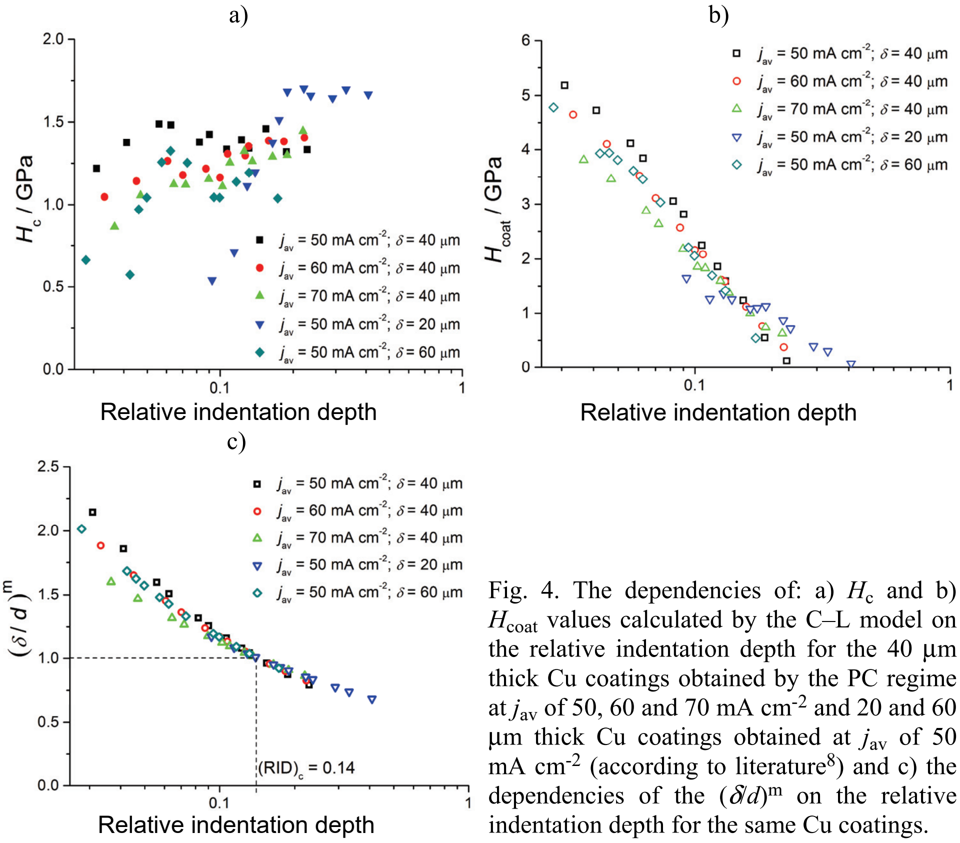

Fig. 4. The dependencies of: a) H_c and b) H_{coat} values calculated by the C–L model on the relative indentation depth for the 40 μm thick Cu coatings obtained by the PC regime at j_{av} of 50, 60 and 70 mA cm^{-2} and 20 and 60 μm thick Cu coatings obtained at j_{av} of 50 mA cm^{-2} (according to literature[8]) and c) the dependencies of the $(\delta/d)^m$ on the relative indentation depth for the same Cu coatings.

Hence, the critical (or limiting) *RID* value of 0.14 separating the zone of the absolute coating hardness from the zone of strong effect of substrate was determined. This value was independent of parameters of the PC regime, such as pause duration and the current density amplitude (*i.e.*, independent of frequency and the average current density). Also, this value was independent of the coating thickness and the type of cathode. This clearly indicates that the *RID* value of 0.14 can represent a general characteristic of Cu coatings.

The obtained *RID* value of 0.14 was in excellent agreement with the results of an estimation of effect of a substrate on coating hardness found in the literature.[4,23] Namely, for a polycrystalline soft films on hard substrate like the coatings of Cu on Si(111), a critical indentation depth, h_c above which a substrate achieves a strong effect on a hardness is related with a coating thickness as $h_c > 0.20\delta$. For $h_c < 0.20\delta$, a substrate has a negligible effect on the hardness. Hence, the critical *RID* value which separates area of absolute hardness of coating from that one where an effect of substrate cannot be neglected on measured hardness is 0.20. This clearly indicates that the here obtained value of 0.14 was inside this zone. The advantage of the proposed procedure in this study is that it is not necessary to do a cross section analysis of coating in order to establish whether a critical indentation depth, with maximum value of 20 % of the overall thickness of coating, is exceeded. In this proposed procedure, based on the application of the C–L model, considering the existing relation between a diagonal size and an indentation depth, it is possible to define a maximum load for any coating thickness, which can be applied to ensure that a measured composite hardness corresponds to a coating hardness. In this moment, the proposed *RID* value of 0.14 is valid for the electrolytically obtained copper coatings on the hard substrates like brass and Si(111). For any other metals and substrates, it will be a subject of future investigations.

CONCLUSIONS

The coatings of copper were electrolytically produced by electrodeposition of Cu on the Si(111) hard substrate, under the regime of the pulsating current (PC) varying a duration of pause (5, 7.5, 15 and 28.3 ms) and the current density amplitude (100, 120 and 140 mA cm^{-2}) values. The corresponding average current densities were in the 15–70 mA cm^{-2} range, and the frequencies were in the 30–100 Hz range. The examined thicknesses of the coatings were 20, 40 and 60 μm. The topography and the hardness of Cu coatings were characterized by AFM and by Vickers microindentation test using the C–L composite hardness model for data processing.

By the application of the C–L model, it is established the critical (or limiting) relative indentation depth $(RID)_c$, of 0.14, which is independent of the parameters of the PC regime and of the thickness of the coatings. This value separated the zone in which the measured hardness corresponds to a hardness of the coating from the zone which requires an application of the C–L model for a determination of an absolute hardness of the coating.

This critical *RID* value was in excellent agreement with the *RID* value of 0.20 found in the literature for the same type “soft film on hard substrate” composite system.

Acknowledgement. This work was financially supported by the Ministry of Education, Science and Technological Development of the Republic of Serbia (Grants No. 451-03-9/ /2021-14/200026 and 451-03-9/2021-14/200135).

ИЗВОД

ОДРЕЂИВАЊЕ АПСОЛУТНЕ ТВРДОЋЕ ЕЛЕКТРОЛИТИЧКИ ДОБИЈЕНИХ ПРЕВЛАКА БАКРА ПРИМЕНОМ CHICOT–LESAGE КОМПОЗИТНОГ МОДЕЛА ТВРДОЋЕ

ИВАНА О. МЛАДЕНОВИЋ[1], ЈЕЛЕНА С. ЛАМОВЕЦ[2], ДАНА ВАСИЉЕВИЋ-РАДОВИЋ[1], ВЕСНА РАДОЈЕВИЋ[3] и НЕБОЈША Д. НИКОЛИЋ[1]

[1]*Универзитет у Београду, Институт за хемију, технологију и металургију, Његошева 12, Београд,* [2]*Криминалистичко-полицијски универзитет, Цара Душана 196, Земун, Београд и* [3]*Универзитет у Београду, Технолошко-металуршки факултет, Карнегијева 4, Београд*

Предложен је нови поступак заснован на примени Chicot–Lesage (C–L) композитног модела тврдоће за одређивање апсолутне тврдоће електролитички добијених превлака бакра. Превлаке бакра су електрохемијски исталожене на силицијуму (111) оријентације режимом пулсирајуће струје варирањем следећих параметара: трајање паузе, амплитудна густина струје и дебљина превлаке. Топографија произведених превлака је окарактерисана микроскопијом атомских сила, док је тврдоћа превлака испитивана Викерсовим тестом утискивања. Применом C–L композитног модела тврдоће, одређена је критична релативна дубина утискивања (*RID*), од 0,14, која је независна од свих испитиваних параметара режима пулсирајуће струје. Ова вредност раздваја област у којој композитна тврдоћа превлаке може да се изједначи са њеном апсолутном тврдоћом ($RID < < 0,14$) од области у којој је неопходно применити C–L модел за одређивање апсолутне тврдоће превлаке ($RID \geq 0,14$). Добијена вредност *RID* показује добро слагање са вредностима публикованим у литератури.

(Примљено 14. октобра, ревидирано 6. децембра, прихваћено 7. децембра 2021)

REFERENCES

1. Copper, https://www.sharrettsplating.com/coatings/copper (accessed on 23 August 2021)
2. N. Bharadishettar, U. K. Bhat, D. B. Panemangalore, *Metals* **11** (2021) 711 (https://doi.org/10.3390/met11050711)
3. K. I. Popov, S. S. Djokić, N. D. Nikolić, V. D. Jović, *Morphology of Electrochemically and Chemically Deposited Metals*, Springer International Publishing, 2016 (doi: 10.1007/978-3-319-26073-0)
4. I. Manika, J. Maniks, *J. Phys., D* **41** (2008) 074010 (http://dx.doi.org/10.1088/0022-3727/41/7/074010)
5. J. Lesage, A. Pertuz, E. S. Puchi-Cabrera, D. Chicot, *Thin Solid Films* **497** (2006) 232 (http://doi:10.1016/j.tsf.2005.09.194)
6. J. Lesage, D. Chicot, *Surf. Coat. Technol.* **200** (2005) 886 (https://doi.org/10.1016/j.surfcoat.2005.01.056)
7. D. Chicot, J. Lesage, *Thin Solid Films* **254** (1995) 123 (https://doi.org/10.1016/0040-6090(94)06239-H)
8. I. O. Mladenović, J. S. Lamovec, D. G. Vasiljević Radović, R. Vasilić, V. J. Radojević, N. D. Nikolić, *Metals* **10** (2020) 488 (https://doi.org/10.3390/met10040488)
9. J. L. He, W. Z. Li, H. D. Li, *Appl. Phys. Lett.* **69** (1996) 1402 (https://doi.org/10.1063/1.117595)
10. Q. Hou, J. Gao, S. Li, *Eur. Phys. J., B* **8** (1999) 493 (https://doi.org/10.1007/s100510050716)

11. I. O. Mladenović, J. S. Lamovec, D. G. Vasiljević-Radović, V. J. Radojević, N. D. Nikolić, *Int. J. Electrochem. Sci.* **15** (2020) 12173 (http://dx.doi.org/10.20964/2020.12.01)
12. A. M. Korsunsky, M. R. Mc Gurk, S. J. Bull, T. F. Page, *Surf. Coat. Technol.* **99** (1998) 171 (https://doi.org/10.1016/S0257-8972(97)00522)
13. J. R. Tuck, A. M. Korsunsky, S. J. Bull, R. I. Davidson, *Surf. Coat. Technol.* **137** (2001) 217 (doi:10.1016/S0257-8972(00)01063-X)
14. J. Lamovec, V. Jovic, D. Randjelovic, R. Aleksic, V. Radojevic, *Thin Solid Films* **516** (2008) 8646 (https://doi.org/10.1016/j.tsf.2008.06.035)
15. I. O. Mladenović, J. S. Lamovec, V. B. Jović, M. Obradov, D. G. Vasiljević Radović, N. D. Nikolić, V. J. Radojević, *J. Serb. Chem. Soc.* **84** (2019) 729 (https://doi.org/10.2298/JSC181003023M)
16. D. Lebouvier, P. Gilormini, E. Felder, *Thin Solid Films* **172** (1989) 227 (https://doi.org/10.1016/0040-6090(89)90651-2)
17. S. J. Bull, *J. Phys., D* **38** (2005) R393 (https://doi.org/10.1088/0022-3727/38/24/R01)
18. D. E. Kramer, A. A. Volinsky, N. R. Moody, W. W. Gerberich, *J. Mater. Res.* **16 (**2001) 3150 (https://doi.org/10.1557/JMR.2001.0434)
19. T. W. Wu, M. Moshref, P. S. Alexopoulos, *Thin Solid Films* **187** (1990) 295 (https://doi.org/10.1016/0040-6090(90)90051-E)
20. D. Beegan, S. Chowdhury, M.T. Laugier, *Thin Solid Films* **466** (2004) 167 (https://doi.org/10.1016/j.tsf.2004.03.006)
21. I. O. Mladenović, N. D. Nikolić, J. S. Lamovec, D. Vasiljević-Radović, V. Radojević, *Metals* **11** (2021) 111 (https://doi.org/10.3390/met11010111)
22. I. Horcas, R. Fernández, J. M. Gómez-Rodríguez, J. Colchero, J. Gómez-Herrero, A. M. Baro, *Rev. Sci. Instrum.* **78** (2007) 013705 (doi:10.1063/1.2432410)
23. I. Manika, J. Maniks, *Thin Solid Films* **208** (1992) 223 (https://doi.org/10.1016/0040-6090(92)90646-S).

Journal of the Serbian Chemical Society
JSCS-info@shd.org.rs • www.shd.org.rs/JSCS

J. Serb. Chem. Soc. 87 (7–8) 911–924 (2022)
JSCS–5567

Original scientific paper
Published 28 April 2022

Heat transfer by liquid convection in particulate fluidized beds

DARKO R. JAĆIMOVSKI[1], DANICA V. BRZIĆ[2]*, RADMILA V. GARIĆ-GRULOVIĆ[1],
RADA V. PJANOVIĆ[2], MIHAL M. ĐURIŠ[1], ZORANA LJ. ARSENIJEVIĆ[1]
and NEVENKA M. BOŠKOVIĆ-VRAGOLOVIĆ[2#]

[1]University of Belgrade – Institute of Chemistry, Technology and Metallurgy – National institute of the Republic of Serbia, Belgrade, Serbia and [2]University of Belgrade – Faculty of Technology and Metallurgy, Belgrade, Serbia

(Received 16 December 2021, revised 20 February, accepted 21 February 2022)

Abstract: In this work the theoretical model for heat transfer from a wall to a liquid-solid fluidized bed by liquid convective mechanism has been proposed and developed. The model is based on thickness of boundary layer and film theory. The key parameter in the model is the distance between two adjacent particles which collide with the wall. According to the proposed model, the liquid convective heat transfer in a fluidized bed is 4 to 5 times more intense than in a single-phase flow. Additionally, the wall-to-bed heat transfer coefficient has been measured experimentally in water–glass particles fluidized bed, for different particle sizes. Comparison of the model prediction with experimental data has shown that size of the particles strongly influences the mechanism of heat transfer. For fine particles of 0.8 mm in diameter, the liquid convective heat transfer model represents adequately the experimental data, indicating that particle convective mechanism is negligible. For coarse particles of 1.5–2 mm in diameter, the liquid convective heat transfer mechanism accounts for 60 % of the overall heat transfer coefficient.

Keywords: model; boundary layer; film theory.

INTRODUCTION

Liquid–solid fluidized beds are characterized by high heat and mass transfer rates, uniform temperature, and ability to reduce fouling. These specific features give rise to their numerous traditional and novel applications as: reactors,[1] bioreactors,[2–4] in food processing,[5] for waste water treatment[6] and thermal energy generation.[7]

---

[*] Corresponding author. E-mail: danica@tmf.bg.ac.rs
[#] Serbian Chemical Society member.

https://doi.org/10.2298/JSC211216020J

Heat transfer in liquid-solid fluidized beds is a complex phenomenon, affected by physical properties of liquid and solid, operational parameters and geometry factors. Wall-to-bed heat transfer coefficient is commonly interpreted as a sum of contributions of liquid convective (α_{lc}) and particle convective heat transfer mechanisms (α_{pc}). The major resistance to heat transfer is considered to be in the laminar sublayer at the wall, where forced liquid convection takes place. Particle convective contribution refers to the heat transferred by particles due to their collisions with the wall, and the movement in and out of the thermal boundary layer. The key factors affecting the heat transfer rate are thickness of boundary layer (liquid convective mechanism) and the particle velocities, which determine the frequency of contacts between particles and wall (particle convective mechanism). Both the thickness of boundary layer and the particle velocities are generally difficult to quantify, and that can explain the fact that there is a very few theoretical studies on mechanism of heat transfer in liquid-solid fluidized in literature.[8,9]

Heat transfer in liquid–solid fluidized beds has been much more investigated experimentally,[10–15] yielding in empirical correlations for the prediction of heat transfer coefficient, which are limited to the certain ranges of operating conditions. The typical forms of empirical correlations have been suggested by Mouroyama *et al.*:[11]

$$\text{Nu}_\text{p} = \frac{0.137}{\varepsilon}(1-\varepsilon)^{0.271}\,\text{Re}_p^{0.729}\,\text{Pr}^{1/3} \tag{1}$$

and Haid *et al.*:[13]

$$\text{Nu}_\text{p} = 0.1493\,\text{Re}_\text{p}^{0.729}\,\text{Pr}^{0.52}\left(\frac{\rho_\text{p}-\rho}{\rho}\right)^{0.03}\left(\frac{d_\text{p}}{D}\right)\varepsilon^{-1.41}(1-\varepsilon)^{0.271} \tag{2}$$

Jamialahmadi *et al.*[16] have compared the predictions for heat transfer coefficient from a number of empirical correlations, and concluded that there are quite big discrepancies among them. Therefore, the same authors attempted to generalize the correlation for heat transfer coefficient. They suggested an approach where the total heat transfer area (A) is divided into the part where the heat is transferred by liquid convection (A_c) and the part where the particle convective mechanism takes place (A_p). Each of the mechanisms contribute to the overall heat transfer coefficient (α) proportionally to the fraction of area where it occurs, as it is given by:

$$\alpha = \alpha_{\text{lc}} + \alpha_{\text{pc}} = \left(1-\frac{A_\text{p}}{A}\right)\alpha_\text{c} + \frac{A_\text{p}}{A}\alpha_\text{p} \tag{3a}$$

They assumed the local liquid convective heat transfer coefficient (α_c) to be as in the single phase flow, defined by equation of Gnielinski *et al.*[17] and the particle convective heat transfer coefficient (α_p) is represented by unsteady-state heat transfer defined by equation of Mickley and Faribacks.[18] The fraction of area affected by particles (A_p/A) has been defined by an empirical Eq. (3b), as the dependence on particle concentration (1–ε) and particle to column diameter ratio (d_p/D):

$$\frac{A_p}{A}=1.5\left(\frac{d_p}{D}\right)^{0.256}\left(1-\varepsilon\right)^{0.507} \tag{3b}$$

The exponents in Eq. (3b) have been determined by fitting the large number of experimental data for the heat transfer coefficient, measured by various authors, to the Eq. (3a).

Khan and Elkamel[9] have proposed the theoretical model for heat transfer coefficient between immersed flat element and fluidized bed. That model includes the energy balance equation in order to assess the fluid convective contribution and Fourier equations for the unsteady-state thermal conduction in order to assess the particle conductive and fluid conductive components of the heat transfer coefficient. The necessity of numerical solutions of the rigorous model equations restricts the practical applicability of this model.

Wasmund and Smith[8] have developed the model for the contribution of the particle convective heat transfer mechanism, based on the particle velocities and radial temperature profiles. By comparison of the modelled particle convective contribution, with the experimental data for overall heat transfer coefficient, they concluded that the particle convective mechanism accounts for 30–60 % of the overall heat transfer coefficient, depending on the ratio of particle to fluid thermal resistance.

The aim of this work was a theoretical study of liquid convective heat transfer mechanism in liquid–solid fluidized bed. A new model, which predicts the contribution of liquid convective mechanism, has been developed based on the boundary layer thickness and film theory. For comparison, the wall-to-bed heat transfer coefficients have been measured experimentally for different particle sizes.

Theoretical model for liquid convective heat transfer

Some of the early theories of heat transfer in fluidized beds are based on the existence of the fluid boundary layer adjacent to the column wall.[19,20] The developed theoretical models[8,9,16] are commonly based on the fact that the main resistance to heat transfer lies in the fluid film next to the column wall, while the resistance of the bed is assuming to be negligible. The fluidizing particles influence the heat transfer in two ways: a) their motion affects the thickness of boundary layer, a result of which is the liquid convective heat transfer and b) they transfer heat themselves by absorbing it on the hot wall and releasing it in the bulk of the bed.

The model for liquid convective heat transfer from the wall, which will be presented in this work, is based on the concept that the presence of fluidizing particles has two effects: a) it reduces the thickness of the liquid boundary layer compared to the single-phase flow and b) the free area for heat transfer by liquid convection is reduced, since a certain part of the area is occupied by particles which collide with it.

In the single-phase flow of liquid over a flat surface, the continuous hydrodynamic boundary layer is formed. Under laminar conditions ($\mathrm{Re}_x < 2\times10^5$), the local thickness of the boundary layer at is defined by:[21]

$$\delta_{\mathrm{H}x} = 4.64x\mathrm{Re}_x^{-1/2} \tag{4}$$

where Re_x is the local Reynolds number at a distance x from the leading edge. An average thickness over a certain length L is defined by:

$$\delta_{\mathrm{H}} = \frac{1}{L}\int_0^L \delta_{Hx}\mathrm{d}x = 3.09L\,\mathrm{Re}_L^{-1/2} \tag{5}$$

When the heat transfer between the surface and fluid takes place the thermal boundary layer has been formed parallelly with hydrodynamic boundary layer. If Prandtl number (Pr) is larger than unity, the thermal boundary layer is contained within the hydrodynamic one and the thicknesses of those two layers are related by:[21]

$$\frac{\delta_{\mathrm{T}}}{\delta_{\mathrm{H}}} = \mathrm{Pr}^{-1/3} \tag{6}$$

Considering Eq. (5), the thickness of the thermal boundary layer can be expressed by:

$$\delta_{\mathrm{T}} = 3.09L\mathrm{Re}_{\mathrm{L}}^{-1/2}\mathrm{Pr}^{-1/3} \tag{7}$$

According to the film theory, the heat transfer coefficient can be defined as the ratio of fluid thermal conductivity and the thickness of the thermal boundary layer as it is given by:

$$\alpha_{\mathrm{sf}} = \frac{\lambda_{\mathrm{f}}}{\delta_{\mathrm{T}}} = 0.324\frac{\lambda_{\mathrm{f}}}{L}\mathrm{Re}_L^{1/2}\,\mathrm{Pr}^{1/3} \tag{8}$$

Eq. (8) gives the value of the convective heat transfer coefficient in a single--phase flow (α_{sf}). In the case of fluidized bed, the moving particles collide with the heat transfer surface (column wall) and cause brakeage of the continuous boundary layer. We assume that the thermal boundary layer is formed on the distance between two adjacent particles which collide with the wall, as it is depicted in Fig. 1a. This distance has been approximated by the mean distance between collisions according to the kinetic theory of gases. This approximation is based on the study of Carlos and Richardson,[22] who have shown that the movement of the particles in the particulate fluidized bed can be satisfactorily represented by the movement of molecules in the kinetic theory of gases. Consequently, the authors define the mean distance between collisions by Eq. (9), analogously to a mean free path of molecules:[22]

$$L = \frac{d_\mathrm{p}}{6\sqrt{2}\left(1-\varepsilon\right)} \tag{9}$$

By incorporating Eq. (9) into the Eq. (7), the thickness of thermal boundary layer in the fluidized bed is defined by:

$$\delta_\mathrm{Tfb} = 1.06\frac{d_\mathrm{p}}{\sqrt{\left(1-\varepsilon\right)}}\mathrm{Re}_\mathrm{p}^{-1/2}\,\mathrm{Pr}^{-1/3} \tag{10}$$

In Eq. (10) Re_p is the particle Reynolds number. The local liquid convective heat transfer coefficient in a fluidized bed (α_sf) is then defined by:

$$\alpha_\mathrm{fb} = \frac{\lambda_\mathrm{f}}{\delta_\mathrm{Tfb}} = 0.943\frac{\lambda_\mathrm{f}}{d_\mathrm{p}}\sqrt{\left(1-\varepsilon\right)}\,\mathrm{Re_p}^{1/2}\,\mathrm{Pr}^{1/3} \tag{11}$$

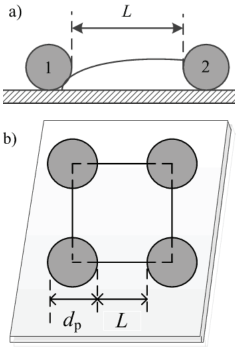

Fig. 1. a) Distance between adjacent particles which collide with the wall and b) segment of the wall representing the coverage of the area by colliding particles.

Similarly to the approach of Jamialahmadi *et al.*,[16] we assumed that the liquid convective mechanism occurs at the part of the heat transfer area which is not occupied by particles. In order to estimate the fraction of free area, we would use the simplified representation based on the square setup of particles which collide with the wall as it is depicted in Fig. 1b. The total area of the square unit is $(d_\mathrm{p}+L)^2$ and the area covered by particles is $(d_\mathrm{p}^2\pi)/4$. The fraction of free area (θ_free) can be calculated using:

$$\theta_\mathrm{free} = \frac{\left(d_\mathrm{p}+L\right)^2 - \dfrac{d_\mathrm{p}{}^2\pi}{4}}{\left(d_\mathrm{p}+L\right)^2} \tag{12}$$

The contribution of liquid convective mechanism to the heat transfer coefficient in a fluidized bed is defined by:

$$\alpha_\mathrm{lc} = \theta_\mathrm{free}\alpha_\mathrm{fb} \tag{13}$$

EXPERIMENTAL

The heat transfer coefficients have been measured in the experimental apparatus schematically shown in Fig. 2. The fluidization column was the copper pipe equipped with the heating jacket. The diameter of the inner pipe was D = 25.4 mm and the length of heating section was H = 0.7 m. The fluidizing liquid was water, which was at the room temperature at inlet, and the heating medium was saturated water vapour, flowing in a counter current mode. The experiments have been performed at atmospheric pressure. Fluidizing particles of different sizes were made of glass and their characteristics are given in Table I. According to the diagram of the hydrodynamic behaviour of fluidized systems, given by Jamialahmadi *et al.*,[16] glass particles smaller than 2.2 mm fluidized by water exhibit particulate behaviour, which is the case for all particles used in this study.

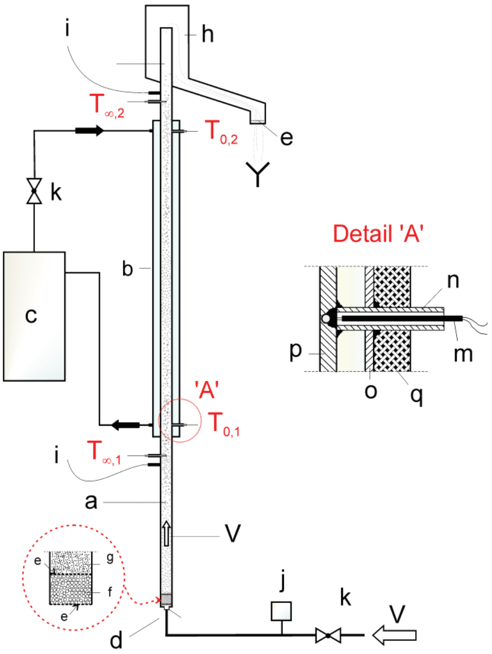

Fig. 2. Experimental apparatus (a – column, b – heating section, c – steam generator, d – inlet nozzle, e – screen, f – distributor, g – fluidized bed, h – overflow, i – pressure taps, j – flowmeter, k – valve, m – Ni–Cr thermocouple, n – cooper tube 8/6 mm, o – jacket wall, p – column wall, q – thermoisolation).

TABLE I. Characteristics of the particles and range of superficial liquid velocity

d_p / mm	ρ_p / kg m^{-3}	$U_{t\infty}$ / m s^{-1}	U / m s^{-1}	Re$_p$
0.8	2923	0.148	0.04–0.139	60–160
1.20	2641	0.188	0.05–0.206	100–280
1.52	2710	0.260	0.06–0.209	200–400
1.94	2507	0.288	0.06–0.28	265–620

After establishing the desired water flowrate, the following quantities have been measured in a steady-state: wall temperature at inlet and outlet ($T_{0,1}$ and $T_{0,2}$), water temperature at inlet and outlet ($T_{\infty,1}$ and $T_{\infty,2}$) and pressure drop over the heating section (ΔP). The range of the tested superficial liquid velocities for each particle diameter is given in Table I, together with the corresponding particle Reynolds number. The bed voidage corresponding to each superficial velocity is calculated based on the pressure drop using the basic equation of fluidization:

$$\varepsilon = 1 - \frac{\Delta P}{\left(\rho_{\mathrm{p}} - \rho\right) g H} \tag{14}$$

The wall-to-bed heat transfer coefficient has been calculated based on the heat balance for heating section:

$$\alpha = \frac{G_{\mathrm{f}} c_{\mathrm{pf}} \left(T_{\infty,2} - T_{\infty,1}\right)}{D \pi H \Delta T_{\mathrm{ln}}} \tag{15}$$

In Eq. (15) G_{f} is the mass flow rate of water, c_{pf} is the specific heat capacity of water and the logarithmic mean temperature difference is defined by:

$$\Delta T_{\mathrm{ln}} = \frac{\left(T_{0,2} - T_{\infty,2}\right) - \left(T_{0,1} - T_{\infty,1}\right)}{\ln((T_{0,2} - T_{\infty,2} / (T_{0,1} - T_{\infty,1}))} \tag{16}$$

RESULTS AND DISCUSSION

As it can be concluded from empirical correlations as well as the proposed model (Eq. (13)), the bed voidage has a key influence on the heat transfer in fluidized bed. Therefore, it is important to have the appropriate correlation for prediction of the dependence of the bed voidage on superficial velocity. Firstly, we attempted to correlate the experimental data for bed voidage with classical Richardson-Zaki correlation[23] (Eq. (17)), based on free particle terminal velocity ($U_{\mathrm{t}\infty}$, Table I):

$$\varepsilon = \left(\frac{U}{U_{\mathrm{t}\infty}}\right)^{1/n} \tag{17}$$

It turned out that Eq. (17) fits the experimental data only for particles $d_{\mathrm{p}} =$ $= 0.8$ mm (Fig. 3). For all larger particles Eq. (17) underestimates experimental data, which means that the effect of the column wall reduces the particle terminal velocity. This effect has been taken into account by correction factor K (Eq. (18)), suggested by Khan and Richardson.[24] The modified Richardson–Zaki equation (Eq. (19)) fits adequately the experimental bed voidage for particles of 1.1, 1.52 and 1.97 mm (only the data for $d_{\mathrm{p}} = 1.97$ mm has been shown on Fig. 3):

$$K = 1 - 1.15 \left(\frac{d_{\mathrm{p}}}{D}\right)^{0.6} \tag{18}$$

$$\varepsilon = \left(\frac{U}{K U_{\mathrm{t}\infty}}\right)^{1/n} \tag{19}$$

Fig. 4 shows the experimental heat transfer coefficient *vs*. bed voidage for all four particle sizes. Similar to the findings of other authors, the heat transfer coefficient rises with the increase of particle size in the given rage of particle diameters. The difference is more pronounced for lower bed voidage, while for the loose beds ($\varepsilon > 0.9$) the size of particles has no influence on heat transfer coefficient.

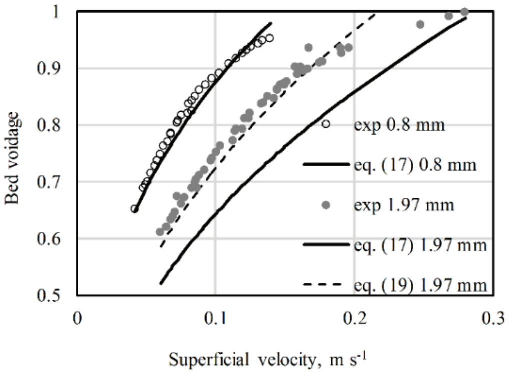

Fig. 3. Bed voidage *vs*. superficial velocity.

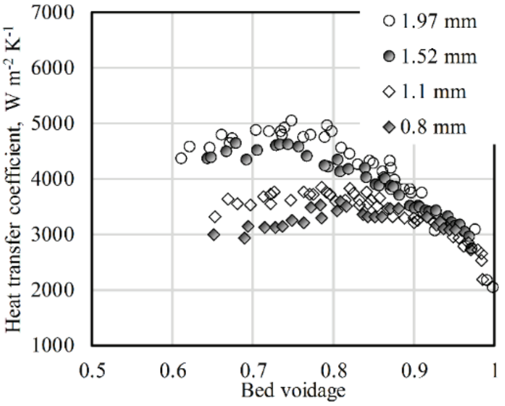

Fig. 4. Experimental heat transfer coefficient *vs*. bed voidage.

It can be also observed from Fig. 4, that the heat transfer coefficient exhibits a slight maximum for the bed voidage of about 0.74 for coarser particles, while it is somewhat shifted towards higher bed voidage (about 0.8) for smaller particles. This maximum has been usually interpreted in literature[9] as a consequence of the opposed effects of increase in the liquid velocity and particle velocity on one side and decrease in particle concentration on the other side.

The comparison of the experimental data for heat transfer coefficient with predictions of literature correlations defined by Eqs. (1), (2) and (3a) has been shown in Fig. 5a for $d_p = 0.8$ mm and in Fig. 5b for $d_p = 1.52$ mm. It can be seen that the correlation of Muroyama *et al.*[11] (Eq. (1)) fits very well the experimental data for $d_p = 1.52$ mm (mean relative deviation 3.5 %, Fig. 5b), while all three correlations overpredict the experimental data for $d_p = 0.8$ mm (Fig. 5a).

Fig. 6 shows the liquid convective heat transfer contribution (α_{lc}) *vs*. bed voidage, calculated from the model Eq. (13), for different particle sizes. The liquid convective heat transfer coefficient for the single-phase flow (α_{sf}), calculated from Eq. (8), using the pipe diameter D = 25.4 mm as characteristic geometry, is given for comparison. It should be noted that bed voidage at abscissa corresponds to superficial velocity according to Eq. (17).

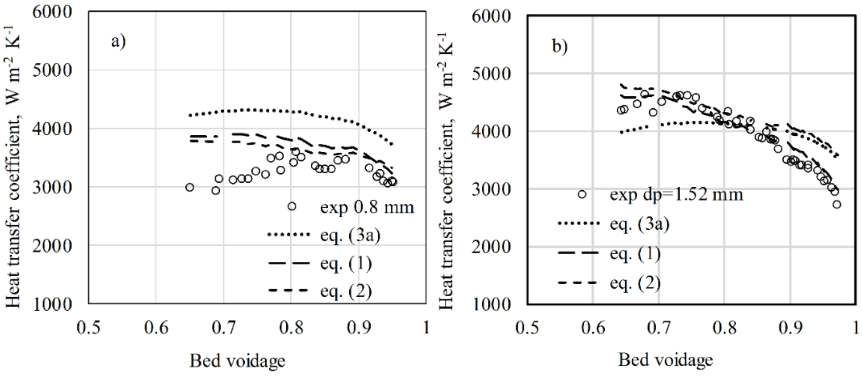

Fig. 5. Comparison of experimental data with literature correlations for d_p: a) 0.8 and b) 1.52 mm.

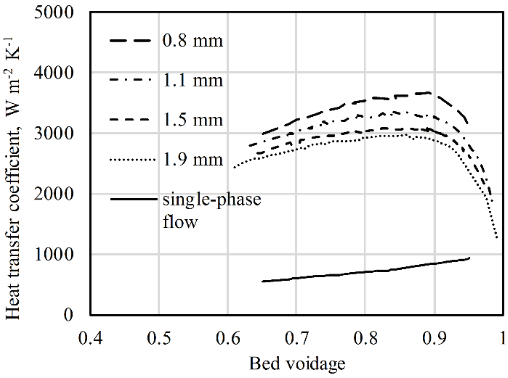

Fig. 6. Model prediction for liquid convective heat transfer contribution in fluidized and single-phase flow.

The predicted values of α_{lc} in the fluidized bed are 4–5 times higher compared to the single-phase flow. The values of α_{lc} in the fluidized bed exhibit slight increase with bed voidage up to the maximum at $\varepsilon \approx 0.87$ followed by a sharp decrease. Since α_{lc} depends on δ_T and θ_{free}, in order to explain the trend α_{lc} *vs.* ε, the dependence of δ_T and θ_{free} on superficial velocity (*i.e.*, bed voidage) will be analysed. The equation for the thickness of the thermal boundary layer (Eq. (7)) can be written in the form:

$$\delta_T \propto \left(\frac{L}{U}\right)^{1/2} \tag{20}$$

The increase in superficial velocity directly influences δ_T such that it decreases it, as in the single-phase flow. However, in the fluidized bed, the increase in velocity simultaneously increases the distance between two collisions, L (Fig. 7), which increases the thickness of the boundary layer (Eq. (19)). Those two opposed effects lead to the nearly constant value of δ_T in fluidized bed (δ_{Tfb}) up to $\varepsilon \approx 0.87$, as it is presented in Fig. 7. For $\varepsilon > 0.87$, the sharp increase in L predominates the increase in the velocity, causing the increase of δ_{Tfb}. The fraction of free area (θ_{free}) increases with bed voidage as it is presented in Fig. 8. Regarding the trend of α_{lc} *vs.* ε (Fig. 6), it can be concluded that the increase in α_{lc} for $\varepsilon < 0.87$ is due to the increase in θ_{free}, since $\delta_{Tfb} \approx$ const. The sharp decrease in α_{lc} for $\varepsilon > 0.87$ is due to the increase in δ_{Tfb}. It can be seen from Fig. 6 that the size of the particles does not have a strong influence on α_{lc}. However, the higher values of α_{lc} are obtained for smaller particle diameter. That is the consequence of lower L for the smaller d_p for the same bed voidage (Eq. (9)).

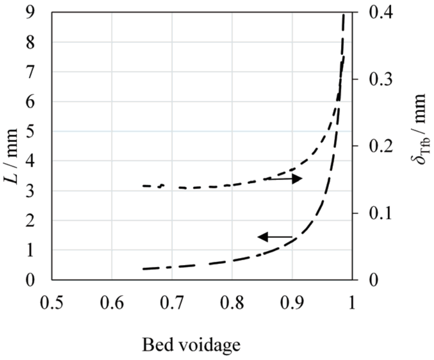

Fig. 7. Distance between two consecutive collisions and thickness of thermal boundary layer in a fluidized bed *vs.* bed voidage (d_p = 1.1 mm).

Fig. 9 shows the comparison of the modelled liquid convective component (Eq. (13)) with the experimental data for overall heat transfer coefficient for each particle diameter. As expected, the curves which represent the liquid convective component (α_{lc}) lie below the experimental data for d_p 1.1, 1.52 and 1.97 mm (Fig. 9b–d). The difference between the experimental data and model prediction for α_{lc} corresponds to the contribution of particle convective heat transfer (α_{pc}), which is larger for larger particle diameter and accounts for 17 % for d_p = 1.1 mm, 40 % for d_p = 1.52 mm and 43 % for d_p = 1.97 mm. This is logical since in the bed of larger particles higher liquid velocity is needed to achieve the same bed voidage. Higher liquid velocity cause higher particle velocity and consequently higher frequency of contacts between particles and the wall. This is in agreement with the findings of Wasmund and Smith.[8] According to their model for the system water – 1.53 mm glass particles, the particle convective contribution accounts for 50 % of the overall heat transfer coefficient, which is close to our result of 40 % for the same system.

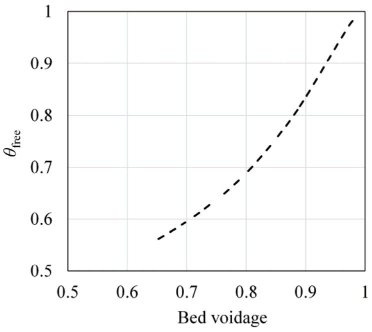

Fig. 8. Fraction of heat transfer area free for liquid flow *vs.* bed voidage (d_p= 1.1 mm).

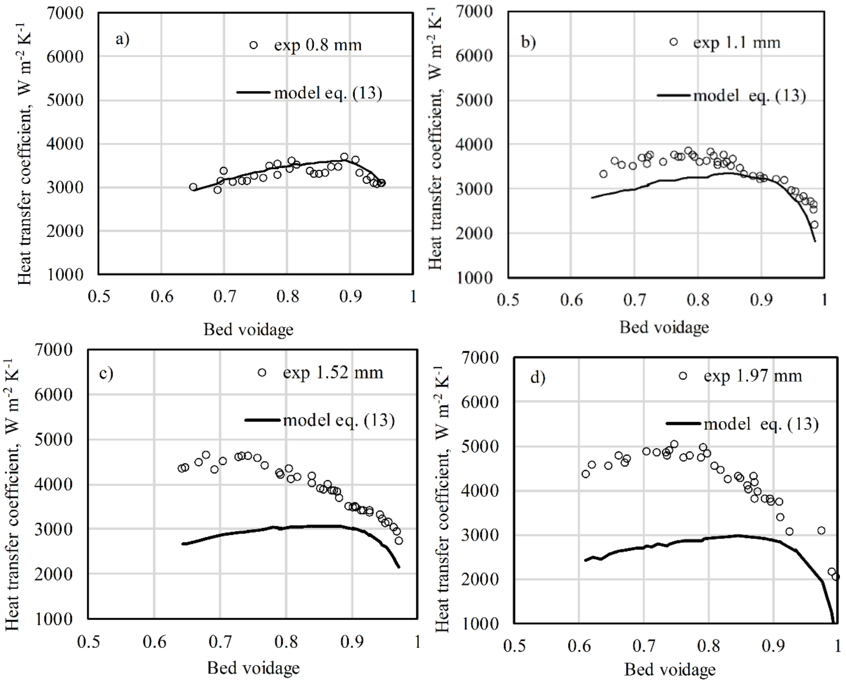

Fig. 9. Comparison of the experimental data for heat transfer coefficient with modelled liquid convective contribution for d_p: a) 0.8, b) 1.1, c) 1.52 and d) 1.97 mm.

One very interesting result has been obtained for the smallest particles d_p = = 0.8 mm where the model for liquid convective contribution adequately represents the experimental data (Fig. 9a), which indicates that the particle convective contribution is negligible for such a small particle. Although this in accordance with the decreasing trend of α_{pc} with decrease in the particle diameter, more experimental work on different fluid-particle fluidized beds is needed in order to confirm the indication.

CONCLUSIONS

Despite of numerous available empirical correlations for heat transfer coefficient in liquid-solid fluidized beds, there is only a few studies regarding the mechanisms of heat transfer. In this work the liquid convective heat transfer mechanism in fluidized bed has been studied theoretically. A new model based on the thickness of thermal boundary layer and film theory has been proposed for the prediction of liquid convective heat transfer. The distance between two adjacent particles which collide with the wall is a key model parameter which determines the thickness of boundary layer and the fraction of heat transfer area where liquid convective mechanism takes place. The model predicts the values of liquid convective component ($\alpha_{\rm lc}$) in fluidized bed which are 4–5 times higher compared to the single-phase flow. By comparison of the model prediction with the experimental data for heat transfer coefficient for different particle sizes, it was concluded that size of the particles strongly influences the mechanism of heat transfer. For very fine particles $d_{\rm p}$ = 0.8 mm, the liquid convective heat transfer model represents adequately the experimental data for the overall heat transfer coefficient, indicating that the particle convective heat transfer is negligible. With the increase in particle size, the contribution of particle convective heat transfer becomes more significant, such as that for coarse particles of $d_{\rm p}$ 1.5–2 mm, in case of which the liquid convective component accounts for 60 % of the overall heat transfer coefficient.

Acknowledgment. This work was supported by the Ministry of Education, Science and Technological Development of the Republic of Serbia (Contract Nos. 451-03-68/2022-14/ /200135 and 451-03-68/2022-14/200026).

ИЗВОД

ПРЕНОС ТОПЛОТЕ КОНВЕКТИВНИМ МЕХАНИЗМОМ У ПАРТИКУЛАТИВНО ФЛУИДИЗОВАНОМ СЛОЈУ

ДАРКО Р. ЈАЋИМОВСКИ[1], ДАНИЦА В. БРЗИЋ[2], РАДМИЛА В. ГАРИЋ-ГРУЛОВИЋ[1], РАДА В.ПЈАНОВИЋ[2], МИХАЛ М. ЂУРИШ[1], ЗОРАНА Љ. АРСЕНИЈЕВИЋ[1] и НЕВЕНКА М. БОШКОВИЋ-ВРАГОЛОВИЋ[2]

[1]*Универзитет у Београду – Институт за Хемију, Технологију и Металургију – Институт од националног значаја за Републику Србију, Београд и* [2]*Универзитет у Београду – Технолошко–металуршки факултет, Београд*

У овом раду развијен је теоријски модел преноса топлоте конвективним механизмом са зида колоне на течност у партикулативно флуидизованом слоју. Модел је заснован на дебљини граничног слоја и теорији филма. Кључни параметар модела је растојање између две суседне честице које се сударају са зидом колоне. Према предложеном моделу пренос топлоте конвекцијом на течност у флуидизованом слоју је 4 до 5 пута интензивнији него у једнофазном току. Коефицијенти преноса топлоте су експериментално одређени у флуидизованом слоју вода–стаклене сфере, за различите пречнике честица. Поређење експерименталних резултата и предвиђања модела је показало да пречник честица значајно утиче на механизам преноса топлоте. За веома ситне честице пречника 0,8 mm, модел преноса топлоте конвекцијом на течност у потпуности описује

експерименталне резултате, указујући да је пренос топлоте честицама занемарљив. За крупне честице, пречника 1,5–2 mm, конвективни пренос на течност чини 60 % од укупног коефицијента преноса топлоте.

(Примљено 16. децембра 2021, ревидирано 20. фебруара, прихваћено 21. фебруара 2022)

REFERENCES

1. W. Liang, Z. Yu, Y. Jin, Z. Wang, Y. Wang, M. He, E. Min, *J. Chem. Technol. Biotechnol.* **62** (1995) 98 (https://doi.org/10.1002/jctb.280620116)
2. Q. Lan, A. Bassi, J.-X. (Jesse) Zhu, A. Margaritis, *Biotechnol. Bioeng.* **78** (2002) 157 (https://doi.org/10.1002/bit.10171)
3. Q. Lan, A. S. Bassi, J.-X. (Jesse) Zhu, A. Margaritis, *AIChE J.* **48** (2002) 252 (https://doi.org/10.1002/aic.690480209)
4. U. Trivedi, A. Bassi, J.-X. (Jesse) Zhu, *Powder Technol.* **169** (2006) 61 (https://doi.org/10.1016/j.powtec.2006.08.001)
5. B. Habib, M. Farid, *Chem. Eng. Process. Process Intensif.* **46** (2007) 1400 (https://doi.org/10.1016/j.cep.2006.11.008)
6. R. Sowmeyan, G. Swaminathan, *Bioresour. Technol.* **99** (2008) 3877 (https://doi.org/10.1016/j.biortech.2007.08.021)
7. M. Tan, R. Karabacak, M. Acar, *Geothermics* **62** (2016) 70 (https://doi.org/10.1016/j.geothermics.2016.02.009)
8. B. Wasmund, J. W. Smith, *Can. J. Chem. Eng.* **43** (1965) 246 (https://doi.org/10.1002/cjce.5450430505)
9. A. R. Khan, A. Elkamel, *Appl. Math. Comput.* **129** (2002) 295 (https://doi.org/10.1016/S0096-3003(01)00039-X)
10. Y. Kato, K. Uchida, T. Kago, S. Morooka, *Powder Technol.* **28** (1981) 173 (https://doi.org/10.1016/0032-5910(81)87040-4)
11. K. Muroyama, M. Fukuma, A. Yasunishi, *Can. J. Chem. Eng.* **64** (1986) 399 (https://doi.org/10.1002/cjce.5450640307)
12. Y. Kang, L. T. Fan, S. D. Kim, *AIChE J.* **37** (1991) 1101 (https://doi.org/10.1002/aic.690370715)
13. M. Haid, H. Martin, H. Müller-Steinhagen, *Chem. Eng. Process. Process Intensif.* **33** (1994) 211((https://doi.org/10.1016/0255-2701(94)01003-X)
14. H. R. Jin, H. Lim, D. H. Lim, Y. Kang, K.-W. Jun, *Chin. J. Chem. Eng.* **21** (2013) 844 (https://doi.org/10.1016/S1004-9541(13)60556-X)
15. M. H. Maddahi, M. S. Hatamipour, M. Jamialahmadi, *Int. J. Therm. Sci.* **125** (2018) 11 (https://doi.org/10.1016/j.ijthermalsci.2017.11.007)
16. M. Jamialahmadi, M. R. Malayeri, H. Müller-Steinhagen, *Can. J. Chem. Eng.* **73** (1995) 444 (https://doi.org/10.1002/cjce.5450730404)
17. V. Gnielinski, in *VDI-Wärmeatlas*, Springer, Berlin, 2002, p. 593 (http://dx.doi.org/10.1007/978-3662-10743-0)
18. H. S. Mickley, D. F. Fairbanks, *AIChE J.* **1** (1955) 374 (https://doi.org/10.1002/aic.690010317)
19. O. Levenspiel, J.S. Walton, *Chem. Eng. Symp. Ser.* **50** (1954) 1
20. D.T. Wasan, M.S. Ahluwalia, Chem. Eng. Sci. **24** (1969) 1535 (https://doi.org/10.1016/0009-2509(69)80092-8)
21. C. J. Geankoplis, *Transport processes and separation process principles*, 5th ed., Prentice Hall, Boston, MA, 2018 (ISBN: 978-0-13-418102-8)

22. C. R. Carlos, J. F. Richardson, *Chem. Eng. Sci.* **23** (1968) 813 (https://doi.org/10.1016/0009-2509(68)80016-8)
23. D. Kunii, O. Levenspiel, *Fluidization engineering*, 2nd ed., Butterworth-Heinemann, Boston, MA, 1991 (ISBN: 978-0-08-050664-7)
24. A. R. Khan, J. F. Richardson, *Chem. Eng. Commun.* **78** (1989) 111 (https://doi.org/10.1080/00986448908940189).

Journal of the Serbian Chemical Society
Version electronic
JSCS-info@shd.org.rs • www.shd.org.rs/JSCS

J. Serb. Chem. Soc. 87 (7–8) 925–937 (2022)
JSCS–5568

Original scientific paper
Published 23 March 2022

A study of copper leaching from the tailings of the Karagaily (Republic of Kazakhstan) concentrating factory using an electric hydropulse discharge

ASKHAT BORSYNBAYEV[1]*, KHYLYSH OMAROV[1], YEDIGE MUSTAFIN[1], DAVID HAVLÍČEK[2], ZAURE ABSAT[1], AIGUL MURATBEKOVA[1], DAULETKHAN KAIKENOV[1], ALEXANDR PUDOV[1] and NIKITA SHUYEV[1]

[1]*Academician E. A. Buketov Karaganda University, Karaganda, Kazakstan and* [2]*Department of Inorganic Chemistry Charles University in Prague Faculty of Science, Praha, Czech Republic*

(Received 22 June 2021, revised 3 February, accepted 5 February 2022)

Abstract: The method for using concentration plants tailings is proposed for the first time in this study. These tailings contain a number of valuable metals, such as Cu, Fe, Zn, *etc*., and are a potential raw material for obtaining concentrates of some elements. An electrohydropulse discharge was used to intensify the process of copper leaching and other metals. Ammonium bifluoride, the most effective of the ammonium salts used in copper leaching by the ammonization method, was chosen as the reagent. The influences of significant leaching parameters were studied and optimized using probabilistic deterministic planning of experiment. Based on the study findings, the following process conditions were found to be optimal: mass ratio of solid to liquid (S:L) of 1:1; Cu:F = 1:6; sulphuric acid concentration 40 g L^{-1}; experiment duration 30 min; discharge voltage 10 kV and a leaching efficiency of 80-85 % could be achieved. Comparative features of tailings samples from the Karagaily (Republic of Kazakhstan) concentration plant were studied using X-ray diffraction (XRD), scanning electron microscope (SEM) and atomic emission spectral analysis. The study results showed that copper was maximally transferred to the aqueous phase.

Keywords: chalcopyrite; ammonium bifluoride; water leaching; copper tetraamine sulfate.

INTRODUCTION

The tailings of concentration plants of non-ferrous metallurgy enterprises negatively affect the environment, especially water bodies, air basin, as well as agriculture, being sources of pollution with heavy metals, silicates, sulphates, *etc.* Today, special attention is paid to the problem of the utilization of mining waste,

---

[*] Corresponding author. E-mail: askhat.9@mail.ru

https://doi.org/10.2298/JSC210622005B

since the use of such accumulations of technogenic minerals is not only sources of raw materials for the mining industry, but also an important part of the state policy of resource conservation and environmental protection. The flotation tailings consist mainly of vein minerals in the form of quartz, pyrite and silicates with low copper content and other valuable metals that have not been recovered from the ore by froth flotation.

Heap and underground leaching, as well as vat dissolution with stirring or percolation, are widely used in the extraction of copper from lean and off-balance ores or tailings. The main solvent in heap leaching is iron sulphate solutions which are obtained by irrigating heaps with water as a result of pyrite oxidation. Irrigation is carried out alter-natively with water and solution, followed by cementation of copper with iron scrap.[1–4] Ammonization methods (ammonia–ammonium extraction) using leaching solutions of ammonia and ammonium salts in the presence of free oxygen or air are known. First of all, an effective and complete uncovering of raw materials and deep separation of the target and by-products occur due to this method.[5–8]

However, all known leaching methods require large amounts of reagents, high temperatures, high pressures, and a long duration of the process itself. For the treatment of mining waste in particular the tailings of concentrating plants that are technogenic mineral raw materials in terms of resource value, new technologies are required that allow deep selective separation of metals with a high degree of their extraction from the feedstock. Ensuring environmental friendliness and wastelessness are the main conditions for the method of processing manmade material that are been developed. Therefore, for the first time, an electrohydropulse discharge was to extract copper from the current tailings of the Karagaily concentrating plant (Republic of Kazakhstan). Based on the analysis of the nature of the reagent used in the known methods for leaching copper from technogenic raw materials, ammonium hydrobifluoride was chosen as a reagent. The goal of leaching experiments using ammonium hydrobifluoride in combination with sulphuric acid was to estimate the total amount of copper available for leaching from oxide and sulphide mineral phases using an electro-pulse discharge.

EXPERIMENTAL

Materials and methods

The object of the research was the current tailings of the Karagaily Concentrating Plant (KCP). X-Ray diffraction studies of the samples were performed on a D8 Advance Eco powder diffractometer (Bruker, Germany). The shooting mode is Bragg–Brentano geometry, the angular range was from 15 to 75°, with a step of 0.03°, the spectrum acquisition time was 2 s. X-Ray radiation was generated using a copper tube with a CuK wavelength $\lambda = 1.5406$ Å. DiffracEVA decryption software, v.4.2, PDF-2 matching phase search database (2016). The weight ratio of the phases was estimated using the standard Eq. (1), which is based on the determination of the values of integral intensities and an assessment of their contributions:

$$V_{\text{admixture}} = \frac{RI_{\text{phase}}}{I_{\text{admixture}} + RI_{\text{phase}}} \tag{1}$$

I_{phase} – average integrated intensity of the main phase of the diffraction line, $I_{\text{admixture}}$ – average integral intensity of the additional phase, R – structural factor equal to 1.45.

The content of copper and other valuable metals in the original tailings, solid residues after leaching, and in the working solution were measured on atomic emission spectrometer with microwave plasma Agilent 4210 MP-AES ("Agilent Technologies Bayan Lepas Free", Malaysia). The mineralogical composition of the tailings samples was determined using a Micromed POLAR 2 polarizing microscope (Micromed, China).

The electrohydraulic effect (EH, the Yutkin effect) for the leaching of copper from the tailings of the copper concentration plant was used for the first time in this work.[9] The advantages of EH technologies are the following: the ability to directly convert electrical energy into mechanical energy (with high efficiency – up to 80 %); energy can simply be realized at a given point (both in the bladder – for crushing stones, and in water well, at a depth of tens of meters); the process is easily regulated by changing the discharge parameters (operating voltage and capacitance of the capacitor bank). The process of copper leaching from tailings was studied using probabilistic-deterministic planning of the experiment,[10] and a five-factor matrix at five levels. The leaching experiments were performed in a 1 L cell. In each experiment, 250 g of tailings were leached. At the end of the experiment, the mixture was filtered, the solid residue was washed with water and dried in an oven.

Experiments of the tailings leaching were realized using a laboratory setup, the scheme of which is shown in Fig. 1. A hydro-impulse discharge in cell (6) was created by the laboratory setup developed and assembled in house with a high-voltage generator. It allows experiments to be performed over a wide range of changes in the characteristics of an electric discharge. A general view of the laboratory cell for electrohydro-impulse treatment of the copper concentration plant tailings is shown in Fig. 1. It has a hermetically sealed lid made of high-strength insulating material. On the lid with a plug an electrode of positive polarity (platinum) is screwed in, connected by means of a high-voltage cable with a controlled spark gap of an electrohydraulic installation. The negative electrode is a graphite rod, fixed to the inner rod, the body of which is electrically connected to the negative pole of the generator by means of grounding buses. The oval container made of Teflon contains the working pulp. The distance between the electrodes that is the working discharge gap can be changed by screwing in the plug. The height of the rod is chosen so that the working gap is located in the geometric centre of the object being processed.

In order to confirm the formation of tetraammine copper(II) sulphate in the working solution, it was dried under vacuum. The spectral characteristics of the sediment were obtained on an FSM1201 infrared Fourier spectrometer (LLC "Infraspek", Russia). The sediments obtained after drying were mixed with potassium bromide (Fluka, Germany) in the ratio of 1:100, and a disk was formed using a hydraulic press. The measurement was performed in the range of 4000–400 cm^{-1}, with a resolution of 2 cm^{-1} and the number of scans was 25. The device was controlled and data processed using the Fspec 4.0 program.

The results of X-ray diffraction of the studied samples before and after leaching are shown in Fig. 2. According to the X-ray phase analysis of the obtained diffraction patterns, the most intense reflections at 2θ 20.9, 27.4, 37.2, 39.2, 50.5, 60.3, 68.2 and 68.7° correspond to the structure of silicon dioxide, which is characteristic of most silicon-containing or silicate rocks. Reflections characteristic of FeS_2 (pyrite), $CaSiO_3$ (wollastonite), Cu_2S (chalcocite) phases were also observed. A new reflection for the KCP (Karagaily Concentrating Plant) samples after leaching was not observed, which indicates the absence of phase transformation processes as a result of the actions performed on the sample.

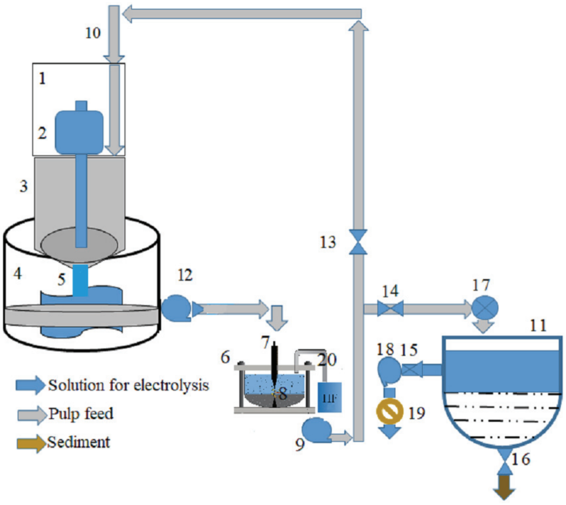

Fig. 1. The flowchart of the laboratory setup for extracting copper from the tailings of the concentrating plant (1 – casing; 2 – electric drive; 3 – pulp and reagent supply tank; 4 – mixing vessel with a lid; 5 – stirrer; 6 – cell for HID; 7 – electrodes; 8 – discharge; 9 – slurry pump; 10, 13, 14, 15, 16 – taps; 11 – tank for settling; 12 – pump for supplying slurry to the reactor; 17 – coarse filter; 18 – pump for removing copper-containing solution for further processing; 19 – fine filter; 20 – a vessel for capturing ammonia).

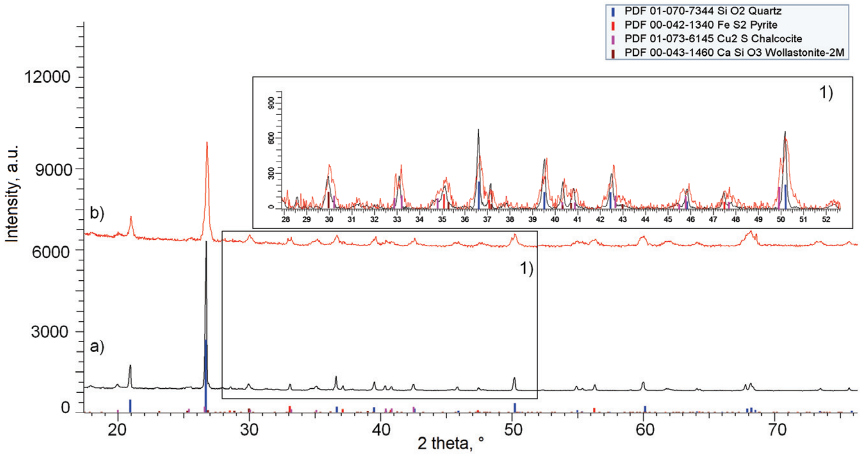

Fig. 2. X-Ray diffraction patterns of KCP tailings before (a) and after leaching (b); roasting temperature was 500 °C.

The main changes of the KCP sample after leaching are associated with the change in the intensity of the reflections, which indicates the processes of changes in the concentration of phases (see Fig. 2), as well as the appearance of impurity phases in the form of changes in their concentration (see the results presented in the diagram in Fig. 3). The phase composition, as well as the concentration of phases were determined using Eq. (1). The presented data showed a decrease in the content of phases FeS_2 from 5.9 to 4.4 % and Cu_2S from 10.9 to 4.1 % after leaching. The diagram shows the content of metals decreases in the sediment after leaching which characterizes their transition into the solution.

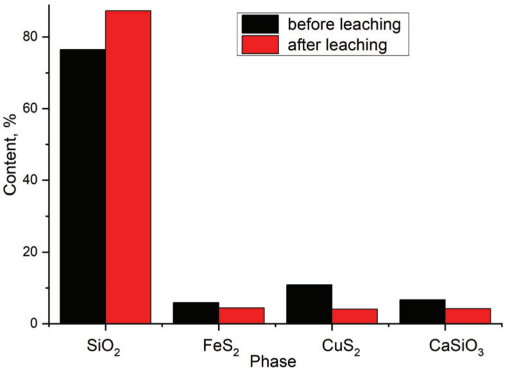

Fig. 3. Results of changes in phase composition.

The mineralogy of copper compounds in the studied samples KCP was determined on a polarizing microscope Micromed POLAR 2 (Micromed, China). The results are given in Table I, which indicate that copper is contained in the samples of the current KCP tailings before leaching mainly in the form of chalcopyrite. After leaching, mineralogical analysis of the solid phase indicates complete destruction of chalcopyrite.

TABLE I. Mineralogy of copper compounds in samples of current KCP tailings

Copper form	Content, %	
	Before leaching	After leaching
Total	0.210	<0.02
CuΣ-oxidized phase	<0.02	<0.02
Free oxidized	<0.02	<0.02
Associated oxidized	<0.02	<0.02
CuΣ malachite + azurite + atacamite ($Cu_2CO_3(OH)_2$+$2Cu[CO_3]\times Cu[OH]_2$+$Cu_2Cl(OH)_3$)	<0.02	<0.02
Chrysocolla $Cu_{2-x}Al_x(H_{2-x}Si_2O_5)(OH)_4\times nH_2O)$, $x < 1$	<0.02	<0.02
Chalcocite (Cu_2S)	<0.02	<0.02
Bornite (Cu_5FeS_4)	<0.02	<0.02
Copper iron sulfide (chalcopyrite) ($CuFeS_2$)	<0.143	<0.014

Quantitative indicators of the main valuable components in the original tailings, solid residues after leaching and in the working solution are presented in the Table II. The amount of copper in the working solution was determined using a microwave plasma atomic emission spectrometer Agilent 4210 MP-AES (Agilent Technologies Bayan Lepas Free, Malaysia). The process of leaching copper from the tailings was performed in a cell with a volume of 1 L. 250

g of raw materials (tailings, waste) was poured then water 1:1 was added to prepare the working pulp (mixture). 4 g of ammonium bifluoride, NH_4HF_2, was added and the pulp mixed thoroughly for 5 min, then it was pumped into the reactor (cell), where through the built-in electrodes periodically in 1–2 s. A high-voltage discharge of 10 kV was produced, for 15 min and then the slurry was pumped into a mixing vessel. Then the mixing was stopped and 40 ml of sulphuric acid was added to the pulp, mixing continued for another 5 min, and then the pulp was pumped into the reactor. After processing the HID for another 15 min, the slurry was fed through a coarse filter into a settling tank.

TABLE II. Chemical composition of KCP tailings from Karagaily Concentrating Plant

Source	Content, %							
	Cu	Fe	Cr	Mn	Zn	SiO_2	Al_2O_3	Ag
In tailings before leaching	0.210	4.44	0.03	0.05	0.13	62.81	11.02	–
In the solid phase after leaching	0.035	3.68	0.0024	0.0025	0.012	62.81	11.02	–
	Concentration, g/L							
In the working solution after leaching	1.02	2.79	–	–	1.67	–	–	–

Leaching of concentrator tailings

The extraction of copper from the tailings was realised under the following conditions: a mass ratio of S:L (x_1) – 1:2.5, 1:2, 1:1.5, 1:1 and 1:0.5; the mass ratio of Cu:F (x_2) – 1:8, 1:7, 1:6, 1:5 and 1:4; sulphuric acid concentration (x_3) – 20, 40, 60, 80 and 100 g L^{-1}; the duration of the experiments (x_4) – 10, 20, 30, 40 and 50 min, and discharge voltage, (x_5) – 5, 7, 10, 12 and 15 kV. The experimental conditions and the obtained results are given in Table III.

TABLE III. Plan – matrix and results of a five-factor experiment at five levels (α – copper leaching indicator)

No.	x_1	x_2	x_3	x_4	x_5	α_{Cu} / %	
						Experimental	Theoretical
1	1:2.5	1:8	20	10	5	60.5	66.95
2	1:2.5	1:6	60	30	10	84.0	80.71
3	1:2.5	1:7	40	20	7	70.2	74.32
4	1:2.5	1:4	100	50	15	74.5	83.25
5	1:2.5	1:5	80	40	12	65.5	84.40
6	1:1.5	1:8	60	20	15	79.3	75.69
7	1:1.5	1:6	40	50	12	82.9	81.95
8	1:1.5	1:7	100	40	5	78.2	75.88
9	1:1.5	1:4	80	10	10	77.0	78.05
10	1:1.5	1:5	20	30	7	70.6	75.93
11	1:2	1:8	40	40	10	70.6	74.60
12	1:2	1:6	100	10	7	71.2	75.10
13	1:2	1:7	80	30	15	69.2	79.35
14	1:2	1:4	20	20	12	75.6	74.57
15	1:2	1:5	60	50	5	77.5	82.73
16	1:0.5	1:8	100	30	12	76.2	75.11
17	1:0.5	1:6	80	20	5	74.3	78.41
18	1:0.5	1:7	20	50	10	73.0	76.03

TABLE III. Continued

No.	x_1	x_2	x_3	x_4	x_5	α_{Cu} / %	
						Experimental	Theoretical
19	1:0.5	1:4	60	40	7	79.2	81.67
20	1:0.5	1:5	40	10	15	80.3	80.39
21	1:1	1:8	80	50	7	81.2	77.09
22	1:1	1:6	20	40	15	83.0	78.53
23	1:1	1:7	60	10	12	77.5	76.55
24	1:1	1:4	40	30	5	83.5	77.59
25	1:1	1:5	100	20	10	82.3	79.59

Based on the experiments results, a sample of the obtained data was made and partial dependencies on the relevant factors were built (Figs. 4–8).

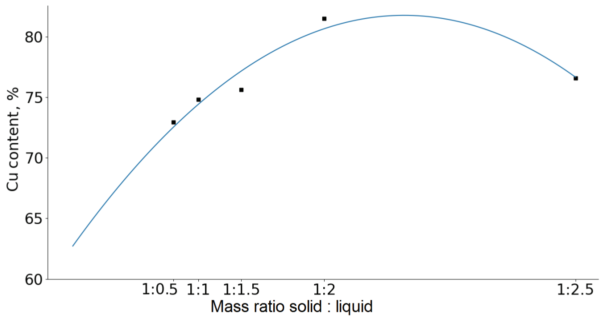

Fig. 4. Dependencies of the degree of copper leaching on mass ratio S:L.

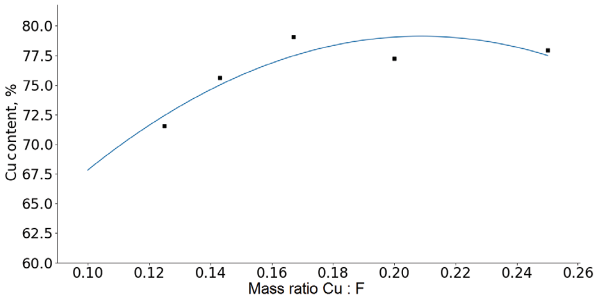

Fig. 5. Dependencies of the degree of copper leaching on mass ratio Cu:F.

The calculated correlation coefficients and their significance are presented in Table IV.

The statistical description of the partial dependencies of copper leaching is presented by the generalized Protodyakonov Equation (2):

$$Up = (-0.6057x_1^2 + 2.2343x_1 + 76.256)(-955.5x_2^2 + 398.86x_2 + 37.506)\times$$
$$\times(-0.0021x_3^2 + 0.2941x_3 + 67.996)(0.12x_4 + 72.692)(0.3222x_5 + 73.135)/75.9^{-4} \quad (2)$$

where the correlation coefficient $R = 0.67$, significance $t_R = 2.04$, the error of the equation $\sigma = 8.62$ %.

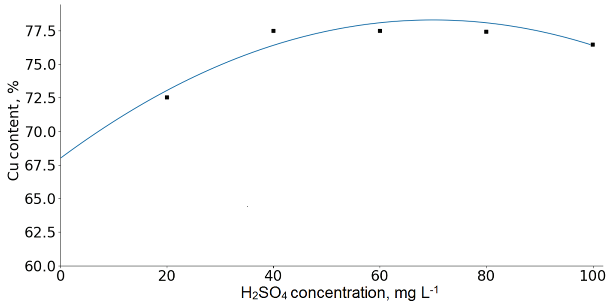

Fig. 6. Dependencies of the degree of copper leaching on sulphuric acid concentration.

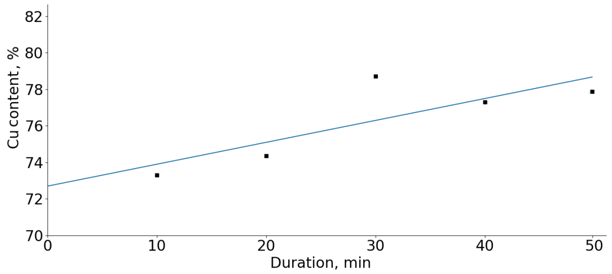

Fig. 7. Dependencies of the degree of copper leaching on process duration.

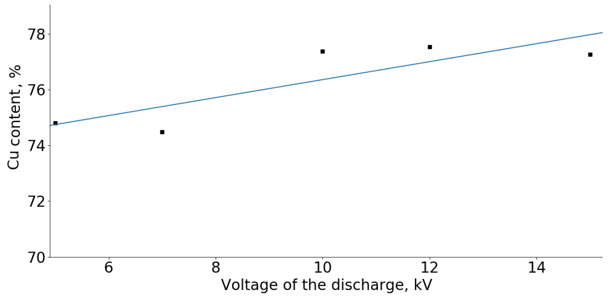

Fig. 8. Dependencies of the degree of copper leaching on the discharge voltage.

TABLE IV. Correlation coefficients (R) and their significance (t_R) for the partial dependencies of the degree of copper leaching

Function	R	t_R
$\alpha (x_1) = –0.6057x_1^2 + 2.2343x_1 + 76.256$	0.78	>0.66
$\alpha (x_2) = –955.5x_2^2 + 398.86x_2 + 37.506$	0.89	>0.66
$\alpha (x_3) = –0.0021x_3^2 + 0.2941x_3 + 67.996$	0.94	>0.66
$\alpha (x_4) = 0.12x_4 + 72.692$	0.81	>0.66
$\alpha (x_5) = 0.3222x_5 + 73.135$	0.84	>0.66

An analysis of the partial dependences in accordance with Figs. 4–6 shows that the functions of the degree of copper leaching on the S:L ratio, the Cu:F ratio and the sulphuric acid concentration pass through a maximum. The influences of the process duration and the discharge voltage (Figs. 7 and 8) are characterized by increases in the rates of copper extraction into solution. However, increases in their values over 40 g L^{-1} and 10 kV, respectively, does not give any significant additional effect. Based on the study findings, the following parameters of copper leaching from tailings of the Karagaily concentration plant were found to be optimal: S:L mass ratio of 1:1; Cu:F mass ratio of 1:6; sulphuric acid concentration, 40 g L^{-1}; the duration of the experiments, 30 min; discharge voltage, 10 kV. Under these conditions, the copper leaching efficiency was 80–85 %.

RESULTS AND DISCUSSION

The physicochemical basis of the fluorination process of ammonium hydrodifluoride is that transition oxygen-containing compounds and many non-transition elements interact with NH_4HF_2 to form ammonium fluoro- or oxofluorometallates. They are very convenient for processing[11] and due to their physicochemical properties, ensure the solubility of products and the possibility of separating mixtures by sublimation. A great advantage of these complex salts is the selective tendency to sublimate or thermally dissociate to non-volatile fluorides, which guarantees a wide separation of the components. Thus, taking into account the differences in the physicochemical properties of ammonium fluorometallates, it is possible to select the conditions for separating the mineral product fluorinated with ammonium hydrodifluoride into individual components or to concentrate some of the valuable components in the residue.

The uncovering of “encapsulated” metals of mineral raw materials with ammonium bifluoride has undeniable advantages: fluorination occurs at a temperature not higher than 200 °C, and some reactions do not require heating at all, fluorination by-products (water and ammonia vapours) do not contain fluorine, which ensures environmental safety of the production and allows their use in the condensed state in the processes of ammonia hydrolysis.[5–8] The release of NH_4F during the hydrolysis of fluoroammonium salts or NH_3 and HF during the thermal decomposition of these substances create favourable conditions for the regeneration of NH_4HF_2 and the creation of environmentally friendly technological industries. The transition of copper into solution is a complex and staged process, which begins with the opening of the silicates surface under the action of ammonium bifluoride:[12,13]

$$SiO_2 + 3NH_4HF_2 \rightarrow (NH_4)_2SiF_6 + NH_3 + 2H_2O \qquad (3)$$

The use of a hydro-impulse discharge (HID) in the process of tailings leaching in an aqueous solution in the presence of ammonium hydrodifluoride and sulphuric acid creates the necessary redox medium. Under conditions of direct polarity (minimum for positive and maximum for negative electrodes), the processes in the volume between the electrodes will be characterized by a predominance of oxidative reactions. Thus, conditions are created under which metallogenic associates are actively decomposed, access to them is provided by the action of fluorides on silicates, in which metal-containing minerals are "encapsulated", in the present case, chalcopyrite.

Oxygen formation

$$2H_2O \rightarrow 2H_2 + O_2 \quad (4)$$

further is the oxidation of chalcopyrite:

$$CuFeS_2 + 3O_2 \rightarrow CuO + FeO + 2SO_2 \quad (5)$$

formation of copper fluoride:[14]

$$CuO + NH_4HF_2 \rightarrow CuF_2 + NH_3 + H_2O \quad (6)$$

formation of a complex – tetraamine copper sulphate (II):[15,16]

$$CuF_2 + H_2SO_4 + 4NH_4OH \rightarrow [Cu(NH_3)_4]SO_4 + 2HF + 4H_2O \quad (7)$$

The IR spectra (Fig. 9) of the studied sediment revealed absorption bands in the region of 1400 and 1643 cm^{-1}, characteristic of NH_4^+ , and in the region of 578–1114 cm^{-1}, characteristic of SO_4^{2-}. These results are consistent with literature data.[17,18] Comparative analysis of the IR spectra of three objects – the precipitate obtained by evaporation of the working solution, copper sulphate and tetraammine copper (II) sulphate (Fig. 6) also confirms the participation of NH_4^+ and SO_4^{2-} in the formation of the composition of the working solution in the process of leaching of KCP tailings using HID. Samples of tetraamminemed sulphate were obtained in accordance with the procedure.[15] The reagent $CuSO_4 \cdot 5H_2O$ (reagent grade) was used as samples of copper(II) sulphate.

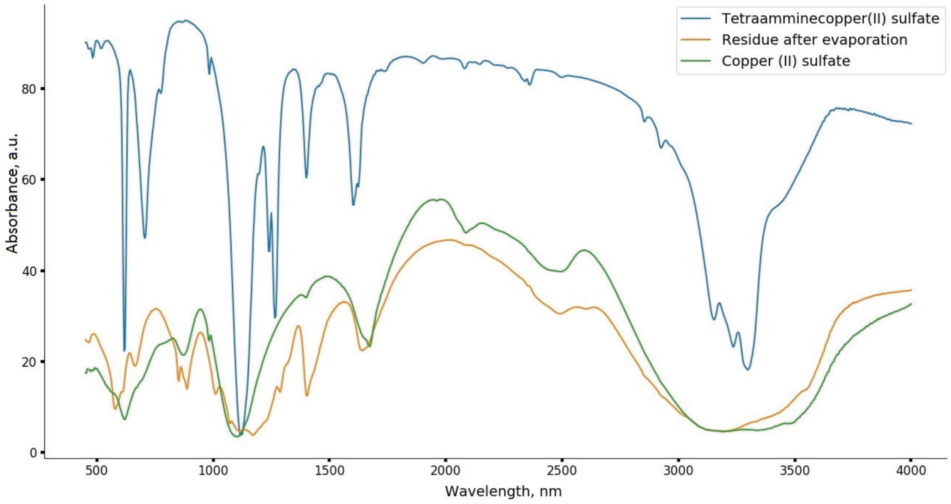

Fig. 9. IR spectra of samples of tetraamminecopper (II) sulphate (blue line), copper (II) sulphate (green line), precipitate obtained by evaporation of the working solution (orange line).

Quantitative analysis of metals in the working solution (Table I) after separation of the solid phase showed the presence of copper, iron and zinc. Al, Cr, Mn and partly Fe, forming the following fluorides that remain in the solid phase,[11,14] reactions (8)–(11):

$$Al_2O_3+3NH_4HF_2 \rightarrow 2AlF_3+ 3NH_3+3H_2O \tag{8}$$

$$Fe_2O_3+3NH_4HF_2 \rightarrow 2FeF_3+ 3NH_3+3H_2O \tag{9}$$

$$MnO_2 + 2NH_4HF_2 \rightarrow MnF_4 + 2NH_3 + 2H_2O \tag{10}$$

$$Cr_2O_3+3NH_4HF_2 \rightarrow 2CrF_3+ 3NH_3+3H_2O \tag{11}$$

Selective extraction of copper from a working solution containing iron and zinc is not difficult and could be realised by known methods.[19,20]

The sediment was studied before and after leaching using a scanning electron microscope (Tescan Mira, Czech Republic). SEM analysis of the samples is shown in Fig. 10.

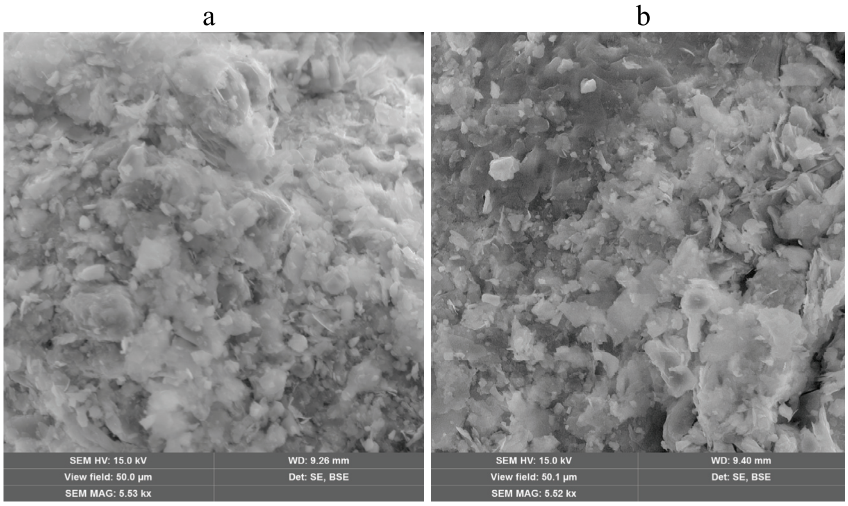

Fig. 10. SEM images of KCP tailings before (a) and after leaching (b).

There were noticeable differences between tailings samples before and after HID treatment: all clay fine particles crumbled and dissolved, all fibrous formations disappeared, there was no adhesion of particles to each other, and quartz crystals were clearly visible.

CONCLUSIONS

As a result of the experiments, it was found that of the five studied parameters the following ones determine the process of copper leaching from the tailings of the Karagaily concentrating plant (KCP) using a hydro-pulse discharge (HID): S:L ratio, Cu:F ratio and sulfuric acid concentration. The optimal leaching conditions were established under which ensures 80–85 % of copper extraction into the aqueous phase. The main advantage of using an electrohydroimpulse discharge is a significant reduction in the experiment time with a high yield of copper into the solution and low energy consumption.

X-ray, scanning electron microscope (SEM) and spectral studies of the KCP tailings before and after leaching with the use of HID indicate deep processes in the reaction zone occur. They aimed at the formation of developed microcracks and micropores in the tailings, which leads to the uncovering of copper minerals "encapsulated" in silicates, their oxidation, fluorination and the formation of copper ammonia complexes in the aqueous phase.

ИЗВОД

ПРОУЧАВАЊЕ ИСПИРАЊА БАКРА ИЗ ЈАЛОВИНЕ КОНЦЕНТРАЦИОНОГ ПОСТРОЈЕЊА KARAGAILY (РЕПУБЛИКА КАЗАХСТАН) ПОМОЋУ ЕЛЕКТРОХИДРОПУЛСНОГ ПРАЖЊЕЊА

ASKHAT BORSYNBAYEV[1], KHYLYSH OMAROV[1], YEDIGE MUSTAFIN[1], DAVID HAVLÍČEK[2], ZAURE ABSAT[1], AIGUL MURATBEKOVA[1], DAULETKHAN KAIKENOV[1] И ALEXANDR PUDOV[1] и NIKITA SHUYEV[1]

[1]*Academician E. A. Buketov Karaganda University, Karaganda, Kazakstan и* [2]*Department of Inorganic Chemistry Charles University in Prague Faculty of Science, Praha, Czech Republic*

У овом раду први пут је предложен начин коришћења постројења за концентрацију јаловине. Ова јаловина садржи низ вредних метала, као што су Cu, Fe, Zn, и др., и потенцијална је сировина за добијање концентрата неких елемената. Електрохидропулсно пражњење је искоришћено за интензивирање процеса лужења бакра и других метала. За реагенс је изабран амонијум бифлуорид, који је ефикаснији од амонијум соли, које се користе у лужењу бакра методом амонизације. Утицај значајних параметара испирања је проучаван и оптимизован коришћењем вероватноће детерминистичког планирања експеримента. На основу добијених резултата, утврђено је да су следећи процесни услови оптимални: однос масе чврсто:течно (S:L) = 1:1; Cu:F = 1:6; концентрација сумпорне киселине – 40 g/l; трајање експеримента – 30 min; напон пражњења – 10 kV и ефикасност испирања може достићи 80-85 %. Упоредне карактеристике узорака јаловине из Karagaily постројења за концентрацију (Република Казахстан) проучаване су уз помоћ рендгенске дифракције (XRD), скенирајућег електронског микроскопа (SEM) и атомске емисионе спектралне анализе. Утврђено је да су минерали бакра садржани у јаловини потпуно разбијени и бакар је максимално прешао водену фазу.

(Примљено 22. јуна 2021, ревидирано 3. фебруара, прихваћено 5. фебруара 2022)

REFERENCES

1. I. V. Ukraintsev, V. S. Trubilov, A. S. Klepikov, *Non-ferrousMetals* **10** (2016) 27 (https://doi.org/10.17580/tsm.2016.10.05) in Russian
2. L. Sinclair, J. Thompson, *Hydrometallurgy* **157** (2015) 306 (https://doi.org/10.1016/j.hydromet.2015.08.022)
3. M. Sokovć, N. Radonijević, B. Marković, J. Stojanović, Z. Kamberović, N. Petronijević, S. Stanković, *Hem. Ind.* **73** (2019) 115 (https://doi.org/10.2298/HEMIND181009010S)
4. M. M. Antonijević, M. D. Dimitrijević, Z. O. Stevanović, S. M. Šerbula, G. D. Bogdanović, *J. Hazard. Mater.* **158** (2008) 23 (https://doi.org/10.1016/j.jhazmat.2008.01.063)

5. K. Ochromowicz, M. Jeziorek, K. Wejman, *Physicochem. Probl. Miner. Process.* **50** (2014) 327 (https://doi.org/10.5277/ppmp140127)
6. A. A. Baba, M. K. Ghosh, S. R. Pradhan, D. S. Rao, A. Baral, F. A. Adekola, *Trans. Nonferrous Met. Soc. China* **24** (2014) 1587 (https://doi.org/10.1016/S1003-6326(14) 63229-5)
7. I. A. Varlamova, N. A. Churlyaeva, N. L. Kalugina, Kh. Ya. Girevaya, *Modern Problems Sci. Educ.* **1** (2015) 1161 (https://www.science-education.ru/pdf/2015/1/1268.pdf)
8. A. A. Goryachev, E. V. Chernousenko, S. S. Potapov, N. S. Tsvetov, D. V. Makarov, *Metals* **11** (2021) 422 (https://doi.org/10.3390/met11030422)
9. L. A. Yutkin, *Electrohydraulic effect and its application in industry*, Mechanical Engineering, Leningrad, 1986, p. 253 (https://www.twirpx.com/file/85915/)
10. V. P. Malyshev, *Probabilistic-deterministic planning of the experiment*, The science, Alma-Ata, 1981, p. 116 (https://search.rsl.ru/ru/record/01001059848)
11. E. G. Rakov, *Ammonium fluorides*, VINITI, Moscow, 1988, p. 154 (https://www.twirpx.com/file/561942/)
12. M. A. Medkov, G .F. Krysenko, D. G. Epov, *Far Eastern Branch RAS* **5** (2011) 60 (https://cyberleninka.ru/article/n/gidrodiftorid-ammoniya-perspektivnyy-reagent-dlya-kompleksnoy-pererabotki-mineralnogo-syrya) in Russian
13. L. P. Demyanova, A. S. Buinovskiy, V. S. Rimkevich, Yu. N. Malovitskiy, *Bull. TPU* **317** (2010) 77 (https://cyberleninka.ru/article/n/ratsionalnaya-pererabotka-kvartssoderzhaschego-syrya-ftoridnym-sposobom) in Russian
14. R. I. Kraydenko, *PhD Thesis*, Tomsk Polytechnic University, Tomsk, 2008, p. 34 (http://earchive.tpu.ru/handle/11683/6398)
15. N. G. Klyuchnikov, *Inorganic Synthesis Guide*, Khimiya, Moscow, 1965, p. 373 (http://chemteq.ru/library/inorganic/2027.html)
16. B. Morosin, *Acta Cryst*. **25** (1969) 19 (https://doi.org/10.1107/S0567740869001725)
17. K. Nakamoto, *IR Spectra of inorganic and coordination compounds*, Mir, Moscow, 1991, p. 536 (https://www.twirpx.com/file/56977/)
18. I. I. Plyusnina, *Infrared spectra of minerals*, Publishing House of Moscow University, Moscow, 1976, p. 175 (https://www.twirpx.com/file/2096078/)
19. *New methods of metal extraction*, M. J. Collie, Ed., Metallurgy, Moscow, 1987
20. V. A. Andreev, A. S. Buinovskiy, A. A. Andreev, A. N. Dyachenko, *Bull. TPU* **311** (2007) 30 (http://earchive.tpu.ru/handle/11683/1788).

Journal of the Serbian Chemical Society
JSCS-info@shd.org.rs • www.shd.org.rs/JSCS

J. Serb. Chem. Soc. 87 (7–8) 939–952 (2022)
JSCS–5569

Original scientific paper
Published 28 April 2022

Removal of heavy metals from aqueous media by sunflower husk: A comparative study of biosorption efficiency by using ICP-OES and LIBS

MARINA RADENKOVIĆ[1#], MILOŠ MOMČILOVIĆ[1#], JELENA PETROVIĆ[1#],
ANA MRAKOVIĆ[1], DUBRAVKA RELIĆ[2], ALEKSANDAR POPOVIĆ[2#]
and SANJA ŽIVKOVIĆ[1*#]

[1]*Vinča Institute of Nuclear Sciences – National Institute of the Republic of Serbia, University of Belgrade, P.O. Box 522, 11001 Belgrade, Serbia and* [1]*Faculty of Chemistry, University of Belgrade, Studentski trg 12–16, 11158 Belgrade, Serbia*

(Received 5 January, revised 4 March, accepted 7 March 2022)

Abstract: Presented research aimed to develop an alternative approach for the estimation of biosorption capability of sunflower husk. The acid-pretreated sunflower biomass was characterized by scanning electron microscopy combined with energy dispersive X-Ray spectroscopy (SEM-EDX) analysis and Fourier transform infrared (FTIR) spectroscopy. Biosorption efficiency has been evaluated using inductively coupled plasma optical emission spectroscopy (ICP-OES) and laser-induced breakdown spectroscopy (LIBS). The adsorption capacity of the adsorbent was determined as the function of the pH of the solution, the initial concentration of heavy metal solutions, and contact time. The optimal conditions were achieved after 15 min of contact at pH 6, while the percentage of the removal was from 80.0–98.7 %, depending on the element. The results obtained from the kinetic and isotherm studies show that maximum adsorption of ions was quickly reached and followed the pseudo-second-order kinetic model. Real samples were tested and obtained Ni values by LIBS method were 3100±200 and 1240±100 mg kg^{-1}, while estimated values by the ICP-OES were 2995±20 and 1130±10 mg kg^{-1}, respectively. The obtained results prove that LIBS method can be used as a “green alternative“ for the evaluation of biosorption efficiency.

Keywords: spectrochemistry; adsorption; wastewater treatment; laser; green analytical chemistry.

---

* Corresponding author. E-mail: sanjaz@vinca.rs
# Serbian Chemical Society member.
https://doi.org/10.2298/JSC220105022R

INTRODUCTION

In the past decades, rapid world progress and the constant rise of anthropogenic activities caused serious contamination of the environment by a whole range of pollutants. As a result of growing industrial and technological applications wastewater can often contain a wide range of heavy metals. Heavy metals represent metallic elements that have at minimum 5 times larger atomic weight and a density than water.[1] These elements are known as non-degradable in the environment and due to their toxicity for living organisms, their presence in the water resources making those resources unavailable for ecosystem and human activities. Furthermore, these elements are usually persistent in the soil with a very long residence time because heavy metal ions do not reduce into harmless compounds.[2]

At the same time, there is a general recognition that future global prosperity is directly dependent on the availability of clean water and soil and consequently wastewater polluted by heavy metals should be treated prior to their release to the environment. However, removing metal ions from wastewater is a great challenge for their significant solubility in water solutions. There are various conventional treatment technologies developed for the removal of heavy metals from the wastewater such as chemical precipitation, ion exchange, membrane filtration and separation, solvent extraction, reverse osmosis, electrochemical treatment, *etc.*[3] However, these techniques are commonly having some drawbacks associated with incomplete metal removal, generation of sludge with secondary pollution, and generally high cost due to high reagent and energy requirements.

As an alternative, the biosorption process was proposed approximately 70 years ago and since then it has been a target of numerous research in order to prepare more efficient, more effective, and more economic biomaterials.[4,5] Due to the fascinating features primarily the availability of different low-cost adsorbents and easy operation, this eco-friendly method can be considered a sustainable and more efficient method for the removal of heavy metals from aqueous solutions.[5,6] According to Robalds *et al*., metals biosorption is a process of catching heavy metals by physical adsorption, chemisorption (complexation, coordination, and chelation), ionic exchange, and microprecipitation.[7] Biomaterials have no significant costs and their sorption potentials are mainly due to the presence of carboxylic and phenolic functional groups in the cellulosic matrix or components associated with cellulose such as lignin and hemicellulose which are found to be responsible for metal sorption.[6]

Biosorbents are typically prepared from naturally waste biomass and therefore agricultural waste materials have been used as a rich source for low-cost biosorbents.[5,8] Serbia is traditionally an agricultural country while sunflower is the most common oil plant. It is grown on around 180,000 ha and it is one of the most important export products.[9] After industrial processing of sunflower, between 325,000 and 360,000 t of the sunflower husk waste often ends up at landfills or being used as an energy source.[10]

Toxic and not biodegradable heavy metals, included in this study are Pb, Cu, Ni, Co, Cd, and their toxicity can be determined from the absorbed amount, the route of introduction and duration of exposure.[11] They tend to accumulate in the living organisms and induce numerous health problems including the weakening of the immune system, cardiac dysfunction, fetal malformation, impaired psychological and neurological behavior, and cancer when present in the range of ppb.[12] Sunflower residues such as stalk and husk can be used for the removal of heavy elements and there are several reports regarding this topic.[2,10,13–15] Sunflower-derived adsorbents as raw material, such as in this manuscript, or as thermally treated materials (biochar and activated carbons) have shown great efficiency for the removal of various toxic elements and organic pollutants from synthetic wastewaters.[15]

Conventional and well-established spectrochemistry methods (ICP-OES, AAS and XRF) are usually dedicated to the estimation of biosorption efficiency of heavy metals by providing information about heavy metals concentration before and after sorption.[16,17] However, laser-induced breakdown spectroscopy (LIBS) that uses a pulsed laser as an excitation source attaches more and more interest and importance as a modern analytical method for fast, easy scale-up and *in situ* elemental analysis of the various types of samples.[18] Furthermore, as a cost-effective alternative to commercial LIBS systems, a transversely excited atmosphere carbon dioxide (TEA CO_2) laser-based LIBS setup was proposed by Momcilovic *et al.*[19] Some exclusive properties such as rapid, multi-element analysis of any kind of material, non-contact and almost nondestructive, independent of sample conductivity, geometry and size make this method superior to the other standard optical emission techniques.[20,21] Moreover, TEA CO_2 LIBS method does not use any hazardous reagents and solvents and maximizes safety for operators and the environment which creates it in full accordance with the principles of green analytical chemistry.[21,22]

The main aim of the present research was to study the adsorption properties of sunflower seeds husk in relation to heavy metal ions present in mono- and multi-cationic aqueous solutions in order to obtain a higher sorption capacity. The influence of various metal ion concentrations, pH levels, contact time, and the kinetics of adsorption were investigated. To the best of our knowledge, this is the first report on the application of transversely excited atmospheric (TEA) CO_2 based LIBS for fast and effective estimation of biosorption efficiency.

EXPERIMENTAL

Biosorbent preparation

Treatment of sunflower husk and stock solutions of heavy metals. Sunflower seeds were obtained from a local market, and husks were manually separated from the core. Then, in order to remove the potential impurities, obtained husk was washed thoroughly with deionized water. Furthermore, obtained material was treated with a 0.5 % solution of hydrochloric acid. The mixture was stirred periodically, and the pretreatment was carried out for 1 h. The residue material was rinsed with deionized water. The sunflower husk was dried in an oven at 100 °C. In addition, dried sunflower husk was grounded and sieved to obtain sorbent with a size of grains less than 1 mm and stored in the desiccator.

Stock solutions of heavy metals were prepared by resolving the appropriate amount of water-soluble salts of these elements in deionized water ($CuSO_4\cdot5H_2O$ Centrohem; $CdNO_3\cdot4H_2O$ Superlab; $NiCl_2\cdot6H_2O$ Merck and $Pb(NO_3)_2$ Centrohem). The final concentrations in these solutions were determined by ICP-OES method, and were used for adsorption experiments.

The percent of metal ion removal (R / %) was calculated using the following equation:

$$R = 100\frac{c_\mathrm{i} - c_\mathrm{e}}{c_\mathrm{e}} \tag{1}$$

where c_i and c_e are the initial and final concentrations of metal ions in the solution, respectively.[2,12] The adsorption capacity of adsorbent for the metal ions at equilibrium is calculated using the following formula:

$$q_\mathrm{e} = \frac{V\left(c_\mathrm{i} - c_\mathrm{e}\right)}{m} \tag{2}$$

where V is the volume of solution and m mass of the used biosorbent.[12]

Effect of pH. The effect of pH on biosorption was investigated by using batch mode in a pH range of 2.0–7.0. Other parameters that were held constant were as follows: concentrations of Cu, Ni, Pb and Cd ions (50.1, 51.7, 53.6 and 52.0 mg L^{-1}, respectively), time of contact between sorbent and solution (15 min) and mass of adsorbent (0.5 g). A 40 mL of stock solutions of Cu, Ni, Pb and Cd were measured and placed in polyethylene (PE) bottles. After that the pH was adjusted with 1% solutions of hydrochloric acid or sodium hydroxide to the desired value. Then, the sorbent material was weighed in the amount of 0.50 g, and the PE bottles with this content were agitated at 200 rpm on a platform shaker for 15 min. Finally, the supernatant was filtered and stored in the refrigerator for the ICP-OES analysis.

Effect of contact time. Effect of contact time was studied in a batch system, maintaining the constant initial conditions as the following: concentrations of Cu, Ni, Pb and Cd ions (obtained by ICP-OES analysis) were 50.1, 51.7, 53.6 and 52.0 mg L^{-1}, respectively, pH of ions solution was set at 6, and the mass of the adsorbent was 0.50 g. A 40 mL of Cu, Ni, Pb and Cd solutions were mixed with 0.50 g of sorbent material in PE bottles. The samples were shaken for 1, 3, 5, 15, 30 and 45 min, and thereafter the supernatant was filtered and stored in the fridge for the ICP-OES analysis. The residual sorbent was dried in an oven at 70 °C. The dried sorbent was placed in a plastic bag and stored in the desiccator for the LIBS analysis.

Simultaneous adsorption of Cd, Cu, Pb and Ni by treated sunflower husk. In order to test a tendency of Cd, Cu, Pb and Ni to be adsorbed from multielement solutions, seven samples containing similar concentrations of elements were prepared: Cu–Pb; Cu–Cd; Cu–Ni; Pb–Cd; Pb–Ni; Ni–Cd; Cu–Pb–Cd–Ni. A 40 mL of each sample was mixed with 0.50 g of sorbent material and the PE bottles with this content were agitated at 200 rpm on a platform shaker for 15 min. Finally, the supernatant was filtered and stored in the refrigerator for the ICP-OES analysis.

Adsorption isotherm. Adsorption isotherm experiments were carried out using seven single element solutions per element in a concentration range from 10 to 200 mg L^{-1}. A 20 mL of each solution was mixed with 0.50 g of sorbent material in PE bottles, and this content was agitated at 200 rpm on a platform shaker for 15 min. The supernatant was filtered and metal concentrations in the filtrates were determined by ICP-OES. The experiment data have been analyzed by the use of linear forms of Langmuir and Freundlich isotherms. The Langmuir isotherm model is represented by the following equation, in linear expression:

$$\frac{c_\mathrm{e}}{q_\mathrm{e}}=\frac{1}{q_\mathrm{m}K_\mathrm{L}}+\frac{c_\mathrm{e}}{q_\mathrm{m}} \tag{3}$$

where q_e is the sorption uptake; c_e is the equilibrium concentration of the sorbate; q_m is the maximum amount of the sorbate per unit of the weight of the sorbent, and K_L is the Langmuir constant and it is related to the free energy of sorption.[14]

The linear expression of the Freundlich isotherm is represented by the following equation:

$$\log q_\mathrm{e}=\log K_\mathrm{F}+\frac{1}{n}\log c_\mathrm{e} \tag{4}$$

where q_e is the metal uptake at equilibrium, K_F is the measure of the sorption capacity, $1/n$ is the sorption intensity, and c_e is the final ion concentration in the solution.[23]

Calibration set preparation for LIBS analysis. In order to prepare a calibration, set for the LIBS analysis, a previously developed method for the matrix-matched standards was applied.[24] A 2 g of biosorbent were mixed with appropriate amounts of multielement standard. Mixtures were diluted with deionized water, homogenized, and dried at 70 °C overnight. The resulting dry mixture was homogenized. To check the concentration of the analytes in the LIBS calibration set, a small amount of samples were acid digested in the microwave and analyzed by ICP-OES.

Use of sorbent in wastewater. Two real samples were used in this study: a sample of technical water was spiked with a solution of the spectroscopically pure standard of Ni and one sample of industrial wastewater with elevated concentrations of Ni. A 40 mL of sample was treated with ~0.50 g of sorbent in a polypropylene bottle. The sample was shaken for 30 minutes at pH 6. The supernatant was filtered and stored in a fridge for ICP-OES analysis. The residual sorbent was dried in an oven at 70°C after that were placed in a plastic bag and stored in the desiccator for LIBS analysis.

ICP-OES analysis

All aqueous solutions, stock solutions of heavy metals, synthetic wastewater (spiked sample of technical water), and the real sample of wastewater, used for this research, were analyzed by Thermo Scientific iCap 7400 duo ICP-OES instrument before and after contact with the biosorbent. For calibration, 1000 mg L^{-1} Multi-element ICP Standard solution (Chem-Lab, Belgium) was used. All measurements were performed in triplicate. The Thermo Scientific Qtegra Intelligent Scientific Data Solution (ISDS) software was used for data acquisition and processing.

LIBS analysis

The experimental setup used for the determination of heavy metals in the biosorbent is shown in Fig. 1. A 10.6 μm TEA $\mathrm{CO_2}$ laser with a repetition rate of 1 Hz and output energy of 160 mJ was used to induce a plasma on the biosorbent surface. Optical emission from plasma was recorded using a Carl Zeiss PGS2 spectrometer equipped with an Apogee CCD camera. The entrance slit of the spectrometer was set at 30 μm, while the time of spectra acquisition was 5 s. Biosorbent sample was applied with adhesive tape on the metal sub-target (>99.9 % pure aluminum) and it was put on a continual motor to achieve that with every single pulse a fresh area of the sample was analyzed.

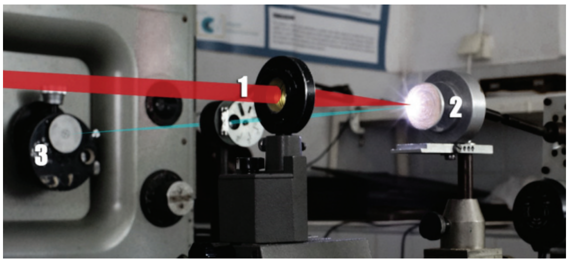

Fig. 1. LIBS experimental setup: 1) TEA CO_2 laser beam focus by ZnSe lens in front of the 2) metal sub-target covered with the biosorbent; 3) spectrometer for the acquisition of optical emission from laser-induced plasma.

Fourier transform infrared spectroscopy and scanning electron microscopy

Before and after being used, biosorbents were analyzed by Fourier transform infrared (FTIR) spectroscopy and scanning electron microscopy (SEM). FTIR spectra of the samples were recorded at ambient conditions in the mid-IR region (400–4000 cm^{-1}) with a Nicolet IS 50 FT-IR spectrometer (Thermo Fisher Scientific) operating in the ATR mode and measuring resolution of 4 cm^{-1} with 32 scans. The peaks existing in the 2300–1800 cm^{-1} spectral range represent artifacts from diamond crystal. ATR-FTIR spectra analyses served as a probe for the identification of surface functional groups before and after copper sorption. SEM was used to characterize the morphological changes of the surface of the sunflower husk before and after the biosorption process. SEM analysis of samples was performed using a JEOL JSM-6610LV scanning electron microscope (JEOL GmbH, Germany). The SEM instrument was operated at 20 kV. Before analysis, all samples were gold coated for electrical conduction.

RESULTS AND DISCUSSION

Biosorbent characterization

Fourier transform infrared spectroscopy. The ATR-FTIR spectra of biosorbent before and after copper ions sorption are presented in Fig. 2. Several absorption bands were detected which is in accordance with the complex nature of adsorption material. The spectra of non-treated biosorbent (Fig. 2a) contain bands that stem from vibrations of functional groups characteristic for lignocellulosic material. Strong and wide band originating from O–H stretching vibrations caused by the presence of alcoholic (cellulose, lignin) and phenolic hydroxyl groups (lignin) is appearing at 3337 cm^{-1} in the spectrum of non-treated biosorbent (Fig. 2a). This band is shifted towards 3342 cm^{-1} after Cu(II) solution adsorption, indicating the involvement of the OH group in the Cu^{2+} adsorption process. A very weak band observed at 3008 cm^{-1} is due to =C–H stretching vibrations of phenyl propane lignin structure or unsaturated fatty acid,[10] which disappeared after treatment of the sunflower seed hull sample with Cu(II) solution (Fig. 2b). The presence of $-CH_2-$ (acyclic) in the sample was confirmed by the existence of two bands at 2923 and 2854 cm^{-1} that are assigned to asymmetric and symmetric C–H stretching vibrations, respectively.[25] The structure of these two bands has been disrupted after treatment with a copper ions solution. A sharp band of medium intensity appearing at 1741 cm^{-1} originates from characteristic vibration of the carbonyl group (C=O)[26] and is shifted towards 1734 cm^{-1} after Cu(II) sorption. The bands appearing at 1637, 1508 and 1420 cm^{-1} are related to the aromatic skeletal vibrations of benzene ring in lignin and are assigned as follows:[27] C=O stretching conjugated to the aromatic ring, aromatic skeletal vibrations of the benzene ring in lignin and C–H deformation vibrations, respectively. The shift of a band originating from the C=O stretching conjugated to the aromatic ring to a higher wavenumber value (1653 cm^{-1}) has been observed. Strong absorption observed at 1031 cm^{-1} is attributed to C–O–C pyranose ring skeletal vibration (cellulose).[28]

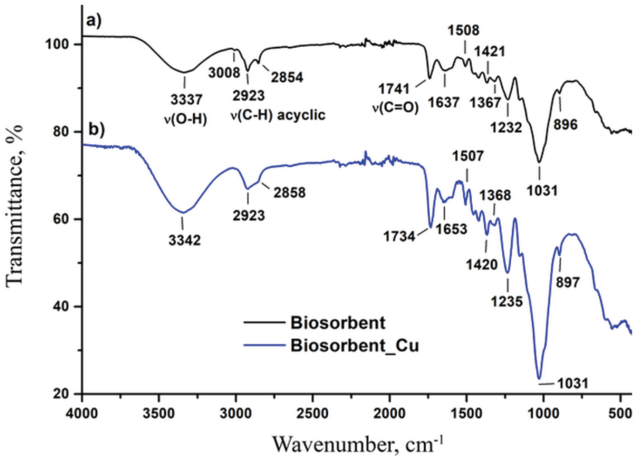

Fig. 2. Comparison of ATR FT-IR spectra of sunflower seed husk before (a) and after (b) sorption of Cu (II).

Scanning electron microscopy. The micrographs were recorded at two magnification scales using secondary electron image (SEI). Topography images are shown in Fig. 3. As can be observed from Fig. 3a, the surface of the sunflower husk is asymmetrical, heterogeneous, and has a microporous structure. There are no significant differences between these two samples regarding the morphology, but it seems that the surface of the sunflower husk becomes more heterogeneous after the sorption of copper from the aqueous solution. Additionally, EDX analysis is performed and approximately 0.68 % of Cu was detected in the biosorbent after the contact of the biosorbent with the aqueous solution of copper.

Effect of contact time and pH on biosorption. The effect of the contact time on the batch adsorption of Cu, Ni, Pb and Cd in an aqueous solution with pH 6 is shown in Fig. 4A. According to the results, it can be concluded that the uptake of these elements occurred almost instantly within the first 5 min. This fact implies that, on the surface of the sunflowers husk, there was a large number of funct ional

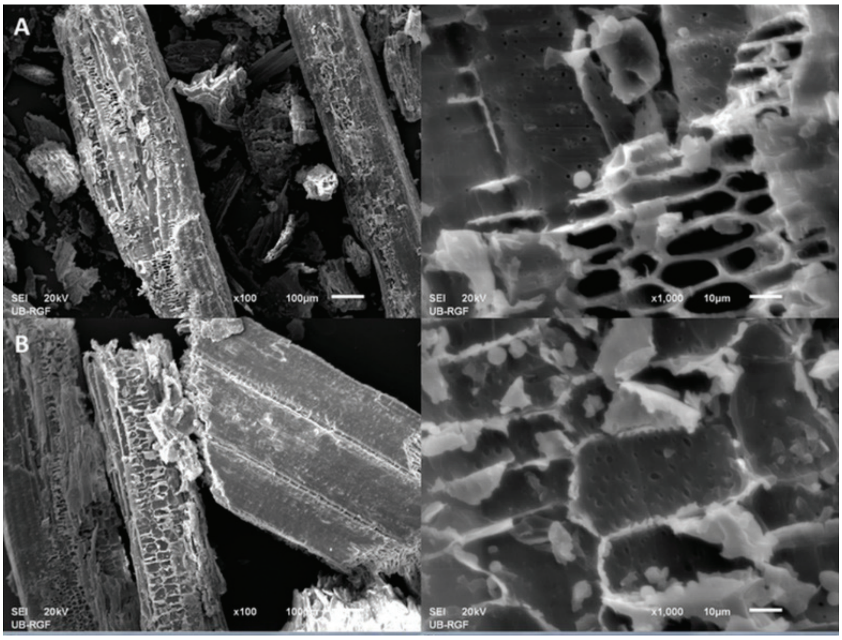

Fig. 3. Scanning electron micrographs of sunflower husk: A) before contact and B) after sorption of Cu from the aqueous solution (enlargement 100 and 1000×).

groups available to interact with the metal cations in the water solution. Two distinguished stages of adsorption can be observed. The first one is rapid and quantitatively predominant while the second one is slow and quantitative, Fig. 4A. This observation can be connected to the fact that initially the adsorption sites are available for interaction with these elements, and they can easily interact with them. After 5 min, these elements are accumulated in the large available

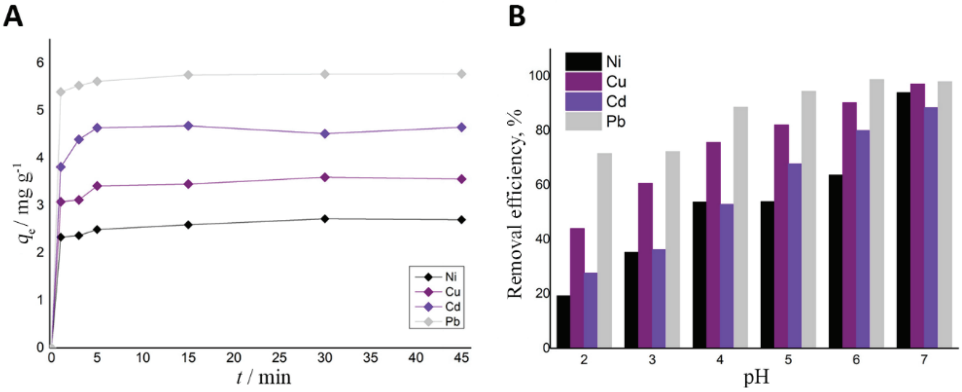

Fig. 4. Biosorbent efficiency evaluation using ICP-OES: A) effect of the time of contact and B) pH of aqueous solutions.

surface binding sites slowing down adsorption.[23] Competition of these elements has also been investigated. Several multi-element models were evaluated using their removal efficiency: Cu–Ni (94.4, 77.7 %), Pb–Ni (98.8, 83.65 %), Cu–Pb (94.5, 99.0 %), Ni–Cd (73.7, 86.4 %), Pb–Cd (92.82, 87.9 %) and Cu–Cd–Pb–Ni (76.4, 66.7, 77.4, 63.2 %). As it can be seen the highest removal efficiency is obtained for Pb in all combinations, and it can be acknowledged that the biosorbent shows an affinity for these elements in the following order Pb > Cu > Cd > Ni at pH 6.

Biosorbent efficiency evaluation using ICP-OES technique

The initial pH of the aqueous solution can affect the sorption process due to complexation reactions, electrostatic interactions, and precipitation between the heavy metal ions and biosorbent.[29] Fig. 4B illustrates a variation of the removal efficiency of Ni, Cu, Cd and Pb by sunflower husk-based biosorbent. At pH > 8 precipitations of all hydroxides started, and hence, higher pH was not investigated for the present study. At pH 2 sorption is negligible compared to the higher pH values. This can be associated with the competition of H^+ with heavy metals ions for the adsorption sites. The highest removal efficiency was achieved at pH 7 for Ni and pH 6 for Pb. In Fig. 4B it can be seen that the highest removal efficiency for Cu and Cd is at pH 7. Considering that at this pH concentration of both elements available for the sorption decrease due to the formation and precipitation in form of hydroxides, it cannot be considered as a maximum efficiency of removal with the proposed method.

Biosorbent isotherms and kinetics. The adsorption isotherms describe the relationship between amount of adsorbate per unit mass of biosorbent and the concentration of the adsorbate when the equilibrium is reached. The experimental results obtained, for this purpose, were fitted to Eqs. (3) and (4) according to Langmuir and Freundlich model. Results are summarized in Table I. The biosorption process was well described by the linear form of the Freundlich model, and the adsorption intensity $1/n$ was less than 1 for all investigated elements, showing that this is favorable sorption. Furthermore, the values of regression coefficients (R^2) higher than 0.97 for Cu, Ni and Cd suggest that Langmuir isotherm well described the sorbent process for these elements.

TABLE I. Parameters of Langmuir and Freundlich isotherms models used to describe the adsorption of heavy metals on sunflower husk

Ion	Langmuir model			Freundlich model		
	q_m / mg g^{-1}	K_L / L mg^{-1}	R^2	$1/n$	K_F / mg g^{-1} (L mg^{-1})$^{1/n}$	R^2
Cu (II)	4.1697	0.8628	0.998	0.6335	0.7191	0.981
Ni (II)	2.4297	0.3276	0.9727	0.5509	0.3368	0.9626
Cd (II)	5.3302	0.6517	0.9831	0.5214	0.7145	0.9803
Pb (II)	9.9124	1.2538	0.2878	0.7404	1.6911	0.8399

The pseudo-second-order Eq. (5) where q_t is metal uptake capacity at any time t and k_2 is the rate constant,[23] fitted the experimental data fit very well with the correlation coefficient $R^2 > 0.999$:

$$\frac{t}{q_t} = \frac{1}{k_2 {q_e}^2} + \frac{t}{q_e} \tag{5}$$

The equilibrium rate constant of the pseudo-second-order k_2 was in the range from 0.31–2.60 g mg^{-1} min^{-1} while the q_e were 2.69, 3.54, 4.85 and 5.82 for Ni ($y = 0.1616 + 0.3714x$), Cu ($y = 0.1616 + 0.3714x$), Cd ($y = 0.1616 + 0.3714x$) and Pb ($y = 0.1616 + 0.3714x$) respectively which is in accordance with the experimentally obtained values. These observations indicate that the biosorption of the tested metal cations follows a pseudo-second-order kinetic model and suggest that the cation adsorption process is controlled by a chemical reaction that has already been successfully applied to describe heavy metal biosorption on similar biosorbents.[30,31]

Biosorbent efficiency evaluation using LIBS technique

Plasma was induced by irradiation of the biosorbent by TEA CO_2 laser at atmospheric pressure. Optical plasma emissions were observed at 1 mm from the surface of the target and each spectrum (Fig. 1) was recorded three times. Each time-integrated LIBS spectrum was recorded by accumulation measurements of 5 consecutive spectra (from 5 different positions on the sample), and the obtained emission lines of the elements of interest are given in Fig. 5A. By using synthetic standards, calibration curves have been constructed and used for the evaluation of the adsorbed concentration of heavy metals by biosorbent, Fig. 6. These calibration curves showed a low sensibility. This is caused by the strong matrix effect due to the large size of biosorbent particles and the complex nature of laser-sample interaction processes.[21] It can be concluded that using finely ground materials can provide lower limits of detection. Furthermore, the effect of the contact

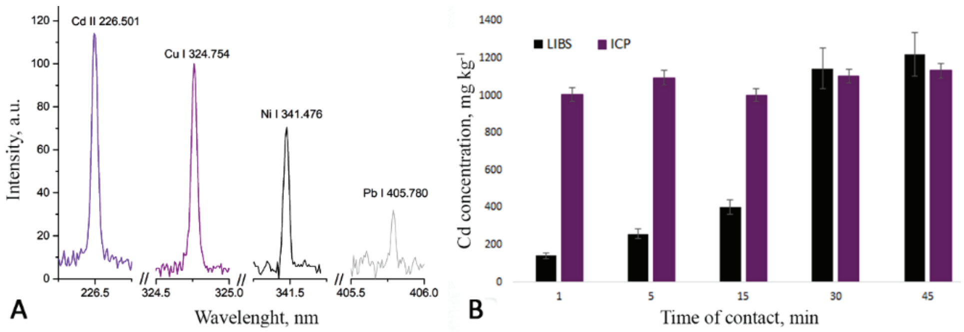

Fig. 5. LIBS analysis: A) segments of the LIBS spectra with the focus on the emission lines of analytes used in this study; B) comparison of measured concentration by LIBS and by ICP-OES technique.

time was investigated using this technique, and results were compared to the results estimated using the results of ICP-OES analysis of the supernatant. From Fig. 5B it can be observed that concentrations obtained by these two methods are in agreement when the contact time is about 30 min. Each LIBS spectrum represents an average spectrum from 5 different locations of the sample. Obtained results may indicate that sorption sites of biosorbent might be locally filled and need more time to achieve the equilibrium concentration. Even though the time for the batch testing is longer for the LIBS analysis than for the ICP-OES analysis, it cannot be considered time-consuming.

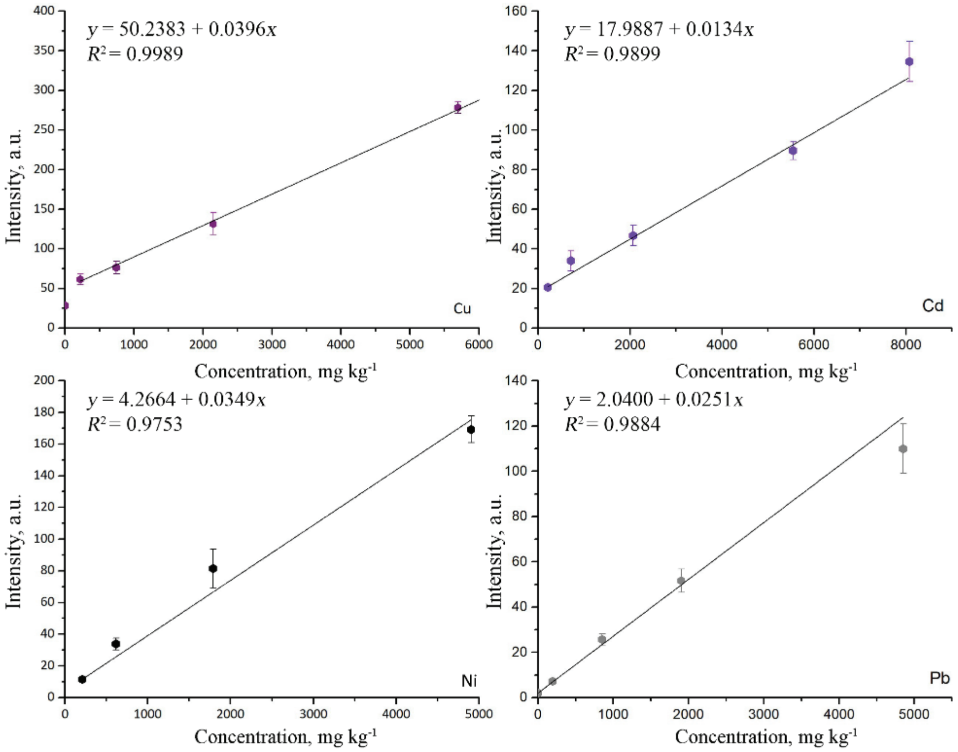

Fig. 6. LIBS calibration curves for 4 investigated elements.

Furthermore, the proposed method has been tested on the real sample of the industrial wastewater and one spiked sample of technical water. After the treatment, the biosorbent was analyzed by LIBS method while the supernatant was tested by ICP-OES technique. Using the results obtained by the ICP-OES analysis, the concentration of Ni in the sorbent after sorption was estimated. The obtained Ni values by LIBS method were 3100±200 mg kg^{-1} for the wastewater sample and 1240±100 mg kg^{-1} for the spiked technical water, while estimated values by the reference method (ICP-OES) were 2995±20 and 1130±10 mg kg^{-1}, respectively. The difference between values obtained by these two methods is within the uncertainty of the LIBS method, proving that LIBS can be used as a "green alternative" for the evaluation of biosorption efficiency. Furthermore, LIBS instrumentation can be modified to be mobile, and it can be used for on-site measurements, which is not the case with the ICP-OES method. Moreover, zero waste is generated during the LIBS analysis while the sustainable character of the proposed method is additionally reinforced by the possibility of recovery and reuse of biosorbent.

CONCLUSION

The obtained results in the presented study revealed that acid pretreated biomass of sunflower husk can be used for the removal of heavy metals from aqueous solutions. Prepared biosorbent material was characterized by FTIR and SEM-EDS which showed shifting the bands of –OH and carbonyl (C=O) groups while the surface of the biosorbent became more heterogeneous affected by the adsorptions of copper ions. The removal percentage of heavy metals by biosorbent was investigated and results showed that for the Pb, Cu, Cd at pH 6 removal efficiency were 98.7, 90.3 and 80.0 %, respectively, and for Ni at pH 7 was 94.0 %. Langmuir and Freundlich isotherm models provide a good fit with the experimental data. The pseudo-second-order kinetic model fit excellent the experimental data while the calculated q_e these elements were in accordance with the experimentally obtained values. Furthermore, the efficiency to remove toxic metal ions from the real wastewater sample by the usage of the sunflower husk as a biosorbent was evaluated by LIBS, and these results were validated by the standard ICP-OES method. Even though TEA CO_2 LIBS method cannot be used for kinetic studies, from a green analytical chemistry point of view, it is a promising tool for on-site measurements.

Acknowledgements. Authors thank the Ministry of Education, Science and Technological Development of the Republic of Serbia for the financial support to the research through institutional funding (Contract numbers 451-03-68/2022-14/200017 and 451-03-68/2022-14/200168) and Dr Vesna Vasić for proofreading the English of the manuscript.

ИЗВОД

УКЛАЊАЊЕ ТЕШКИХ МЕТАЛА ИЗ ВОДЕНИХ РАСТВОРА ПОМОЋУ ЉУСКЕ СУНЦОКРЕТА: УПОРЕДНА СТУДИЈА ЕФИКАСНОСТИ БИОСОРПЦИЈЕ КОРИШЋЕЊЕМ ICP-OES И LIBS МЕТОДЕ

МАРИНА РАДЕНКОВИЋ[1], МИЛОШ МОМЧИЛОВИЋ[1], ЈЕЛЕНА ПЕТРОВИЋ[1], АНА МРАКОВИЋ[1],
ДУБРАВКА РЕЛИЋ[2], АЛЕКСАНДАР ПОПОВИЋ[2] и САЊА ЖИВКОВИЋ[1]

[1]*Институт за нуклеарне науке „Винча" – Институт од националног значаја за Републику Србију, Универзитет у Београду, Београд и* [1]*Универзитет у Београду, Хемијски факултет, Студентски трг 16, 11158 Београд*

Представљено истраживање имало је за циљ развој алтернативног поступка за процену биосорпционе ефикасности љуске сунцокрета. Биомаса сунцокрета, модификована киселином, окарактерисана је скенирајућом електронском микроскопијом у комбинацији са енергетски дисперзивном спектроскопијом рендгенског зрачења (SEM-EDX) и инфрацрвеном спектроскопијом са Фуријеовеом трансформацијом (FT-IR). Ефикасност биосорпције је процењена коришћењем оптичке емисионе спектроскопије индуктивно спрегнуте плазме (ICP-OES) и спектроскопије ласерски индуковане плазме (LIBS). Капацитет адсорпције адсорбента одређен је као функција pH раствора, почетне концентрације раствора тешких метала и времена контакта. Оптимални услови су постигнути након 15 min контакта на pH 6, док је проценат уклањања био од 80,0-98,7 %, у зависности од елемента. Резултати добијени кинетичким и изотермним студијама показују да је максимална адсорпција јона брзо постигнута и да прати кинетички модел псеудо-другог реда. Реални узорци су тестирани и добијене концентрације никла LIBS методом су биле 3100±200 и 1240±100 mg kg^{-1}, док су процењене вредности ICP-OES методом биле 2995±20 и 1130±10 mg kg^{-1}, респективно. Добијени резултати потврђују да се LIBS метода може користити као „зелена алтернатива“ за процену ефикасности биосорпције.

(Примљено 5. јануара, ревидирано 4. марта, прихваћено 7. марта 2022)

REFERENCES

1. P. B. Tchounwou, C. G. Yedjou, A. K. Patlolla, D. J. Sutton, *EXS* **101** (2012) 133 (https://doi.org/10.1007/978-3-7643-8340-4_6)
2. M. Jalali, F. Aboulghazi, *J. Mater. Cycles Waste Manage.* **15** (2013) 548 (https://doi.org/10.1007/s10163-012-0096-3)
3. A. M. Hamdan, H. Abd-El-Mageed, N. Ghanem, *Sci. Rep.* **11** (2021) 9314 (https://doi.org/10.1038/s41598-021-88843-y)
4. I. Michalak, K. Chojnacka, A. Witek-Krowiak, *Appl. Biochem. Biotechnol.* **170** (2013) 1389 (https://doi.org/10.1007/s12010-013-0269-0)
5. A. Othmani, S. Magdouli, P. Senthil Kumar, A. Kapoor, P. V. Chellam, Ö. Gökkuş, *Environ. Res.* **204** (2022) 111916 (https://doi.org/10.1016/j.envres.2021.111916)
6. A. Ali Redha, *Arab J. Basic Appl. Sci.* **27** (2020) 183 (https://doi.org/10.1080/25765299.2020.1756177)
7. A. Robalds, G. M. Naja, M. Klavins, *J. Hazard. Mater.* **304** (2016) 553 (https://doi.org/10.1016/j.jhazmat.2015.10.042)
8. D. Sud, G. Mahajan, M. P. Kaur, *Bioresour. Technol.* **99** (2008) 6017 (https://doi.org/10.1016/j.biortech.2007.11.064)
9. Y. Kaya, *Agric. For.* **60** (2014) 95 (https://dergipark.org.tr/en/pub/ssrj/issue/32264/343313)
10. S. Stankovic, T. Sostaric, M. Bugarcic, A. Janicijevic, K. Pantovic-Spajic, Z. Lopicic, *Acta Period. Technol.* (2019) 268 (https://doi.org/10.2298/APT1950268S)
11. M. Jaishankar, T. Tseten, N. Anbalagan, B. B. Mathew, K. N. Beeregowda, *Interdiscip. Toxicol.* **7** (2014) 60 (https://doi.org/10.2478/intox-2014-0009)
12. S. L. R. K. Kanamarlapudi, V. K. Chintalpudi, S. Muddada, in *Biosorption*, InTech, Rijeka, 2018 (https://doi.org/10.5772/intechopen.77315)
13. S. A. Abdulhussein, A. I. Al wared, *Assoc. Arab Univ. J. Eng. Sci.* **26** (2019) 35 (https://doi.org/10.33261/jaaru.2019.26.1.005)
14. M. M. el-Halwany, *J. Chromatogr. Sep. Tech.* **04** (2013) 183 (https://doi.org/10.4172/2157-7064.1000183)

15. I. Anastopoulos, J. O. Ighalo, C. Adaobi Igwegbe, D. A. Giannakoudakis, K. S. Triantafyllidis, I. Pashalidis, D. Kalderis, *J. Mol. Liq.* **342** (2021) 117540 (https://doi.org/10.1016/j.molliq.2021.117540)
16. K. Chojnacka, M. Samoraj, Ł. Tuhy, I. Michalak, M. Mironiuk, M. Mikulewicz, *Molecules* **23** (2018) 2076 (https://doi.org/10.3390/molecules23082076)
17. I. Michalak, K. Chojnacka, K. Marycz, *Microchim. Acta* **172** (2011) 65 (https://doi.org/10.1007/s00604-010-0468-0)
18. R. Gaudiuso, M. Dell'Aglio, O. De Pascale, G. S. Senesi, A. De Giacomo, *Sensors* **10** (2010) 7434 (https://doi.org/10.3390/s100807434)
19. M. Momcilovic, M. Kuzmanovic, D. Rankovic, J. Ciganovic, M. Stoiljkovic, J. Savovic, M. Trtica, *Appl. Spectrosc.* **69** (2015) 419 (https://doi.org/10.1366%2F14-07584)
20. S. Zivkovic, J. Savovic, M. Trtica, J. Mutic, M. Momcilovic, *J. Alloys Compd.* **700** (2017) 175 (https://doi.org/10.1016/j.jallcom.2017.01.060)
21. S. Zivkovic, J. Savovic, M. Kuzmanovic, J. Petrovic, M. Momcilovic, *Microchem. J.* **137** (2018) 410 (https://doi.org/10.1016/j.microc.2017.11.020)
22. A. Gałuszka, Z. Migaszewski, J. Namieśnik, *TrAC Trends Anal. Chem.* **50** (2013) 78 (https://doi.org/10.1016/j.trac.2013.04.010)
23. K. D. Kowanga, E. Gatebe, G. O. Mauti, E. M. Mauti, *J. Phytopharm.* **5** (2016) 71 (https://doi.org/10.31254/phyto.2016.5206)
24. S. Zivkovic, M. Momcilovic, A. Staicu, J. Mutic, M. Trtica, J. Savovic, *Spectrochim. Acta, B* **128** (2017) 22 (https://doi.org/10.1016/j.sab.2016.12.009)
25. M. Tammer, *Colloid Polym. Sci.* **283** (2004) 235 (https://doi.org/10.1007/s00396-004-1164-6)
26. K. Sarkanen, H.-M. Chang, B. Ericsson, *Tappi* **50** (1967) 572
27. S. G. Wi, E. J. Cho, D. S. Lee, S. J. Lee, Y. J. Lee, H. J. Bae, *Biotechnol. Biofuels* **8** (2015) 228 (https://doi.org/10.1186/s13068-015-0419-4)
28. Nu, Hung, Hoang, Van der Bruggen, *Appl. Sci.* **9** (2019) 3347 (https://doi.org/10.3390/app9163347)
29. Y. Du, F. Lian, L. Zhu, *Environ. Pollut.* **159** (2011) 1763 (https://doi.org/10.1016/j.envpol.2011.04.017)
30. F. Ogata, M. Kangawa, H. Tominaga, Y. Tanaka, A. Ueda, Y. Iwata, N. Kawasaki, *J. Oleo Sci.* **62** (2013) 949 (https://doi.org/10.5650/jos.62.949)
31. A. Buasri, N. Chaiyut, K. Tapang, S. Jaroensin, S. Panphrom, *APCBEE Procedia* **3** (2012) 60 (https://doi.org/10.1016/j.apcbee.2012.06.046).

Journal of the Serbian Chemical Society
eVersion electronic
JSCS@tmf.bg.ac.rs • www.shd.org.rs/JSCS

J. Serb. Chem. Soc. *87* (7–8) 953–967 (2022)
JSCS–5570

Original scientific paper
Published 21 May 2022

The sources and seasonal variations of the chemical components in the deposition samples in Kirklareli, Turkey

ILKER ORUC[1]*, BULENT OKTAY AKKOYUNLU[2] and ILHAN ERDOGAN[3]

[1]*Vocational College of Technical Sciences, Kirklareli University, Kirklareli, Turkey,* [2]*Faculty of Arts and Sciences, Marmara University, Goztepe, Istanbul, Turkey and* [3]*Faculty of Sciences, Trakya University, Edirne, Turkey*

(Received 3 December 2021, revised 9 March, accepted 11 March 2022)

Abstract: This study was carried out in the central district of Kirklareli province in Turkey. It presents the chemical composition of three deposition types, namely wet, bulk and dry. In this study, 150 deposition samples (wet + bulk + dry) were collected for a year in the urban and suburban areas in the central district of Kirklareli. The concentrations of the main cations (Ca^{2+}, K^+, Na^+, Mg^{2+}, NH_4^+) and main anions (SO_4^{2-}, Cl^-, NO_3^-) in the collected deposition samples were determined. The seasonal variations of the concentrations of the major ions in the three deposition types were studied. The wet and dry deposition fluxes of major ions were calculated. Among the major ions, the ion with the highest annual mean flux values in the wet deposition is Ca^{2+} in the urban area, while it is Cl^- in the suburban area. In the wet deposition, the annual mean flux values of Ca^{2+} in the urban area and Cl^- in the suburban area were 65.40 and 38.09 mg m^{-2} h^{-1}, respectively. The relationship between ion concentrations and acid deposition was also investigated and the sources of ions were determined. The arithmetic mean pH values of the samples in the urban and suburban areas were 6.39 and 6.14 in wet deposition, 6.75 and 6.41 in bulk deposition, and 7.36 and 6.56 in dry deposition, respectively. The backward trajectories arriving at the region during the study period were divided into two groups. In the first cyclone group, SO_4^{2-} was to 97 % of anthropogenic origin in both the urban and suburban areas.

Keywords: ion concentration; deposition flux; trajectory analysis; enrichment factor.

INTRODUCTION

Air pollution has become a global problem due to the emissions of anthropogenic pollutants into the atmosphere.[1,2] Air pollution is often thought of as a distinguishing characteristic of industrial and urban centers. There are certain pro-

---

* Corresponding author. E-mail: ilkeroruc@klu.edu.tr
https://doi.org/10.2298/JSC211203025O

cesses that affect the life of the particles in the atmosphere. The residence time of the particles in the lower atmosphere can range from a few days to a week. The main mechanism for the effective removal of particles that are very close to the ground is settling on surfaces, although rainout and washout are superior removal mechanisms at altitudes above approximately one hundred meters.[1] Natural processes, such as the scavenging of materials by cloud and fog drops, snow and rain, are known as wet deposition (WD).[3] Dry deposition (DD), which involves the direct collection of airborne particles and gases in the solid and liquid surfaces of the earth and vegetation, is a much slower and continuous process than wet deposition.[4] Bulk deposition (BD) is the sum of wet deposition and dry deposition. Contamination of soil and water is the result of not only wet deposition but also dry deposition.[5] In fact, bulk deposition studies may be more meaningful in determining the chemistry of natural deposition, as the natural process does not distinguish between wet and dry deposition.[6] Variations between the concentrations of chemical components in wet, bulk, and dry deposition and their effects on acid deposition and changes according to atmospheric conditions have been the subjects of many studies.

The sampling of wet, bulk, and dry deposition was performed between September 2010 and September 2011 in the urban and suburban areas in the central district of Kirklareli (Turkey). Estimations of the enrichment factor (*EF*) and non-sea salt (NSS) were performed to identify the ion sources in the three deposition types. The pH values of samples in the three deposition types were compared and the factors affecting acidity were discussed. The difference between wet and dry deposition rates was calculated. For the three deposition types, the difference between the urban and suburban areas was revealed, and the effect of long-range transport on wet deposition was investigated. In the study performed by Oruç[7] in Kirklareli, it was stated that all the dry deposition samples collected from two stations (Central District and Kaynarca Town) were alkaline. In both sampling stations, it was stated that the dominant cation was Ca^{2+} and the dominant anion was SO_4^{2-}. It was stated that the mean concentration values of Ca^{2+} in Central District and Kaynarca Town were 4.37 and 4.81 mg L^{-1}, respectively, and the mean concentration values of SO_4^{2-} were 6.33 and 6.12 mg L^{-1}, respectively.[7] In the study conducted by Oruc *et al.*,[8] wet deposition sampling was carried out in the cross-border region between Bulgaria and Turkey. It was stated that the percentage distributions of the SO_4^{2-}, Cl^-, NO_3^-, Ca^{2+}, NH_4^+, K^+, Na^+ and Mg^{2+} concentrations in the wet deposition samples collected in the Turkish sites (Kirklareli and Kaynarca) were 45.68, 13.99, 3.21, 12.06, 11.00, 8.00, 4.64 and 1.07 %, respectively. In addition, it was stated that the percentage distributions of the concentrations of these ions in the wet deposition samples collected in the Bulgarian sites (Burgas and Ahtopol) were 19.46, 39.01, 14.14, 11.92, 1.39, 3.27, 2.64 and 8.17 %, respectively. As a whole, samples of the wet deposition in the study region and period have been reported to be characterized by high Cl^- and SO_4^{2-}, as well as Ca^{2+} concentration and alkaline pH values.[8] In another study conducted in Kirklareli, it was stated that the mean concentration values of Ca^{2+}, K^+, Mg^{2+}, NH_4^+, Na^+, SO_4^{2-}, Cl^- and NO_3^- were found to be higher in bulk deposition samples than that in the wet deposition samples. The relative contribution of dry deposition to bulk deposition for Ca^{2+}, K^+, Mg^{2+}, NH_4^+, Na^+, SO_4^{2-}, Cl^- and NO_3^- were reported to be 23.27, 15.75, 14.90, 13.68, 10.52, 10.20, 6.69 and 4.99 %, respectively.[9] The novelty of this study, which was conducted in Kirklareli (Turkey), is that it covers the chemical evaluation of three atmospheric sampling types collected – wet, bulk, and dry deposition. The data obtained and the sampling period provide an opportunity to understand the air pollution dynamics.

EXPERIMENTAL

Details related to sampling areas are given in Supplementary material to this paper.

Deposition sampling and analysis

During the sampling period, a total of 150 deposition samples were collected including 54 wet depositions (27 urban and 27 suburban areas), 48 bulk depositions (24 urban and 24 suburban areas), and 48 dry depositions (24 urban and 24 suburban areas). The concentrations of major ions (Ca^{2+}, K^+, Na^+, Mg^{2+}, NH_4^+, SO_4^{2-}, Cl^-, NO_3^-) and the pH values in the wet, bulk, and dry deposition samples were determined. The hybrid single-particle Lagrangian integrated trajectory (HYSPLIT) model was run to determine the backward trajectories of the air masses,[11,12] and Sat24 satellite images were examined to observe the movements of air masses.[13] For the temperature values, the data obtained from Kirklareli Atatürk soil, Water and Agricultural Meteorology Research Institute Directorate, were used. Only the wet and dry deposition sampling in the summer season was performed with an automatic wet/dry deposition device. During the sampling period, all other samplings were carried out manually. For this purpose, polyethylene funnels having 23 cm diameter and containers were used in the samples. Containers and funnels were mounted 180 cm above the ground. This height is necessary to avoid mixing dust on the ground. In wet deposition sampling, clean sampling containers were placed at sampling stations in the urban and suburban areas just before precipitation and the samples were transferred to bottles and stored for analysis at the end of precipitation. pH measurements of the samples were performed immediately at the sampling sites. In the bulk deposition sampling, after precipitation, clean funnels and containers were kept open to the atmosphere until the next precipitation event. At the end of the precipitation, the samples were transferred to bottles. Dry deposition sampling was carried out in 15-day periods. The containers and funnels were placed in an arbor with a high roof, without walls. In this way, contamination of the sampler was minimized. The sampling bowl was washed with 1 L of deionized water at the end of 15 days. The wash-water was transferred to bottles for analysis. The same storage and analysis procedure applied in wet deposition was applied to bulk and dry deposition samples. Funnels and sampling containers were rinsed with deionized water before starting the sampling, then soaked in nitric acid (5 %) and then rinsed with deionized water and dried. The samples were stored in pre-cleaned polyethylene bottles in a refrigerator at 4 °C before the chemical analysis.[6,14-18] An Orion Aplus Portable pH and ISE meter device was used for pH measurement. The pH meter was calibrated using standard pH

4.00 and 7.00 buffer solutions before each measurement. A Shimadzu UV-1601 spectrophotometer for NH_4^+, SO_4^{2-} and NO_3^- analysis and a Jenway flame photometer (Clinical PFP7) device for Na^+ and K^+ analysis were used. Ca^{2+}, Mg^{2+} and Cl^- analysis were performed by titration.[19]

Ion sources

The enrichment factor (*EF*), one of the methods used to classify natural or anthropogenic sources of the pollutants was calculated as:[8,18,20-23]

$$EF = \frac{(X/c)_{\text{precipitation}}}{(X/c)_{\text{reference material}}} \tag{1}$$

While calculating the enrichment factors of ions in the deposition samples according to the sea, Na^+ was chosen as the reference element and the concentration values of ions in seawater were used.[24] $(X/c)_{\text{precipitation}}$ is the ratio of the concentration of interested ion to the concentration of reference ion (Na_+) in the precipitation samples and $(X/c)_{\text{reference material}}$ is the ratio of the concentration of interested ion to the concentration of reference ion (Na^+) in the seawater. While enrichment factor values close to 1 indicate predominantly marine source, enrichment factor values higher than 1 indicate an enrichment compared to the seawater.[21]

Non-sea salt (NSS) ion concentrations were found using by:[8,18]

$$c_{\text{NSS}} = \text{Total } X_{\text{p}} - c_{\text{p}}(X_{\text{n}}/c_{\text{r}}) \tag{2}$$

where X and c represent the concentration of the respective ion and the reference ion respectively, p and r represent ions in precipitation and ions in the reference material, respectively. The ratio of non-sea salt concentration to total concentration is the non-sea salt fraction (NSSF).[8,18]

The wet deposition flux (F_{w} / mg m^{-2} h^{-1}) of any chemical component in a rain event is expressed by:[25]

$$F_{\text{w}} = c_{\text{i}}P_{\text{i}} \tag{3}$$

where, c_{i}, is the concentration of the said chemical component in the precipitation (mg L^{-1}), and P_{i} is the rain intensity (mm h^{-1}).

Dry deposition flux (F_{d} / mg m^{-2} h^{-1}) is acquired using as:[26]

$$F_{\text{d}} = \frac{c\Delta V}{A\Delta \tau} \tag{4}$$

where, c / mg m^{-3} is the concentration (rinsing water included), ΔV / m^3 is volume (rinsing water included), A / m^2 is the surface area, and $\Delta\tau$ / h is the sampling period.

RESULTS AND DISCUSSION

Seasonal variations of deposition samples

In the wet deposition, it was found that Ca^{2+} has the highest seasonal volume-weighted mean (*VWM*) concentration values among ions in autumn, both in the urban and suburban areas. The *VWM* concentrations of Ca^{2+} in autumn were 7.87 and 5.11 mg L^{-1} in the urban and suburban areas, respectively. Among all ions in wet deposition, it was observed that SO_4^{2-} had the highest seasonal *VWM* concentration (8.62 mg L^{-1}) in winter in the urban area. The *VWM* concentration of SO_4^{2-} in this season was 3.74 mg L^{-1} in the suburban area. The seasonal *VWM* concentration values of Na^+ in wet deposition in all four seasons were found to be higher in the urban area than in the suburban area. In the bulk deposition, the *VWM* concentration values of $Cl^–$ in autumn in the urban and suburban areas were 7.57 and 5.12 mg $L^{–1}$, respectively. The seasonal *VWM* concentration values of Ca^{2+} and Mg^{2+} in the bulk deposition were higher in the urban area than in the suburban area in all four seasons. The *VWM* concentrations of K^+ were 1.23 and 1.19 mg $L^{–1}$ in autumn in the urban and suburban areas, respectively. In the bulk deposition, anions other than $Cl^–$ were found to have higher seasonal *VWM* concentration values in the urban area than in the suburban area in all four seasons. In the dry deposition, it was observed that $Cl^–$ had the highest seasonal *VWM* concentration value among ions in summer both in the urban and suburban areas. It was observed that seasonal *VWM* concentration values of Ca^{2+} were higher than the other cations in the dry deposition both in the urban and suburban areas in four seasons (Fig. 1). It has been stated that calcium is abundant in the soil in the form of $CaCO_3$ and can be mixed into the tropo-

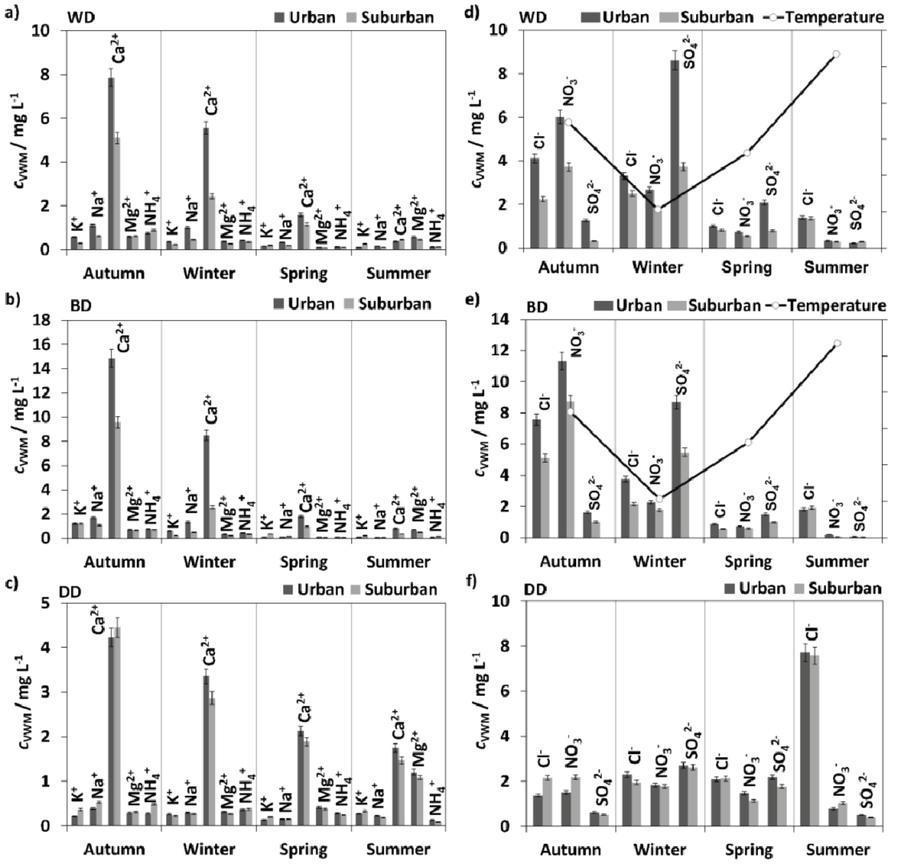

Fig. 1. Seasonal distribution of *VWM* concentrations of major cations in: a) wet, b) bulk and c) dry deposition and major anions in: d) wet, e) bulk and f) dry deposition.

sphere as a result of wind erosion.[8,18,27] Okay *et al.*[27] stated that generally continental air masses and storms can increase the deposition rates of calcium, ammonium, and potassium cations in the autumn and winter seasons.

Although no significant change was observed in the mean concentration of NO_3^- at air temperatures up to 20 °C, however, a decrease was observed in the mean concentration of this ion at 20 °C and higher air temperatures. Although the NO_3^- originated from the combustion of low-efficiency fossil fuels and biomass burning, another important source of this ion was motor land vehicles. It was clearly seen that as the air temperature increases, the mean concentration of SO_4^{2-} decreases (Fig. 2). The relationship of sulfate to temperature originates indirectly from emissions that were higher during the colder seasons. The ratio of the mean concentration of SO_4^{2-} in precipitations that took place on days with air temperature above 20 °C to the mean concentration of SO_4^{2-} in precipitations on days with air temperatures lower than 10 °C is 5.89 and 19.65 %, respectively, in the urban and suburban areas. It was understood that the main reason for the high sulphate ratio on cold days was SO_2 emission resulting from industry as well as domestic heating. No direct relations of other ions to the air temperature were observed.

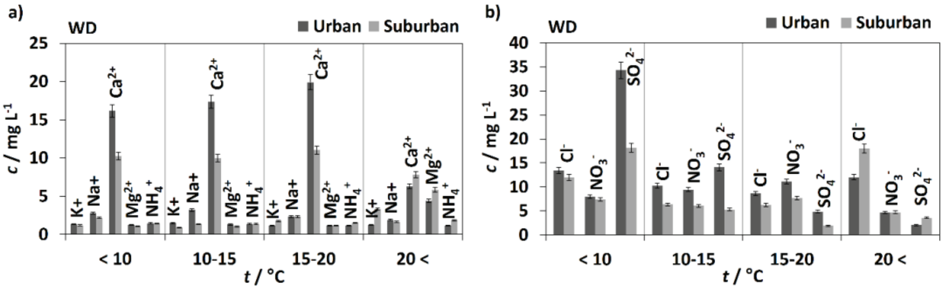

Fig. 2. Distribution of arithmetic mean concentrations of: a) major cations and b) major anions in the wet deposition by temperature ranges.

It was observed that the mean concentration of SO_4^{2-} measured in the suburban area at air temperatures above 20 °C was higher than that in the urban area. Assuming that there were no domestic origin of SO_4^{2-} in this temperature range, it could be concluded that the industrial sourced SO_2 emission is higher in the suburban area compared to the urban area. Anatolaki and Tsitouridou,[28] in their study showed that the gas and particle phase sulfur species have the highest concentration among all ions, and they found high SO_2 concentration in cold months.

Wet and dry deposition fluxes

In wet deposition, the annual mean flux values of K^+, Na^+, Ca^{2+}, Mg^{2+}, NH_4^+, Cl^-, NO_3^-, SO_4^{2-} were calculated as 8.80, 15.87, 65.40, 20.29, 9.04, 60.86, 40.87 and 31.88 mg m^{-2} h^{-1} in the urban area, and as 12.05, 8.52, 35.57, 13.05, 8.44, 38.09, 26.30 and 18.33 mg m^{-2} h^{-1} in the suburban area, respectively. In dry deposition, the annual mean flux values of these ions were calculated 0.06, 0.07, 0.77, 0.15, 0.07, 0.90, 0.38 and 0.40 mg m^{-2} h^{-1} in the urban area, and as 0.07, 0.08, 0.71, 0.14, 0.08, 0.92, 0.41 and 0.35 mg m^{-2} h^{-1} in the suburban area, respectively (Fig. 3).

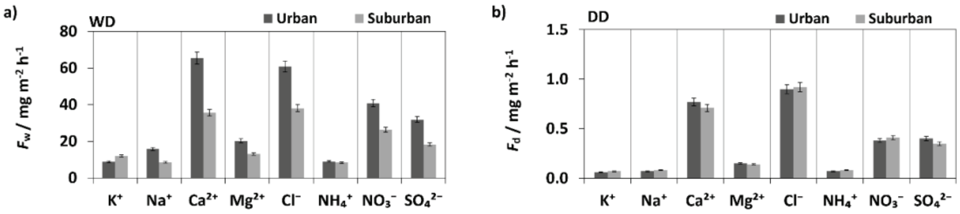

Fig. 3. Annual arithmetic means of: a) the wet and b) dry deposition fluxes of major ions.

In general, the least difference between ion fluxes in the urban and suburban areas in wet and bulk deposition was observed for ions in the dry deposition. Especially for Ca^{2+} contained in coarse particles, the difference in wet deposition was higher than for other ions. Coarse particles containing large amounts of Ca^{2+}, K^+ and Mg^{2+} have a higher dry deposition rate than fine particles.[18] In the wet deposition, it was observed that all ions except K^+ had a higher deposition rate in the urban area than in the suburban area. However, it was calculated that the difference in the rate of deposition decreases in the dry deposition in the urban and suburban areas and that K^+, Na^+, Cl^-, NH_4^+ and NO_3^- have a higher deposition rate in the suburban area.

Acid deposition

The arithmetic mean pH values of the samples in wet, bulk, and dry deposition were 6.39, 6.75, and 7.36 in the urban area, and 6.14, 6.41, and 6.56 in the suburban area, respectively. Minimum and maximum pH values of the samples were 5.35 and 7.16 in wet deposition, 5.87 and 7.41 in bulk deposition, 5.60 and 8.56 in dry deposition, in the urban area; and 5.25 and 7.25 in wet deposition, 5.6 are in the acid range and 7.52 in bulk deposition, 5.73 and 7.88 in dry deposition, in the suburban area, 6respectively. The pH values of samples in the wet deposition of the highest frequency value (37.03 %) in the urban area are between 6.50–7.00. In the suburban area, the pH values between 6.0 and 6.5 are of the highest frequency value (55.56 %), Fig. 4.

It can be said that as a result of the conversion of SO_2 originating from fossil fuels used for heating in cold months to SO_4^{2-} in the rain, relatively more acidic precipitation occurs in these months. Praveen *et al.* (2007) reported that the rainwater samples were acidic in the winter monsoon and alkaline in the summer monsoon.[29] Anatolaki and Tsitouridou[30] stated that 67 % of rain acidity was caused by sulfuric acid and 33 % by nitric acid. It was determined that the pH values of bulk deposition samples with the highest frequency value vary between 6.5 and 7.0 in the urban area and 6.0 and 6.5 in the suburban area. The pH values of dry deposition samples with the highest frequency value were higher than 7.0 in the urban area, while they had values varying between 6.0 and 6.5, and 6.5 and 7.0, in the suburban area. It could be said that the reason why the bulk and dry deposition samples are relatively alkaline compared to the wet deposition samples is due to more soil-borne particles collected in the sampler as a result of the bulk and dry deposition. These particles contain alkalinity-causing compounds such as Ca^{2+}, K^+ and Mg^{2+} compared to sulfate-containing fine particles formed as a result of gas-to-particle transformation and settle faster as compared to acidic fine particles.[18]

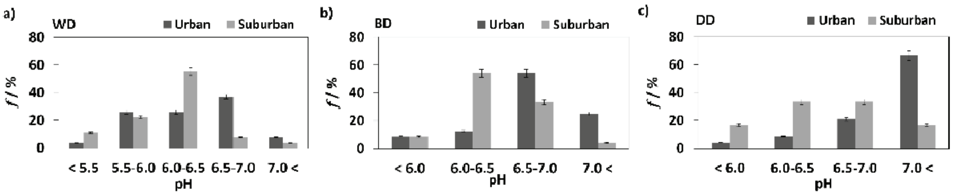

Fig. 4. Frequency distribution of pH values in the urban and suburban areas in: a) wet, b) bulk and c) dry deposition.

Determination of ion sources

In the wet and bulk deposition, the annual *NSS-VWM* concentrations of K^+, Ca^{2+}, Mg^{2+}, Cl^- and SO_4^{2-} in the urban area were found to have higher values than the annual NSS-*VWM* concentrations of these ions in the suburban area. The annual NSS-*VWM* concentration values in the urban area of ions other than K^+ and Cl^- in the dry deposition were higher than the annual NSS-*VWM* concentration values in the suburban area. In the wet and bulk deposition, it has been observed that Ca^{2+} had the highest annual NSS-*VWM* concentration values in the urban and suburban areas. In the dry deposition, Cl^- was found to have the highest annual *NSS-VWM* concentrations in both the urban and suburban areas (Fig. 5).

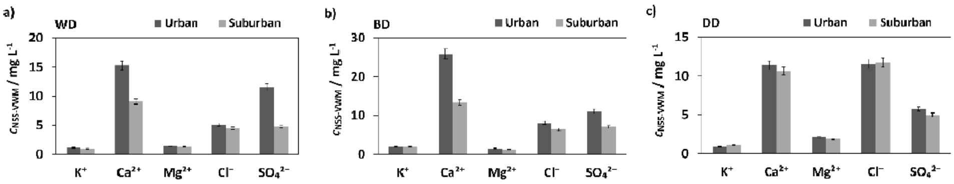

Fig. 5. Annual mean NSS-*VWM* concentrations of ions in: a) wet, b) bulk and c) dry deposition.

It was observed that Ca^{2+} has the highest values in the seasonal mean *EF* values among ions in all four seasons in both the urban and suburban areas in the three deposition types (Fig. 6). In the three deposition types, SO_4^{2-} was found to have lower *NSSF* values in the suburban area compared to the urban area. The main source of Ca^{2+} was soil by 100 and 99 %, respectively in the bulk deposition both in the urban and suburban areas. The main source of K^+, as in the wet

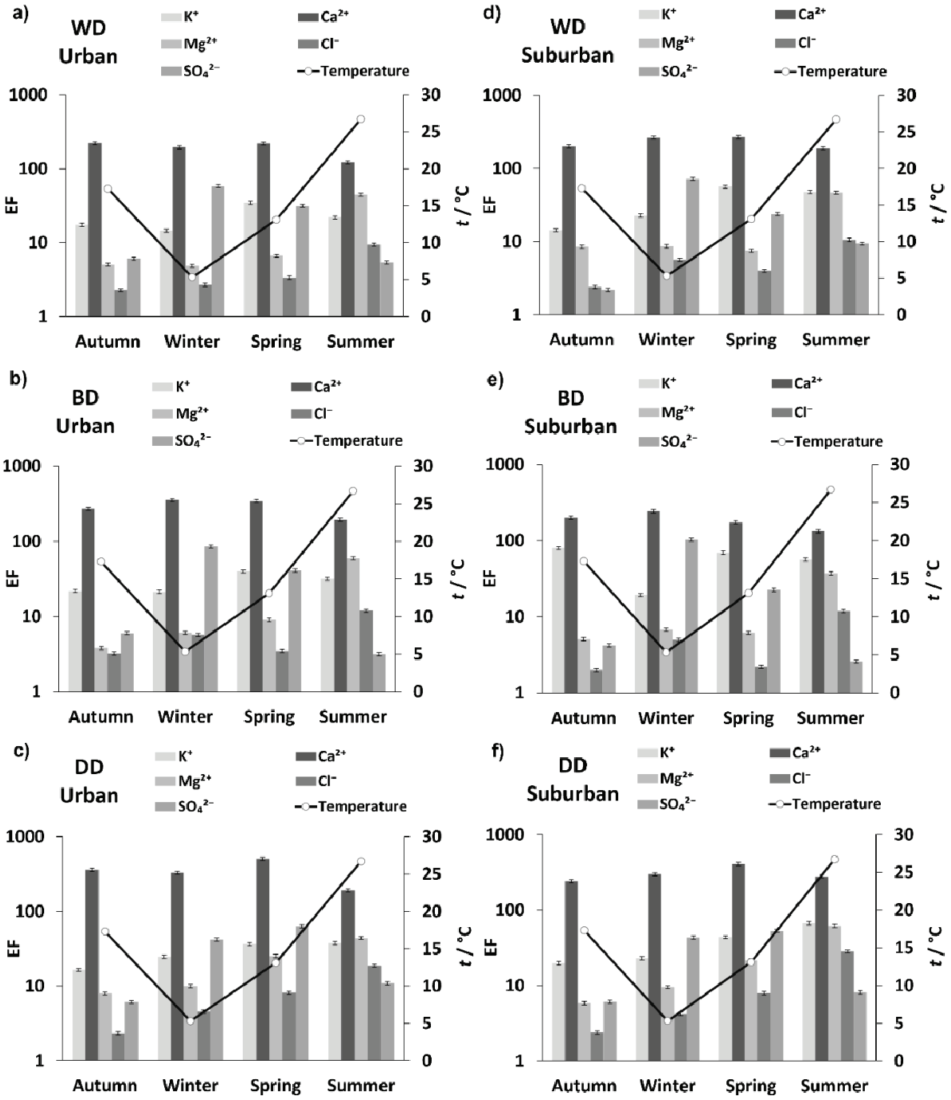

Fig. 6. Seasonal arithmetic means of enrichment factors of ions in the urban area in: a) wet, b) bulk and c) dry deposition, and the suburban area in: d) wet, e) bulk and f) dry deposition.

deposition, was soil. It was determined that the lowest anthropogenic contribution to the SO_4^{2-} concentration in bulk deposition occurred in the summer period. In the dry deposition in both areas, the K^+ was soil-borne as in the wet and bulk deposition. Mg^{2+} originated from non-sea in the proportion of 93 and 92 % in the dry deposition in the urban and suburban areas, respectively. In dry deposition in both the urban and suburban areas, 79 and 80 % of Cl^- originated from non-sea, respectively. Wang and Han[31] stated that SO_4^{2-}, NO_3^-, NH_4^+ and Ca^{2+} are mostly of anthropogenic origin and K^+, Mg^{2+} and partially Ca^{2+} are mostly of mineral origin. Teixeira *et al.*[32] explained that Cl^-, Na^+ and Mg^{2+} in wet deposition are of marine origin, and SO_4^{2-}, NO_3^-, NH_4^+ and F^- are of anthropogenic origin. According to the results of the *EF* analysis in the study by Feng *et al.*,[33] half of Mg^{2+} was of crustal origin and half was of ocean origin, most of the Cl^- and K^+ were of ocean origin, and most of the Ca^{2+} was of crustal origin. They explained that human activities contribute most of the SO_4^{2-} and NO_3^-.

To evaluate the ion sources, Pearson's correlation coefficients between the analyzed species in the three deposition types in both urban and suburban areas were also examined. In wet deposition in the urban area, the correlation coefficients were found between K^+ and Na^+, Na^+ and Cl^-, Mg^{2+} and Cl^- as 0.459, 0.416, 0.510 respectively. The correlation coefficients between Na^+ and Cl^-, Mg^{2+} and Cl^-, and K^+ and Mg^{2+} in wet deposition in the suburban area were found to be 0.513, 0.698, and 0.517, respectively. The correlation coefficients between K^+ and Na^+, Na^+ and Cl^-, K^+ and Ca^{2+}, Na^+ and Ca^{2+}, and Ca^{2+} and Cl^- in bulk deposition in the urban area were found to be 0.453, 0.447, 0,444, 0,569, and 0.575, respectively. The correlation coefficients between Na^+ and Cl^-, and Mg^{2+} and Cl^- were found to be 0.516 and 0.520, respectively, in the bulk deposition in the suburban area. The highest value of correlation coefficient in the three deposition types was determined for 0.742 between Na^+ and Cl^- in the dry deposition in the urban area. In the dry deposition, the correlation coefficients between K^+ and Na^+, Mg^{2+} and Cl^-, and Na^+ and Ca^{2+} were found to be 0.445, 0.677, and 0.460, respectively, in the urban area, and 0.420, 0.544, and 0.671, respectively, in the suburban area. In addition, the correlation coefficients between Na^+ and Cl^-, K^+ and Ca^{2+}, and K^+ and Cl^- in the dry deposition in the suburban area were found to be 0.693, 0.444, and 0.640, respectively. Low correlation coefficients were determined between other ions in the three deposition types in both the urban and suburban areas. Na^+ and Cl^- indicate the sea-salt source.[18,27] The good correlation was observed between these two ions in all three deposition types in both the urban and suburban areas. Mg^{2+} is partly of marine origin[18,27] and the highest correlation coefficient was observed between Mg^{2+} and Cl^- after the correlation coefficient between Na^+ and Cl^- in the three deposition types in both the areas. The main source of K^+ and Ca^{2+} is soil. The concentrations of these ions in sea salt are lower than Na^+, Mg^{2+} and Cl^-.[18,27]

Moderate correlation of K^+ and Ca^{2+} indicates that the common source of these ions may be soil. The correlations of these ions with Cl^- and Na^+ indicate that these ions may also be partially of marine origin.

Comparison of precipitation in the urban and suburban areas by cyclone groups

The backward trajectories were determined using the HYSPLIT model,[11,12] and Sat24 satellite images have been studied to observe the movements of air masses.[13] In the HYSPLIT model, the backward trajectories were run by going back 72 h. Sat24 satellite images were obtained in 6-hour periods by going back 24 h. The backward trajectories were classified into two groups. The first group included trajectories arriving from the upper parts of the 42nd north latitude, while the second group includes the trajectories arriving from the lower parts of the 42nd north latitude. This separation was carried out according to the results of some studies conducted to determine the dominant cyclone groups.[34] During the one-year sampling period, 48 % of the total precipitation originated from the first cyclone group and 52 % from the second cyclone group. Okay *et al.*[27] showed in their trajectory analysis that high sulphate and nitrate concentrations generally originate from northwest, central, and eastern Europe. Ion concentrations in precipitations were evaluated by comparing the outputs of the HYSPLIT model and Sat24 satellite images. In this evaluation, 27 HYSPLIT model outputs and 135 Sat24 satellite images were studied. In Fig. 7, two HYSPLIT model outputs are given to represent the separations carried out according to the cyclone groups of 09.10.2010 (originating from the first cyclone group) and 03.01.2011 (originating from the second cyclone group).

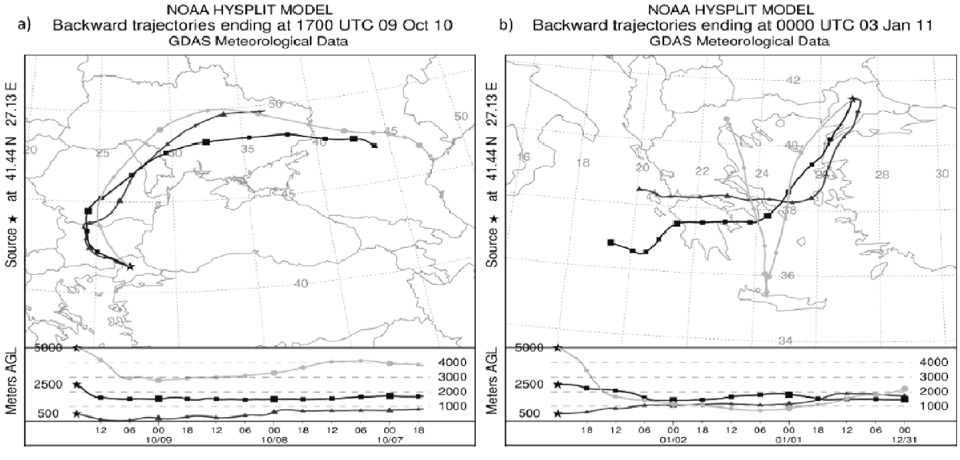

Fig. 7. HYSPLIT model backward trajectories on: a) 09.10.2010 and b) 03.01.2011.

All the precipitation in the summer was in the first cyclone group. The mean pH values of wet deposition in the first cyclone group in the urban and suburban areas were 6.25 and 6.16, respectively. In the second cyclone group, it was 6.51 and 6.12 in the urban and suburban areas, respectively. In the wet deposition, the ratio of mean concentration and NSS concentration of SO_4^{2-} in the first cyclone group to the mean concentration and NSS concentration of SO_4^{2-} in the second cyclone group was higher by approximately 46 and 49 %, respectively, in the suburban area. In the wet deposition, the ratio of mean concentration and NSS concentration of Mg^{2+} in the first cyclone group to the mean concentration and NSS concentration of Mg^{2+} in the second cyclone group was higher by approximately 53 and 63 %, respectively, in the urban area. In the wet deposition, the ratio of mean concentration of Na^+ in the second cyclone group to that in Na^+ in the first cyclone group was higher by approximately 26 % in the urban area and higher by approximately 24 % in the suburban area. In the wet deposition, the ratio of the mean concentration and NSS concentration of K^+ in the first cyclone group to the mean concentration and NSS concentration of K^+ in the second cyclone group was higher by approximately 13 and 15 %, respectively, in the urban area. In the wet deposition in the urban and suburban areas, the mean *EF* values of K^+, Ca^{2+}, Mg^{2+}, Cl^- and SO_4^{2-} in the first cyclone group were higher than the *EF* values of K^+, Ca^{2+}, Mg^{2+}, Cl^- and SO_4^{2-} in the second cyclone group. Ca^{2+} originated from non-sea at the same proportion (100 %) in the first cyclone group and the same proportion (99 %) in the second cyclone group in both the urban and suburban areas. SO_4^{2-} was of anthropogenic origin at the same ratio in both areas (97 %) in the first cyclone group, and 96 and 95 % in the urban and suburban areas in the second cyclone group, respectively.

CONCLUSIONS

In this study, it was determined that Ca^{2+} has the highest seasonal *VWM* concentration values among cations in all three deposition types. Among anions, it was found that SO_4^{2-} in the wet deposition, NO_3^- in the bulk deposition, and Cl^- in the dry deposition had the highest seasonal *VWM* concentration values. In the wet deposition, 3.7 % of the total precipitation was acidic in the urban area, while 11.1 % in the suburban area was acidic. In the wet deposition, all the acidic precipitation in the urban and suburban areas occurred during the colder months. In the wet deposition, it was determined that the highest anthropogenic contribution to the SO_4^{2-} concentration occurred in the winter in the urban and suburban areas. In this period, the *NSSF* values of SO_4^{2-} in the urban and suburban areas were 98 and 99 %, respectively. In the urban and suburban areas, all the samples in bulk and dry deposition were alkaline. The annual *VWM* concentration values in the bulk deposition of all the ions except for SO_4^{2-} in the urban area and Mg^{2+} and NH_4^+ in the suburban area were higher than the annual *VWM* concentration values in wet deposition. The annual *VWM* concentration values of K^+, Na^+, Ca^{2+}, Mg^{2+}, Cl^-, NH_4^+ and NO_3^- in the bulk deposition in the urban area were found to be higher than wet deposition at values varying between 2–42 %. The annual *VWM* concentration values of K^+, Na^+, Ca^{2+}, $Cl^–$, $NO_3^–$ and $SO_4^{2–}$ in the bulk deposition in the suburban area were found to be higher at values varying between 26–49 % in the wet deposition.

Acknowledgments. This study was produced from the PhD thesis of Ilker Oruc and financially supported by the Trakya University Scientific Research Projects (TUBAP) Directorate with the project number 2010/111. We would like to thank Kirklareli Atatürk Soil, Water and Agricultural Meteorology Research Institute Directorate for the temperature values.

ИЗВОД

ИЗВОРИ И СЕЗОНСКЕ ВАРИЈАЦИЈЕ ХЕМИЈСКИХ КОМПОНЕНТИ У УЗОРЦИМА ТАЛОЖЕЊА У ОКРУГУ KIRKLARELI, ТУРСКА

ILKER ORUC[1], BULENT OKTAY AKKOYUNLU[2] и ILHAN ERDOGAN[3]

[1]*Vocational College of Technical Sciences, Kirklareli University, Kirklareli, Turkey,* [2]*Faculty of Arts and Sciences, Marmara University, Goztepe, Istanbul, Turkey и* [3]*Faculty of Sciences, Trakya University, Edirne, Turkey*

Ова студија је спроведена у централном округу провинције Kirklareli у Турској. Односи се на хемијски састав три типа таложења: мокро, укупно и суво. У овој студији, 150 узорака таложења (мокри + укупни + суви) прикупљено у периоду од годину дана у урбаним и приградским подручјима провинције Kirklareli. У прикупљеним узорцима одређене су концентрације главних катјона (Ca^{2+}, K^+, Na^+, Mg^{2+}, NH_4^+) и главних анјона (SO_4^{2-}, Cl^-, NO^{3-}). Проучаване су сезонске варијације концентрација јона у три типа таложења. Израчунати су токови влажног и сувог таложења главних јона. Међу главним јонима, јон са највишим годишњим средњим вредностима флукса у влажном таложењу је јон Ca^{2+} у урбаном подручју, док је Cl^- у приградском подручју. Код влажног таложења, средње годишње вредности флукса Ca^{2+} у урбаном подручју и Cl^- у приградском подручју су 65,40 и 38,09 mg m^{-2} h^{-1}, редом. Такође је испитан однос између концентрација јона и киселог таложења и утврђени су извори јона. Средње аритметичке pH вредности узорака у градским и приградским насељима биле су 6,39 и 6,14 у мокром таложењу, 6,75 и 6,41 у укупном таложењу и 7,36 и 6,56 у сувом таложењу, редом. Повратне путање које су стизале у регион током периода истраживања подељене су у две групе. У првој групи циклона, SO_4^{2-} је био 97 % антропогеног порекла, како у градским тако и у приградским подручјима.

(Примљено 3. децембра 2021, ревидирано 9. марта, прихваћено 11. марта 2022)

REFERENCES

1. J. H. Seinfeld, *Air pollution: physical and chemical fundamentals*, McGraw-Hill, Inc., New York, 1975, p. 2 (ISBN-10: 0070560420)
2. M. Z. Jacobson, *Atmospheric pollution: history, science, and regulation*, Cambridge University Press, Cambridge, 2002, p. 81 (ISBN-10: 0-521-81171-6)
3. J. H. Seinfeld, S. N. Pandis, *Atmospheric chemistry and physics: from air pollution to climate change*, 2nd ed., John Wiley&Sons, Inc., Hoboken, NJ, 2006, p. 932 (ISBN-10: 0-471-72018-6)
4. J. M. Wallace, P. V. Hobbs, *Atmospheric science: an introductory survey*, 2nd ed., Academic Press, London, 2006, p. 162 (ISBN-10: 0-12-732951-X)
5. B. O. Akkoyunlu, *PhD Thesis*, Marmara University, Istanbul, 2003 (in Turkish)

6. İ. Oruç, *PhD Thesis*, Trakya University, Edirne, 2012 (in Turkish)
7. İ. Oruç, *UMAGD* **12** (2020) 631 (https://doi.org/10.29137/umagd.705861)
8. I. Oruc, E. Georgieva, E. Hristova, K. Velchev, G. Demir, B. O. Akkoyunlu, *Bull. Environ. Contam. Toxicol.* **106** (2021) 812 (https://doi.org/10.1007/s00128-021-03210-x)
9. I. Oruc, *Int. J. Environ. Sci. Technol.* **19** (2022) 1601 (https://doi.org/10.1007/s13762-021-03621-7)
10. *ÇDR, Kırklareli Province Environmental Status Report 2019*, T. C. Kırklareli Provincial Directorate of Environment and Urbanization, EIA, Permit and Inspection Branch Office, Kızılay, 2020 (https://webdosya.csb.gov.tr/db/ced/icerikler/kirklarel-_-cdr2019-20200708151830.pdf) (in Turkish)
11. A. F. Stein, R. R. Draxler, G. D. Rolph, B. J. B. Stunder, M. D. Cohen, F. Ngan, *Bull. Amer. Meteor. Soc.* **96** (2015) 2059 (http://dx.doi.org/10.1175/BAMS-D-14-00110.1)
12. G. Rolph, A. Stein, B. Stunder, *Environ. Model. Softw.* **95** (2017) 210 (https://doi.org/10.1016/j.envsoft.2017.06.025)
13. Sat24, Sat24.com-The Meteo Company B.V. (2011) (http://www.sat24.com/history.aspx)
14. I. Oruc, Y.E. Acar, B. O. Akkoyunlu, I. Erdogan, M. Tayanc, M. Dogruel, in *Proceedings of International Conference on Biology, Environment and Chemistry, IPCBEE*, Vol. 24, 2011, IACSIT Press, Singapore, p. 118 (ISBN: 978-981-07-1052-1)
15. I. Oruc, B. O. Akkoyunlu, I. Erdogan in *Proceedings of Unitech 12th International Scientific Conference*, (2012), Gabrovo, Bulgaria, Volume II, 2012, p. 391 (ISSN: 1313-230X)
16. I. Oruc, B. O. Akkoyunlu, I. Erdogan in *Proceedings of 13th International Multidisciplinary Scientific GeoConference, SGEM* (2013), Albena, Bulgaria, Vol. 559 (ISBN: 978-619-7105-03-2)
17. I. Oruc, B. O. Akkoyunlu, I. Erdogan, in *Proceedings of 13th International Multidisciplinary Scientific GeoConference, SGEM* (2013), Albena, Bulgaria, p. 683 (ISBN: 978-619-7105-03-2)
18. B. O. Akkoyunlu, M. Tayanç, *Atmos. Environ.* **37** (2003) 3571 (https://doi.org/10.1016/S1352-2310(03)00349-2)
19. E. Eltan, *Drinking and irrigation water analysis methods.* T. C. Prime Ministry General Directorate of Rural Services, Ankara, 1998, Vol. 15, Publication No: 18, (in Turkish)
20. S. J. Vermette, J. J. Drake, S. Landsberger, *Water Air Soil Pollut.* **38** (1988) 37 (https://doi.org/10.1007/BF00279584)
21. D. D. Alves, E. Backes, L. Rocha-Uriartt, R. P. Riegel, D. M. de Quevedo, J. L. Schmitt, G. M. da Costa, D. M. M. Osório, *Environ. Sci. Pollut. Res.* **25** (2018) 24150 (https://doi.org/10.1007/s11356-018-2505-1)
22. Á. Keresztesi, M-V. Birsan, I-A. Nita, Z. Bodor, R. Szép, *Environ. Sci. Eur.* **31** (2019) 50 (https://doi.org/10.1186/s12302-019-0234-9)
23. L. Tripathee, J. Guo, S. Kang, R. Paudyal, C. M. Sharma, J. Huang, P. Chen, P. S. Ghimire, M. Sigdel, M. Sillanpää, *Atmos. Res.* **234** (2020) 104691 (https://doi.org/10.1016/j.atmosres.2019.104691)
24. P. G. Brewer, in *Chemical oceanography,* J. P. Riley, G. Skirrow, Eds., 2nd ed., Academic Press, London, 1975, p. 417 (ISBN: 0-12-588601-2)
25. W. Baeyens, F. Dehairs, H. Dedeurwaerder, *Atmos. Environ., A* **24** (1990) 1693 (https://doi.org/10.1016/0960-1686(90)90503-F)
26. J. Zobrist, P. Wersin, C. Jaques, L. Sigg, W. Stumm, *Water Air Soil Pollut.* **71** (1993) 111 (https://doi.org/10.1007/BF00475515)

27. C. Okay, B. O. Akkoyunlu, M. Tayanç, *Environ. Pollut.* **118** (2002) 401 (https://doi.org/10.1016/S0269-7491(01)00292-5)
28. Ch. Anatolaki, R. Tsitouridou, *Atmos. Res.* **85** (2007) 413 (https://doi.org/10.1016/j.atmosres.2007.02.010)
29. P. S. Praveen, P. S. P. Rao, P. D. Safai, P. C. S. Devara, D. M. Chate, K. Ali, G. A. Momin, *Atmos. Environ.* **41** (2007) 825 (https://doi.org/10.1016/j.atmosenv.2006.08.049)
30. Ch. Anatolaki, R. Tsitouridou, *Atmos. Res.* **92** (2009) 100 (https://doi.org/10.1016/j.atmosres.2008.09.008)
31. H. Wang, G. Han, *Atmos. Res.* **99** (2011) 190 (https://doi.org/10.1016/j.atmosres.2010.10.004)
32. E. C. Teixeira, D. Migliavacca, S. P. Filho, A. C. M. Machado, J. B. Dallarosa, *An. Acad. Bras. Ciênc.* **80** (2008) 381 (https://doi.org/10.1590/S0001-37652008000200016)
33. Q. Feng, Y. Li, J. Wen, H. Wang, L. Liao, *Environ. Monit. Assess.* **193** (2021) 597 (https://doi.org/10.1007/s10661-021-09396-1)
34. M. Karaca, A. Deniz, M. Tayanç, *Int. J. Climatol.* **20** (2000) 1225 (https://doi.org/10.1002/1097-0088(200008)20:10<1225::AID-JOC535>3.0.CO;2-1).

Journal of the Serbian Chemical Society
JSCS@tmf.bg.ac.rs • www.shd.org.rs/JSCS
J. Serb. Chem. Soc. 87 (7–8) S297–S298 (2022)
Supplementary material

SUPPLEMENTARY MATERIAL TO

The sources and seasonal variations of the chemical components in the deposition samples in Kirklareli, Turkey

ILKER ORUC[1]*, BULENT OKTAY AKKOYUNLU[2] and ILHAN ERDOGAN[3]

[1]Vocational College of Technical Sciences, Kirklareli University, Kirklareli, Turkey, [2]Faculty of Arts and Sciences, Marmara University, Goztepe, Istanbul, Turkey and [3]Faculty of Sciences, Trakya University, Edirne, Turkey

J. Serb. Chem. Soc. 87 (7–8) (2022) 953–967

SAMPLING AREAS

Kirklareli is located in the Thrace part of the Marmara Region in Northwest of Turkey. It is located between 41° 13' and 42° 05' north latitudes, 26° 54' and 28° 06' east longitudes. Kirklareli is surrounded by Bulgaria to the North, the Black Sea to the East, Tekirdag to the South and Southeast, and Edirne to the West. Kirklareli has 180 km of the land border to Bulgaria and 60 km of the seacoast to the Black Sea. Continental climate is dominant in the city center and the temperature difference is high between the summer and winter seasons. The population of Kirklareli city center is approximately 80,000 people.[10] The urban area (41° 44' 03" N and 27° 13' 15" E) and the suburban area (3 km southwest of the city center) (41° 43' 13" N and 27° 11' 36" E) were selected for sampling wet, bulk and dry depositions (Fig. S-1).

---

* Corresponding author. E-mail: ilkeroruc@klu.edu.tr

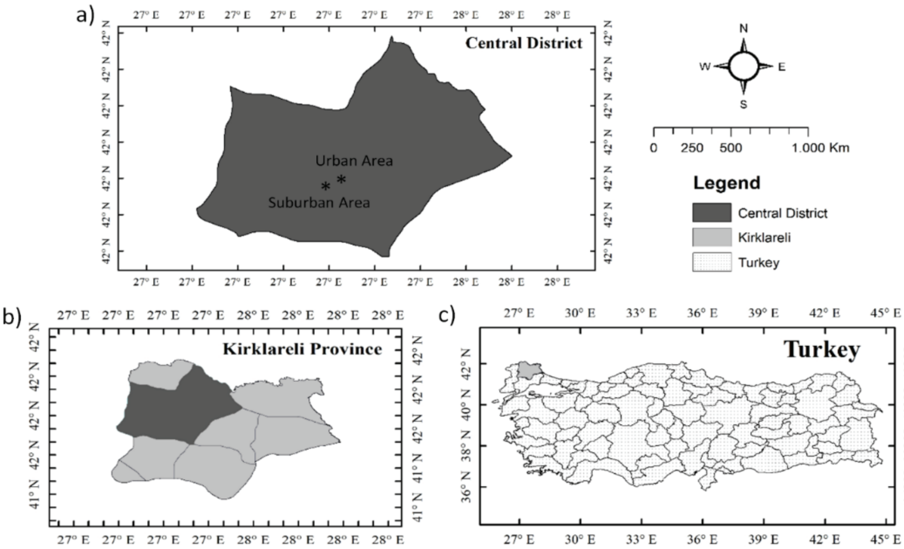

Fig. S-1. The locations of a - Central District of Kirklareli, b - Kirklareli Province, c – Turkey.